



I, undersigned, Camille GILLOT, hereby declare that the work presented in this manuscript is my own work, carried out under the scientific direction of Yanick SARAZIN in accordance with the principles of honesty, integrity and responsibility inherent to the research mission. The research work and the writing of this manuscript have been carried out in compliance with both the french national charter for Research Integrity and the Aix-Marseille University charter on the fight against plagiarism.

This work has not been submitted previously either in this country or in another country in the same or in a similar version to any other examination body.

Cadarache, March 7, 2021



Cette œuvre est mise à disposition selon les termes de la Licence Creative Commons Attribution  
- Pas d'Utilisation Commerciale - Pas de Modification 4.0 International.

## Résumé

L'optimisation et le contrôle des plasmas de tokamak demande de prédire le transport de matière et de chaleur de manière à la fois efficace et fidèle. Déclenchée par des instabilités cinétiques, la turbulence sature par l'interaction de plusieurs échelles. Depuis la petite échelle des tourbillons, jusqu'à la rétro-action sur les profils, en passant par la génération spontanée d'écoulements zonaux et par le transit balistique d'avalanches, tout conspire et s'auto-organise. Des codes de simulation « premiers principes » comme GYSELA résolvent l'évolution de la fonction de distribution gyro-cinétique. Cette voie a beau être fidèle, elle est insuffisamment efficace. Il faut réduire la description. La suppression des dimensions de vitesse intervient à travers le problème de la fermeture non-collisionnelle des équations fluides. Les approches antérieures sont étendues et généralisées en faisant appel à la littérature d'analyse des systèmes dynamiques et de théorie du contrôle. En particulier, nous appliquons les méthodes de réduction par troncature équilibrée et par interpolation rationnelle au modèle Vlasov–Poisson unidimensionnel linéaire. La méthode d'interpolation se distingue par son faible coût et sa facilité d'utilisation, ouvrant des perspectives pour la modélisation de phénomènes plus complexes.

La théorie quasi-linéaire est un passage obligé dans l'abstraction des effets turbulents. Les résultats de simulations non-linéaire par GYSELA sont analysés afin d'identifier la robustesse des propriétés quasi-linéaires des filaments turbulents. Les résultats quasi-linéaires clés sont qualitativement validés. Les vitesses et formes des filaments sont inférés algorithmiquement, et correspondent aux vitesses de groupe et aux modes propres attendus. Toutefois, le chaînon manquant qu'est le spectre du potentiel électrique turbulent doit être spécifié. Un modèle de cinétique d'ondes est établi pour établir les conséquences du déplacement des filaments turbulents sur la génération des écoulements zonaux en géométrie toroidales. Il apparaît que la vitesse de groupe radiale des filaments turbulents peut résonner avec la vitesse de phase des modes acoustiques géodésiques (GAM). Apparaissent alors des dynamiques couplées instables munies d'une propagation radiale balistique. Celles-ci partagent plusieurs propriétés avec les avalanches observées dans les simulations non-linéaires.

## Abstract

Optimal control of tokamak plasmas requires efficient and accurate prediction of heat and matter transport. Growing from kinetic resonant instabilities, turbulence saturates by involving many scales, from the small vortex up to the back-reaction on the density and temperature profiles. Self-organisation processes are of particular interest, encompassing spontaneous zonal flow generation and transport by avalanche. “First principle” numerical simulation codes like GYSELA allow studying the gyro-kinetic evolution of the particle distribution function. The large model size and cost prompts the need for reduction.

Removing velocity dimensions is the so-called collisionless closure problem for fluid equations. Earlier approaches are extended and generalised by calling to the dynamical systems and optimal control literature. In particular, we apply the balanced truncation and rational interpolation to the one-dimensional linear Vlasov–Poisson problem. The interpolation method features a cheap and versatile formulation, opening the door to wider use for more complex phenomena.

Quasi-linear theory is the reference model for abstracting away turbulent effects. The GYSELA three-dimensional output is analysed to estimate the robustness of linear properties in turbulent filaments. Key quasi-linear quantities carry over to the non-linear regime. Effective velocities and shape of turbulent structures are computed, and match expected group velocities and linear eigenmode. Nevertheless, the turbulent potential spectrum must be specified externally to quasi-linear models. Consequences of the turbulent filament motion on the dynamics of the spectrum are investigated using a wave-kinetic model in toroidal geometry. When coupled to the axisymmetric Vlasov equations, the radial filament group velocity resonates to the radial phase velocity of geodesic acoustic modes. Results in radially travelling unstable linear solutions that share many properties of turbulent avalanches seen in numerical simulations.

## Remerciements

En premier lieu, je tiens à remercier Yanick Sarazin et Guilhem Dif-Pradalier pour leur encadrement tout au long de cette thèse. J'ai beaucoup apprécié leur disponibilité et leur réactivité pour répondre à mes questions, interrogations, spéculations et doutes. Je leur suis notamment reconnaissant pour leur conseil, leur confiance, leur soutien (et parfois leur patience) pendant plusieurs périodes de redéfinition, parfois ambitieuses, du programme de recherche.

Je suis reconnaissant aux membres du jury de thèse, Éric Sonnendrücker, Fulvio Zonca, Jérôme Bucalossi, Claudia Negulescu et Jean-Marcel Rax pour leur lecture de ce manuscrit et leur examen exigeant de cette thèse.

Je tiens aussi à remercier l'ensemble de l'équipe des groupes « Théorie et Simulation » et « Divertor et Interaction Plasma-Paroi », et en particulier Xavier Garbet, Virginie Grandgirard et Philippe Ghendrih, pour leur engagement auprès de tous les étudiants sous leur tutelle, ainsi que pour leur disponibilité face au grand nombre de questions plus ou moins saugrenues dont ils ont aussi été servis. Par extension, je souhaite remercier les Chefs d'Institut Alain Bécoulet et Jérôme Bucalossi ainsi que tout le personnel de l'IRFM pour leur accueil bienveillant.

En second lieu, je souhaite remercier la commission de formation doctorale des IPEF et son Président Benoît Lesaffre pour la confiance qu'ils m'ont accordée en m'affectant en formation doctorale, ainsi que Françoise Préteux, Directrice de la Recherche à l'ENPC, pour ses conseils lors de la constitution du dossier devant cette commission. J'en profite pour de nouveau remercier toutes les personnes que j'ai sollicitées en préparation de ce dossier.

En troisième lieu, je remercie les camarades et amis, Guillaume, Elisabetta, Peter, Anastasia, Laurent, Valentin, Mathieu, Robin, Éléonore, Thomas ; et en particulier les colocataires de Pomone, Damien, Axel, Adrien, Lucie, Clément et Mylène<sup>1</sup>, ceux-ci ayant eu à me supporter hors heures ouvrables.

En quatrième lieu, je souhaite remercier les agents de la DDT de la Nièvre, ses Directeurs Nicolas Hardouin et Sylvain Rousset, et en particulier le service Loire Sécurité Risques pour leur accueil depuis septembre 2020.

Enfin, je remercie ma famille pour sa présence.

En espérant faire honneur à la qualité de ce cadre,

---

<sup>1</sup>Quant à Jerry le chat, il connaît mes réserves.

# Introduction

The energy transition is a challenge for this generation. Global warming restructures ecosystems, floods and droughts upset vital resources, and the geopolitical balance are challenged. Since the first oil crisis, an ambitious energy efficiency public policy has been in place in France. This is a long-term endeavour, requiring changing the models of energy production and consumption. The national research strategy has identified clean energy as a central pillar. Fusion research aims at providing a way out, as a “safe, non-carbon emitting and virtually limitless energy”.

Operating a sustainable tokamak requires heating a plasma at temperatures above 150 millions degrees. This energy has to be provided up front, for fusion processes to kick in. The profiles of density and temperature from the tokamak’s core up to its edge need to keep sufficiently peaked, keeping the hot matter away from the energy sink that are the walls. In consequence, the balance is set: the input energy shall not exceed the output. How to maximise the ratio between energy output and input? An answer to this question is provided by Lawson’s criterion (Lawson, 1957). We have confine the heat inside the device for as long as possible. The longer the heat stays inside the plasma core before coming to crash against the device walls, the less energy is required to access the desired temperature.

But heat transport in tokamaks turbulent. And nobody understands turbulence, much less controls it. From the small vortex scale up to the back-reaction on the density and temperature profiles, zonal flows are spontaneously generated, and avalanches cross the lines. Physicists and engineers have been working on both practical and fundamental aspects of turbulent transport for a few centuries now. The problem is perpetually beyond reach. What can be done to overcome this state of facts? We can live with it and hope for the best. We can hammer it with numerical simulations. We can stare and hopefully come up with some insight. The very nature of turbulents asserts itself in its complexity. First-principle simulations allow to witness some complexity. They unlock “God mode” vision, alas without the required God mind. The scientist is provided with an unwieldy puzzle, limited only by his grasping of his own creation.

Simulating tokamak core turbulence usually requires a kinetic description of the phenomena (Dimits *et al.*, 2000). This corresponds to solving the Boltzmann equation for the dynamics of the particle distribution function, coupled to Maxwell’s equations for the electromagnetic field. This description aims to be faithful to the physical phenomena, at the cost of computational and cognitive time. Furthermore, six-dimensional kinetic models are still out of reach for modern supercomputers. Predicting and controlling a fusion device will require a much lighter model, prompting the need to reduce the dynamics.

From there, many attempts models have been developed. The minimal —and most pervasive— is the gyro-kinetic reduction, presented chapter 2. It leverages the strong background magnetic field, and averages out the fast cyclotron motion of charged particles. Codes such as GYSELA solve for the distribution function of particles over a five-dimensional phase space, the cyclotron phase omitted. A five-dimensional phase space being yet too large, a more drastic reduction is required. An entire hierarchy of models has been devised by the scientific community, removing dimension after dimension, until reaching scaling laws. In this manuscript, we will discuss two landmarks in this effort: the removal of the velocity direction, going from the kinetic to the fluid family of models; the removal of the small turbulent scales using generalised quasi-linear formulations. The two processes focus respectively on the two crucial phenomena that are the wave–particle resonance and the non-linear turbulent advection.

The typical method to obtain fluid equations from the Boltzmann equation is integration against moments. The resulting equations are the so-called moment hierarchy, where the evolution of each

moment depends on the value of higher-order moments. Some kind of truncation is necessary to obtain a finite-dimensional system. The closure rule specifying the truncated moments plays a crucial part in the accessible dynamics. Most importantly, the emulation of wave–particle resonances like Landau damping requires a so-called *collisionless* closure (Hammett & Perkins, 1990). Many have been proposed in the community, founded on various physical considerations.

Among the scientific community, a large body of work is devoted to the mathematical problem of model order reduction. The starting point is an open control system: an exciting low-dimensional input forces the evolution of a larger-dimensional system, which is observed using a reduced amount of outputs. Then, how to most efficiently reproduce the input–output relation, without resorting to simulations of the full system? Many methods have been proposed in the linear case. In chapter 3, we chose to apply two of them. Balanced truncation is rooted in control theory, dynamical subspaces by reachability and observability, then truncating on these grounds. Rational interpolation attempts to directly formulate a reduced transfer function from the analytically computed kinetic transfer function. Both resulting models will be numerically compared to earlier closure proposals.

The other curse of tokamak modelling lies in the non-linear advection fueling turbulent processes. Thin magnetic-field-aligned filaments of electric potential grow inside the plasma, and act as vortices mixing it. As these filaments typically correspond to toroidally asymmetric components, so the problem is double: how to stop describing the toroidal direction, without a catastrophic mis-estimation of turbulence? The unavoidable method is the so-called quasi-linear model. It consists in approximating the turbulent filament with the linear unstable eigenmode from which they grow. The problem of transport is then focused on the saturation of turbulence, how much energy it stores. The quasi-linear model has been heated debated (Adam *et al.*, 1979; Elskens & Escande, 2002; Diamond *et al.*, 2010; Besse *et al.*, 2011), concerning its limits of validity. Meanwhile, we would like to decypher the self-organisation of the plasma, separating the transport through avalanche processes from diffusive mixing. In this vein, a natural question is whether avalanches are composed of a single turbulent filament or of an assemblage. In addition, can quasi-linear models recover such avalanching?

To this end, we perform a detailed analysis of the turbulent filaments from the GYSELA non-linear simulations in chapter 4 and 5. Notably, we leverage the available three-dimensional outputs to access a key linear estimate: the magnitude ratio and phase shift between the pressure and potential fluctuations, to compare it to the output of the quasi-linear code QuaLiKiz. Avalanches being recognised by their motion, we design, implement and operate an image registration algorithm to compute effective velocities and shape of turbulent filaments. The results are compared to expected group velocities and mode structure from linear analysis. These velocities are then used to estimate a Lagrangian correlation time of the filaments. Kubo numbers constructed from this correlation time are of a few units: the non-linear regime is on par with the stochastic transport regime. The linear properties of the filaments appear to be robust, even in this regime, but the integrated heat fluxes depart from QuaLiKiz’s saturation rule.

As filaments retain their linear properties, we turn ourselves to the turbulent potential spectrum. Numerical analysis suggests the spectrum’s fluctuations to be responsible for most of the fluctuations of the heat flux in GYSELA data. In chapter 6, the dynamics of this spectrum are investigated using a wave–kinetic formulation. This approach is the natural continuation of the quasi-linear model: it considers the statistics of turbulent filament, viewed as pseudo-particles with a motion dictated by their linear dispersion relation. Coupling the wave–kinetic dynamics to axisymmetric Vlasov dynamics reveals the possibility of a resonance between the wave radial group velocity and the geodesic–acoustic modes. The resulting unstable mode is radially travelling, and features similarity with observed properties of turbulent avalanches.

Finally, chapter 7 details the extension of GYSELA to electromagnetic fluctuations. The determining equations are derived, along with the adopted implementation strategy. Test simulations are presented.

# Table of contents

<b>Résumé</b>	<b>3</b>
<b>Abstract</b>	<b>3</b>
<b>Remerciements</b>	<b>4</b>
<b>Introduction</b>	<b>4</b>
<b>1 Plasmas, tokamaks, and their modelling</b>	<b>11</b>
1.1 Fusion, plasmas, and tokamaks . . . . .	11
1.1.1 Statement of the problem . . . . .	11
1.1.2 Dynamics of hot plasmas . . . . .	12
1.1.3 The transport problem . . . . .	13
1.2 Model order reduction . . . . .	14
1.2.1 The gyro-kinetic model . . . . .	15
1.2.2 GYSELA . . . . .	15
1.2.3 Closure problem for reduction of kinetic systems . . . . .	16
1.2.4 Closure problem for non-linear dynamics . . . . .	17
1.2.5 Beyond the GYSELA model . . . . .	17
1.3 Outline of the thesis . . . . .	18
1.4 Conventions . . . . .	19
<b>2 Gyrokinetic model for the plasma core</b>	<b>21</b>
2.1 Gyrokinetic particle dynamics . . . . .	21
2.1.1 Equations of motion . . . . .	21
2.1.2 Unperturbed dynamics . . . . .	22
2.1.3 Finite Larmor radius effects . . . . .	23
2.1.4 Coupling to the Poisson equation . . . . .	24
2.1.5 Treatment of the electrons . . . . .	25
2.1.6 Coupling to the Ampère equation . . . . .	26
2.1.7 Conservation laws . . . . .	28
2.2 Linear kinetic interchange instability . . . . .	30
2.2.1 Particle dynamics . . . . .	31
2.2.2 Fluid response . . . . .	33
2.2.3 Effect of a corrugated zonal flow . . . . .	37
2.2.4 Kinetic response . . . . .	39
2.3 Ideal MHD instabilities . . . . .	41
2.3.1 Equilibrium current profile . . . . .	41
2.3.2 Non-resonant region . . . . .	42
2.3.3 Resistive resonant current sheet . . . . .	43

<b>3</b>	<b>Model order reduction approach to the collisionless closure problem</b>	<b>47</b>
3.1	Review of the Landau mechanism . . . . .	48
3.2	The fluid hierarchy truncation . . . . .	49
3.3	Review of the balanced truncation method . . . . .	50
3.3.1	Notions of reachability and observability . . . . .	50
3.3.2	Usage for model order reduction . . . . .	51
3.3.3	Numerical investigation . . . . .	52
3.4	Review of interpolation-based reduction . . . . .	52
3.4.1	Construction of the matrices . . . . .	54
3.4.2	Collisionless closures as special cases . . . . .	55
3.5	Numerical comparison with known closure schemes . . . . .	56
3.5.1	Accuracy of the Vlasov dynamics . . . . .	56
3.5.2	Coupled Vlasov-Poisson problem . . . . .	57
3.6	Discussion of the method . . . . .	59
3.6.1	Back to real space . . . . .	59
3.6.2	Application to other kinetic problems . . . . .	59
3.6.3	Non-linear extension . . . . .	60
3.7	Conclusion . . . . .	60
<b>4</b>	<b>Persistence of linear properties in flux-driven turbulence</b>	<b>63</b>
4.1	Quasi-linear estimation of the fluxes . . . . .	63
4.1.1	The quasi-linear problem . . . . .	64
4.1.2	The saturation issue . . . . .	64
4.1.3	Relation to the Hopf hierarchy . . . . .	65
4.1.4	The locality assumption . . . . .	66
4.2	Persistence of linear properties in turbulent dynamics . . . . .	67
4.2.1	The setup . . . . .	67
4.2.2	Strength of the non-linear effects . . . . .	68
4.2.3	Comparison of heat fluxes . . . . .	69
4.2.4	Possible origin of the discrepancy . . . . .	71
4.3	Influence of the turbulent intensity . . . . .	72
4.4	Conclusion . . . . .	73
<b>5</b>	<b>Kinematics of turbulent fluctuations</b>	<b>75</b>
5.1	Interplay between turbulence and zonal flows . . . . .	75
5.2	Motion inside the flux-surface . . . . .	77
5.3	Dimensions of the turbulent filaments . . . . .	79
5.3.1	Typical correlation lengths . . . . .	79
5.3.2	Principal directions . . . . .	80
5.4	Radial motion of the structures . . . . .	81
5.4.1	Lagrangian correlation time . . . . .	81
5.4.2	Partition of energy . . . . .	83
5.4.3	Non-linear radial velocity . . . . .	84
5.5	Radial patterns in turbulence . . . . .	85
5.6	Conclusion . . . . .	87
<b>6</b>	<b>Investigation of tokamak turbulent avalanches using wave-kinetic formulation</b>	<b>89</b>
6.1	Derivation of the wave-kinetic equation . . . . .	91
6.2	Coupling to the profile . . . . .	94
6.3	Drift wave model . . . . .	96
6.4	Generalised ITG model . . . . .	97
6.5	Effect of toroidicity on the zonal instability . . . . .	97
6.6	Conclusion . . . . .	101

<b>7</b>	<b>Electromagnetic effects in GYSELA</b>	<b>103</b>
7.1	Statement of the problem . . . . .	103
7.1.1	Magnetic cancellation . . . . .	104
7.1.2	Methods from the other codes . . . . .	105
7.1.3	Change of variable scheme . . . . .	106
7.1.4	Boundary conditions . . . . .	108
7.1.5	Conserved quantities in mixed variables . . . . .	108
7.2	Application to GYSELA . . . . .	109
7.2.1	Modifications to data structures . . . . .	110
7.2.2	Modification to the time stepper . . . . .	110
7.2.3	Change of variable . . . . .	111
7.2.4	Modifications to the advection equations . . . . .	112
7.2.5	Initial distribution function . . . . .	112
7.3	Numerical tests . . . . .	113
7.3.1	Internal kink mode test . . . . .	113
7.3.2	Tearing mode test . . . . .	115
7.4	Future directions . . . . .	116
<b>A</b>	<b>Derivation of the drift-kinetic Lagrangian</b>	<b>119</b>
<b>B</b>	<b>Derivation of the electromagnetic action principle</b>	<b>121</b>
<b>C</b>	<b>Linearized Vlasov equation</b>	<b>123</b>



# Chapter 1

## Plasmas, tokamaks, and their modelling

Relevant simulations of heat transport in tokamaks are kinetic and non-linear. Such numerical works make equations hard to think about, and heavy to simulate. We need to reduce them in some way, make them more amenable to numerical and analytical work.

### 1.1 Fusion, plasmas, and tokamaks

Most of the material in this chapter is considered fundamental knowledge in the community. Practical references include (Rax, 2005; Wesson, 2011), and will not be cited in-text.

#### 1.1.1 Statement of the problem

Fusion is a nuclear reaction: two light atomic nuclei come together, and fuse. The mass of the reaction products is lower than the one of the reactants, the excess energy is transformed into kinetic energy of the products. Achieving it is subtle: atomic nuclei have a positive electric charge, and repel each other. In order to approach each other enough, the atomic nuclei need to overcome this repulsion by collide at a sufficient velocity. In a gas, the typical velocity of particles is measured using the temperature: in order to achieve fusion, we need a hot enough gas. The most accessible reaction is the deuterium–tritium fusion, which requires temperature of the order of 150 million degrees, ten times the temperature in the core of the Sun. To achieve fusion, we need to create a hot enough gas to trigger reactions. This heating costs energy, the very thing we are trying to produce. In order to keep have a net production, we need to keep this heat confined somehow.

Actually, stars cheat. They are massive and have time before them. The confinement is guaranteed by gravity, and they can make do with horribly slow reactions. On Earth, gravitational confinement is not an option, and we need to produce energy at a reasonable pace.

At the large temperature required for fusion to take place, particles collisions are more than sufficient to tear the electrons away from their atom. Results a bath of ions and electrons moving around, and getting forcefully separated at each encounter. This state of matter is called a plasma. As the ions and electrons are untied, the overall matter is responsive to electromagnetic fields.

This property can be used for confinement, opening the field of “magnetically confined fusion”. Instead of using the plasma’s own weight to press on it as stars do, we can use magnetic pressure. Charged particles in a magnetic field follow the cyclotronic motion, turning around the magnetic field lines, while traveling freely along the magnetic direction. To avoid leaks, the magnetic field lines must close on themselves, and the fusion devices must have a torus shape. Coils generate a toroidal magnetic field inside the chamber where the plasma is confined (figure 1.1). The design is simple to state: heat the core of the plasma near 150 million degrees to trigger fusion reactions, and keep the plasma cool (less than 5 000 °C) in its edge, near the device walls, to avoid melting them. The problem is to do this in an economical way, consuming less energy than is output by

the fusion reactions. Energetic efficiency happens by maximising Lawson’s triple product  $nT\tau_E$  of density, temperature and confinement time (Lawson, 1957).

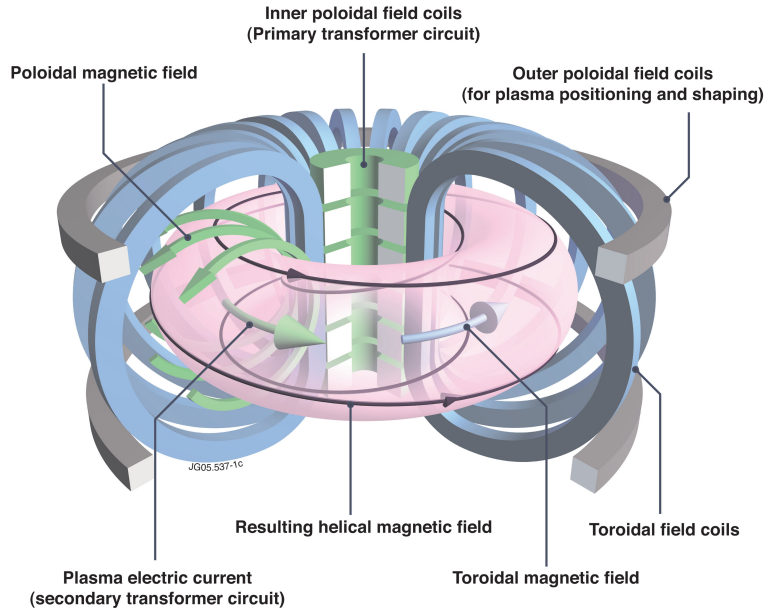


Figure 1.1: Schematic picture of a tokamak, featuring the plasma (pink). The different sets of coils generate the background toroidal magnetic field and control the position of the plasma. Image: EuroFusion.

### 1.1.2 Dynamics of hot plasmas

As the plasma is constituted by disordered charged particles, it generates its own electromagnetic fields. When positive and negative charges get too far away, an electric field pulls them back together. The charges oscillate around each other in their organisational attempt. The information is carried by Langmuir waves, oscillating at the plasma frequency  $\omega_p = \sqrt{n_e e^2 / \epsilon_0 m_e}$ . The typical allowed distance is the Debye length  $\lambda_D = v_{th,e} / \omega_p$ . ( $e$ ,  $m_e$ ,  $n_e$  and  $v_{th,e}$  are the electron charge, mass, density and thermal velocity.  $\epsilon_0$  is the vacuum permittivity.) For larger scales, the plasma self-organises so as to screen naked charges, and appears globally neutral. This time and space scales are very small, of the order of  $\lambda_D \sim 2\mu m$  and  $\omega_p / 2\pi \sim 90$  GHz for typical fusion plasmas.

The strong magnetic field  $\vec{B}$  dictates a preferred direction for the particle motion. Along the field, they roam almost free. In the other directions, the Larmor motion makes them loop around the field at the cyclotron frequency  $\omega_c = eB/m$ , with a typical radius around of the Larmor radius  $\rho = v_{\perp} / \omega_c$ . The current loop produces a magnetic moment  $\mu = mv_{\perp}^2 / 2B$ , with  $v_{\perp}$  the particle perpendicular velocity. For electrons,  $\omega_{ce} / 2\pi \sim 140$  GHz and  $\rho_e \sim 50\mu m$ . For ions,  $\omega_{ci} / 2\pi \sim 80$  MHz, and  $\rho_i \sim 2$  mm. Those frequency ranges are used to heat the plasma using resonant cyclotron waves.

The macroscopic scales are the plasma minor radius  $a$ , of a few metres, and the major radius  $R$  about three times larger. Following the direction of the magnetic field, an electron at thermal velocity turns around the torus at 500 kHz, and an ion at 10 kHz. The inhomogeneous electromagnetic field warps Larmor current loops so that their magnetic moment  $\mu$  is conserved. Particles move faster on the one side, slower on the other, and drift from one field line to the next in average. The electric field  $\vec{E}$  induces the  $E \times B$  drift 1.1. The inhomogeneous magnetic field induces the curvature and “grad  $B$ ” drifts 1.2. Let  $v_{\parallel}$  be the velocity parallel to the magnetic field,  $v_{\perp}$  the

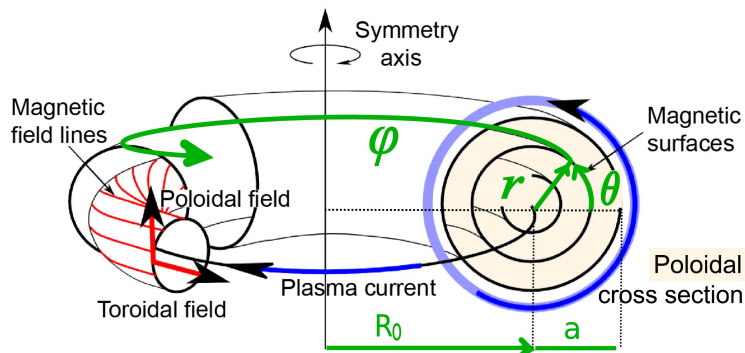


Figure 1.2: Coordinate system and used notations inside the tokamak.

particle velocity perpendicular to the magnetic field,

$$\vec{v}_E = \frac{\vec{E} \times \vec{B}}{B^2} \quad (1.1)$$

$$\vec{v}_D = \frac{mv_{\parallel}^2}{eB} [\vec{\nabla} \times \vec{b}]_{\perp} + \frac{mv_{\perp}^2}{e} \frac{\vec{B} \times \vec{\nabla} B}{B^3} \quad (1.2)$$

Because of the vertical magnetic drift, ions move downwards, and electron upwards. To avoid a charge separation, the magnetic field lines need to be helical, instead of purely toroidal, and assemble into nested closed magnetic surfaces. The particles then split their time above and below the plasma core, and on average stay on their magnetic surface. The helicity of the magnetic field is called the safety factor,  $q = rB_{\phi}/RB_{\theta}$  with  $B_{\theta,\phi}$  the poloidal and toroidal components of the magnetic field. There are two ways to achieve that: generating the helical field directly using the coils, making a stellarator device; or by inducing an electrical current inside the plasma itself, making a tokamak. We will focus on the latter.

For toroidally symmetric electromagnetic fields, the motion of the particles admits three invariants: their energy  $E = mv_{\parallel}^2/2 + \mu B$ , their magnetic moment  $\mu$ , and their toroidal momentum  $P_{\phi} = mRv_{\parallel}B_{\phi}/B$ . As a consequence, the motion is integrable: the deviation due to the drifts is bounded, and particles are confined. Particles in the tokamak observe two typical categories of motion. Passing particles run freely along the magnetic field, and make the full run around the poloidal direction. Trapped particles do not have enough energy, and bounce back pushed by magnetic pressure (figure 1.3) Because of the magnetic drift, their orbits have finite extent around a reference magnetic surface. Because the magnetic field is sheared, the followed direction changes with their position. As a consequence, the magnetic drift induces a toroidal motion. A toroidal drift for passing particles, a precession for trapped ones. This toroidal motion is much slower, and can be estimated to turn around the tokamak at around 0.8 kHz. A more precise description of the particle trajectory will be given in paragraph 2.1.

### 1.1.3 The transport problem

Deconfinement happens whenever one of the three invariants is lost. The transport problem involves understanding how much it happens: how much heat crosses each magnetic surface. Two processes can deconfine them: collisions (changing  $\mu$ ) and turbulence (changing  $E$  and  $P_{\phi}$ ). After a collision, the involved particles have redistributed their energy and momentum. This redistribution modifies their trajectory, swaps between passing and trapped motions, and change their reference field line. This process is the basis for the so-called neoclassical transport. Neoclassical transport is predicted by a mature and well tested theory (Helander & Sigmar, 2005).

The other process is the generation of electromagnetic perturbations. While the magnetic drift effect has been mitigated by the helical magnetic field, it has not been eliminated, and pursues its dark design. Particles on the low-field side of the tokamak are still pushed outwards. In addition, the pressure gradient also pushes outwards. This creates the ground for the interchange instability. The interchange instability develops filaments aligned along the magnetic field, of a few Larmor

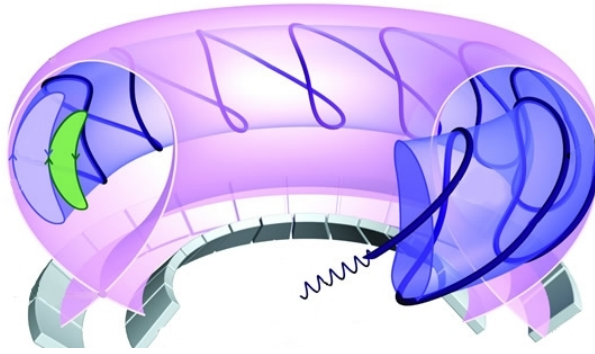


Figure 1.3: Schématic view of the trajectory of a trapped particle in the tokamak, featuring the cyclotron motion, the poloidal bouncing and the toroidal precession. The safety factor  $q$  is very low for image clarity. Image: EuroFusion.

radii wide in the perpendicular directions, and grows at the curvature drift time scale. Those filaments create a local  $E \times B$  drift, which tends to mix the plasma. Heat gets transported out. The mechanism of the ion-temperature-gradient mode is discussed paragraph 2.2.

Many other unstable mechanisms exist in the tokamak. The helicity of the magnetic field lines requires the presence of a current running toroidally inside the plasma. Some field lines close on themselves, and may trap current inside of them, which would start running helically instead of toroidally. By attracting neighbouring currents, this current sheet can grow. This results in a magnetic perturbation. This perturbation can for instance move the plasma out of its flux surfaces. Another possibility is the creation of “magnetic islands”, inside which the plasma is mixed, and heat gets transported. Those effects will be discussed in paragraph 2.3 and chapter 7.

The behaviour of infinitesimal perturbations is dictated by the equilibrium magnetic field and properties of the laminar plasma. When these perturbations grow, this linearity hypothesis is no longer valid, and the perturbations influence and couple each another. While the linear regime is understood and efficiently computed by numerical codes, most traditional tools break down in this non-linear regime. Most importantly, the saturation of those perturbations precisely comes from such non-linear behaviours.

The generic behaviour of an electromagnetic perturbation is to get damped by the Landau damping effect (Elskens & Escande, 2002). Electromagnetic perturbations exchange energy back and forth with particles. When there is a resonance, particles closest to this resonance are most involved. When a slow particle is accelerated, get even more involved. Conversely, decelerated slow particles get exonerated. Conversely for fast particles. As there are more slow particles than fast particles, the wave attracts more energy sinks than energy sources, and gets damped. This effect will be discussed more precisely in chapter 3. An electromagnetic perturbation is unstable when the particles give it energy, instead of depleting it. The drive for many instabilities is mixed between a reactive component and a kinetic component (Melrose, 1989; Garbet, 2001). In the former case, the thermodynamical plasma exchanges energy with the perturbation. In the latter, only particular family of particles resonates with the perturbation and feeds it, while the rest of the plasma remains passive.

Because of the very low collisionality, turbulence in the core tokamak plasma is kinetic. As a consequence, many modelling attempts based on fluid equations miss important features (Dimitis *et al.*, 2000): they consider the plasma as a Maxwellian, in a thermodynamical limit. Modern core plasma simulations require kinetic formulations. Because of the increased dimension of the phase space, the simulation cost explodes. This is a challenge for practical applications of numerical works for day-to-day operations of fusion devices.

## 1.2 Model order reduction

The prediction of tokamak performances faces two issues: the model size —because of the kinetic description—, and its complexity —because of the non-linearity and the geometry. Both trigger

the need for a reduced description of the system, reducing both the dimension and the subtlety of the dynamics. Reduced models aim at finding the optimal tradeoff between accuracy and rapidity.

### 1.2.1 The gyro-kinetic model

Before constructing a reduced model, we need a full model. The six-dimensional dynamics is expensive to compute, both by the required time stepping, and by the size of the six-dimensional phase space. In order to perform tractable simulations, we need a minimal reduction step. At the time scales of turbulence, a few kiloHertz, the precision of the cyclotron motion is not relevant. This motion is very fast even in comparison to the transit along magnetic field lines. The gyro-kinetic model aims at abstracting out this fast Larmor motion. The motion of the particle is replaced by the motion of the centre of the loop  $\vec{X}$  and its radius. The position of the particle on the loop is removed from the description. As the gyro-centre moves by the parallel transit along the magnetic field, the simulation time steps can be much larger.

This gyro-centre reduction relies on the conservation of the magnetic moment  $\mu$  (equation 1.3) of the cyclotron loop, related to its radius. The conservation of  $\mu$  allows to further simplify the model, as the kinetic dynamics for different values of  $\mu$  are independent.

$$\mu = \frac{mv_{\perp}^2}{2B} \quad (1.3)$$

with  $v_{\perp}$  the velocity of the particle in its cyclotron motion. Several subtleties arise when taking full account of the perturbations to the electromagnetic fields. Those will be detailed in chapter 2. The dynamics of the gyro-centre distribution function  $\mathcal{F}(\vec{X}, v_{\parallel}, \mu)$  is given by the Boltzmann equation

$$\partial_t \mathcal{F} + \text{div}(\dot{\vec{X}} \mathcal{F}) + \partial_{v_{\parallel}}(\dot{v}_{\parallel} \mathcal{F}) = \text{Collisions} + \text{Sources} \quad (1.4)$$

where  $v_{\parallel}$  is the velocity in the direction parallel to the magnetic field.  $\dot{\vec{X}}$  is the sum of the parallel velocity, the curvature drift and the  $E \times B$  drift.  $\dot{v}_{\parallel}$  is the sum of the ‘‘magnetic mirror’’ force due to the conservation of  $\mu$ , and the parallel Coulomb force. The collision term contains the effect of all the short-distance interaction between particles, taking place below the Debye scale. The sources correspond to the matter and heat feeding terms. This Vlasov equation is coupled to the quasi-neutrality equation 1.5 (often called Poisson equation for its form).  $n_e$  and  $n_i$  are the electron and ion densities. The right-hand-side, the ion density, contains two terms. The integral is the density of gyro-centres. The divergence is the so-called polarisation density, accounting for the deformation of the Larmor loops by the electric field.

$$n_e = \int J[\mathcal{F}] \frac{2\pi B}{m} d\mu dv_{\parallel} + \text{div} \left( \frac{m n_i}{B^2} \vec{\nabla}_{\perp} \phi \right) \quad (1.5)$$

where  $J$  is the gyro-average operator, taking into account the finite Larmor radius.

### 1.2.2 GYSELA

Even the gyro-kinetic dynamics remain intractable for by-hand computations. In order to simulate the gyro-kinetic equations, we will use the GYSELA code (Grandgirard *et al.*, 2016). GYSELA is a semi-Lagrangian non-linear global flux-driven full- $f$  electrostatic gyro-kinetic code for tokamak turbulence simulations.

**Backward Semi-Lagrangian** The semi-Lagrangian scheme exploits the conservation of the distribution function along the trajectories of particles. For each arrival phase space position  $(\vec{X}, v_{\parallel}, \mu)$ , the particle’s trajectory is computed backwards, to find their position at an earlier time. The value of the latter distribution function at the arrival time is obtained by interpolating the earlier distribution at the particles’ origin position. Alternative schemes are the forwards semi-Lagrangian scheme, computing the particles trajectories forward in time and performing a projection (Crouseilles *et al.*, 2009); the Eulerian scheme, directly using discrete derivatives in equation 1.4 (Candy & Waltz, 2003b; Peeters *et al.*, 2009; Görler *et al.*,

2011; Idomura, 2016); and the PIC scheme, tracking the position of macro-particles from the beginning of time (Bottino *et al.*, 2010). The semi-Lagrangian scheme benefits from good stability properties, and is notably free of tight CFL conditions bounding the allowed time steps in Eulerian schemes.

**Electrostatic** Only the evolution of the electrostatic potential  $\phi$  is computed, and with it the fluctuations of the electric field. This approximation is acceptable in the plasma core, where turbulence is expected to have a small magnetic component. However, magnetic fluctuations reveal particularly important at the edge because of larger gradients.

**Non-linear** The trajectories of the particles contain the entirety of the  $E \times B$  drift, without a splitting between equilibrium flow and perturbations. Most concurrent codes have both the linear and the non-linear versions. By construction, GYSELA does not separate equilibrium from fluctuations, so has no linear version.

**Full- $f$**  The complete distribution function is simulated. This is contrary to *delta- $f$*  codes, which simulate the departure from a reference distribution function. GYSELA's description avoids prescribing an expected shape to the distribution function  $\mathcal{F}$  and allows for arbitrary deviation from the reference solution (except for the ion polarisation, but this limitation is planned for removal).

**Global** The core plasma is simulated in its entirety, from the very core to the wall. This is in opposition to *local* codes which only simulate a reduced set of magnetic surfaces by usually focusing on so-called flux tubes. This distinction will be discussed paragraph 4.1.4.

**Flux-driven** The forcing of the dynamics is done using a heat source at near the core, letting it be transported, and removing the excess at the edge. As such, the values of the thermodynamical gradients evolve self-consistently, instead of being constrained in the neighbourhood of a chosen profile in *gradient-driven* codes. This approach aims at reproducing the experimental set-up where all the quantities evolve on an equal footing.

Simulations using GYSELA cost 2 millions CPU hours for approximately 1 millisecond in real time. This cost is highly inadequate for integrated modelling of a fusion device. An additional model reduction is required. The goal is twofold: faster simulations using a smaller simulation state space, and a more interpretable model, by reducing the subtlety of the non-linearity.

### 1.2.3 Closure problem for reduction of kinetic systems

Consider the Boltzmann equation 1.4 on a distribution function  $\mathcal{F}(r, \theta, \varphi, v_{\parallel}, \mu)$ . Most of the numerical cost comes from the dimension of the problem: five variables, with a grid for each one. This information is too abundant, and the interest lies on its first few statistical moments: density  $N$ , parallel momentum  $NV_{\parallel}$ , parallel and perpendicular pressures  $P_{\parallel}, P_{\perp}$ , flux tensor  $Q...$  with a catch: the dynamics of any such cumulant depends on the next one. We get an infinite hierarchy of equations, and need to close it. For instance, the so-called gyro-fluid hierarchy is given by

$$\partial_t N + \operatorname{div} \left( NV_{\parallel} \vec{b} + N \frac{\vec{b} \times \vec{\nabla} \phi}{B} - \frac{mNV_{\parallel}^2 + P_{\parallel} + P_{\perp}}{eB} \frac{\vec{b} \times \vec{\nabla} B}{B} \right) = \text{Particle source} \quad (1.6)$$

$$\begin{aligned} & \partial_t (NV_{\parallel}) + \operatorname{div} \left( NV_{\parallel}^2 \vec{b} + P_{\parallel} \vec{b} + NV_{\parallel} \frac{\vec{b} \times \vec{\nabla} \phi}{B} \right) \\ & - \operatorname{div} \left( \frac{mNV_{\parallel}^3 + 3P_{\parallel} V_{\parallel} + Q_{\parallel, \parallel} + Q_{\parallel, \perp}}{eB} \frac{\vec{b} \times \vec{\nabla} B}{B} \right) = \text{Torque source} \quad (1.7) \end{aligned}$$

A truncation needs to be done somehow. The definition of the truncated moments is subtle: an arbitrary choice of moments does not necessarily produce a positive distribution function (Lukacs, 1970, thm. 7.3.5). The choice of the closure subtly influences the way the distribution function evolves. Several propositions exist in the literature, formulating different gyro-fluid models (Brizard, 1992; Madsen, 2013). The traditional fluid models suppose the distribution remains close to a

Maxwellian: a quasi-normal distribution function or a generalisation of it. More elaborate models aim at choosing the right closure so as to recover the collisionless dynamics (Hammett & Perkins, 1990; Chang & Callen, 1992; Mattor & Parker, 1997; Smith, 1997; Sarazin *et al.*, 2009). We will discuss this collisionless closure problem in chapter 3, and will propose a general method based on dynamical system theory.

### 1.2.4 Closure problem for non-linear dynamics

The kinetic and the non-linear problem share a key feature: both can be framed as an infinite hierarchy of systems. In the kinetic case, this is the fluid moment hierarchy. In the non-linear case, the equivalent curse is the Hopf distribution (Hopf, 1952) stating the probability of plasma states. The non-linear system is generally chaotic, meaning that repeated experiments lead to different realisations of turbulence. The exact properties of the distribution function up to the Debye length are irrelevant, we perform an *average over experiments*. Instead of averaging on velocity like the kinetic to fluid reduction, we average on ignored space directions, and on all experiments that are indistinguishable below a certain scale. Again, a truncation needs to be done. The mean value gives us the equation for the profiles 1.8. Closing after it requires modelling the turbulent flux term in equation 1.8, akin to Reynolds-averaged models. Several solutions exist, we mention direct-interaction approximation (Yakhot & Orszag, 1986; Krommes, 2002) and quasi-linear theories (Adam *et al.*, 1979).

$$\begin{aligned} \partial_t \langle \mathcal{F} \rangle + \underbrace{\operatorname{div}(\langle \dot{\vec{X}} \rangle \langle \mathcal{F} \rangle) + \partial_{v_{\parallel}}(\langle \dot{v}_{\parallel} \rangle \langle \mathcal{F} \rangle)}_{\text{Laminar average flow}} \\ + \underbrace{\operatorname{div}(\delta \dot{\vec{X}} \delta \mathcal{F}) + \partial_{v_{\parallel}} \langle \delta \dot{v}_{\parallel} \delta \mathcal{F} \rangle}_{\text{Turbulent fluxes}} = \text{Sources} + \text{Collisions} \end{aligned} \quad (1.8)$$

where the  $\langle \cdot \rangle$  denotes this average on experiments, and  $\delta \mathcal{F} = \mathcal{F} - \langle \mathcal{F} \rangle$ .

The idea behind quasi-linear theory is to consider a turbulence of interacting waves. The full gyro-kinetic problem can be linearised around the average state  $\mathcal{F}$ . The solution to the linearised problem are electromagnetic waves, propagating in the plasma as a dielectric medium. Those waves involve a fluctuation  $\delta \dot{\vec{X}}$  of the  $E \times B$  drift and  $\delta \mathcal{F}$  of the distribution function. Their product contributes to the turbulent flux. However, because the problem has been linearised, the information on the wave amplitude is lost. There is no information on how unstable waves stop growing and saturate. This has to be closed using a saturation rule, essentially an approximation of the spectrum of turbulent electromagnetic fluctuations. The quasi-linear approximation and its application in tokamak plasmas will be discussed in chapter 4.

This turbulent spectrum is directly related to the quadratic average  $\langle \delta \mathcal{F}^2 \rangle$ . Its evolution depends on some cubic term. The latter can be closed by zeroing it out, giving second cumulant models (Farrell & Ioannou, 2007; Marston *et al.*, 2008; Srinivasan & Young, 2012), or by relating it to the spectrum, giving quasi-normal models (Benney & Saffman, 1966; Newell, 1968; Briard, 2017). As in the kinetic case, great care has to be taken to ensure the model is realisable (Pope, 2000): the ignored details should not correspond to nonphysical states. Chapter 5 discusses the kinematic phenomenology of turbulent structures, and their motion inside the plasma. The modelling choice is reminiscent of the wave-kinetic system, but for self-consistent non-linear turbulent structures. As the turbulent fluctuation are modified by the variations of the background flows, an analytic exploration of the coupling of a wave-kinetic model to the background plasma will be attempted chapter 6.

### 1.2.5 Beyond the GYSELA model

GYSELA simulates the behaviour of the turbulence in an electrostatic limit with limite electron dynamics. When studying turbulent transport in the core, we choose plasma without any violent magneto-hydro-dynamic instabilities. The micro-instabilities constitutive of turbulence have a small magnetic component (Garbet, 2001), and all works well. This causes difficulties in two cases.

Limited electron dynamics reduce the access to relevant turbulent micro-instabilities, like the trapped electron modes (TEM) and the electron temperature gradient modes (ETG). Furthermore, the transport of density is severely limited to ensure quasi-neutrality. In order to consistently model those effects, we need fully kinetic electrons. Electrostatic simulations with fully kinetic electrons feature spurious unphysical modes, like the  $\omega_H$  mode (Lee, 1986). Simulating perturbations of the magnetic field transforms those modes into lower-frequency and more sensible Alven modes.

The current trend is to investigate the effects of turbulence towards the plasma edge. Farther from the plasma core, the magnetic component of the turbulent fluctuations increase. The relevant parameter is the normalised  $\beta$  parameter (Maget, 2009), which scales like the inverse density gradient. In a tokamak pedestal, the density gradient is stronger, and magnetic fluctuations are significant. In order to increase the relevance of GYSELA for edge turbulence modelling, the extension of the code to handle magnetic fluctuations will be discussed chapter 7.

### 1.3 Outline of the thesis

Chapter 2 reviews the derivation of the electrostatic and electromagnetic gyro-kinetic models. Their principal conservation properties are emphasised. A summary derivation of the ITG instability is provided, providing a justification of the main results.

Chapter 3 reviews the phenomenology of Landau damping, and its connection to the collisionless closure problem. The problem of the fluid closure for the collisionless linear Vlasov system is investigated using a perspective from control theory and model order reduction. Two methods are borrowed from model order reduction literature, namely balanced truncation and interpolatory model reduction. Their principal results are stated and briefly justified. The methods are applied to the 1D–1V Vlasov–Poisson problem. The first few reduction singular values from balanced truncation are well-separated, indicating potentially low-dimensional dynamics. To avoid large-dimensional numerical work, a reduced model is formulated using rational interpolation, generalising the seminal work from Hammett and Perkins. The resulting models are found to outperform the state-of-the-art models for thermal phase velocities. Thanks to the versatility of this formulation, an application to toroidal gyro-kinetic dynamics is discussed. The contents of this chapter have been submitted as (Gillot *et al.*, 2020c).

Chapter 4 reviews the assumptions behind the quasi-linear model for plasma turbulence. Both quasi-linear assumptions and predictions are confronted to the data output by non-linear GYSELA simulations. The output of the quasilinear integrated modelling code QuaLiKiz is compared to the GYSELA heat fluxes. An article stating the results of this chapter has been submitted as (Gillot *et al.*, 2020b).

In chapter 5, the motion and shape of turbulent filaments in GYSELA output are computed. The general algorithm is stated, using non-linear image registration as its base. The results are compared to expected properties of the ITG mode. An article stating the results of this chapter is in preparation.

In chapter 6, the interplay between toroidal drift wave turbulence and tokamak profiles is investigated using a wave–kinetic description. The coupled system is used to investigate the interplay between marginally stable toroidal drift-wave turbulence and geodesic-acoustic modes (GAM). The coupled system is found to be unstable. Notably, the most unstable mode corresponds to the resonance between the turbulent wave radial group velocity and the GAM phase velocity. For a low-field-side ballooned drift wave growth, a background flow shear breaks the symmetry between inwards- and outwards-travelling instabilities. This mechanism is generic and displays many of the features expected for avalanches in developed tokamak turbulence. The contents of this chapter have been submitted as (Gillot *et al.*, 2020a).

Chapter 7 discusses the extension of GYSELA to support electromagnetic fluctuations. The founding equations are quoted from chapter 2. The numerical and data processing methods in GYSELA are presented, along with the required modifications. Preliminary simulations results are presented.

## 1.4 Conventions

Velocities will be denoted using a  $v$ . Angular velocities will be noted  $u$ . Frequencies will be denoted  $\omega$ . The vector components will be denoted using co-variant and contra-variant bases

$$\begin{aligned} A^i &= \vec{A} \cdot \vec{\nabla} x^i \\ A_i &= \vec{A} \cdot \vec{\partial}_{x^i} \end{aligned}$$

The normalised vectors are

$$\begin{aligned} \hat{e}_r &= \vec{\nabla} r = \vec{\partial}_r \\ \hat{e}_\theta &= r \vec{\nabla} \theta = \frac{1}{r} \vec{\partial}_\theta \\ \hat{e}_\varphi &= R \vec{\nabla} \varphi = \frac{1}{R} \vec{\partial}_\varphi \end{aligned}$$



## Chapter 2

# Gyrokinetic model for the plasma core

Core plasma turbulence can only be approached through simulations. Past numerical evidence has shown the inadequacy of fluid simulations (Dimitis *et al.*, 2000), leaving the burden to full-blown kinetic simulations. Simulation of six-dimensional dynamics only today peeps around the corner (Brochard *et al.*, 2020), and remains computationally challenging. While not mandatory for core turbulence, this more complete model may become required at the edge where the gyrokinetic ordering may break down. Nevertheless, simulations of long time periods require a minimal reduction step.

### 2.1 Gyrokinetic particle dynamics

The presence of a strong magnetic field in a tokamak binds charged particle to their Larmor motion. Particles loop tightly around magnetic field lines at the cyclotron frequency. These loops almost freely travel along the field lines, and slowly drift from them. Abstracting away this gyration—confusing different particles on the same loop—produces the gyro-kinetic model (Sugama, 2000; Brizard & Hahm, 2007).

#### 2.1.1 Equations of motion

We consider particle of mass  $m$  and charge  $e$ , in an ambient magnetic field deriving from the static vector potential  $\vec{A}$ . The dynamics of the particle is given by the Lagrangian

$$\mathcal{L} = m\vec{v} \cdot \dot{\vec{x}} + e\vec{A}(\vec{x}) \cdot \dot{\vec{x}} - \frac{mv^2}{2} \quad (2.1)$$

where  $\vec{x}$  is the position of the particle, and  $\vec{v}$  its velocity. We expand the position of the particle as a centre of gyration  $\vec{X}(t)$  and a perpendicular excursion  $\vec{\rho}(t)$ . The velocity is expanded into its parallel and perpendicular components as  $\vec{v} = mv_{\parallel}\vec{b} + \vec{\pi}$ . For a smooth enough magnetic field, if  $\rho_i \nabla \ln B \ll 1$ , the coupling to the magnetic field can be expanded in powers  $\vec{\rho}$ . We parameter the Larmor motion by the Larmor radius  $\rho$  and the gyro-phase  $\xi$ . The computations are done appendix A. The perturbed Lagrangian becomes

$$\begin{aligned} \mathcal{L} &\approx mv_{\parallel}\vec{b} \cdot \dot{\vec{X}} + e\vec{A}(\vec{X}) \cdot \dot{\vec{X}} - \frac{m}{2}v_{\parallel}^2 \\ &+ \frac{eB\rho^2}{2}\dot{\xi} - \frac{eB^2\rho^2}{2m} \\ &+ \frac{e}{2}\vec{\nabla} \times [\vec{B} \times \vec{\rho}] \times \vec{\rho} \cdot \dot{\vec{X}} + \mathcal{O}(\rho^3) \end{aligned}$$

The first line corresponds to the free streaming dynamics of the guiding centre  $\vec{X}$ . The second line corresponds to the Larmor motion. The third line is a correction to the the vector potential  $\vec{A}$  due

to the inhomogeneity of the magnetic field at the Larmor scale. As a consequence, the axis of the Larmor loop is shifted by  $\vec{\nabla} \times [\vec{\nabla} \times [\vec{B} \times \vec{\rho}] \times \vec{\rho}]$ . This correction to  $\vec{B}$  is of order  $\rho_i^2 \nabla^2 \ln B$ . We chose to neglect it for simplicity.

With this simplification, the system is independent of the gyro-phase  $\xi$ . From Lagrange's equations of motion, this implies the conservation of the magnetic momentum

$$\mu = \frac{\partial \mathcal{L}}{\partial \dot{\xi}} = \frac{eB\rho^2}{2} \quad (2.2)$$

This conservation is of practical use for gyro-kinetic codes. Ignoring the gyro-phase removes the fastest dynamic in the problem. This effectively softens the numerical constraint for simulation codes. Leveraging this conservation, the equations of motion can be written in a compact form as

$$\mathcal{L} = mv_{\parallel} \vec{b} \cdot \dot{\vec{X}} + e\vec{A} \cdot \dot{\vec{X}} - \mathcal{H} \quad (2.3)$$

$$\mathcal{H} = \frac{m}{2} v_{\parallel}^2 + \mu B \quad (2.4)$$

$$B_{\parallel}^* \dot{\vec{X}} = \frac{1}{m} \frac{\partial \mathcal{H}}{\partial v_{\parallel}} \vec{B}^* + \frac{\vec{b}}{e} \times \nabla \mathcal{H}$$

$$B_{\parallel}^* \dot{v}_{\parallel} = -\vec{B}^* \cdot \vec{\nabla} \mathcal{H}$$

$$\vec{B}^* = \vec{B} + \frac{mv_{\parallel}}{e} \vec{\nabla} \times \vec{b}$$

$$B_{\parallel}^* = \vec{b} \cdot \vec{B}^*$$

$\mathcal{H}$  is the Hamiltonian of the gyro-kinetic motion. The Lagrangian principle guarantees the conservation of the phase-space volume element  $B_{\parallel}^*$ . The value  $eB_{\parallel}^*/m$  itself corresponds to a vorticity carried by each gyro-centre, counting both the Larmor loop's vorticity  $eB/m$  and a moving frame effect due to magnetic curvature.

### 2.1.2 Unperturbed dynamics

In a first approximation, the magnetic field inside a tokamak is invariant in the toroidal direction. At equilibrium, the electromagnetic field is stationary. Thanks to Noether's theorem, to these invariances are associated conserved quantities: the toroidal angular momentum  $P_{\varphi}$  and the energy  $E$ , in addition to the conservation of  $\mu$ .

$$P_{\varphi} = mv_{\parallel} b_{\varphi} + eA_{\varphi} \quad (2.5)$$

$$E = \frac{m}{2} v_{\parallel}^2 + \mu B \quad (2.6)$$

where we denote the toroidal co-variant component  $b_{\varphi} = \vec{b} \cdot \vec{\partial}_{\varphi} = R\vec{b} \cdot \hat{e}_{\varphi}$ . As a consequence, the motion of a particle in such a magnetic field is integrable. Both conservations imply the shape of the motion on the poloidal plane. Depending on  $P_{\varphi}$ ,  $E$ , the poloidal angle  $\theta$ , and the sign of  $v_{\parallel}$ , we can compute the radial position  $r$  and the parallel velocity  $v_{\parallel}$  by solving the non-linear system 2.5–2.6. This is equivalent to finding the level lines  $r(\theta)$  of the following formulation of the energy

$$E = \frac{(P_{\varphi} - eA_{\varphi}(r))^2}{2mb_{\varphi}^2(r, \theta)} + \mu B(r, \theta) \quad (2.7)$$

As the magnetic field varies along the poloidal direction, two classes of particles emerge. If  $E < \mu B_{\text{HFS}}$ , the particle does not have enough energy to go all the way to the high-field-side (HFS). It is said trapped. Otherwise, it is said passing. The dynamics can then be computed through the ordinary differential system

$$\begin{aligned} v(\theta) &= \frac{P_{\varphi} - eA_{\varphi}(r(\theta))}{mb_{\varphi}(r, \theta)} \\ B_{\parallel}^* \frac{d\theta}{dt} &= v_{\parallel}(\theta) B^{*,\theta}(r(\theta), \theta) + \frac{\mu}{er(\theta)R} \partial_r B(r(\theta), \theta) \\ B_{\parallel}^* \frac{d\varphi}{dt} &= v_{\parallel}(\theta) B^{*,\varphi}(r(\theta), \theta) - \frac{\mu}{eq(r(\theta))R^2} \partial_r B(r(\theta), \theta) \end{aligned}$$

where  $q = B^\varphi/B^\theta$  is the safety factor. Sample trajectories in the poloidal plane are shown figure 2.1. Passing particles exhibit a quasi-circular motion, shifted horizontally by  $\delta R = (\vec{v}_D \times \vec{b})qR/v_{\parallel}$ . This shift can be understood exactly the same way as the  $E \times B$  drift. A force averaged on a rotation motion yields a drift perpendicular to both the force and the rotation axis. Similarly, a vertical drift averaged on a rotation (around the  $\vec{\nabla}\varphi$  axis) yields an horizontal shift.

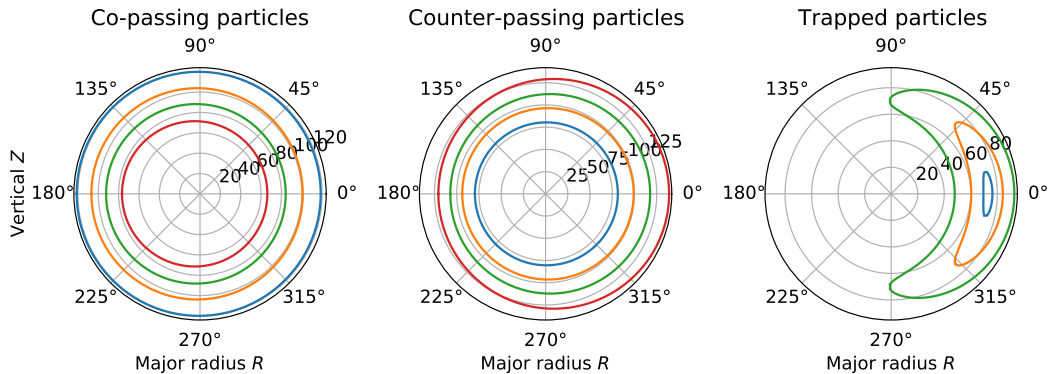


Figure 2.1: Sample of guiding-centre trajectories in the poloidal plane, computed as level lines of equation 2.7 for the GYSELA magnetic equilibrium. Co- and counter-passing particles are defined by positive (resp. negative) sign of the parallel velocity. Trapped particles are defined by the non-solvability of equation 2.7 at  $\theta = \pi$ .

### 2.1.3 Finite Larmor radius effects

The conservation of the magnetic momentum is broken when introducing a fluctuating electrostatic potential  $\phi$ . The guiding-centre feels the electric field at the position of the particle. The potential may vary at sub-Larmor scale, so the Taylor expansion we used for the background magnetic field is invalid. However, for turbulence, the typical time scales are much slower than the cyclotron frequency,  $\omega \ll \omega_{ci}$ . In this limit, the potential is quasi-static during a Larmor loop. The Larmor motion does not describe perfect circles, but rather level lines of  $\phi$ . As a result, the magnetic momentum  $\mu$  is no longer constant. We work around the problem by modifying  $\mu$  to label deformed Larmor loops instead of circles. This is usually done perturbatively using the so-called gyrokinetic pull-back transform (Brizard & Hahm, 2007). In the fully non-linear setting, the change of variable can be computed by homogenisation of the Hamiltonian (Lions *et al.*, 1987). The exact Larmor dynamics of a particle at energy  $\bar{\mathcal{H}}$  is given by solving the Hamilton–Jacobi equation for a generating function  $S(\xi)$

$$\bar{\mathcal{H}} = \frac{m}{2}v_{\parallel}^2 + \left( \bar{\mu} + \frac{e}{m} \frac{\partial S}{\partial \xi} \right) B(X) + e\phi \left( \vec{X} + \vec{\rho} \left( \xi, \mu = \bar{\mu} + \frac{e}{m} \frac{\partial S}{\partial \xi} \right) \right)$$

where  $\bar{\mathcal{H}}$  is the energy of the particle with average magnetic momentum  $\bar{\mu}$ , and  $\xi$  the gyro-phase. This dynamics does not necessarily correspond to a loop. However, by constraining  $S(\xi)$  to be periodic, both  $S$  and  $\bar{\mathcal{H}}$  are uniquely determined for each phase-space position  $(\vec{X}, v_{\parallel}, \bar{\mu})$ . The function  $\bar{\mathcal{H}}(\vec{X}, v_{\parallel}, \bar{\mu})$  can now serve as an effective Hamiltonian for the Larmor motion. For small perturbations of the potential, it can be approximated at second order as

$$\bar{\mathcal{H}} \approx \frac{m}{2}v_{\parallel}^2 + \bar{\mu}B + eJ[\phi] - \frac{e^2}{2B} \partial_{\bar{\mu}}[J[\phi^2]] - J[\phi^2] \quad (2.8)$$

The different terms correspond to statistical cumulants of the values of  $\phi$  along the Larmor loop. The first-order correction is the gyro-averaged potential  $J[\phi]$ , stating the guiding-centre feels the electric field at all the similarly-centred particles. The second-order correction is the electric potential energy contained inside the Larmor loop, yielding the so-called polarisation effect. In the following, we will only use this gyro-averaged formulation, and drop the bar notation.

### 2.1.4 Coupling to the Poisson equation

Given the Lagrangian for each particle, we can construct the action principle for the full distribution function. For a finite number of particles, we can construct an action principle in the electrostatic regime as (see paragraph 2.1.6 for the electromagnetic case)

$$\begin{aligned} \mathcal{S}[\mathbf{Z}_i, \phi] &= \sum_i \left[ m v_{\parallel} \vec{b} \cdot \dot{\vec{X}} + e \vec{A} \cdot \dot{\vec{X}} - \frac{m}{2} v_{\parallel}^2 - \mu B - e J[\phi] + \frac{e^2}{2B} \partial_{\mu} [J[\phi^2] - J[\phi]^2] \right] \\ &+ \int \frac{\varepsilon_0}{2} [\vec{\nabla} \phi]^2 d^3 x \end{aligned} \quad (2.9)$$

where  $\mathbf{Z}_i = (\vec{X}_i, v_i, \mu_i)$  is the phase space position of the particle  $i$ . The first line corresponds to the Lagrangians of all the particles. The second line is the Lagrangian of the electrostatic field. The electromagnetic case will be treated paragraph 2.1.6. The sum can be carried out to the continuum limit using the Euler–Poincaré formalism (Arnold, 1966; Ebin & Marsden, 1970; Holm *et al.*, 1998; Arnold & Khesin, 1999). Using an action principle allows to derive easily conserved quantities, but also to consistently apply approximations to keep them conserved (Scott & Smirnov, 2010). For the simple case of a kinetic system, the procedure is as follows (Marsden & Weinstein, 1981)(Cendra *et al.*, 1998; Squire *et al.*, 2013). First, we relabel the particles from the integer  $i$  to their position in phase space at  $t = 0$ . This allows to write state of the system as a mapping  $\mathbf{Z}_0 \mapsto \mathbf{Z}$  from the phase space onto itself. We introduce the distribution function at  $t = 0$  as  $\mathcal{F}_0(\mathbf{Z}_0)$

$$\begin{aligned} \mathcal{S}[\mathbf{Z}(\mathbf{Z}_0), \phi] &= \int \left[ m v_{\parallel} \vec{b} \cdot \dot{\vec{X}} + e \vec{A} \cdot \dot{\vec{X}} - \frac{m}{2} v_{\parallel}^2 - \mu B - e J[\phi] + \frac{e^2}{2B} \partial_{\mu} [J[\phi^2] - J[\phi]^2] \right] \mathcal{F}_0(\mathbf{Z}_0) \\ &+ \int \frac{\varepsilon_0}{2} [\vec{\nabla} \phi]^2 d^3 \vec{x} \end{aligned}$$

Until this point, the Euler–Lagrange equations keep the same form, stating the stationarity of  $\mathcal{S}$  with respect to variations of the mapping  $\mathbf{Z}_0 \mapsto \mathbf{Z}$ . From there, we can introduce the current distribution function  $\mathcal{F}(t, \mathbf{Z}(t, \mathbf{Z}_0)) = \mathcal{F}_0(\mathbf{Z}_0)$ , which verifies by construction the Vlasov equation

$$\partial_t \mathcal{F} + \text{div}_{\mathbf{Z}}(\dot{\mathbf{Z}} \mathcal{F}) = 0 \quad (2.11)$$

The integral can be recast as an integral on the current distribution function  $\mathcal{F}$  by introducing a Lagrange multiplier to enforce the Vlasov equation. The only remaining dynamical variable is the 5D particle velocity field  $\dot{\mathbf{Z}}(\mathbf{Z})$ .

$$\begin{aligned} \mathcal{S}[\dot{\mathbf{Z}}(\mathbf{Z}), \phi, \lambda, \mathcal{F}] &= \int \left[ m v_{\parallel} \vec{b} \cdot \dot{\vec{X}} + e \vec{A} \cdot \dot{\vec{X}} - \frac{m}{2} v_{\parallel}^2 - \mu B - e J[\phi] + \frac{e^2}{2B} \partial_{\mu} [J[\phi^2] - J[\phi]^2] \right] \mathcal{F} d\mathbf{Z} dt \\ &+ \int [\partial_t \lambda + \dot{\mathbf{Z}} \cdot \partial_{\mathbf{Z}} \lambda] \mathcal{F} d\mathbf{Z} dt \\ &+ \int \frac{\varepsilon_0}{2} [\vec{\nabla} \phi]^2 d^3 \vec{x} dt \end{aligned}$$

In this form, the Vlasov equation is given by the variations with respect to  $\lambda$ . The velocity  $\dot{\mathbf{Z}}$  is given by the usual Euler–Lagrange equations for the particle Lagrangian, which we define as the integrand against  $\mathcal{F}$ . The bracket in the second integral is a total derivative, so  $\lambda$  does not appear in the particle motion. In the following, this  $\lambda$  integral will be implied.

Using this action principle, we can derive easily conserved quantities using Noether’s theorem. Direct manipulation of the action allows to access energetically consistent approximate theories (Scott & Smirnov, 2010). For instance, the often-used Boussinesq approximation is accessible by integrating the polarisation term  $\frac{e^2}{2B} \partial_{\mu} [J[\phi^2] - J[\phi]^2]$  against a reference distribution function  $\mathcal{F}_0$  instead of the current one. In the long wavelength limit, the double gyro-average can be approximated as a squared gradient, giving the usual polarisation term. The combined approximations

give the simpler action principle

$$\begin{aligned} \mathcal{S}[\dot{\mathbf{Z}}(\mathbf{Z}), \phi, \mathcal{F}] &= \int \left[ m v_{\parallel} \dot{\mathbf{b}} \cdot \dot{\mathbf{X}} + e \dot{\mathbf{A}} \cdot \dot{\mathbf{X}} - \frac{m}{2} v_{\parallel}^2 - \mu B - e J[\phi] \right] \mathcal{F} d\mathbf{Z} dt \quad (2.12) \\ &+ \int \frac{m}{2B^2} [\nabla_{\perp} \phi]^2 n_0 d^3 \vec{X} dt \\ &+ \int \frac{\varepsilon_0}{2} [\nabla \phi]^2 d^3 \vec{x} dt \end{aligned}$$

where  $n_0$  is the reference density. The polarisation term accounts for the energy stored in the deformation of the Larmor loops. In the long-wavelength limit, it reduces to the kinetic energy of the  $E \times B$  velocity. Comparing the polarisation and self-energy terms (respectively lines 2 and 3 of equation 2.12), their ratio is of the order of  $\rho_i^2/\lambda_D^2$  with  $\lambda_D$  the Debye length. For tokamak plasma,  $\rho_i$  is much larger than  $\lambda_D$ , allowing for the so-called Darwin approximation: we neglect the field self-energy. This replaces the Poisson equation by a quasi-neutrality equation. In the parallel direction, this approximation is less justified. It is still usually carried out for numerical simplicity, removing fast parallel Langmuir waves from the problem. With these approximations, the Poisson equation is written as

$$-\operatorname{div}_{\perp} \left( \frac{m n_0}{B^2} \nabla_{\perp} \phi \right) = \sum_s e_s \int J^{\dagger}[\mathcal{F}_s] dv_{\parallel} d\mu \quad (2.13)$$

where  $s$  denotes the species.  $J^{\dagger}$  is adjoint of the gyro-average operator: while  $J$  averages on the particles associated with a gyro-centre,  $J^{\dagger}$  averages on the gyro-centres which own a particle. While the two operations are mathematically different, they are often conflated because the difference is of order  $(\rho_i/R)^4$ . The Laplace operator on the left-hand-side of 2.13 corresponds to the polarisation density. Because the Larmor loops are deformed, particles are not evenly distributed on those, and create this additional charge density. Thanks to the invariance of  $B_{\parallel}^*$ , the Vlasov equation is often formulated using the distribution function  $F = \mathcal{F}/2\pi B_{\parallel}^*$ . In that case, the Vlasov–Poisson system becomes

$$\partial_t F_s + \dot{\mathbf{Z}} \cdot \nabla_{\mathbf{Z}} F_s = 0 \quad (2.14)$$

$$-\operatorname{div}_{\perp} \left( \frac{m n_0}{B^2} \nabla_{\perp} \phi \right) = 2\pi \sum_s e_s \int J^{\dagger}[F_s B_{\parallel, s}^*] dv_{\parallel} d\mu \quad (2.15)$$

The Vlasov equation has now become an advection equation, and can be solved using the method of characteristics, as does GYSELA.

### 2.1.5 Treatment of the electrons

Solving the quasi-neutrality equation 2.13 requires several distribution functions, one for each species, including the electrons. Obviously, the electron dynamics can be solved using in the gyrokinetic framework all the way. However, this is numerically delicate. An electron is 1 800 times lighter than a proton. At the same energy, it moves 43 times faster in the parallel direction, with a 43 times smaller Larmor radius. Turbulent simulations need to resolve the Larmor radius, the requirements in the transverse direction are multiplied by this amount squared. The time step is also much smaller, to account for the increased parallel velocity.

Furthermore, bare kinetic electrons in a gyro-kinetic simulation come with the so-called  $\omega_H$  mode (Lee, 1986; Idomura, 2016). In an electromagnetic setting, this mode becomes an Alfvén wave (Scott, 1997). Four possibilities exist to avoid these difficulties: (1) don't simulate the electrons, (2) simulate only the trapped electrons, (3) simulate full electrons and filter the spurious modes, (4) simulate full electrons with magnetic perturbations. Case (1), (2) and (3) are already handled in GYSELA (Grandgirard *et al.*, 2016, 2019). Chapter 7 discusses the extension to case (4).

Not simulating the electron dynamics requires to model the electron response in an adiabatic manner. Electrons move along the field line much faster than ions, they homogenise also much

faster. The dynamics of the electrons can be replaced by a thermodynamical response on each magnetic surface. The electron density can be written as

$$n_e = \langle n_i \rangle_{\text{FS}} \exp\left(-e \frac{\phi - \langle \phi \rangle_{\text{FS}}}{T_e}\right) \approx n_0 \left(1 - e \frac{\phi - \langle \phi \rangle_{\text{FS}}}{T_e}\right) \quad (2.16)$$

where  $\langle \cdot \rangle_{\text{FS}}$  denotes the average on the magnetic surface, and  $T_e$  the electron temperature. Plugging this response in the action principle 2.12 gives the adiabatic electron action

$$\begin{aligned} \mathcal{S}[\dot{Z}(Z), \phi] &= \int \left[ m v_{\parallel} \vec{b} \cdot \dot{\vec{X}} + e \vec{A} \cdot \dot{\vec{X}} - \frac{m}{2} v_{\parallel}^2 - \mu B - e J[\phi] \right] \mathcal{F} d\mathbf{Z} dt \\ &+ \int \frac{e^2}{2T_e} (\phi - \langle \phi \rangle_{\text{FS}})^2 n_0 d^3 \vec{X} dt \\ &+ \int \frac{m}{2B^2} [\vec{\nabla}_{\perp} \phi]^2 n_0 d^3 \vec{X} dt \end{aligned} \quad (2.17)$$

The associated Poisson equation becomes

$$-\text{div}_{\perp} \left( \frac{m n_0}{B^2} \nabla_{\perp} \phi \right) + \frac{e^2 n_0}{T_e} (\phi - \langle \phi \rangle_{\text{FS}}) = \sum_s e_s \int J_s^{\dagger}[\mathcal{F}_s] dv_{\parallel} d\mu$$

### 2.1.6 Coupling to the Ampère equation

The above derivation gives the so-called electrostatic gyro-kinetic theory. In general, the magnetic field is perturbed too. Perturbations to the magnetic field can give rise to the zoo of magneto-hydrodynamic (MHD) instabilities. Macroscopic instabilities, with the notable internal kink (Bussac *et al.*, 1975) and tearing (Drake & Lee, 1977) modes, can have a very strong effect on the confinement. In addition, microscopic magnetic instabilities, such as the micro-tearing mode, are likely to be excited in the plasma edge due to strong density gradients.

Let the total magnetic vector potential  $\vec{A}(\vec{x}) = \vec{A}_0(\vec{x}) + \vec{A}_1(\vec{x})$  decompose into the background time-independent potential and a fluctuating component. The particle Lagrangian 2.1 becomes

$$\mathcal{L} = m \vec{v} \cdot \dot{\vec{x}} + e \vec{A}_0(\vec{x}) \cdot \dot{\vec{x}} + e \vec{A}_1(\vec{x}) \cdot \dot{\vec{x}} - \frac{m v^2}{2} - e \phi(\vec{x}) \quad (2.18)$$

$$= m \vec{u} \cdot \dot{\vec{x}} + e \vec{A}_0(\vec{x}) \cdot \dot{\vec{x}} - \frac{[m \vec{u} - e \vec{A}_1(\vec{x})]^2}{2m} - e \phi(\vec{x}) \quad (2.19)$$

where  $\vec{v}$  is the particle velocity and  $m \vec{u} = m \vec{v} + e \vec{A}_1(\vec{x})$  a partial momentum. The same computations as in paragraph 2.1.1 can be re-done. The vector  $\vec{u}$  is split into a parallel  $u_{\parallel}$  and a perpendicular part  $\vec{u}_{\perp}$ . The position of the particle is decomposed into the position of the gyrocentre and the Larmor radius  $\vec{x} = \vec{X} + \vec{\rho}$ . The resulting Lagrangian is be written as earlier, with a modified Hamiltonian

$$\begin{aligned} \mathcal{L} &= m u_{\parallel} \vec{b} \cdot \dot{\vec{X}} + e \vec{A}_0 \cdot \dot{\vec{X}} - \mathcal{H} \\ \mathcal{H} &= \frac{m u_{\parallel}^2}{2} + \mu B(\vec{X}) + e \phi(\vec{x}) \\ &+ e u_{\parallel} A_{1,\parallel}(\vec{X} + \vec{\rho}) + e \vec{u}_{\perp} \cdot \vec{A}_1(\vec{X} + \vec{\rho}) + \frac{e^2}{2m} \vec{A}_1^2(\vec{X} + \vec{\rho}) \end{aligned} \quad (2.20)$$

The first line of the Hamiltonian 2.20 has the same form as in the electrostatic case. The second line contains three coupling terms. The first is to the parallel magnetic flux at the position of the particle  $\psi(\vec{x}) = A_{1,\parallel}(\vec{x})$ . This term is responsible for the bending of the magnetic field-lines. As such, it allows for ideal magneto-hydro-dynamic behaviours like kink and tearing modes.

The perpendicular coupling term can be expanded for a small Larmor radius.

$$\begin{aligned} \vec{u}_{\perp} \cdot \vec{A}_{1,\perp}(\vec{X} + \vec{\rho}) &\approx \vec{u}_{\perp} \cdot \vec{A}_{1,\perp}(\vec{X}) + (\vec{\rho} \cdot \vec{\nabla}) \vec{A}_{1,\perp} \cdot \vec{u}_{\perp} + \mathcal{O}(\rho^3) \\ &\approx \frac{\rho u_{\perp}}{2} B_{1,\parallel}(\vec{X}) + \mathcal{O}(\rho^4) \end{aligned}$$

where the second line corresponds to an average on the gyro-phase. This term couples to the fluctuations of the parallel component of the magnetic field  $B_{1,\parallel}$ . It is related to magnetic compression effect and to fast magnetosonic waves. We will neglect it in the following. Likewise, we neglect the non-parallel components in the ponderomotive potential  $\bar{A}_1^2$ .

In this description,  $mu_{\parallel}$  is the parallel guiding-centre momentum. It is not the parallel guiding-centre velocity because it still includes the parallel part of the vector potential fluctuations  $\psi$ . The gyro-averaging procedure can be carried out at order 2 in the fluctuations, giving the gyro-centre Hamiltonian (Brizard & Hahm, 2007)

$$\bar{\mathcal{H}} \approx \frac{m}{2}u^2 + \mu B + eJ \left[ \phi - u\psi + \frac{e}{2m}\psi^2 \right] - \frac{e^2}{2B} \partial_{\mu} [J[(\phi - u\psi)^2] - J[\phi - u\psi]^2]$$

Once again, we place ourselves in the Boussinesq approximation and in the long-wavelength limit  $J \approx 1 - \rho_i^2 k_{\perp}^2 / 2$ . The action principle 2.12 becomes (see appendix B)

$$\begin{aligned} \mathcal{S}[\dot{\mathbf{Z}}(\mathbf{Z}), \phi, \psi] &= \int \left[ m\mathbf{v}\vec{b} \cdot \dot{\vec{X}} + e\vec{A} \cdot \dot{\vec{X}} - \frac{m}{2}v^2 - \mu B - eJ[\phi - u\psi] \right] \mathcal{F} d\mathbf{Z} \quad (2.21) \\ &+ \int \frac{e^2}{2m} |\psi|^2 n_0 d^3 \vec{X} \\ &+ \int \frac{m}{2B^2} [\vec{\nabla}_{\perp} \phi - V_{\parallel} \vec{\nabla}_{\perp} \psi]^2 n_0 d^3 \vec{X} \\ &+ \int \frac{T_{\parallel}}{2B^2} |\vec{\nabla}_{\perp} \psi|^2 n_0 d^3 \vec{X} \\ &- \int \frac{1}{2\mu_0} |\vec{B} + \vec{\nabla} \times (\psi \vec{b})|^2 d^3 \vec{x} \end{aligned}$$

as earlier, we have neglected the electric permeability term. We have introduced the fluid velocity  $V_{\parallel}$  of our species and the parallel temperature  $T_{\parallel}$ . The parallel velocity introduces a coupling between the Ampère and Poisson equation, which complicates the problem significantly. In order to remove it, we assume the plasma to be globally at rest

$$0 = \sum_{\text{species}} m n_0 V_{\parallel}$$

In addition, we simplify the magnetic self-energy term  $\vec{\nabla} \times (\psi \vec{b}) \approx \vec{b} \times \vec{\nabla} \psi$ . The dropped term  $\psi \vec{\nabla} \times \vec{b}$  runs as the inverse magnetic shear length  $L_s^{-1}$ , while the transverse gradient is of order of the electron skin depth (Porcelli, 1991). The field equations reduce to

$$-\text{div}_{\perp} \left( \sum_{\text{species}} \frac{m n_0}{B^2} \nabla_{\perp} \phi \right) = \sum_{\text{species}} e_s \int J^{\dagger}[\mathcal{F}_s] du d\mu \quad (2.22)$$

$$-\mu_0^{-1} \text{div}_{\perp} ((1 - \beta_{\parallel} + \beta_{\perp}) \nabla_{\perp} \psi) + \sum_{\text{species}} \frac{n_0 e^2}{m} \psi = \sum_{\text{species}} e_s \int u J^{\dagger}[\mathcal{F}_s] du d\mu - J_{\parallel, \text{eq}} \quad (2.23)$$

$$\beta_{\parallel} = \frac{\mu_0}{B^2} \sum_{\text{species}} m n_{0,s} V_{\parallel,s}^2 + n_{0,s} T_{\parallel,s} \quad (2.24)$$

The Poisson equation keeps exactly the same form as for the electrostatic case. In the Ampère equation 2.23, the equilibrium current appears in the right-hand side to account for the equilibrium magnetic field. In its left-hand side, the magnetic permeability is modified by a factor  $(1 - \beta)^{-1}$ . We choose to neglect this modification, since we care about plasmas in the low- $\beta$  limit,  $\beta \lesssim 1\%$ . The second term is responsible for the magnetic skin effect, making the typical length scale in the Ampère equation the electron skin depth  $\delta_e = \rho_e / \sqrt{\beta}$  where  $\rho_e$  is the electron Larmor radius. The

motion equations write

$$\begin{aligned} B_{\parallel}^* \dot{\vec{X}} &= v \vec{B}^* + \vec{b} \times \vec{\nabla} \left[ \frac{\mu B}{e} + J[\phi - u\psi] \right] \\ m B_{\parallel}^* \dot{u} &= -\vec{B}^* \cdot \vec{\nabla} [\mu B + eJ[\phi - u\psi]] \\ v &= u - \frac{e}{m} J[\psi] \\ \vec{B}^* &= \vec{B} + \frac{mu}{e} \nabla \times \vec{b} \end{aligned}$$

The added terms correspond to the bending of the field line due to the changed magnetic configuration. Numerically, they are of the same form as the  $E \times B$  velocity. We have introduced the material parallel velocity  $v$  —as opposed to the momentum  $mu$ — because it dictates the motion in the physical space. However,  $v$  is an unpractical variable for simulation: it is accelerated by the electric field, which contains the term  $\partial_t J[\psi]$ .

### 2.1.7 Conservation laws

The symmetries of the action principle given equation 2.21 guarantees conservations thanks to Noether's theorem (Brizard & Tronko, 2011; Abiteboul *et al.*, 2011; Abiteboul, 2012). The system admits three symmetric coordinates: time, the toroidal angle, and the gyro-phase. To these symmetries, we associate the conservation of energy, toroidal momentum, and magnetic momentum. The expressions here are very close to those from (Abiteboul, 2012). The conservation equations can be written as follows

$$\partial_t \mathcal{Y} + \text{div} \Gamma_{\mathcal{Y}}^r = 0$$

with  $\mathcal{Y} = \{\mathcal{E}, n, m, \mathcal{P}\}$  the energy, density, magnetic moment and toroidal momentum, and  $\Gamma_{\mathcal{Y}}^r$  the associated radial flux. The energy and its flux can be written as

$$\begin{aligned} \mathcal{E} &= \sum_s \int \left[ \frac{mu^2}{2} + \mu B + eJ[\phi - u\psi] \right] \mathcal{F}_s \text{d}u \text{d}\mu \text{d}S_{\text{FS}} \\ &- \sum_s \int \frac{m}{2B^2} [\vec{\nabla}_{\perp} \phi - V_{\parallel} \vec{\nabla}_{\perp} \psi]^2 n_{0,s} \text{d}S_{\text{FS}} \\ &+ \int \frac{e^2 \psi^2}{2m} n_s \text{d}S_{\text{FS}} + \int \frac{[\vec{\nabla}_{\perp} \psi]^2}{2\mu_0} \text{d}S_{\text{FS}} \\ \Gamma_{\mathcal{E}}^r &= \sum_s \int \left[ \frac{mu^2}{2} + \mu B - eJ[\phi - u\psi] \right] r \mathcal{F}_s \text{d}u \text{d}\mu \text{d}S_{\text{FS}} \end{aligned}$$

with  $S_{\text{FS}} = R \text{d}\theta \text{d}\varphi$  the flux-surface surface element. The expression of the energy deserves a few comments. It is not obviously positive, we re-express it using the particle velocity  $v$  instead of its momentum, and using the Poisson equation for the polarisation energy

$$\begin{aligned} \mathcal{E} &= \sum_s \int \left[ \frac{m \left( u - \frac{e}{m} J[\psi] \right)^2}{2} + \mu B \right] \mathcal{F}_s \text{d}u \text{d}\mu \text{d}S_{\text{FS}} + \int \frac{[\vec{\nabla}_{\perp} \psi]^2}{2\mu_0} \text{d}S_{\text{FS}} \\ &+ \sum_s \int \frac{m}{2B^2} [\vec{\nabla}_{\perp} \phi]^2 n_{0,s} \text{d}S_{\text{FS}} \\ &+ \sum_s \frac{e^2}{2m} \left[ \int \psi^2 n_s \text{d}S_{\text{FS}} - \int J[\psi]^2 \mathcal{F} \text{d}u \text{d}\mu \text{d}S_{\text{FS}} \right] \end{aligned}$$

The first two terms correspond to the thermal energy in the plasma and the usual magnetic self-energy. The third term corresponds to the polarisation energy. In our ordering, it is the kinetic energy stored as  $E \times B$  velocity. The last term is due to our treatment of the ponderomotive force, introducing an additional magnetisation of the plasma. This is a small correction to the magnetic self-energy (in  $\beta_{\perp} = \mu_0 P_{\perp} / B^2 \approx \beta \ll 1$ ).

The conservation of the number of particles does not come from a space-time symmetry, but rather from a relabelling symmetry. The model is invariant by relabelling the particles inside each specie. This enforces the conservation of the number of particles for each specie independently. The associated particle fluxes write

$$\begin{aligned} n_s &= \int \mathcal{F}_s du d\mu dS_{\text{FS}} \\ \Gamma_{n,s}^r &= \int \dot{r} \mathcal{F}_s du d\mu dS_{\text{FS}} \end{aligned}$$

The conservation of the electrical charge  $\mathcal{Q} = \sum e_s n_s$  comes directly from the one of particles. A consequence of the invariance of  $\mu$  for each particle, the total magnetic momentum  $\mathcal{M}$  of the plasma is conserved and convected by the dynamics

$$\begin{aligned} \mathcal{M} &= \sum_s \int \mu \mathcal{F}_s du d\mu dS_{\text{FS}} \\ \Gamma_{\mathcal{M}}^r &= \sum_s \int \mu \dot{r} \mathcal{F}_s du d\mu dS_{\text{FS}} \end{aligned}$$

The invariance by toroidal rotation implies the conservation of the toroidal momentum  $\mathcal{P}$ . This invariance is related to charge transport properties: the second term in  $\mathcal{P}$  is related to an average position of the charge density. A change in the distribution of charges implies a parallel acceleration of the plasma.

$$\begin{aligned} \mathcal{P} &= \sum_s \int [mub_\varphi + eA_{0,\varphi}] \mathcal{F}_s du d\mu dS_{\text{FS}} = m\mathcal{N}V_{\parallel} + \mathcal{Q}A_\varphi \\ \Gamma_{\mathcal{P}}^r &= \sum_s \int [mub_\varphi + eA_{0,\varphi}] \dot{r} \mathcal{F}_s du d\mu dS_{\text{FS}} \end{aligned}$$

In addition, the relabelling symmetry provides insight into the role of the  $B_{\parallel}^*$  term. Using Ertel's theorem as stated in (Cotter & Holm, 2012), the natural conserved vorticity 2-form for the gyrokinetic equation is given by  $B^* = \vec{B}^* \cdot d\vec{S} + \frac{m}{e} du \wedge b$ . By taking the component in the direction of the magnetic field, we obtain the vorticity around the parallel direction  $B_{\parallel}^*$ . It contains 2 terms: the vorticity due to the Larmor loop motion, and the vorticity due to the motion along an helical field line.

## 2.2 Linear kinetic interchange instability

The principal mechanism for turbulence in core tokamak plasmas is due to the interchange instability. This instability is due to the direction of the magnetic drift in the low-field side of the tokamak. Consider the poloidal plane, with the magnetic field pointing towards the reader. Let a localised positive charge in that region. It creates a locally positive electrostatic potential, and a clockwise  $E \times B$  flow around it. This flow pushes dense matter from the core above our charge, and pull rarefied matter from the edge below it. The magnetic drift pushes the ions downwards from the new denser region, and the electrons upwards from the sparser zone. As currents are unbalanced, our initial positive charge finds itself enhanced. The cooperation between the magnetic velocity and the distribution function gradient destabilises the system.

This was the so-called “reactive” interchange instability. In a kinetic setting, all particles do not follow the same trajectories, and are not eligible to this behaviour. More generally, the potential perturbation may have a toroidal phase velocity. Because of the toroidal drift of particles with the curvature drift, some categories of particles may resonate with this perturbation. Close to this resonant velocity, more energetic particles drift faster, less energetic particles drift slower. Because of the temperature gradient, there are more faster particles towards the core. Those are pushed above the potential perturbation, and descend into it. Conversely, the edge has more slower particles, which are pulled below the perturbation, and ascend. In that case, the cooperation is between the magnetic velocity and the derivative of distribution function with respect to the toroidal drift velocity. This involves a different trade off between temperature and density gradients.

We consider an ambient Maxwellian plasma with distribution function  $\mathcal{F}$ , density  $n$ , no mean velocity, and temperature  $T$ . We suppose a non-zero axisymmetric potential  $\Phi$  generating an equilibrium  $E \times B$  flow  $\vec{v}_E$ . A small perturbation  $eJ[\phi]$  to the Hamiltonian leads to a small perturbation  $f$  to the distribution function. Both are related by the linearised Vlasov equation

$$\begin{aligned} \mathcal{F} d^3v &= \mathcal{F} \frac{2\pi}{m} B_{\parallel}^* dv_{\parallel} d\mu = \frac{n}{T^{3/2} \sqrt{2\pi/m}} \exp\left(-\frac{\frac{m}{2}v_{\parallel}^2 + \mu B}{T}\right) B_{\parallel}^* dv_{\parallel} d\mu \\ (\partial_t + v_{\parallel} \nabla_{\parallel} + \vec{v}_E \cdot \vec{\nabla} + \vec{v}_D \cdot \vec{\nabla})g &= \frac{e\mathcal{F}}{T} (\partial_t + \vec{v}_E \cdot \vec{\nabla} + u_* \partial_{\varphi}) J[\phi] \end{aligned} \quad (2.25)$$

with  $g = f + e\phi\mathcal{F}/T$ . The partial derivatives on the left-hand side are taken at constant energy  $E = mv_{\parallel}^2/2 + \mu B$  and magnetic moment  $\mu$ . A derivation of this equation can be found appendix C. We introduce the following notations

$$\begin{aligned} \vec{v}_D \cdot \vec{\nabla} &= -u_{\text{DT}} \frac{mv_{\parallel}^2 + \mu B}{qT} (\cos\theta \vec{\partial}_{\theta} + \sin\theta r \vec{\partial}_r) \\ u_* &= -\frac{qT}{eBr} \partial_r \ln \mathcal{F} = u_{\text{DT}} \left( A_N + A_T \left( \frac{\frac{m}{2}v_{\parallel}^2 + \mu B}{T} - \frac{3}{2} \right) \right) \\ u_{\text{TR}} &= \frac{1}{qR_0} \sqrt{\frac{T}{m}} \\ u_{\text{DT}} &= \frac{qT}{eBR_0 r} \\ A_N &= -R \partial_r \ln n \\ A_T &= -R \partial_r \ln T \end{aligned}$$

$A_N$  and  $A_T$  are the normalised density and temperature logarithmic gradients. The zonal flow poloidal advection is denoted  $u_E$ .  $u_{\text{TR}}$  and  $u_{\text{DT}}$  are respectively the poloidal transit frequency and the toroidal curvature angular drift. In order to perform the computations, we place ourselves in toroidal Fourier space with mode number  $n > 0$ . We introduce the toroidal angular phase velocity  $c$ . We expand the fields in mixed Fourier space in the radial direction

$$\phi(t, r, \theta, \varphi) = \Re \sum_{n>0} \phi_n(\theta, \zeta) \exp(in(\varphi + \kappa r - ct)) \quad (2.26)$$

With this representation,  $\theta$  a coordinate along the magnetic field line, while  $\varphi$  labels the field line inside a flux surface.  $\zeta$  is the so-called ballooning angle. The partial derivatives become

$$\begin{aligned}\partial_r &\rightarrow in\kappa \\ \partial_\theta &\rightarrow -inq + \partial_\theta \\ \nabla_{\parallel} = \frac{\partial_\varphi}{R} + \frac{\partial_\theta}{qR} &\rightarrow \frac{\partial_\theta}{qR}\end{aligned}$$

### 2.2.1 Particle dynamics

For simplicity, we will only discuss strongly passing particles. We introduce the variable  $w$  to write the distribution function, and the pitch-angle variable  $\lambda$  as

$$\begin{aligned}\lambda &= \frac{\mu B_0}{E} \\ w &= \text{sign}(v_{\parallel}) \sqrt{\frac{E}{T}} \\ \mathcal{F} \frac{2\pi}{m} B_{\parallel}^* dv_{\parallel} d\mu &\approx n \exp\left(-\frac{E}{T}\right) \frac{B_0 dv_{\parallel} d\mu}{T^{3/2} \sqrt{2\pi/m}} \\ &= n \exp(-w^2) \frac{w^2 dw d\lambda}{\sqrt{\pi} \sqrt{1 - \frac{\lambda B}{2B_0}}}\end{aligned}$$

The Vlasov equation 2.25 becomes

$$\begin{aligned}\left(\frac{v_{\parallel}}{qR} + u_E + u_{\text{DT}} \cos \theta\right) \partial_\theta g_n &- in \left(c + qu_E + u_{\text{DT}} w^2 \left(2 - \frac{\lambda B}{B_0}\right) \cos \theta - \kappa r \sin \theta\right) g_n \\ &= -in \frac{e\mathcal{F}}{T} \left(c + qu_E - u_{\text{DT}} \left(A_N + A_T \left(w^2 - \frac{3}{2}\right)\right)\right) J[\phi_n] J[\phi_n^*] 27\end{aligned}$$

with  $s$  the magnetic shear. Since the parallel velocity is large compared to the poloidal drifts, we choose to neglect these in front of the  $\theta$  derivative. The first parenthesis reduces to the poloidal transit  $v_{\parallel}/qR$ . This is equivalent to neglecting ‘‘orbit squeezing’’ effects (Landreman & Catto, 2010), the deformation of the orbits due to the  $E \times B$  velocity. This equation is solvable formally using Duhamel’s formula, as done in (Garbet, 2001, eq. 98).

$$g_n(\theta) = -in \frac{e\mathcal{F}}{T} \int_{\pm\infty}^{\theta} e^{in[\Lambda(\theta) - \Lambda(\theta')]} \frac{c + qu_E - u_{\text{DT}} (A_N + A_T (w^2 - \frac{3}{2}))}{\frac{v_{\parallel}}{qR} + u_E + u_D \cos \theta} J[\phi_n](\theta') d\theta' \quad (2.28)$$

$$\partial_\theta \Lambda = -q(r(\theta)) + \frac{c + qu_E(r(\theta))}{v_{\parallel}(\theta)/qR} - \frac{u_{\text{DT}} w^2 \left(2 - \frac{\lambda B}{B_0}\right) \cos \theta}{v_{\parallel}(\theta)/qR} + \kappa \frac{dr(\theta)}{d\theta} \quad (2.29)$$

The phase function  $\Lambda$  contains the information on the toroidal and poloidal dynamics of particles. The lower bound for the integral in equation 2.28 is chosen by causality. We only integrate on poloidal positions that were visited earlier by the particle: from  $-\infty \times \text{sign}(w)$  to  $\theta$ . The functions  $r(\theta)$  and  $v_{\parallel}(\theta)$  are the radial position and parallel velocity of the particle, taking into account the radial extent  $\delta r(\theta)$  of the orbit. Both can be obtained by solving respectively the conservation of the energy and toroidal momentum, as done paragraph 2.1.2.

$$\frac{v_{\parallel}}{qR} = w u_{\text{TR}} \sqrt{2} \frac{R_0}{R} \sqrt{1 - \frac{\lambda B}{B_0}} \quad (2.30)$$

$$\delta r(\theta) = w \sqrt{2} \frac{u_{\text{DT}} R}{u_{\text{TR}} q} \sqrt{1 - \frac{\lambda B}{B_0}} - r_* \quad (2.31)$$

with  $r_*$  a reference radial position. We note that this radial extent  $\delta r(\theta)$  has a non-zero temporal average. This is due to the asymmetry of the excursion. This implies the relevant magnetic surface

for the computation of the toroidal drift is not  $r$  but is shifted by an amount proportionate to  $w$ . The choice of the reference radial position is subtle, see for instance the discussion in (Brochard, 2020, Annex B).

For an analytically tractable solution to the perturbed distribution function, we need to simplify the expression of  $\Lambda$ . The denominator contains implicit dependencies on  $\theta$  through the parallel velocity  $v_{\parallel}$  and the radial position  $r$ . The zonal flow velocity on the reference flux-surface can be thought as a toroidal reference frame effect. Since the zonal flow depends on the radial position, and the particles have a radial excursion, the zonal flow acts on the instability through its shear  $\gamma_E$ . Meanwhile, the zonal flow velocity itself acts as a solid-body rotation of the reference flux-surface. To simplify the notations, we set ourselves in this reference frame, and will swap back later. For simplicity, we neglect the effect of the zonal flow shear on the shape of the particle trajectories, and will only consider the reference-frame effect in paragraph 2.2.3.

We approximate the right-hand-side of equation 2.29 by its average and first harmonic in  $\theta$ . The averages correspond to the characteristic frequencies for the motion of the particles. Those can be computed exactly without zonal flows.

$$\partial_{\theta}\Lambda \approx -q + \frac{c - \Omega_3}{\Omega_2} + \dots \quad (2.32)$$

$$\Omega_2 = \left\langle \frac{1}{v_{\parallel}/qR} \right\rangle_{\theta}^{-1} = wu_{\text{TR}}\Omega_b(\lambda, \varepsilon) \quad (2.33)$$

$$\Omega_3 = \Omega_2 \left\langle \frac{u_{\text{DT}}w^2 \left(1 - \frac{\lambda B}{2B_0}\right) \cos \theta}{v_{\parallel}/qR} + q'\delta r \right\rangle_{\theta} = w^2 u_{\text{DT}}\Omega_d(\lambda, \varepsilon) \quad (2.34)$$

The averages  $\langle \cdot \rangle_{\theta}$  are done on the poloidal trip of the particle. For passing particles, this is an average on the full-trip around the poloidal section. For trapped particles, it averages the back and forth motion between the bounce angles  $\theta_{\text{bounce}} = \pm \cos^{-1}\left(\frac{\lambda-1}{\varepsilon}\right)$ .  $\Omega_2$  is the characteristic frequency for poloidal trip.  $\Omega_3$  corresponds to the drift in the transverse  $\varphi - q\theta$  direction.  $\Omega_b$  and  $\Omega_d$  are dimensionless functions depending on the pitch angle  $\lambda$ , the radial position  $\varepsilon = r/R$  and the magnetic shear  $s$ . The next-order correction is given by the first-harmonic in  $\theta$

$$\partial_{\theta}\Lambda = \frac{c - \Omega_3}{\Omega_2} \quad (2.35)$$

$$\begin{aligned} & - 2 \cos \theta \left\langle \frac{u_{\text{DT}}w^2 \left(1 - \frac{\lambda B}{2B_0}\right)}{wu_{\text{TR}}\sqrt{2}\sqrt{1 - \frac{\lambda B}{B_0}}} (\cos \theta + s\theta \sin \theta) \cos \theta \right\rangle_{\theta} \\ & + 2s\zeta \sin \theta \left\langle \frac{u_{\text{DT}}w^2 \left(1 - \frac{\lambda B}{2B_0}\right)}{wu_{\text{TR}}\sqrt{2}\sqrt{1 - \frac{\lambda B}{B_0}}} \sin^2 \theta \right\rangle_{\theta} \end{aligned}$$

$$\partial_{\theta}\Lambda \approx \frac{c - w^2 u_{\text{DT}}\tilde{\Omega}_d}{wu_{\text{TR}}\Omega_b} \quad (2.36)$$

$$\tilde{\Omega}_d = \Omega_d(1 + \alpha_c \cos \theta - s\zeta \alpha_s \sin \theta) \quad (2.37)$$

with  $\alpha_c$  and  $\alpha_s$  positive geometrical factors depending on  $\lambda$ ,  $\varepsilon$  and  $s$ . The expressions are computed for deeply passing particles  $\lambda \rightarrow 0$  in the large aspect ratio limit  $\varepsilon \rightarrow 0$ . In this limit, the transit and drift frequencies computed by (Zarzoso *et al.*, 2019) become

$$\begin{aligned} \Omega_b(\lambda) & \approx \sqrt{1 - \lambda} + \mathcal{O}(\varepsilon^2) \\ \Omega_d(\lambda) & \approx (2 - \lambda)s + \mathcal{O}(\lambda\varepsilon) \end{aligned}$$

The toroidal drift is due to the radial extent of the orbits. The magnetic field being sheared, the innermost and outermost points of the trajectory feel different magnetic field direction. On average, the orbit does not quite close on itself, and drifts in the toroidal direction. Similarly, the  $E \times B$  shear modifies the drift velocity  $\Omega_3$ , by changing the poloidal drift depending on the radial position. This term is at next order  $\delta\Omega_3/\Omega_2 \propto \frac{\gamma_E u_{\text{DT}}}{2u_{\text{TR}}^2} \lambda\varepsilon$ . We neglect it in the strongly passing regime. Likewise, the zonal flow curvature is able to modify the drift frequency with a term of the order of  $\rho_i^2 \partial_r^2 (qu_E)$ . We chose to neglect it for simplicity.

## 2.2.2 Fluid response

Going back to the Vlasov equation 2.27, we approximate the left-hand-side using the averaged phase factor equation 2.36. The distribution function response is given by

$$\begin{aligned}
 wu_{\text{TR}}\Omega_b[\partial_\theta g_n - in\partial_\theta \Lambda g_n] &= -in\frac{e\mathcal{F}}{T} \left( c + qu_E - u_{\text{DT}} \left( A_N + A_T \left( w^2 - \frac{3}{2} \right) \right) \right) J[\phi_n] \\
 g &= \frac{e\mathcal{F}}{T} \frac{c - u_{\text{DT}} \left( A_N + A_T \left( w^2 - \frac{3}{2} \right) \right)}{c - w^2 u_{\text{DT}} \tilde{\Omega}_d(\lambda) + wu_{\text{TR}}\Omega_b(\lambda) \frac{i\partial_\theta}{n}} J[\phi_n]
 \end{aligned} \tag{2.38}$$

The quadratic term in  $w$  corresponds to the magnetic drift. The linear term in  $w$  is responsible for parallel dynamics. In a first approach, we expand the response  $g$  in the high phase velocity limit  $c \rightarrow \infty$ . This corresponds to the hydrodynamic approximation: it handles the bulk behaviour of the distribution function. As a consequence, the existence of a resonant velocity layer is neglected. The relevant quantity for the Poisson equation is the gyro-averaged density. It can be computed from  $g = f - \frac{e\phi}{T}\mathcal{F}$  as

$$\begin{aligned}
 \frac{\delta \bar{N}_n}{n} &= - \iint e^{-w^2} \frac{eJ^2[\phi_n]}{T} \frac{w^2 dw d\lambda}{\sqrt{\pi}\sqrt{1-\lambda}} \\
 &+ \iint e^{-w^2} \frac{eJ^2[\phi_n]}{T} \left( 1 - \frac{u_{\text{DT}}}{c} \left( A_N + A_T \left( w^2 - \frac{3}{2} \right) \right) \right) \times \\
 &\quad \left( 1 + \frac{w^2 u_{\text{DT}} \tilde{\Omega}_d(\lambda)}{c} + \frac{w^2 u_{\text{TR}}^2 \Omega_b^2(\lambda)}{c^2} \left( \frac{i\partial_\theta}{n} \right)^2 \right) \times \frac{w^2 dw d\lambda}{\sqrt{\pi}\sqrt{1-\lambda}}
 \end{aligned}$$

For simplicity, we approximate the gyro-average operator as  $J = 1 - \frac{1}{2}k_\perp^2 \rho^2$ . The gyro-averaged charge density is written as

$$\begin{aligned}
 \frac{T\delta \bar{N}_n}{e\bar{n}} &\approx \left( -\frac{u_{\text{DT}}A_N}{c} + \frac{u_{\text{DT}}\tilde{\Omega}_d}{c} - \frac{u_{\text{DT}}^2\tilde{\Omega}_d A_P}{c^2} \right) \phi_n \\
 &+ \frac{u_{\text{TR}}^2}{2c^2} \left( 1 - \frac{u_{\text{DT}}A_P}{c} \right) \left( \frac{i\partial_\theta}{n} \right)^2 \phi_n \\
 &+ k_\perp^2 \rho_i^2 \frac{u_{\text{DT}}A_P}{c} \phi_n
 \end{aligned} \tag{2.39}$$

where  $A_P = A_N + A_T$ . To avoid cluttering the computations, we will keep the same notation  $\Omega_d = 2s$  and  $\tilde{\Omega}_d = \Omega_d(1 + \alpha_c \cos \theta - s\zeta \alpha_s \sin \theta)$  in the following. We have only retained second-order terms in  $1/c$  in front of  $\phi$ , and first-order terms in front of its derivatives  $\partial_\theta^2 \phi_n$  and  $k_\perp^2 \phi_n$ . This gyro-averaged density can be put into the quasi-neutrality equation as

$$k_\perp^2 \rho_i^2 \phi_n + \tau \phi_n = \frac{T\delta \bar{N}_n}{\bar{n}}$$

We obtain the dispersion differential equation in the hydrodynamic limit

$$\begin{aligned}
 0 &= \tau \phi_n + \frac{u_{\text{DT}}A_N}{c} - \frac{u_{\text{DT}}\tilde{\Omega}_d}{c} \left( 1 - \frac{u_{\text{DT}}A_P}{c} \right) \phi_n \\
 &- \frac{u_{\text{TR}}^2}{2c^2} \left( 1 - \frac{u_{\text{DT}}A_P}{c} \right) \left( \frac{i\partial_\theta}{n} \right)^2 \phi_n \\
 &+ k_\perp^2 \rho_i^2 \left( 1 - \frac{u_{\text{DT}}A_P}{c} \right) \phi_n
 \end{aligned} \tag{2.40}$$

### Resolution method

This equation contains a lot of implicit notations. The perpendicular wave vector in ballooning coordinates writes  $k_\perp^2 r^2 \approx n^2 q^2 + n^2 q^2 s^2 (\theta - \zeta)^2$ . Most quantities depend on the radial position, as

$u_{DT}, u_{TR}, \tau, A_N, A_P, \dots$  The ballooning angle  $\zeta$  plays the role of the radial mode number for the untwisted potential  $\phi(r, \theta, \varphi - q\theta)$ . Let us undo this Fourier transform. The dispersion differential equation is written

$$\begin{aligned} \phi(r, \theta, \varphi, t) &= \sum_n \psi_n(r, \theta) \exp(in[\varphi - q\theta - ct]) \\ 0 &= \frac{\tau + \frac{u_{DT}A_N}{c}}{1 - \frac{u_{DT}A_P}{c}} \psi_n - \frac{u_{DT}\Omega_d}{c} \left( 1 + \alpha_c \cos \theta + \frac{ir\partial_r}{nq} \alpha_s \sin \theta \right) \psi_n \\ &\quad - \frac{u_{TR}^2}{2c^2} \left( \frac{i\partial_\theta}{n} \right)^2 \psi_n \\ &\quad + n^2 q^2 \rho_*^2 \psi + n^2 q^2 s^2 \rho_*^2 \left( \theta + \frac{i\partial_r}{nq'} \right)^2 \psi_n \end{aligned} \quad (2.41)$$

where the unknown is the function  $\psi$ . Solving this differential equation for  $\psi$  will give the structure of the global ITG mode. This is difficult. This difficulty can be managed separating different scales. In order to do that, we reintroduce our placeholder notations:  $\partial_r = inq'\zeta$  and  $\partial_\theta = im_\parallel$ . We obtain a scalar algebraic equation.

$$\begin{aligned} 0 &= \frac{\tau + \frac{u_{DT}A_N}{c}}{1 - \frac{u_{DT}A_P}{c}} \psi - \frac{u_{DT}\Omega_d}{c} (1 + \alpha_c \cos \theta - s\zeta \alpha_s \sin \theta) \psi \\ &\quad - \frac{u_{TR}^2}{2c^2} \left( \frac{m_\parallel}{n} \right)^2 \psi \\ &\quad + n^2 q^2 \rho_*^2 \psi + n^2 q^2 s^2 \rho_*^2 (\theta - \zeta)^2 \psi \end{aligned} \quad (2.42)$$

The equation is split on three lines. The first one gives the instability mechanism. The second corresponds to parallel acoustic dynamics. The third corresponds to polarisation effects. The effect of each term will be discussed in due time.

We will solve equation 2.41 in an eikonal fashion. From 2.42, we can express  $m_\parallel$  and  $\zeta$  as functions of  $r$  and  $\theta$ . By definition,  $-i\partial_\theta \ln \psi = m_\parallel(r, \theta)$  and  $-i\partial_r \ln \psi = nq'\zeta(r, \theta)$ . Integrating these two last equations should provide the general shape of the mode. However, this formulation misses coherence effects: the structure of the wave eigenmode is global and must include the finite wave size. This formulation appears in the second derivatives:  $-\partial_\theta^2 \psi = m_\parallel^2 \psi + i\partial_\theta m_\parallel \psi$ , where  $\partial_\theta m_\parallel$  has been neglected. This correction will be added when constructing the final dispersion relation, after having solved the shape of the mode.

The eigenvalue  $c$  is a priori a complex number. In the course of the resolution, we will need to discuss the sign of its imaginary part. The constraints are provided by the Laplace transform prescription: all expressions must be analytic in  $c$ , with no poles in the upper complex plane  $\Im[c] \geq 0$ . The relationship with causality appears when inverting the Laplace transform. For negative times  $t < 0$ , the Fourier–Laplace factor  $e^{inct}$  is bounded for  $\Im[c] \rightarrow +\infty$ . Analyticity allows to close integration contour on the upper complex plane. There are no poles there, so the integral yields zero. Conversely, for  $t > 0$ , the contour needs to be closed in the lower complex plane, where any number of singularities can happen. In practice, (1) the complex conjugate  $c^*$  must not appear anywhere; (2) the computations can be done with a real  $c$ , with (3) its imaginary part vanishing from the positive side  $\Im[c] \rightarrow 0^+$ .

In the rest of this paragraph, we will successively reintroduce the parallel dynamics  $m_\parallel \rightarrow \partial_\theta$ , solve the 1D differential equation in  $\theta$ , then reintroduce the radial dynamics  $\zeta \rightarrow \partial_r$  and solve another 1D differential equation. In the parallel direction, the wave is expected to be coherent at the poloidal transit time scale, while the coherence in the radial direction is expected at the curvature drift time scale. Since the former is much faster, the scales should be separable.

### Slab dispersion relation

In a first approximation, let us neglect the parallel and finite Larmor with effects. They appear respectively as the second and third lines in equation 2.42. This corresponds to the dynamics of the mode in the so-called *slab* limit. The simplified dispersion relation is given by  $\mathcal{D}_0 = 0$  defined

equation 2.43. As a quadratic equation in  $c$ , the instability threshold is easily computed equation 2.44.

$$\mathcal{D}_0 = \tau + \frac{A_N - \tilde{\Omega}_d(\theta, \zeta)}{c/u_{DT}} + \frac{\tilde{\Omega}_d A_P}{c^2/u_{DT}^2} \quad (2.43)$$

$$\frac{A_P}{\tilde{\Omega}_d} > \frac{1}{4\tau} \left( \frac{A_N}{\tilde{\Omega}_d} - 1 \right)^2 \quad (2.44)$$

The system is rendered unstable by the match between two drift velocities. The density is pulled into the potential perturbation at the pressure diamagnetic velocity  $u_{DT}(A_N + A_T)$ , while particles drift at the curvature velocity  $u_{DT}\tilde{\Omega}_d$ . When both match, the seed potential perturbation is reinforced and the system is unstable.

At the same time, the potential drifts at the density diamagnetic drift  $u_{DT}(A_N - \tilde{\Omega}_d)$ . This mixes the system by placing a delay between the pulling of the density into the perturbation, and its charge separation. This provides a stabilising effect on the generic interchange behaviour. When the plasma is very close to marginality, this stabilisation by rotation can be sufficient to partially re-stabilise the mode at  $\theta = 0$ . In this case, the growth rate is a non-monotonic function of  $\tilde{\Omega}_d(\theta, \zeta)$ . It features a secondary maximum for lower  $\tilde{\Omega}_d$ . This secondary maximum corresponds to modes growing at a non-zero ballooning angle (Migliano *et al.*, 2013).

### Shape in the parallel direction

The first-harmonic correction to  $\Omega_d$  involves a term in  $\cos\theta$ . The magnetic drift is higher on the low-field side ( $\theta = 0$ ) than on the high-field side. This additional term enhances the turbulent drive on the low-field side, and reduces it in the high-field side. This implies an asymmetric development of the instability, with more activity on the low-field side. This is called the ballooning effect.

This in-out asymmetry conflicts with the parallel acoustic dynamics. The development of a non-zero parallel mode number  $m_{||} = i\partial_\theta$  strongly stabilises the system. The instability threshold becomes

$$\frac{A_P}{\tilde{\Omega}_d} = \frac{1}{4\tau} \left( \frac{A_N}{\tilde{\Omega}_d} - 1 \right)^2 + \frac{m_{||}^2}{2\rho_*^2 n^2 \tilde{\Omega}_d^2}$$

As soon as the parallel mode number grows, the mode gets strongly stabilised. Equivalently, this requires the mode to have a large parallel correlation length. Turbulent structures need to be very smooth and elongated in the parallel direction. In a kinetic limit, this maximises the parallel phase velocity, and minimises Landau damping.

Parallel acoustic waves tend to smooth the structure along the field line. This dialectic is stressed by a third player. Polarisation stabilises modes with strong variations in the transverse direction. Because of the magnetic shear, field alignment creates a radial pattern:  $k_r = nq'(\theta - \zeta)$ . The longer the filament, the more twisted it is. The balance creates an effective parallel coherence length, related to the radial correlation length by the magnetic shear.

In summary, the turbulent filaments need to be (1) long enough because of parallel acoustic waves, (2) not too long either because of magnetic shear, and (3) centred on the low-field side because this is where the instability is driven. We compute the mode structure in the parallel direction by introducing a phase function  $\sigma$  and an amplitude function  $\chi_n$ .

$$\psi_n(r, \zeta, \theta) = \chi_n(r, \zeta) \exp[in\sigma(r, \theta)]$$

The phase function  $\sigma$  is supposed to encode the fine details of the mode structure along a magnetic field line. On the contrary,  $\chi$  encodes the smoother shape in the radial direction. We inject this form into the dispersion relation 2.42 by defining  $m_{||}/n \rightarrow \partial_\theta\sigma$  and  $\zeta \rightarrow \zeta + \partial_r\sigma/q'$ . This is equivalent to plugging our formulation of  $\psi$  into equation 2.41 neglecting the second derivatives of

$\sigma$ . This allows to look for the structure of the mode oscillations. We compute  $\sigma$  as

$$\begin{aligned}
(\partial_\theta \sigma)^2 &= \frac{2c^2}{u_{\text{TR}}^2} n^2 q^2 \rho_*^2 s^2 (\theta - \zeta - \partial_r \sigma / q')^2 \\
&- \frac{2cu_{\text{DT}}\Omega_d}{u_{\text{TR}}^2} (\alpha_c \cos \theta - s(\zeta + \partial_r \sigma / q') \alpha_s \sin \theta) \\
&+ \frac{2c^2}{u_{\text{TR}}^2} \frac{\mathcal{D}_0(c)}{1 - \frac{u_{\text{DT}} A_F}{c}} - \frac{i\partial_\theta^2 \sigma}{n} + i \frac{2c^2}{u_{\text{TR}}^2} n^2 \rho_i^2 \partial_r^2 \sigma
\end{aligned} \tag{2.45}$$

with  $\mathcal{D}_0$  defined equation 2.43. The first line on the right-hand side corresponds to the polarisation effects discussed earlier. It is the main driver for the parallel dynamics. The second line is the correction to the mode growth due to ballooning effects. The third line contains corrections due to coherence. For simplicity, we consider it as independent of  $\theta$ . The remaining terms are the coherence effect announced earlier. For propagating waves, we expect the phase function to be real. The right-hand-side has to be positive. Taking the square root on both sides yields the following equation

$$\partial_\theta \sigma = \pm \frac{\sqrt{2}c}{u_{\text{TR}}} \sqrt{\frac{n^2 q^2 \rho_*^2 s^2 (\theta - \zeta - \partial_r \sigma / q')^2 - \frac{u_{\text{DT}}\Omega_d}{c} (\alpha_c \cos \theta - s(\zeta + \partial_r \sigma / q') \alpha_s \sin \theta)}{+ \text{indep.} \theta}} \tag{2.46}$$

The choice of branch is dictated by the behaviour at  $\theta \rightarrow \infty$ . There,  $\sigma \approx \pm \text{sign}(\theta) \frac{\sqrt{2}cnq\rho_*s}{2u_{\text{TR}}} \theta^2$ . For an unstable mode  $\Im[c] > 0$ , we need the mode to have a finite energy. This requires that  $\Re[i\sigma] \rightarrow -\infty$  for large  $\theta$ . For  $\theta > 0$ , the branch “+” is required, and “-” for  $\theta < 0$ . We need to switch at some point, therefore the positive radicand must vanish for some  $\theta_0$ . The vanishing position should also correspond to the minimum value, to preserve the positivity of the radicand. Both conditions lead to

$$0 = 2n^2 q^2 \rho_*^2 s^2 (\theta_0 - \zeta - \partial_r \sigma / q') + \frac{u_{\text{DT}}\Omega_d}{c} (\alpha_c \sin \theta_0 + s(\zeta + \partial_r \sigma / q') \alpha_s \cos \theta_0) \tag{2.47}$$

$$\begin{aligned}
0 &= n^2 q^2 \rho_*^2 s^2 (\theta_0 - \zeta - \partial_r \sigma / q')^2 - \frac{u_{\text{DT}}\Omega_d}{c} (\alpha_c \cos \theta_0 - s(\zeta + \partial_r \sigma / q') \alpha_s \sin \theta_0) \\
&+ \frac{\mathcal{D}_0(c)}{1 - \frac{u_{\text{DT}} A_F}{c}} - \frac{i\partial_\theta^2 \sigma}{n} + i \frac{2c^2}{u_{\text{TR}}^2} n^2 \rho_i^2 \partial_r^2 \sigma
\end{aligned} \tag{2.48}$$

Equation 2.47 allows to solve for  $\theta_0$ , and equation 2.48 to prescribe  $\mathcal{D}_0$ . For large  $n$ , the polarisation term dominates, and we approximate  $\theta_0 \approx \zeta$ , with a first-order correction

$$\theta_0 \approx \zeta + \partial_r \sigma / q' - \frac{u_{\text{DT}}\Omega_d}{c} \frac{\alpha_c \sin \zeta + s(\zeta + \partial_r \sigma / q') \alpha_s \cos \zeta}{2n^2 q^2 \rho_*^2 s^2}$$

For  $\theta$  close to  $\theta_0$ , the radicand in equation 2.46 is a parabola. We approximate it as such, which simplifies the equation to  $\partial_\theta \sigma = \frac{\sqrt{2}cnq\rho_*s}{u_{\text{TR}}} (\theta - \theta_0)$ . Using the definition of  $\theta_0$ , we obtain

$$\begin{aligned}
\partial_\theta \sigma + \frac{\sqrt{2}cn\rho_i}{u_{\text{TR}}} \partial_r \sigma - \frac{q\Omega_d}{n\sqrt{2}} \alpha_s \cos \theta \partial_r \sigma &\approx \frac{\sqrt{2}cnq\rho_*s}{u_{\text{TR}}} \times \\
&\left( \theta - \zeta - \frac{u_{\text{DT}}\Omega_d}{c} \frac{\alpha_c \sin \zeta + s\zeta \alpha_s \cos \zeta}{2n^2 q^2 \rho_*^2 s^2} \right)
\end{aligned} \tag{2.49}$$

The presence of a  $\partial_r \sigma$  term in the left-hand side is associated to a tilt of the parallel structure of the mode. Instead of being inside a flux surface, the filament departs from its radial reference position  $r_{\text{ref}}$  as  $r - r_{\text{ref}} = \frac{\sqrt{2}cn\rho_i}{u_{\text{TR}}} (\theta - \theta_0)$ . This departure scales like a fraction of  $q\rho_i$ , which is small in comparison to the profiles. Integrating in  $\theta$ , we can ignore this radial departure, and obtain the mode structure is explicitly

$$\phi = \chi_n(r, \zeta) \exp \left( in[\varphi - q(\theta - \zeta)] - inc \left[ t - \frac{\sqrt{2}nq\rho_*s}{u_{\text{TR}}} \frac{(\theta - \zeta)^2}{2} \right] \right) \tag{2.50}$$

We recover the usual Gaussian form of the mode (Carreras *et al.*, 1994; Garbet, 2001; Garbet *et al.*, 2002). Similarly to the quantum harmonic oscillator, this is only the fundamental harmonic. A hierarchy of modes can be derived by multiplying this form with a Hermite polynomial of  $\theta$ . In the following, we will only keep this fundamental harmonic, because it has the lowest stabilisation. This equation illustrates our earlier discussion on the ballooning effect. The shape of the mode is dictated by the factor before  $(\theta - \theta_0)^2$ , which features the balance between polarisation and parallel acoustic dynamics. The very value of  $\theta_0$  is set by the ballooning angle  $\zeta$ , and only affects this trade off very weakly. The  $E \times B$  shear introduces an additional modulation, as  $\delta m_{\parallel}/n = \gamma_E u_{\text{DT}}/u_{\text{TR}}^2$ . In the stable case with real  $c$ , the poloidal shift of the mode  $\theta_0$  is equivalent to a modulation  $\delta m_{\parallel} \propto \theta_0$ , and because of magnetic shear to a radial shift by  $\delta r = \delta m_{\parallel}/nq'$ .

The presence of a factor  $c$  in 2.49 and 2.50 is significant: it defines the propagation of information in the parallel direction. In the parallel direction, information flows with a time delay given by  $\tau = \frac{\sqrt{2}nq\rho_*s}{u_{\text{TR}}} \frac{(\theta - \theta_0)^2}{2}$ . This has two consequences. For a stable mode (when  $\Im[c] = 0$ ), the shape inside a flux surface is a parabola  $\varphi = q(\theta - \theta_0) - (\dots) \times (\theta - \theta_0)^2$ . For an unstable mode, the mode is being pulled out from  $\theta = \theta_0$ , and his growth propagates to neighbouring parallel positions as  $(\theta - \theta_0)^2$ . This corresponds to the growth of a Gaussian mode. Overall, the equilibrium along the parallel direction is reached in time  $\tau_{\parallel} \sim nq^2\rho_*^2/u_{\text{DT}}$ . This time is very small compared to the time scale of the mode itself  $u_{\text{DT}}^{-1}$ , and justifies the treatment of the coherent mode as a whole.

The reduced dispersion relation is given by equation 2.48. We inject into it the shape  $\psi$  we just found, along with the value of  $\theta_0$ . The dispersion relation for this local mode becomes

$$\begin{aligned} \psi_n(r, \theta) &= \chi_n(r) \exp\left(i \frac{\sqrt{2}cn^2q\rho_*s}{u_{\text{TR}}} \frac{(\theta - \theta_0)^2}{2}\right) \\ 0 = \frac{\mathcal{D}\chi_n}{1 - \frac{u_{\text{DT}}A_P}{c}} &= \frac{\tau + \frac{u_{\text{DT}}A_N}{c}}{1 - \frac{u_{\text{DT}}A_P}{c}} \chi_n + n^2q^2\rho_*^2\chi_n - \frac{u_{\text{DT}}\bar{\Omega}_d}{c} \chi_n \\ &+ i \frac{su_{\text{DT}}}{\sqrt{2}qc} \chi_n - \frac{u_{\text{DT}}^2\Omega_d^2}{c^2} \frac{(\alpha_c \sin \zeta + s\zeta\alpha_s \cos \zeta)^2}{2n^2q^2s^2\rho_*^2} \chi_n \\ \bar{\Omega}_d &= \tilde{\Omega}_d(\theta = \zeta) = \Omega_d(1 + \alpha_c \cos \zeta - s\zeta\alpha_s \sin \zeta) \end{aligned} \quad (2.51)$$

The first line corresponds to the slab dispersion relation 2.43. The imaginary additional term is an unconditional stabilisation of the mode due to coherence effects. It corresponds to the delay incurred by the parallel propagation of information. The second additional term is a ballooning penalty: it requires the mode to remain close to  $\zeta = 0$ . The above discussion covers the *local* ITG mode, with its parallel structure 2.50, and its dispersion relation 2.51. This local mode depends on 4 parameters: the toroidal mode number  $n$ , the parallel harmonic giving the degree of the Hermite polynomial, the ballooning angle, and the radial position. We only considered the fundamental parallel harmonic, and it is the least stabilised. The ballooning angle is associated to the radial wave-number. Computing the coherent interaction between this radial wave-number and the radially dependent background yields the global ITG mode. This is the object of the following section.

### 2.2.3 Effect of a corrugated zonal flow

We now need to compute the radial structure of our mode. This radial structure depends on the variations of the parameters describing the background plasma. Among them, we will focus on the effect of the zonal flow  $u_E$ . We removed it in equation 2.36 by putting ourselves in the moving reference frame. We re-introduce it explicitly as a Doppler effect on the phase velocity  $c \mapsto c + qu_E$ , with  $u_E(r)$  a stationary zonal flow.

#### Shape of the local mode

With only the parallel structure 2.50, we can already discuss the general shape of the local mode

$$\phi(t, r, \theta, \varphi) \propto \exp\left(in[\varphi - q(\theta - \zeta)] - in[c + qu_E] \left[t - \frac{\sqrt{2}nq\rho_*s}{u_{\text{TR}}} \frac{(\theta - \zeta)^2}{2}\right]\right) \quad (2.52)$$

The radial structure of the mode is given by the radial derivative of the phase

$$k_r \approx -nq'(\theta - \zeta) - nq'\gamma_E \left[ t - \frac{\sqrt{2}nq\rho_*s}{u_{\text{TR}}} \frac{(\theta - \zeta)^2}{2} \right] \quad (2.53)$$

This radial wave-number is the combination of three effects. First, there is the usual variation in the poloidal direction due to magnetic shear. Second, we have the dynamic effect of the zonal flow shear

$$\frac{dk_r}{dt} = -nq'\gamma_E \quad (2.54)$$

We also find the zonal flow shear to affect the value of  $k_r$  at  $t = 0$ . The information in the mode spreads from the ballooning position with a delay. As a consequence, the phase front at  $\theta \neq \zeta$  reflects the radial corrugations of the zonal flow.

### Eikonal structure of the mode

Without trying to compute the shape of the function  $\chi$ , some insight can be gained from geometrical optics and eikonal theory (McDonald, 1988). In this framework, a marginally stable wave propagates in  $\vec{x}-\vec{k}$  phase space such as to conserve its frequency  $\omega(\vec{x}, \vec{k})$ .

In the dispersion relation 2.51, the variable  $\zeta$  plays the role of the radial mode number of  $\chi$ , such as  $k_r = nq'\zeta$ . The radial group velocity can be computed as  $\partial\omega/\partial k_r$ , where  $c = \omega/n$  solves the dispersion relation. In our description, this radial velocity writes

$$c = c_0 - qu_E \quad (2.55)$$

$$\frac{\mathcal{D}_{\text{eik}}(c_0)}{1 - \frac{u_{\text{DT}}A_P}{c_0}} \approx \frac{\tau + \frac{u_{\text{DT}}A_N}{c_0}}{1 - \frac{u_{\text{DT}}A_P}{c_0}} + n^2q^2\rho_*^2 - \frac{u_{\text{DT}}\bar{\Omega}_d}{c_0} \quad (2.56)$$

$$\begin{aligned} q' \frac{dr}{dt} = q' v_g^r &= \left( \frac{\partial c}{\partial \zeta} \right)_{\mathcal{D}=0} = -\frac{\partial \mathcal{D}}{\partial \zeta} / \frac{\partial \mathcal{D}}{\partial c} \\ &= -\frac{u_{\text{DT}}\Omega_d}{\tau + n^2q^2\rho_*^2 - \frac{(\tau A_P + A_N)A_P}{\left(\frac{c_0}{u_{\text{DT}}} - A_P\right)^2}} ((A + sB) \sin \zeta + B\zeta \cos \zeta) \quad (2.57) \\ \frac{d\zeta}{dt} &= -\frac{1}{q'} \left( \frac{\partial c}{\partial r} \right)_{\mathcal{D}=0} = \gamma_E - \frac{1}{q'} \left( \frac{\partial c_0}{\partial r} \right)_{\mathcal{D}=0} \end{aligned}$$

where  $c_0$  is the phase velocity in the frame moving toroidally at velocity  $qu_E$ . We have neglected the additional penalty terms in the second line of 2.51 to get 2.56.

This radial group velocity  $v_g^r$  depends on both the sign of  $\zeta$  and of the denominator. Far from the diamagnetic resonance  $c = u_{\text{DT}}A_P$ , the denominator is positive. The group velocity is inwards for positive  $\zeta$ , outwards for negative  $\zeta$ . This is expected since the ITG mode is carried by the ions. Indeed, for positive ballooning angle, most of the perturbation lies above the mid-plane. The curvature drift in the ion direction is vertically downwards, so it tends to push this perturbation inwards. Conversely, the perturbation is pushed outwards when it is concentrated below the mid-plane. Close to the diamagnetic resonance  $c = u_{\text{DT}}A_P$ , the denominator becomes negative, and the behaviour is reversed. When the magnetic field is reversed, the signs are swapped.

In figure 2.2, we show the level lines of  $c$  solving  $\mathcal{D}_{\text{eik}} = 0$  equation 2.56 with a uniformly sheared plasma. The eikonal dynamics follows those contour lines clockwise. In the stable case, the two branches appear distinct for each value of  $c$ . In the unstable case (figure 2.2 right), the two branches merge, and are transformed into a growing and a damped branch.

The radial group velocity 2.57 estimates the time required to establish the global structure of the mode. It scales like the magnetic curvature drift. Specifically, it may be slower than typical dynamics of the background plasma, like zonal fluctuating flows. As such, the global radial structure of the ITG mode may not have the time to establish itself, unless long-living staircase structures appear.

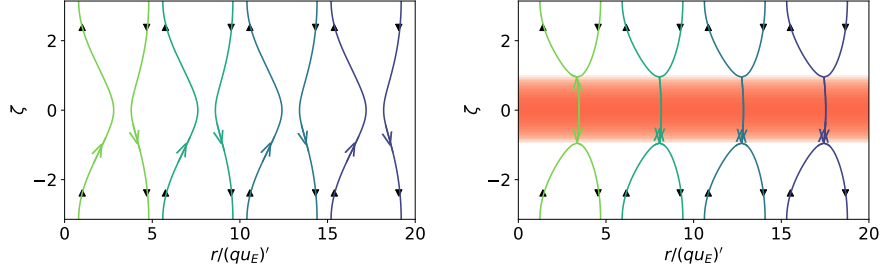


Figure 2.2: Level lines of  $c(r, \zeta)$  in an uniformly sheared plasma. Left:  $A_N = 8$ ,  $A_T = 4$ . Right:  $A_N = 8$ ,  $A_T = 5$ .  $\Omega_d = 0.5 + 0.5 \cos(\zeta)$ . The pink shading corresponds to the unstable parameter region.

## 2.2.4 Kinetic response

Because of the hydrodynamic development, the dispersion relation is real, and we only capture reactive instabilities. The instabilities are paired with a stable mode with opposite growth rate (actually a damping rate). The other consequence is that below the instability threshold, only undamped modes exist. In order to grasp the fuller dynamics, we need to compute the kinetic dispersion relation.

We go back to the solution of the Vlasov equation 2.38. Instead of developing in powers of  $c$ , we can keep the kinetic resonant denominator, and develop in powers of  $c - w^2 u_{\text{DT}} \Omega_d$ . We discussed the parallel dynamics in the previous section, we shall ignore it here, and drop all  $\theta$  dependencies. This simplification amounts to focusing on the deeply passing particles only. The distribution function response is given by

$$\begin{aligned} g_n &= \frac{\mathcal{F}}{T} \frac{c - u_{\text{DT}} \left( A_N + A_T \left( w^2 - \frac{3}{2} \right) \right)}{c - w^2 u_{\text{DT}} \Omega_d + w u_{\text{TR}} \Omega_b \left( \frac{i \partial_\theta}{n} + B \frac{\gamma_E u_{\text{DT}}}{u_{\text{TR}}^2} \cos \theta \right)} e \phi_n \\ &\approx \frac{\mathcal{F}}{T} \left( c - u_{\text{DT}} \left( A_N + A_T \left( w^2 - \frac{3}{2} \right) \right) \right) \frac{e \phi_n}{c - w^2 u_{\text{DT}} \Omega_d} \end{aligned}$$

The density response is given by the integral in  $w$  and pitch-angle  $\lambda$ , with odd terms cancelled by  $w \mapsto -w$  symmetry. The denominator features a resonance due to the toroidal drift at a specific energy  $w^2$ . The resonance condition can be computed as

$$w_{\text{res}} \approx \pm \sqrt{\frac{c}{u_{\text{DT}} \Omega_d}}$$

We introduce the following family of functions  $G_m$ , for  $m \geq 0$ . They are related to the Fried and Conte function  $Z$  (Fried & Conte, 1961; Lehtinen, 2010).

$$\begin{aligned} G_m(c) &= \int \frac{w^{2m} e^{-w^2}}{c - w^2} \frac{dw}{\sqrt{\pi}} \\ G_{m+1}(c) &= c G_m(c) - \frac{(2m)!}{4^m m!} \quad G_1(c) = -1 - \sqrt{c} Z[\sqrt{c}] \end{aligned}$$

The density fluctuation is given by the integral

$$\begin{aligned} \frac{T \delta \bar{N}_n}{eN} + \phi_n &\approx \iint \frac{c - u_{\text{DT}} \left( A_N + A_T \left( w^2 - \frac{3}{2} \right) \right)}{c - w^2 u_{\text{DT}} \Omega_d} \frac{w^2 dw d\lambda}{\sqrt{\pi} \sqrt{1 - \lambda}} \phi_n \\ &= \left[ \frac{c}{u_{\text{DT}}} - A_N + \frac{3}{2} A_T \right] G_1 \left( \frac{c}{u_{\text{DT}} \Omega_d} \right) \frac{\phi_n}{\Omega_d} \int_0^1 \frac{d\lambda}{\sqrt{1 - \lambda}} \\ &\quad - A_T G_2 \left( \frac{c}{u_{\text{DT}} \Omega_d} \right) \frac{\phi_n}{\Omega_d} \int_0^1 \frac{d\lambda}{\sqrt{1 - \lambda}} \\ &\approx \frac{A_T}{\Omega_d} \phi_n + \frac{2\phi_n}{\Omega_d} \left[ \frac{c}{u_{\text{DT}}} \left( 1 - \frac{A_T}{\Omega_d} \right) - A_N + \frac{3}{2} A_T \right] G_1 \left( \frac{c}{u_{\text{DT}} \Omega_d} \right) \end{aligned}$$

As earlier, we compute the coupling to the Poisson equation and obtain the dispersion relation

$$0 = \tau + n^2 q^2 \rho_*^2 + 1 - \frac{A_T}{\Omega_d} - \frac{2}{\Omega_d} \left[ \frac{c}{u_{DT}} \left( 1 - \frac{A_T}{\Omega_d} \right) - A_N + \frac{3}{2} A_T \right] G_1 \left( \frac{c}{\Omega_d u_{DT}} \right) \quad (2.58)$$

We can already formulate the kinetic stability boundary for the plasma. The above equation is linear in  $A_N$  and  $A_T$ . It can be solved for them, and the stability boundary is described by the path for real  $c$ . For  $c > 0$ , there exists resonant energies  $w_{\text{res}} = \pm \sqrt{c/\Omega_d u_{DT}}$ , the instability is kinetic. The associated stability boundary is given by

$$\begin{aligned} \frac{A_N}{\Omega_d} &= \frac{3}{2} + (\tau + n^2 q^2 \rho_*^2) \left( \frac{3}{2} - \frac{c}{u_{DT} \Omega_d} \right) \\ \frac{A_T}{\Omega_d} &= \tau + n^2 q^2 \rho_*^2 + 1 \end{aligned}$$

Close to this boundary, the temperature gradient governs the instability growth, while the density gradient defines the phase velocity of the wave.

For  $c < 0$ , no resonance occurs,  $G_1$  is a real function: the instability is reactive, closer to its fluid behaviour. The instability threshold can be obtained by solving both the (real) dispersion relation 2.58 and its derivative with respect to  $c$  to account for the vanishing positive imaginary part of  $c$ . The results are plotted on figure 2.3. This result is qualitatively consistent with the findings of (Romanelli & Briguglio, 1990; Hahm & Tang, 1989; Jenko *et al.*, 2001; Sarazin *et al.*, 2005), for the purely kinetic branch  $A_N < 3(\tau + n^2 q^2 \rho_*^2 + 1)$ , and  $c > 0$ . The kinetic branch disappears when  $A_N$  is too large, and the dynamics is closer to the hydrodynamic limit.

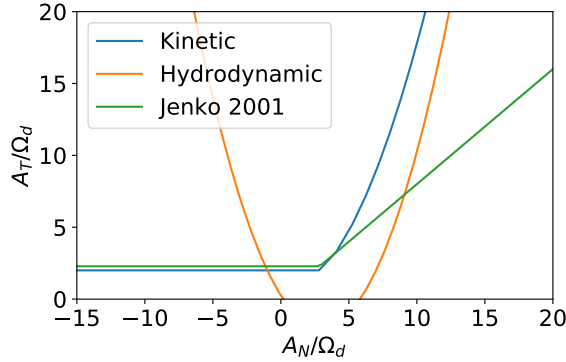


Figure 2.3: Plot of the local stability boundaries equations for the hydrodynamic (equation 2.44) and kinetic (equation 2.58) descriptions. The temperature ratio is  $\tau = 1$ . For reference is plotted (Jenko *et al.*, 2001, eq. 6) for  $\hat{s} = q = 1$ .

In this paragraph, we have recalled the principal features of the toroidal ITG mode. We have recovered the stability limit in both the hydrodynamic and kinetic limit. Using the hydrodynamic limit, we computed the local structure of the mode. In particular, we have shown this local structure is such that the pattern of the zonal flow appears in the mode phase fronts. The permanence of these linear properties in the non-linear regime will be investigated numerically in chapter 5.

## 2.3 Ideal MHD instabilities

The simplest benchmark for our electromagnetic code is its ability to simulate global MHD instabilities. Among those, we are particularly interested in the internal kink (Bussac *et al.*, 1975) and the tearing instabilities (Drake & Lee, 1977). In the following, we will follow a simplified version of the derivation in (Nasr, 2018; Zarzoso *et al.*, 2019). We consider an electromagnetic fluctuation of poloidal mode number  $m$  and toroidal mode number  $n$ .<sup>1</sup> For a kink mode,  $(m, n) = (-1, 1)$ . For a tearing mode,  $(m, n) = (-2, 1)$ . Both instabilities obey to the same ground phenomenon: current and magnetic energy are brought from the whole domain to a resonant magnetic surface  $q = -m/n$ , creating a thin current sheet. Inside this current sheet, the mode is aligned with the magnetic field, creating the grounds for parallel resonant interaction. Because this resonant layer is very thin (a few  $\delta_e$ ), it can be thought as a jump condition between non-resonant regions. Since the current is borne by the electrons, we will neglect the finite Larmor radius effects in this discussion. Diamagnetic effects have been shown to stabilise the modes (Zarzoso *et al.*, 2019). We will neglect them for simplicity in this discussion.

We consider a Maxwellian equilibrium distribution function  $\mathcal{F}$ , with density  $n$  and temperature  $T$ . For this distribution to carry a current, it needs a non-zero mean velocity  $V_{||}$ . In the following, we will denote by  $'$  radial derivatives of profiles.

$$\begin{aligned}
 f &= - \left( 1 - \frac{\omega - k_{||} V_{||} - \omega_*}{\omega - k_{||} v_{||}} \right) \mathcal{F} \frac{e(\phi - v_{||}\psi)}{T} \\
 k_{||} &= \frac{1}{R} \left( n + \frac{m}{q} \right) \\
 \omega_* &= - \frac{nqT}{eB} \partial_r \ln F_{\text{eq}} \\
 &= nu_{\text{DT}} \left( A_N - RV_{||}' \frac{(v_{||} - V_{||})}{v_{\text{th}}^2} + A_T \left( \frac{(v_{||} - V_{||})^2}{2v_{\text{th}}^2} + \frac{\mu B}{T} - \frac{3}{2} \right) \right) \\
 u_{\text{DT}} &= \frac{qT}{eBRr} \\
 v_{\text{th}} &= \sqrt{\frac{T}{\text{mass}}}
 \end{aligned} \tag{2.59}$$

where we have kept the same notation for the logarithmic density and temperature gradients  $A_N$  and  $A_T$ .  $V_{||}'$  denotes the gradient of the species mean velocity.  $v_{\text{th}}$  is the thermal velocity.

### 2.3.1 Equilibrium current profile

We consider a simple cylindrical magnetic field

$$\vec{B} = B_0 R_0 \left( \vec{\nabla} \varphi + \frac{r^2}{q R_0^2} \vec{\nabla} \theta \right) \tag{2.60}$$

The associated current writes

$$\mu_0 \vec{\mathcal{J}} = \frac{B_0}{R_0} \vec{\nabla} \left( \frac{r^2}{q} \right) \times \vec{\nabla} \theta = \mathcal{G} R \vec{\nabla} \varphi \tag{2.61}$$

$$\mu_0 \mathcal{G} = \frac{B_0}{R_0} \frac{1}{r} \partial_r \left( \frac{r^2}{q} \right) = \frac{B_0}{R_0} \frac{2 - s}{q} \tag{2.62}$$

The tearing mode grows by attracting nearby current to a resonant surface. The free energy source is the gradient of the current density  $\mathcal{G}'$

$$\mu_0 \mathcal{G}' = \frac{B_0}{R_0} \frac{-3q'q + 2rq'^2 - rq''}{q^3} \tag{2.63}$$

<sup>1</sup>In this discussion, we will refrain from introducing the species mass, as to avoid notation ambiguities. When required, it will be denoted as “mass”.

For test cases, we will use the Wesson  $q$  profile (Wesson, 2011)

$$q = q_a \frac{(r/a)^2}{1 - (1 - (r/a)^2)^{\nu+1}} \quad (2.64)$$

The parameters are its value  $q_a$  on the last closed magnetic surface  $r = a$  and a peaking factor  $\nu$ . For  $\nu + 1 > q_a$ , this profiles goes below 1 in the centre, so will enable us to discuss the kink mode.

### 2.3.2 Non-resonant region

In this region, the parallel mode number is large. Therefore,  $k_{\parallel}(v_{\parallel} - V_{\parallel}) \gg \omega$ , the mode does not resonate. We can treat the problem in an hydrodynamic fashion. This allows to simplify the response as

$$\begin{aligned} \frac{f T}{\mathcal{F} e} &\approx -(\phi - u\psi) - (\phi - u\psi) \frac{\omega_*}{k_{\parallel}(v - V_{\parallel})} \\ &\approx -(\phi - u\psi) \\ &- (\phi - V_{\parallel}\psi) \frac{nu_{\text{DT}} \left( A_N - RV'_{\parallel} \frac{(v - V_{\parallel})}{v_{\text{th}}^2} + A_T \left( \frac{(v - V_{\parallel})^2}{2v_{\text{th}}^2} + \frac{\mu B}{T} - \frac{3}{2} \right) \right)}{k_{\parallel}(v - V_{\parallel})} \\ &+ \psi \frac{nu_{\text{DT}} \left( A_N - RV'_{\parallel} \frac{(v_{\parallel} - V_{\parallel})}{v_{\text{th}}^2} + A_T \left( \frac{(v_{\parallel} - V_{\parallel})^2}{2v_{\text{th}}^2} + \frac{\mu B}{T} - \frac{3}{2} \right) \right)}{k_{\parallel}} \end{aligned} \quad (2.65)$$

Because of the symmetry of the distribution function in  $v_{\parallel} - V_{\parallel}$ , we can compute the density  $\delta N$  and momentum  $\delta(NV_{\parallel})$  response to the perturbation of  $\phi$  and  $\psi$ .

$$\begin{aligned} \frac{\delta N T}{n e} &\approx -(\phi - V_{\parallel}\psi) + (\phi - V_{\parallel}\psi) \frac{nu_{\text{DT}}}{k_{\parallel}} \frac{RV'_{\parallel}}{v_{\text{th}}^2} + \psi \frac{nu_{\text{DT}}}{k_{\parallel}} A_N \\ \frac{\delta(NV_{\parallel}) - V_{\parallel}\delta N T}{n e} &\approx v_{\text{th}}^2 \psi - (\phi - V_{\parallel}\psi) \frac{nu_{\text{DT}}}{k_{\parallel}} A_N - \psi \frac{nu_{\text{DT}}}{k_{\parallel}} RV'_{\parallel} \\ \frac{\delta(NV_{\parallel}) T}{n e} &= -V_{\parallel}(\phi - V_{\parallel}\psi) + v_{\text{th}}^2 \psi - \psi \frac{nu_{\text{DT}} R (NV_{\parallel})'}{k_{\parallel} n} \\ &+ (\phi - V_{\parallel}\psi) \frac{nu_{\text{DT}} R}{k_{\parallel}} \frac{n'v_{\text{th}}^2 + nV_{\parallel}V'_{\parallel}}{nv_{\text{th}}^2} \end{aligned}$$

Those responses can be input into the Poisson and Ampere equations. As in equations 2.13 and 2.23, we assume the plasma to be at rest. The resulting coupled differential system is

$$\begin{aligned} -\frac{1}{r} \partial_r \left( r \sum_s \frac{\rho_s^2 n_s e_s^2}{T_s} \nabla_{\perp} \phi \right) + \sum_s \frac{\rho_s^2 n_s e_s^2}{T_s} \frac{m^2}{r^2} \phi &= -\sum_s \frac{n_s e_s^2}{T_s} (\phi - V_{\parallel,s} \psi) \\ &- \frac{nq}{k_{\parallel} Br} \psi \mathcal{Q}' \\ &+ \frac{nq}{k_{\parallel} Br} \sum_s e_s (\phi - V_{\parallel,s} \psi) \frac{n_s V'_{\parallel,s}}{v_{\text{th}}^2} \\ -\frac{1}{r} \partial_r (r\psi) + \frac{m^2}{r^2} \psi &= -\mu_0 \sum_s \frac{n_s e_s^2}{T_s} V_{\parallel,s} (\phi - V_{\parallel,s} \psi) \\ &- \mu_0 \frac{nq}{k_{\parallel} Br} \psi \mathcal{G}' \\ &+ \mu_0 \frac{nq}{k_{\parallel} Br} \sum_s e_s (\phi - V_{\parallel,s} \psi) \left( n'_s + \frac{n_s V_{\parallel,s} V'_{\parallel,s}}{v_{\text{th}}^2} \right) \end{aligned}$$

where the sum  $s$  is over the species, ions and electrons.  $\mathcal{Q}'$  and  $\mathcal{G}'$  are the radial derivatives of the charge and current density. The right-hand side of this equations contain many terms. The

first line for each equation is the adiabatic response of the density and velocity. The second lines correspond to the charge and current mixing by magnetic field line bending. The third terms are due to fluctuating mixing by the  $E \times B$  velocity. If we neglect the electrostatic potential and the individual parallel motion, we get the envelope equation as

$$\begin{aligned} -\frac{1}{r}\partial_r(r\partial_r\psi) + \frac{m^2}{r^2}\psi &= -\mu_0\frac{R}{B}\mathcal{G}'\frac{\psi}{r}\frac{nq}{n+\frac{m}{q}} \\ &= -\frac{-3q' + 2rq'^2/q - rq''}{r\left(q + \frac{m}{n}\right)}\psi \end{aligned} \quad (2.66)$$

This equation is singular near the resonant magnetic surface, but otherwise well-behaved. The boundary conditions are at the centre of the plasma, and near the wall. Near  $r = 0$ , we assume  $\psi = 0$  because the mode numbers  $(m, n)$  are non-zero. Close to the wall, a perfectly conducting wall requires vanishing electric field, so  $\psi = 0$ . Around the resonant magnetic surface, the magnetic flux  $\psi$  is continuous, but  $\psi'$  needs not. The jump in slope of  $\psi'$  defines the current that is mobilised on the surface

$$\begin{aligned} \mu_0\mathcal{G}_{\text{res}} &= \int_{\text{res}} \left[ -\frac{1}{r}\partial_r(r\partial_r\psi) + \frac{m^2}{r^2}\psi \right] r dr \\ &= -[[r\psi']]_{\text{res}} + \frac{m^2}{r_{\text{res}}}\psi_{\text{res}} \end{aligned}$$

with  $[[\cdot]]_{\text{res}}$  the discontinuity when passing the resonant radius. We define the stability parameter  $\Delta'$  as

$$\Delta' = \frac{[[\psi']]_{\text{res}}}{\psi_{\text{res}}} \quad (2.67)$$

As will be shown below, the growth rate of the mode is directly proportional to  $\Delta'$ . Sample profiles are shown figure 2.4. Equation 2.66 is solved using shooting from  $r/a = 0$  and  $r/a = 1$  towards the resonance, followed by gluing together the solutions for  $\psi$  at the resonance. The kink mode has a very specific structure  $\psi \approx r(1 - 1/q)$ . That makes  $\psi_{\text{res}}$  vanish. It renders that kink mode much more unstable, as it virtually has infinite  $\Delta'$ .

### 2.3.3 Resistive resonant current sheet

In this region, the parallel mode number  $k_{\parallel}$  vanishes, allowing for a resonant interaction in the parallel direction. We choose to ignore the thin structure, and to only account for the total amount of mobilised charge and current in the layer. This quantity will then serve as a jump condition for the envelope equation. Close to this resonance  $r_0$ , the parallel mode number can be approximated as

$$k_{\parallel} = k'_{\parallel}(r - r_0) = -\frac{1}{R}\frac{mq'}{q^2}(r - r_0)$$

We place ourselves in the frame moving in the parallel direction  $\omega' = \omega - k_{\parallel}V_{\parallel}$ . Let the shifted position  $x = r - r_0$  and velocity  $u = v_{\parallel} - V_{\parallel}$ . The distribution function responds as

$$\begin{aligned} f(u = v_{\parallel} - V_{\parallel}) &= -\left(1 - \frac{\omega' - \omega_*}{\omega' - k_{\parallel}u}\right) \mathcal{F} \frac{e(\phi - (u + V_{\parallel})\psi)}{T} \\ &= -\left(1 - \frac{\omega' - \omega_*}{\omega' - k_{\parallel}u}\right) \mathcal{F} \frac{e(\phi - V_{\parallel}\psi)}{T} + \left(1 - \frac{\omega' - \omega_*}{\omega' - k_{\parallel}u}\right) \mathcal{F} \frac{eu\psi}{T} \end{aligned}$$

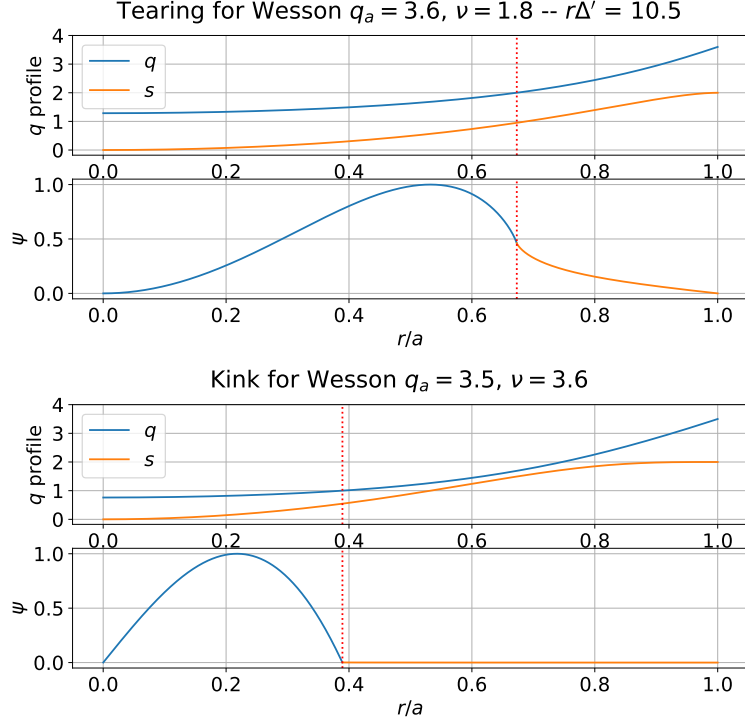


Figure 2.4: Exterior configuration for the (2, 1) tearing mode and the (1, 1) kink mode for the chosen Wesson  $q$  profiles.

The density and current contribution can be computed in the limit of only a parallel resonance (Nasr, 2018; Zarzoso *et al.*, 2019)

$$\begin{aligned}
 \frac{\delta n T}{n e} &= -(\phi - V_{\parallel} \psi) \int \left(1 - \frac{\omega}{\omega - k_{\parallel} u}\right) \frac{\mathcal{F}}{n} d^3 v + \psi \int \left(1 - \frac{\omega}{\omega - k_{\parallel} u}\right) \frac{u \mathcal{F}}{n} d^3 v \\
 &= \frac{1}{2} \left(\phi - V_{\parallel} \psi - \frac{\omega}{k_{\parallel}} \psi\right) Z' \left[ \frac{\omega}{|k_{\parallel}| v_{\text{th}} \sqrt{2}} \right] \\
 \frac{\delta(n V_{\parallel}) - V_{\parallel} \delta n}{n} \frac{T}{e} &= -(\phi - V_{\parallel} \psi) \int \left(1 - \frac{\omega}{\omega - k_{\parallel} u}\right) \frac{u \mathcal{F}}{n} d^3 v + \psi \int \left(1 - \frac{\omega}{\omega - k_{\parallel} v}\right) \frac{u^2 \mathcal{F}}{n} d^3 v \\
 &= \psi v_{\text{th}}^2 + \frac{\omega}{2 k_{\parallel}} \left(\phi - V_{\parallel} \psi - \frac{\omega}{k_{\parallel}} \psi\right) Z' \left[ \frac{\omega}{|k_{\parallel}| v_{\text{th}} \sqrt{2}} \right]
 \end{aligned}$$

where  $Z$  is the derivative of the Fried and Conte function. The mobilised charge and current can be computed by integrating in the radial direction. The integral is taken over the full resonant layer, with width  $\delta r$ . Let  $x = r - r_0$ . The resonant phase velocity varies as  $1/x$ . In the interest of the jump condition 2.67, the relevant behaviour happens at large  $x$ , or small phase velocity. Let the normalised phase velocity  $\zeta = \omega/|k_{\parallel}|v_{\text{th}}\sqrt{2}$  be our integration variable. Farther from the resonant layer, the charge and current can be expanded in powers of  $1/x$  and  $1/|x|$ . Because the volume element  $dx/d\zeta$  is in  $x^2$ , the terms of lower order vanish for  $x \rightarrow 0$ . By symmetry, the odd

functions of  $x$  do not contribute either. The charge in the resonant surface vanishes

$$\begin{aligned}
\mathcal{Q}_{\text{res}} &= \frac{1}{4} \int_{-\delta r}^{\delta r} \frac{e^2}{T} \left( \phi - V_{\parallel} \psi - \frac{\omega}{k_{\parallel}} \psi \right) Z' \left[ \frac{\omega}{|k_{\parallel}| v_{\text{th}} \sqrt{2}} \right] n r dr \\
&\approx \frac{n e^2 r_{\text{res}}}{2T} \frac{\omega}{|k'_{\parallel}| v_{\text{th}} \sqrt{2}} \left[ \frac{\phi_+ + \phi_-}{2} - V_{\parallel} \frac{\psi_+ + \psi_-}{2} - \frac{\omega}{|k'_{\parallel}|} \frac{\psi'_+ + \psi'_-}{2} \right] \int_{\omega/|k'_{\parallel}| \delta r v_{\text{th}} \sqrt{2}}^{+\infty} Z'[\zeta] \frac{d\zeta}{\zeta^2} \\
&\approx \frac{n e^2 r_{\text{res}}}{3T} \left[ \frac{\phi_+ + \phi_-}{2} - V_{\parallel} \frac{\psi_+ + \psi_-}{2} - \frac{\omega}{|k'_{\parallel}|} \frac{\psi'_+ + \psi'_-}{2} \right] \delta r \rightarrow 0
\end{aligned} \tag{2.68}$$

where the “+” and “-” subscripts denote values taken on both sides of the resonant region, to be used as jump conditions. This accumulated charge vanishes for  $\delta r \rightarrow 0$ . The current however has a finite value

$$\begin{aligned}
\mathcal{I}_{\text{res}} &= \psi \frac{n e^2 v_{\text{th}}^2}{T} r_{\text{res}} \delta r + \frac{n e^2 r_{\text{res}}}{2T} \int_{-\delta r}^{+\delta r} \frac{\omega}{k_{\parallel}} \left( \phi - V_{\parallel} \psi - \frac{\omega}{k_{\parallel}} \psi \right) Z' \left[ \frac{\omega}{|k_{\parallel}| v_{\text{th}} \sqrt{2}} \right] dx \\
&\approx -\frac{1}{2} \int_{-\delta r}^{\delta r} \frac{e^2 \omega^2}{T k_{\parallel}^2} \psi Z' \left[ \frac{\omega}{|k_{\parallel}| v_{\text{th}} \sqrt{2}} \right] n r dx + \mathcal{O}(\delta r) \\
&= -\frac{\omega v_{\text{th}} \sqrt{2}}{2 |k'_{\parallel}|} \frac{e^2}{T} n r_{\text{res}} \int_{\omega/|k'_{\parallel}| v_{\text{th}} \sqrt{2}}^{+\infty} \left[ \psi \left( \frac{\omega}{|k'_{\parallel}| v_{\text{th}} \zeta \sqrt{2}} \right) + \psi \left( -\frac{\omega}{|k'_{\parallel}| v_{\text{th}} \zeta \sqrt{2}} \right) \right] Z'[\zeta] d\zeta \\
&\approx \frac{\omega v_{\text{th}} \sqrt{2}}{|k'_{\parallel}|} \frac{e^2}{T} n r_{\text{res}} \frac{\psi_+ + \psi_-}{2} Z[\zeta(\delta r)] \\
&\approx i \sqrt{2\pi} \frac{\omega}{|k'_{\parallel}|} \frac{e^2 n v_{\text{th}}}{T} r_{\text{res}} \psi_{\text{res}}
\end{aligned} \tag{2.69}$$

where we have neglected the terms that vanish for  $\delta r \rightarrow 0$ . The last equality has been derived for  $\delta r$  much larger than the current layer width, or equivalently  $\zeta \ll 1$  at  $x = \delta r$ . The typical width of the current layer is of the order of the electron skin width (Porcelli, 1991), such as the phase velocity becomes

$$\zeta(\delta r) = \frac{\omega \tau_A}{s m \rho_* \sqrt{2}} \tag{2.70}$$

$$\tau_A = \frac{v_{\text{th}}}{R \sqrt{\beta}} \tag{2.71}$$

where  $\tau_A$  is the Alfvén time. Since the real part of  $\omega$  is due to magnetic and diamagnetic drifts (Drake & Lee, 1977),  $\omega \sim n u_{\text{DT}}$  and this condition simplifies to  $\sqrt{\beta} \ll 1$  which is our limit. The current in the resonant layer writes

$$\begin{aligned}
\mu_0 \mathcal{I}_{\text{res}} &= \mu_0 n \frac{e^2 \psi_{\text{res}}}{T} \frac{v_{\text{th}} \omega}{|k'_{\parallel}|} i \sqrt{2\pi} \\
-\Delta' \psi &= \frac{1}{\delta_e^2} \psi \frac{v_{\text{th}} \omega}{|k'_{\parallel}|} i \sqrt{2\pi} \\
\omega &= i \delta_e^2 |k'_{\parallel}| \frac{v_{\text{th}} \Delta'}{\sqrt{2\pi}} = i \delta_e^2 \frac{1}{R} \frac{m s}{q^2 r} \frac{v_{\text{th}} \Delta'}{\sqrt{2\pi}} \\
&= i \frac{\delta_e^2 v_{\text{th}}}{R r^2} \frac{m s}{q^2} \frac{r \Delta'}{\sqrt{2\pi}}
\end{aligned} \tag{2.72}$$

The mode is given by a pure growth dynamic. The growth rate is given by the  $\Delta'$  value (Drake & Lee, 1977), which mostly depends on the magnetic configuration. The Landau damping creates an effective resistivity of the form

$$\mu_0 \eta_{\text{eff}} = \frac{v_{\text{th}}}{\delta_e |k'_{\parallel}|} \sqrt{2\pi}$$

inside the current layer.



## Chapter 3

# Model order reduction approach to the collisionless closure problem

First-principle simulation of plasma turbulence faces a double challenge of cost and complexity. The physical and intellectual complexity stem from the non-linearity of the turbulent dynamics. The cost is induced by the kinetic nature of the instability drive. Simulating the gyro-kinetic description of tokamak turbulence is now routine for numerous codes, but requires maintaining high-performance codes running smoothly on supercomputers. While simulations get longer and longer, the amount of actually analysed information remains limited in proportion. A few fluid moments of the distribution function (density, velocity, pressure...) are extracted out of the tens of grid points used to simulate dynamics in velocity space, and the rest is discarded. Reaching more day-to-day investigation of turbulent transport requires lighter models for tractable simulations. However, the obvious fluid systems fail to simulate dynamics close to the marginal instability threshold (Dimitis *et al.*, 2000). Collisionless closures are a way forward to avoid this shortfall while retaining dynamics in a low-dimensional space (Hammett & Perkins, 1990; Chang & Callen, 1992).

We consider the linear one-dimensional electrostatic Vlasov problem

$$\partial_t f + ikvf = ik\mathcal{F}'\phi \quad (3.1)$$

where  $k$  is the spatial wave-number,  $\mathcal{F}'(v)$  is the derivative of the equilibrium distribution function with respect to the velocity,  $f(v)$  the fluctuation of the distribution function,  $\phi$  the electrostatic potential. The velocity is normalised to the thermal velocity, and the potential to the thermal potential. Without loss of generality, we will only consider one value of  $k > 0$ , the other cases can be deduced by symmetry.

We consider a choice of observable quantities, for instance a few fluid moments like the density  $n$ , the velocity  $u$ , the pressure  $p$ . The electric potential  $\phi$  is considered as an input, unconstrained by Poisson equation, and forces the dynamics of the state  $f$ . The mapping from the electric potential  $\phi$  to these moments is a linear time-invariant dynamical system. This mapping corresponds to an open-loop control system. The eventual Poisson equation provides a closed-loop condition. Control theory and model order reduction theory have developed useful tools for analysing the structure of such systems, and for constructing reduced-order models matching such an input–output relation  $\phi \mapsto (n, u, p)$ , without solving for the full state space, here the distribution function  $f$  (Grivet-Talocia & Gustavsen, 2016).

In this chapter, we will discuss two different methods, namely balanced truncation (Mullis & Roberts, 1976; Moore, 1981; Gugercin & Antoulas, 2004) and rational interpolation (Gugercin *et al.*, 2006; Beattie & Gugercin, 2012; Gugercin, 2017). In a first part, the two methods are reviewed and their connection to the usual collisionless closures are discussed. In a second part, the two methods are applied numerically to the 1D–1V Vlasov–Poisson problem. The precision of the reconstruction and temporal evolution in the Vlasov problem are compared. The influence of the model on the behaviour of the Vlasov–Poisson problem is discussed, using the Landau damping and bump-on-tail instability as benchmarks. Finally, the extensions to the toroidal gyro-kinetic problem and to non-linear simulations are discussed.

### 3.1 Review of the Landau mechanism

The Vlasov equation 3.1 contains no dissipation. In the non-linear regime, the Vlasov dynamics goes as far as to be isentropic. However, the coupled Vlasov–Poisson system demonstrates a damping behaviour. If the particle density bears a small perturbation at initial time, this perturbation tends to shrink and to disappear. This apparently irreversible mechanism is the so-called Landau damping.

This behaviour can be explained as phase mixing (Elskens & Escande, 2002). For each velocity  $v$ , the distribution function layer with reference velocity  $v$  oscillates at its own natural frequency  $kv$ . When exciting the system with a potential perturbation at frequency  $\omega$ , the excitation is spread out on all those natural frequencies, as  $kv/|kv - \omega|^2$ . As time goes, each layer gets slightly more detuned from the initial perturbation. Abundant slower particles are late, scarce faster particles are early. In addition, the electric field is phased  $+\pi/2$ , early with respect to the potential. Early particles give energy to the wave, late particles take from it. In average, the energy is taken from the wave, damping it.

This argument can be made rigorous using dynamical system analysis. The frequency response of the density from the Vlasov dynamics can be computed analytically from equation 3.1 as

$$n(\zeta) = \phi(\zeta) \int_{-\infty}^{+\infty} \frac{\mathcal{F}'(v)}{v - \zeta - i\frac{\sigma}{|k|}} dv \quad (3.2)$$

with  $\zeta = \omega/|k|$  the phase velocity of the perturbation, normalised to the thermal velocity. We have introduced a small damping rate  $\sigma$ . The integral on the right-hand-side is singular if  $\sigma = 0$ . The so-called Landau prescription enables to evaluate it for positive damping rate  $\sigma$ . This corresponds to the Laplace transform formalism, and enforces causality. The resulting  $n/\phi$  function is holomorphic, and can be extended to the negative complex plane.

When the equilibrium distribution function is a Maxwellian, the frequency response if expressed using the Fried and Conte function  $\mathcal{Z}$  (Fried & Conte, 1961; Goodrich, 1972; Lehtinen, 2010), and is plotted figure 3.1.

$$H_{\text{kin}}(\zeta) = \frac{n}{\phi} = -1 - \frac{\zeta}{\sqrt{2}} \mathcal{Z} \left( \frac{\zeta}{\sqrt{2}} \right) \quad (3.3)$$

The phase plot 3.1c shows a positive phase delay  $\tau = \partial_{\omega} \text{angle}[H]$ : the density response is late with respect to the potential. On the Nyquist plot 3.1a, increasing  $\zeta$  corresponds to running counter-clockwise. Holomorphic functions preserve orientation: everything on the right of the curve (ie. outside) corresponds to damped dynamics, everything on its left (ie. inside) corresponds to unstable dynamics.

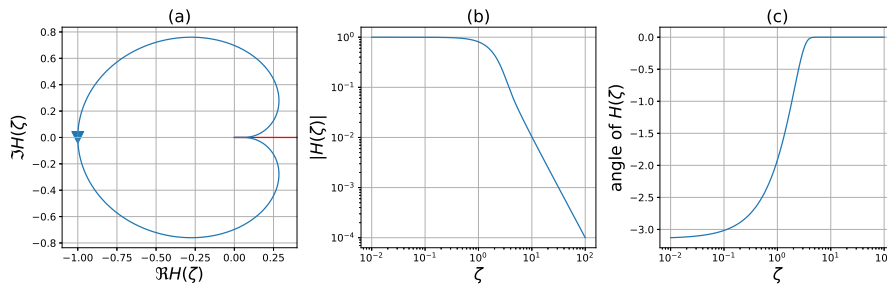


Figure 3.1: (a) Nyquist plot, (b) amplitude and (c) phase for the density response 3.3 for real  $\zeta$ .

The Poisson equation can be written as

$$\frac{n}{\phi} = k^2 \lambda_D^2 \quad (3.4)$$

On the Nyquist plot, this corresponds to crossing the positive real half-line (in red). Because of its imaginary part  $\Im[\mathcal{Z}(\zeta)] \approx \mathcal{F}'(\zeta)$ ,  $n/\phi$  never crosses this resonant line for real  $\zeta$ . This resonant line

always stays on its right, ie. the damped side. In the region where both are very close,  $\zeta$  larger than a few units, we can compute the Landau damping rate  $\sigma_{\text{Landau}}$  as

$$\sigma_{\text{Landau}} \approx \frac{\Im[H_{\text{kin}}(\zeta)]}{\partial_{\zeta}\Re[H_{\text{kin}}(\zeta)]} = \frac{\mathcal{F}'(\zeta)}{\partial_{\zeta}\Re[H_{\text{kin}}(\zeta)]} \quad (3.5)$$

The numerator is negative —particles rarefy when going farther from  $v = 0$ —, and the denominator too —the density goes as  $n \approx \phi/\zeta^2$  at high-frequency. The perturbation is damped. This last equation is the basis for the following rule of thumb: the wave is damped if there are more slower particle than faster particles.

Still, the energy and information are not gone, rather encoded on each particle's position and velocity. This can be seen using the obscurely-named regularity transfer mechanism (Mouhot & Villani, 2009). The Vlasov system is fed energy by the potential. Since the system is conservative, the energy must go somewhere: either through an interaction, or to infinity. As there is no other interaction, the energy has no choice but to go to the only available infinity, velocity wave-number infinity. By performing a Fourier transform into velocity space  $v \rightarrow k_v$ , the Vlasov equation becomes an advection equation

$$\partial_t \hat{f} + k \partial_{k_v} \hat{f} + \sigma \hat{f} = -k k_v \hat{\mathcal{F}} \phi \quad (3.6)$$

As such, all the energy input is shifted in time to  $k_v \rightarrow +\infty \times \text{sign}(k)$ . This makes the distribution function more and more irregular in velocity. The information is not lost. However, the more irregular the distribution function, the more fragile this information, the easier it is to dissipate by collisions. In the non-linear setting, the information can be retrieved using the “plasma echo” experiment: sending a second potential perturbation can scatter this information to another wave-number  $k'$  of opposite sign. The so-scattered information will then come back, get visible when it crosses  $k_v \approx 0$ , and go away to the other infinity.

## 3.2 The fluid hierarchy truncation

In order to reduce the simulation cost, we need a reduction step. The traditional method involves the formulation of the fluid hierarchy. It consists in the projection of the Vlasov equation 3.1 against graded polynomials. For instance, the fluid moments  $m_{\ell}$  verify

$$m_{\ell} = \int v^{\ell} f dv \quad (3.7)$$

$$\partial_t m_{\ell} + ik m_{\ell+1} = -ik \phi \ell \int v^{\ell-1} \mathcal{F} dv \quad (3.8)$$

where  $m_0$  is the density  $n$ ,  $m_1$  is the momentum  $N_{\text{eq}} u$ ,  $m_2$  is the pressure  $p$ . The equation for each moment  $m_{\ell}$  requires the one for the next moment, ad infinitum. Practical applications require to truncate this hierarchy somehow. This truncation dictates the way we model the energy escape to infinity:  $m_{\ell} = (-i \partial_{k_v})^{\ell} \hat{f}(0)$  defines how far in frequency space we are modelling.

The last relevant moment has to be expressed using the available information. In the linear setting, it is just a linear combination of its forebearers and of the forcing  $\phi$ . Once the fluid hierarchy is closed, the frequency response can be constructed, and compared to the kinetic response  $H_{\text{kin}}$ . The standard fluid corresponds to putting the integral of the  $\ell + 1^{\text{st}}$  Hermite polynomial to zero (Smith, 1997, ch. 2)<sup>1</sup>. For instance, the standard 4-field fluid model writes

$$\int (v^4 - 6v^2 + 3) f dv \approx 0 \quad (3.9)$$

$$H_{\text{fluid}}(\zeta) = \frac{\zeta^2 - 3}{\zeta^4 - 6\zeta^2 + 3} \quad (3.10)$$

This transfer function is real, all its poles are on the real axis, so the model is conservative: it is not able to reproduce a damping mechanism as in the kinetic case.

<sup>1</sup>Other definitions are possible, like setting the  $\ell + 1^{\text{st}}$  cumulant to zero. In the linear setting, both are equivalent.

The collisionless closure problem comes from the non-determination of the fluid moment  $\ell + 1$  in the  $\ell$ -fluid reduction. The goal is to find the best linear combination to recover relevant kinetic effects, to recover the kinetic response  $H_{\text{kin}}(\zeta)$ . Several methods have been suggested in the literature (Smith, 1997). Asymptotic methods use a Taylor (Hammett & Perkins, 1990; Sarazin *et al.*, 2009) or Padé (Hunana *et al.*, 2018) expansion of the kinetic response function  $H_{\text{kin}}$  for  $\zeta \ll 1$  and  $\zeta \gg 1$  to constrain the free parameters. As such, they explicitly choose an asymptotic frequency range, and are limited to it. Other authors have introduced the excitation frequency as a parameter (Mattor & Parker, 1997; Wang *et al.*, 2019). This renders the simulation of the closed model very difficult, because strongly non-linear. These methods have an even larger number of free parameters, and rely heavily on physical choices and orderings (Sarazin *et al.*, 2009).

### 3.3 Review of the balanced truncation method

Balanced truncation allows approaching the model reduction problem as a linear optimisation problem (Gugercin & Antoulas, 2004). Instead of a term-by-term matching of some expansion, it can be thought as a uniformly-weighted matching. This method is systematic, and only depends on (i) the original model equation, (ii) an energy functional on the input variables and (iii) a quadratic functional on the output variables. The reduced model is constructed by removing hard-to-reach and hard-to-observe states from the dynamics.

#### 3.3.1 Notions of reachability and observability

Given a potential perturbation  $\phi(t)$ , the response of the distribution function is given by

$$f(t, v) = \int g_\tau(v) ik \phi(t - \tau) d\tau \quad (3.11)$$

$$g_\tau(v) = e^{-ikv\tau - \sigma\tau} \mathcal{F}'(v) \quad (3.12)$$

$g$  defines an infinite family of distribution functions, indexed by  $\tau$ . All solutions to equation 3.1 are superpositions inside this family of states, as given by equation 3.11. From the opposite point of view, let  $f(v)$  be an arbitrary distribution function. The easier  $f$  is to represent as a linear combination of  $g_\tau$ , the closer it is to an actual solution of 3.1. Conversely, the more energy  $k^2|\phi|^2$  a state requires to appear, the more convoluted  $\phi$  is in 3.11, the less reachable it is.

To quantify this, we reduce the infinite family  $g$  to a set of principal components (Jolliffe, 2002). In order to achieve this, we construct the so-called reachability Gramian  $\mathcal{R}$

$$\begin{aligned} \mathcal{R}(v', v'') &= \int_0^{+\infty} g_\tau(v') g_\tau^*(v'') d\tau \\ &= \frac{\mathcal{F}'(v') \mathcal{F}'(v'')}{2\sigma + ik(v' - v'')} \end{aligned} \quad (3.13)$$

This (infinite-dimensional) matrix is symmetric, positive and bounded. It can be diagonalised as

$$\mathcal{R}(v', v'') = \sum_{p=0}^{+\infty} \lambda_p^2 f_p(v') f_p^*(v'') \quad (3.14)$$

The orthonormal eigenvectors  $f_p$  correspond to principal components. The eigenvalues  $\lambda_p^2$  allow to order them from most reachable (high  $\lambda_p$ ) to least reachable (low  $\lambda_p$ ). All the distributions functions in the family  $g_\tau$  can be written as an (infinite) sum of  $f_p$ . For numerical application, we will discretise the velocity space. The Gramian  $\mathcal{R}$  will become a matrix  $\mathcal{R}_{pq} = \mathcal{R}(p\Delta v, q\Delta v)$ .

To diagonalise, we need the  $f_p$  to be orthogonal, but we are yet define with which inner product. We need a second symmetric matrix to define this orthogonality. It can be provided by measuring the observability of the states. Given a distribution function  $f$  at  $t = 0$ , the density at later times is given by

$$n(t) = \int e^{-ikvt - \sigma t} f(v) dv \quad (3.15)$$

A state that cannot be observed is of no interest for us. Conversely, a state that is clearly and strongly visible for a long time is physically relevant and should be captured. For our toy model, we chose to only measure the density response  $n$ . The signal strength for a state  $f$  can be measured as a squared norm of  $n$  for positive times. We introduce the observability Gramian  $\mathcal{O}$  equation 3.16. This can be generalised to several moments by adding the appropriate terms in the integral in the left-hand side.

$$\int_0^{+\infty} |n(t)|^2 dt = \int \mathcal{O}(v', v'') f^*(v') f(v'') dv' dv'' \quad (3.16)$$

$$\mathcal{O}(v', v'') = \frac{1}{2\sigma - ik(v' - v'')} \quad (3.17)$$

Notice the changed sign with respect to 3.13. As a symmetric positive matrix,  $\mathcal{O}$  provides an inner product. We can proceed to computing our principal components equation 3.14. In this case,  $\lambda_p$  is called a Hankel singular value. The orthonormality of the  $f_p$  makes  $\lambda_p^2$  scale with their observability. Therefore, the  $\lambda_p$  measure the product of observability and reachability for a distribution component  $f_p$ . Since the components are orthogonal with respect to  $\mathcal{O}$ , we can construct the dual basis  $\mu_p$

$$\mu_p(v') = \int \mathcal{O}(v', v'') f_p(v'') dv'' \quad (3.18)$$

$$\int \mu_p(v) f_q(v) dv = \delta_{pq} \quad (3.19)$$

### 3.3.2 Usage for model order reduction

We decompose the perturbed distribution function on the basis defined by the  $g_p$ , weighted by new dynamical variables  $x_p$ . The functions  $\mu_p$  give a projection basis, a set of generalised moments to consider for the reduction.

$$f(t, v) = \sum_{p=0}^{+\infty} x_p(t) f_p(v) \quad (3.20)$$

$$x_p(t) = \int \mu_p(v) f(t, v) dv \quad (3.21)$$

By plugging this form into the Vlasov equation 3.1 and projecting against the  $\mu_p$ , we can formulate the evolution of the  $x_p$  as

$$\dot{x}_p = \sum_{q=0}^{+\infty} A_{pq} x_q + B_p \phi \quad (3.22)$$

$$m_\ell = \sum_{q=0}^{+\infty} C_{\ell q} x_q \quad (3.23)$$

with the matrices

$$A_{pq} = \iint dx dv \mu_p(x, v) (-ikv) f_q(x, v) \quad (3.24)$$

$$B_p = \iint dx dv \mu_p(x, v) \mathcal{F}'(v) ik \quad (3.25)$$

$$C_{\ell q} = \int dv v^\ell f_q(x, v) \quad (3.26)$$

Truncating the sum in equation 3.20 provides a finite-dimensional model, with state defined by the  $x_p$ . The relevance of the truncation is defined by the sequence of Hankel singular values  $\lambda_p$ . The accuracy of the reduced model is defined the sum of neglected singular values (Gugercin & Antoulas, 2004). More generally, the sequence of singular values allows to estimate the reducibility

of the original equation. The faster they decay, the shorter the sum 3.20 can be to reach the same accuracy.

This method departs from the more traditional principal component analysis (Pearson, 1901; Jolliffe, 2002) by using the observability Gramian instead of the implicit identity matrix. The latter is determined by the data acquisition choice rather than physics, and leads to poorer reduced models (Rowley, 2005). We remark the scaling of the Gramians does not modify the reduced basis, making the scalar  $\sigma/|k|$  the only regularisation parameter.

### 3.3.3 Numerical investigation

The kinetic equation 3.1 describes dynamics in a continuous-velocity space. Grid-based simulations require a discretisation in the velocity space. Because of the finite grid, the discrete system is plagued by a return to initial conditions. With a uniform radial grid of step  $\Delta v$ , the impulse response is written

$$f(t, j\Delta v) = e^{-ijk\Delta vt - \sigma t} ik\mathcal{F}'(j\Delta v)\phi(t=0) \quad (3.27)$$

The first exponential factor is periodic in time, of period  $T = 2\pi/k\Delta v$ . This periodicity is a spurious numerical echo. It is due to the discretisation, and can be thought as aliasing in  $k_v$  space for equation 3.6. Relevant simulations thus require a regularisation to remove this effect, such as  $\sigma \gg k\Delta v$ . This can be achieved either through a thinner grid, or by strong enough collision term.

We compute numerically the two Gramian matrices 3.13 and 3.17 on a uniform velocity grid between  $-5$  and  $5$  times the thermal velocity, with  $\Delta v = 10^{-2}$ . Regularisation is  $\sigma/k\Delta v = 2$ . It should be noted that up to a scaling factor, the two matrices 3.13 and 3.17 only depend on  $\sigma$  and  $k$  through the ratio  $\sigma/|k|$ . As a consequence, in the following and until paragraph 3.5.2, we shall consider only  $k = 1$ .

We use the Schur-based computation method from (Penzl, 2006). Given the Cholesky factorisation of the matrices  $\mathcal{R} = RR^\dagger$  and  $\mathcal{O} = OO^\dagger$ , the singular value decomposition of  $R^\dagger O$  is computed. The singular values are exactly the Hankel singular values  $\lambda_p$ . The left singular vectors  $u_p$  yield the distribution components  $f_p = Ru_p$ .

Hankel singular values are plotted figure 3.2. The figure outlines seven outstanding well-separated singular values and a bulk of singular values with Gaussian decrease. The first seven correspond to truncation relevant modes. The bulk modes are a reminder of Van-Kampen modes around each velocity grid point. The bulk modes are purely numerical modes, due to the finite-time recurrence of the Fourier-space formulation. Increasing  $\sigma/\Delta v$  decreases the bulk, and unearths additional discrete modes. Nevertheless, modifying  $\sigma/\Delta v$  does not lead to discernible change to the shape of discrete modes.

The strong separation between the first singular values is promising for model order reduction perspectives. In our case, the singular values drop 5 orders of magnitude in the first 7 singular values. The relevance of additional dimensions for the description decays rapidly. From this consideration, the dynamics of the linear Vlasov equation 3.1 appears to be low-dimensional, and a reduced model should be accessible. Conversely, the singular values corresponding to the bulk are very close together. Adding components  $f_p$  from this bulk should not increase the accuracy of a reduced model.

The balanced truncation basis is shown figure 3.3. The structures are different from the Hermite polynomial used for fluid modelling. The complex amplitude of the components  $f_p$  is reminiscent of the derived equilibrium  $|f_p| \sim \mathcal{F}'(v)$ . Surprisingly, the complex argument of the  $f_p(v)$  decreases monotonically with  $v$ . This indicates that only negative velocity-Fourier wave-numbers  $k_v < 0$  are involved. This can be explained by the filamentation process: positive  $k_v$  drift towards  $k_v \rightarrow +\infty$  and are never observed by polynomial moments at  $k_v = 0$ . On the other hand, negative  $k_v$  pass once at  $k_v = 0$  before going away at  $k_v \rightarrow +\infty$ .

## 3.4 Review of interpolation-based reduction

Balanced truncation requires to construct two Gramian matrices. For a velocity grid of size  $N_v$ , each Gramian has size  $N_v^2$ . This renders the method computationally expensive. Furthermore, the performances of the method are bounded by those of the discrete Vlasov model.

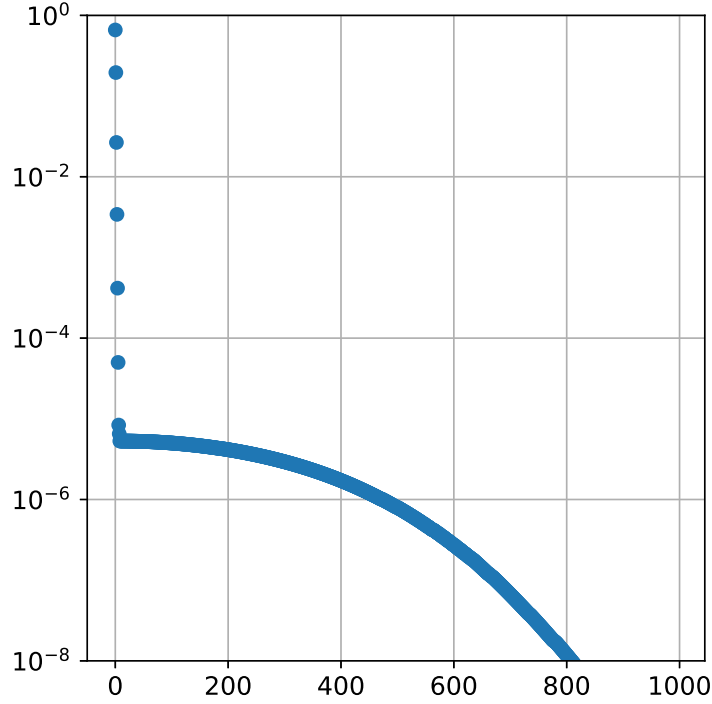


Figure 3.2: Hankel singular values of the balanced truncation problem.

On the contrary, interpolation-based model order reduction is a phenomenological method. It only requires the evaluation of the reference kinetic frequency response function  $H_{\text{kin}}$ , equation 3.3. The closure problem is a reduction of the infinite-dimensional Vlasov equation to a finite dimensional dynamical system whose variables are the fluid moments. Because of the finite dimension, the associated transfer function  $n/\phi$  is a rational function of the phase velocity  $\zeta$ , akin to equation 3.10. Instead of constructing a projection basis equations 3.20–3.21 for the Vlasov equation, we can try to directly approximate the reduced transfer function. Several methods have been employed to this end (Gustavsen & Semlyen, 1999; Grivet-Talocia & Gustavsen, 2016). We chose to present the interpolation framework (Antoulas *et al.*, 2010; Beattie & Gugercin, 2017): how to construct a rational transfer function  $H_{\text{red}}$  which interpolates  $H_{\text{kin}}$  at chosen points?

This can be done using the Loewner framework (Mayo & Antoulas, 2007). The method has found wide applications, not limited to model order reduction (Gosea, 2017; Gosea & Antoulas, 2017; Pontes Duff Pereira, 2017; Karachalios *et al.*, 2018; Vuillemin & Poussot-Vassal, 2019). First, let us generalise the problem. Our reduced linear time-invariant system (equation 3.22) can be written in the so-called descriptor form as

$$E\dot{x} = Ax + B\phi \quad (3.28)$$

$$n = Cx \quad (3.29)$$

where  $E$  and  $A$  are two square matrices, where  $E$  is invertible.  $B$  is a column matrix, and  $C$  is a row matrix.  $x$  is the state variable. The associated response function is

$$H_{\text{red}}(\zeta) = C \cdot (-i\zeta E - A)^{-1} \cdot B \quad (3.30)$$

This representation is highly redundant: changing  $x$  into  $S^{-1}x$  for some matrix  $S$  does not change the dynamics, only the matrices  $E, A, C$ . Neither does left-multiplying the equation 3.28 by a matrix  $T$ , only the matrices  $E, A, B$ . This freedom allows to chose the coefficients in  $B$  and  $C$ , and then to fill-up the matrices  $E$  and  $A$ .

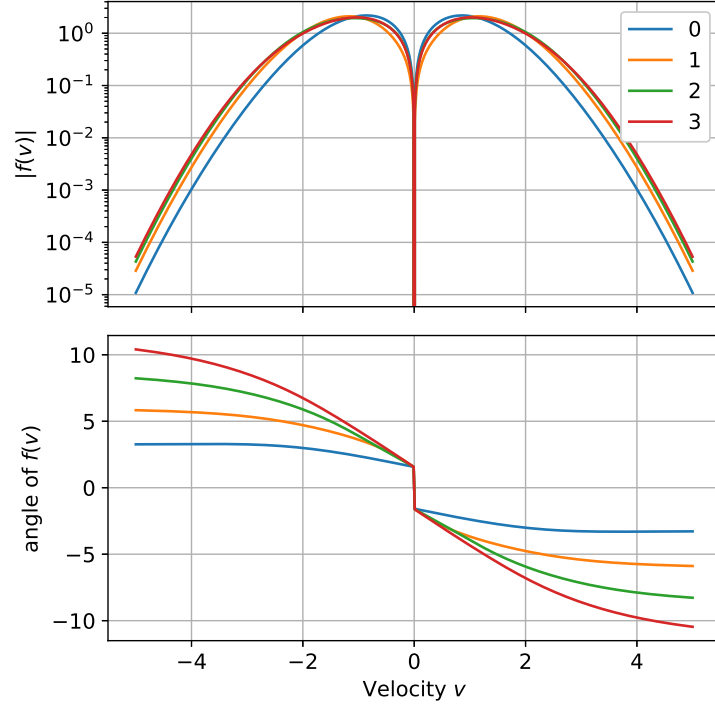


Figure 3.3: Plot of the components corresponding to the first four Hankel singular values. Above: norm of the distribution components  $f_k(v)$ . Below: complex angle of the distribution components  $f_k(v)$ .

### 3.4.1 Construction of the matrices

We want to construct a set of matrices  $E, A, B, C$  such that  $H_{\text{red}}(\alpha_p) = H_{\text{kin}}(\alpha_p)$  and  $H_{\text{red}}(\beta_q) = H_{\text{kin}}(\beta_q)$  for two sets of (possibly complex) frequencies  $\alpha_p$  and  $\beta_q$ . We chose to define arbitrarily  $B_p$  and  $C_q$  to the interpolated values. The response function  $H_{\text{red}}$  will interpolate  $H_{\text{kin}}$  as soon as the inverted matrix  $-i\zeta E - A$  allows to select the right coefficient off  $B_p$  or  $C_q$ . This can be achieved by constructing the two matrices  $E$  and  $A$  such that, for all  $p, q$ ,

$$(-i\alpha_p)E_{pq} - A_{pq} = C_q \quad (3.31)$$

$$(-i\beta_q)E_{pq} - A_{pq} = B_p \quad (3.32)$$

$$B_p = H_{\text{kin}}(\alpha_p) \quad (3.33)$$

$$C_q = H_{\text{kin}}(\beta_q) \quad (3.34)$$

The first equation is our selection rule:  $C$  must be the  $p^{\text{th}}$  row of  $-i\alpha_p E - A$ . This guarantees that  $H_{\text{red}}(\alpha_p) = C \cdot (-i\alpha_p E - A)^{-1} \cdot B = B_p$ . Likewise, the second equation forces  $H_{\text{red}}(\beta_q) = C_q$ . Finally, the definitions of  $B$  and  $C$  give the values to be interpolated.

By modifying equations 3.31–3.34, the method can be generalised to also interpolate the derivatives (Mayo & Antoulas, 2007) and to match the asymptotic behaviour at high frequency. In order to interpolate the point  $\alpha_p$  up to order  $K$ , the trick is to arrange the successive derivatives of  $H_{\text{red}}$  in order after the value. The matrix  $C$  is such that, for  $0 \leq r \leq K$ ,

$$C_{q+r} = \frac{1}{i^r r!} H_{\text{red}}^{(r)}(\beta_q) \quad (3.35)$$

$$= C \cdot [(-i\beta_q E - A)^{-1} \cdot E]^r \cdot (-i\beta_q E - A)^{-1} \cdot B \quad (3.36)$$

By straightforward recursion, this is equivalent to asserting, in addition to 3.31, that for  $1 \leq r \leq K$ ,

$$-i\beta_q E_{p,q+r} - A_{p,q+r} = E_{p,q+r-1} \quad (3.37)$$

For points at infinity, the formulation is reversed: for  $1 \leq r \leq K$ ,

$$H_{\text{red}}(\zeta) = \sum_{r=0}^{+\infty} \frac{C \cdot iE^{-1} \cdot [iA \cdot E^{-1}]^r \cdot B}{\zeta^{r+1}} \approx \sum_{r=0}^K \frac{iB_{p+r}}{\zeta^{r+1}} \quad (3.38)$$

$$E_{0,q} = C_q \quad (3.39)$$

$$E_{p+r,q} = iA_{p+r-1,q} \quad (3.40)$$

Using the two last equations, we recognise the well-known form of the fluid equations 3.8 as

$$A \cdot E^{-1} = \begin{pmatrix} 0 & -i & & \\ & \ddots & \ddots & \\ & & 0 & -i \\ \gamma_0 & \cdots & \cdots & \gamma_N \end{pmatrix} \quad (3.41)$$

$$C \cdot E^{-1} = (1 \ 0 \ \cdots \ 0) \quad (3.42)$$

$$B_p = -ik \int v^p F_{\text{eq}} dv \quad (3.43)$$

where  $\gamma$  gives the coefficient of the closure. We recover that any solution formulated as the closure of the  $N^{\text{th}}$  moment matches the behaviour at infinity at order  $N$ . Two-sided interpolation “ $\alpha = \beta$ ” is possible, doubling the order of interpolation.

### 3.4.2 Collisionless closures as special cases

For instance, to compute an order  $\ell$  realisation matching the high-frequency behaviour at order  $2\ell$ , we consider setting  $\alpha = \beta$  all infinite. If  $\ell$  is even, it corresponds to setting the  $\ell + 1^{\text{st}}$  cumulant to zero. In this case, the Loewner matrices have anti-diagonal (Hankel) structure, and can be written as

$$H_{\text{red}}(\zeta) = \sum_{r \geq 1} \frac{\gamma_r}{\zeta^r} \quad (3.44)$$

$$E = \begin{pmatrix} \gamma_1 & \cdots & i^\ell \gamma_\ell \\ \vdots & \ddots & \vdots \\ i^\ell \gamma_\ell & \cdots & -\gamma_{2\ell-1} \end{pmatrix} \quad A = \begin{pmatrix} \gamma_2 & \cdots & i^\ell \gamma_{\ell+1} \\ \vdots & \ddots & \vdots \\ i^\ell \gamma_{\ell+1} & \cdots & -\gamma_{2\ell} \end{pmatrix} \quad (3.45)$$

$$B_p = C_p = -i\gamma_p \quad (3.46)$$

If  $\ell$  is odd, the matrix  $E$  is singular, the model is degenerate. In order to have the models corresponding to zeroing the  $\ell^{\text{th}}$  cumulant, we need interpolate the adiabatic dynamics by setting  $\beta_\ell = 0$  (but keep  $\alpha_\ell = \infty$ ). In that case, the matrices become

$$E = \begin{pmatrix} \gamma_1 & \cdots & i^{\ell-1} \gamma_{\ell-1} & -H(0) \\ \vdots & \ddots & \vdots & i\gamma_1 \\ \vdots & & \vdots & \vdots \\ i^\ell \gamma_\ell & \cdots & i\gamma_{2\ell-2} & i^\ell \gamma_{\ell-1} \end{pmatrix} \quad A = \begin{pmatrix} \gamma_2 & \cdots & i^{\ell-1} \gamma_\ell & \gamma_1 \\ \vdots & \ddots & \vdots & \vdots \\ i^\ell \gamma_{\ell+1} & \cdots & i\gamma_{2\ell-1} & i^{\ell-1} \gamma_{\ell-1} \end{pmatrix} \quad (3.47)$$

$$B_p = -i\gamma_p \quad (3.48)$$

$$C = (-i\gamma_1 \ \cdots \ -i\gamma_{\ell-1} \ H(0)) \quad (3.49)$$

In addition, the 3-field and 4-field Hammett–Perkins models correspond to all infinite  $\alpha$ , with  $\beta = (\infty, 0, 0)$  and  $\beta = (\infty, 0, 0, 0)$ . This choice of interpolation points directly corresponds to the Padé approximation order in (Hammett & Perkins, 1990). More generally, we expect all the closures found by (Hunana *et al.*, 2018) to be computable by this method, using only high-order interpolation at 0 and  $\infty$ .

This interpolation method is very lightweight, and almost phenomenological: the model is built so as to match the behaviour at phase velocities  $\alpha_p$  and  $\beta_q$ . However, the choice of those  $\alpha_p$  and  $\beta_q$

is completely free, and left to the wisdom of the physicist. The hydrodynamic behaviour is encoded by interpolation at infinity, while kinetic effects happen for finite phase velocities. The symmetry between positive and negative phase velocities advises using interpolation points with the same symmetry. While optimality properties have been shown for some special relations between the interpolation points (Gugercin *et al.*, 2006; Beattie & Gugercin, 2012), this choice has not been retained here because of numerical difficulties.

### 3.5 Numerical comparison with known closure schemes

We compute two interpolated models: a 3-dimensional model matching high-frequency behaviour at order 3 and interpolating  $H_{\text{kin}}$  at  $\zeta = 0, \pm 1.3$ ; and a 4-dimensional model matching high-frequency behaviour at order 2, interpolating at order 2 at  $\zeta = 0$ , and at order 1 at  $\zeta = \pm 1.3$  and  $\zeta = \pm 7.04$ . The value of 1.3 has been chosen inside the thermal region. The value of 7.04 has been chosen so as to preserve the sign of the imaginary part. Choosing symmetric interpolation points makes the model real when written in physical coordinates. Those are compared to the zero-cumulant fluid models and to Hammett–Perkins models. Wang’s closure (Wang *et al.*, 2019) is equivalent to 4-field Hammett–Perkins, and is not studied separately.

For most cases, the stationary limit  $\zeta \rightarrow 0$  verifies  $H \rightarrow -1$ , recovering the expected low-frequency response  $n \sim -n_0 \times e\phi/T$ . For high-frequency waves  $\zeta \rightarrow \infty$ , the fluid, Hammett–Perkins and interpolated formulations correctly give  $H \sim \zeta^{-2}$ . Balanced truncation is worse performing in this region, exhibiting a slower decrease  $H \sim \alpha\zeta^{-1} + (1 + \beta)\zeta^{-2}$ , with  $\alpha$  and  $\beta$  going to 0 when increasing the number of components.

#### 3.5.1 Accuracy of the Vlasov dynamics

The error on density are plotted figure 3.4, as the complex modulus  $|H_{\text{model}}(\zeta) - H_{\text{kin}}(\zeta)|$ . For reference, the kinetic response  $|H_{\text{kin}}(\zeta)|$  is plotted in dotted line. Adding components  $f_p$  to the balanced model from the bulk of Van–Kampen modes does not increase accuracy. Our new models outperforms both Hammett–Perkins formulations in the thermal phase velocity region, without a significant penalty in the low phase velocity region. Unsurprisingly, the best response in the high phase velocity region is obtained from more conventional fluid models, because of very weak kinetic effects in this regime. As the interpolated models explicitly constrain their behaviour at infinity, their performances are comparable. Landau phase-mixing phenomenon is embedded into the balanced truncation formulation as a damping term. This is confirmed by looking at the eigenvalues of the balanced truncation system, table 3.1, whose imaginary part are well below the  $-\sigma = 0.02$  regularisation term. More generally, all the eigenvalues of both the balanced truncation and interpolation model have a larger negative real part than the Hammett–Perkins model, hinting at a stronger damping behaviour. The imaginary parts come in the thermal range, and in conjugate pairs to keep the symmetry between positive and negative phase velocity.

Model	Eigenvalues	
Balanced 3	0.	$\pm 1.576 + 1.222i$
Interpolation 3	0.	$\pm 1.508 + 0.894i$
Hammett-Perkins 3	0.	$\pm 1.472 + 0.463i$
Fluid 3	0.	$\pm 1.732 - 0.i$
Balanced 4	$\pm 0.678 + 1.485i$	$2.087 + 1.479i$
Interpolation 4	$\pm 0.617 + 1.272i$	$1.956 + 1.146i$
Hammett-Perkins 4	$\pm 0.555 + 1.004i$	$1.922 + 0.755i$
Fluid 4	$\pm 0.742 - 0.i$	$2.334 - 0.i$

Table 3.1: Eigenvalues of the reduced models.

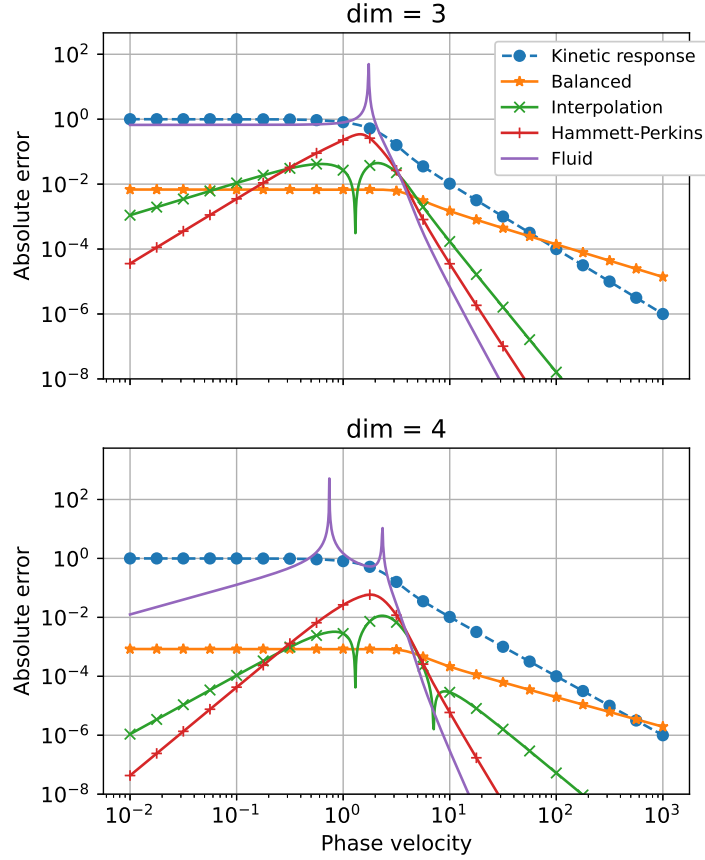


Figure 3.4: Reduced model error for density as a function of phase velocity. The “kinetic response” curve corresponds to  $|H_{\text{kin}}(\zeta)|$ , to be used as a baseline for comparison. The “balanced” curves correspond to the response of the balanced truncation model. The “fluid” curves correspond to the zero-cumulant models.

### 3.5.2 Coupled Vlasov-Poisson problem

The previous section investigated the behaviour of the uncoupled Vlasov equation. We now try to recover two well-known features of the Vlasov-Poisson system: Landau damping and bump-on-tail instability. The dispersion relation is

$$k^2 = H(\zeta) \quad (3.50)$$

with  $H$  one of the frequency responses above, and  $k$  is the spatial wave-number scaled to the Debye length. We solve this dispersion relation by computing the right-hand-side  $H(\zeta)$  on a grid of complex  $\zeta$ . For each value of  $\Re[\zeta]$ , seek the value of  $\Im[\zeta]$  where the imaginary part  $\Im[H[\zeta]]$  is closest to zero. The value of  $k^2$  is given by  $\Re[H[\zeta]]$ . A more elaborate method would be to solve the polynomial equations arising from the transfer functions, but precision is not an issue.

The results are given figure 3.5. We observe that for  $k > 0.4$ , the behaviour of the 4-field balanced truncation model is very close to the kinetic result. Unfortunately, a very low  $k$  instability appears, related to high phase velocities. For the “balanced 4” model, the maximal growth rate is smaller than the regularisation  $\sigma$ . This is due to the aberrant behaviour of the transfer function for high phase velocities: the analytic response is closest to the positive real axis for  $\zeta \rightarrow \infty$ , and the reduced model tends to overshoot. The violated property is known as passivity (Grivet-Talocia & Gustavsen, 2016): the real part of  $i\zeta n/\phi$  must be positive when  $\Im[\zeta] \geq 0$ . This ensures the energy

flows from the wave to the particles, so that  $\vec{j} \cdot \vec{E} \geq 0$ . Passivity-preserving extensions of balanced truncation (Reis & Stykel, 2009) have been tried unsuccessfully.

The interpolation method outperforms the Hammett–Perkins method in both cases. While being less precise than the balanced model for  $k > 0.4$ , the passivity constraint is respected, and Landau damping damps. The optimal choice in terms of interpolation error should be  $\alpha = \beta$  opposite complex conjugates of the dynamical poles (Beattie & Gugercin, 2012). Unfortunately, this choice leads to the same kind of passivity breakage.

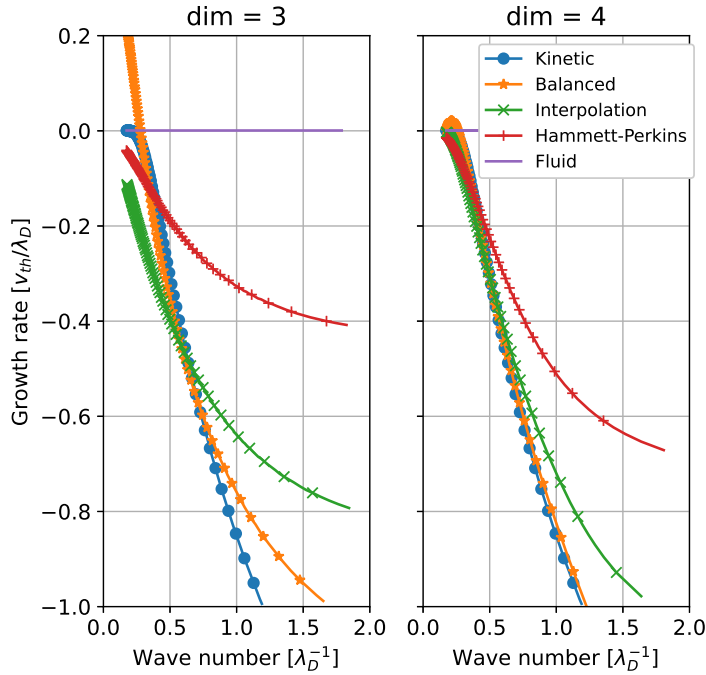


Figure 3.5: Numerical dispersion relations for the Landau-damping test.

We also benchmark the bump-on-tail instability. It can be excited by mixing another cold Maxwellian into the equilibrium. To study it, we double the state space, once for the bulk, once for the beam. We use the same method for solving the dispersion relation

$$k^2 = H(\zeta) + n_1 H\left(\frac{\zeta - u_1}{\sqrt{T_1}}\right) \quad (3.51)$$

where  $n_1 = 0.2$ ,  $u_1 = 3$  and  $T_1 = 0.01$  are the density, velocity and temperature of the cold beam. In the region where the slope of the distribution function is reversed, for  $2.7 < \zeta < 3$ , the system is unstable. Farther for this phase velocity (including opposite phase velocity), the waves are Landau-damped. The results are shown on figure 3.6. As a function of the wave-number  $k$ , two branches appear, corresponding to positive and negative phase velocities. As earlier, both interpolation and balanced truncation methods feature a damped branch, with a modulated shape near  $k\lambda_D = 0.4$  compared to stock Landau damping. In addition, an unstable branch appears in the  $k\lambda_D < 0.5$  region, which corresponds to the expected bump-on-tail instability. Once again, the balanced truncation method fails in the region  $k\lambda_D < 0.1$ . Meanwhile, both interpolation and balanced method outperform both the Hammett–Perkins and the zero-cumulant fluid models for the bump-on-tail instability.

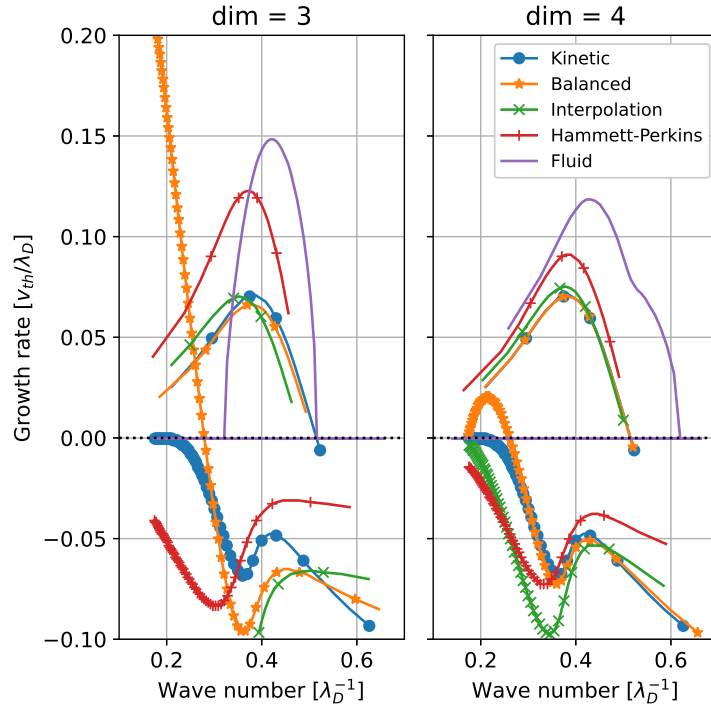


Figure 3.6: Numerical dispersion relations for the bump-on-tail distribution function. The bump-on-tail case uses  $n_1, u_1, T_1 = (.2, 3, .01)$ . The slope of the distribution function is reversed for  $2.7 < v < 3$ .

## 3.6 Discussion of the method

### 3.6.1 Back to real space

The obtained models have been derived in terms of the phase velocity  $\zeta = \omega/k$ . In order to formulate them in real space, they need to be extended to  $k < 0$  (the equations for  $k = 0$  are trivial). The correct way to achieve that is to use the symmetries of the dynamical system. Changing  $k \rightarrow -k$  corresponds to discussing frequencies  $\omega$  with negative real part. To keep the causality properties, the imaginary part of  $\omega$  must remain the same. The transformation rule is then  $\omega \rightarrow -\omega^*$ . The state-space model is

$$\begin{aligned} -i\omega x &= Akx + Bk\phi \text{ for } k > 0 \\ +i\omega^* x &= -Akx - Bk\phi \text{ for } k < 0 \end{aligned}$$

or in general

$$-i\omega x = |k|\Re[A]x + ik\Im[A]x + |k|\Re[B]\phi + ik\Im[B]\phi \quad (3.52)$$

We recover the Hammett–Perkins prescription of an  $|k|$  term. In real space, this is associated to a non-local operator instead of a regular  $x$ -derivative.

### 3.6.2 Application to other kinetic problems

Since the interpolation method only requires evaluations of the frequency response function, it is very versatile and can be applied to other kinetic problems. For instance, we can consider the linear gyro-kinetic problem. Analytical work allows to perform the resonant integrals formally in terms of the Fried and Conte function, leaving smooth integrals in other directions. The KineZero model performs such computations as part of the QuaLiKiz code (Bourdelle *et al.*, 2002; Citrin

*et al.*, 2017; Stephens, 2019). An interpolatory reduced model could be formulated to interpolate simultaneously the few first moments of the perturbed distribution function, as proposed equations 3.53–3.55.

$$H_{*n} \left( \frac{\omega}{n} \right) \approx \int \frac{1}{\omega - k_{\parallel} v_{\parallel} - nu_D} \mathcal{F} dv_{\parallel} d\mu d\theta \quad (3.53)$$

$$H_{*u} \left( \frac{\omega}{n} \right) \approx \int \frac{v_{\parallel}/v_{\text{th}}}{\omega - k_{\parallel} v_{\parallel} - nu_D} \mathcal{F} dv_{\parallel} d\mu d\theta \quad (3.54)$$

$$H_{*e} \left( \frac{\omega}{n} \right) \approx \int \frac{\left( \frac{m}{2} v_{\parallel}^2 + \mu B \right) / T}{\omega - k_{\parallel} v_{\parallel} - nu_D} \mathcal{F} dv_{\parallel} d\mu d\theta \quad (3.55)$$

where  $\omega$  is the mode frequency,  $n$  its toroidal wave number,  $u_D$  the toroidal precession angular velocity. The gyro-kinetic dispersion relation would then be written as

$$1 + n^2 q^2 \rho_*^2 = \int \frac{\omega - \omega_*}{\omega - k_{\parallel} v_{\parallel} - nu_D} \mathcal{F} dv_{\parallel} d\mu d\theta \quad (3.56)$$

$$= (\omega - \omega_{*n}) H_{*n} - \omega_{*u} H_{*u} - \omega_{*T} \left( H_{*e} - \frac{3}{2} \right)$$

$$\omega_* = \omega_{*n} + \frac{v_{\parallel}}{v_{\text{th}}} \omega_{*u} + \omega_{*T} \left( \frac{\frac{m}{2} v_{\parallel}^2 + \mu B}{T} - \frac{3}{2} \right) \quad (3.57)$$

with  $\omega_*$  the diamagnetic frequency split into the contributions  $\omega_{*n,u,T}$  or the density, parallel velocity and temperature gradients. In this local linear setting, the functions  $H_{*n,u,e}$  are independent of the density and temperature gradients. Rather, the gradients only appear in the assembled dispersion equation 3.56. As a consequence, we expect the coefficients of the closure to be independent of the gradients, as seen by (Sarazin *et al.*, 2009). Extensions of the method for parametric model order reduction (Lefteriu *et al.*, 2011) would allow to include the dependency on the ballooning angle or the  $E \times B$  shear.

### 3.6.3 Non-linear extension

The balanced truncation and interpolation methods are built for linear systems, and their applicability to non-linear systems is not straightforward. The simplest heuristic is to simply replace the time derivative  $\partial_t \rightarrow \partial_t + \vec{u} \cdot \vec{\nabla}$  thanks to Galilean invariance. More sophisticated methods have been devised to extend the method systems with a so-called bilinear non-linearity (Benner & Damm, 2011; Benner & Breiten, 2012; Gosea, 2017). Instead of embedding the non-linearity as the Reynolds stress  $\vec{u} \otimes \vec{u}$ , quadratic in fluid moments, the non-linearity would remain as a product of fluid moments and the electric field.

Since the idea is to formulate a reduced order model to accelerate simulations, the interpolation method can be leveraged to compute a reduced model directly in discrete time. This can be done by interpolating at values of  $e^{i\omega\Delta t}$  instead of the frequency  $\omega$  (Vuillemin & Poussot-Vassal, 2019). The complexity would not change much —everything would still be in a largely opaque matrix—, while the numerical accuracy may benefit.

Progress has also been made for fluid systems using balanced proper orthogonal decomposition on nonlinear simulations instead of their linearisation (Rowley, 2005). In the cited works, balancing has shown to improve significantly the relevance of the decompositions. Other methods based on neural networks have also shown promising results (Ma *et al.*, 2020).

## 3.7 Conclusion

The reduction of the collisionless Vlasov equation has been investigated using the balanced truncation method. This method constructs a simplified dynamical space, where the basis is chosen so as to maximise both the reachability and the observability of its individual vectors. The rapid decay of the Hankel singular values indicate a strong reducibility of the Vlasov model. The balanced

truncation reduced model reconstructs the Vlasov dynamics accurately in the thermal phase velocity region, but has degraded performances in the asymptotic low and high phase velocity regimes. This degradation involves a violation of passivity. As a result, the coupled Vlasov–Poisson dynamics features a spurious instability at high phase velocities. This violation comes from the difficulty to approximate the Landau damping rate  $\omega^4/k^3 \exp(-\omega^2/k^2)$  as a rational function. General passivity-preserving model reduction is still an open problem (Grivet-Talocia & Gustavsen, 2016), but existing algorithms may allow more systematic application of the method.

We have formulated a novel non-collisional closure method based on interpolation of the linear response function, and applied it to the Vlasov–Poisson problem. The method generalises derivations based on asymptotic matching at low and high frequency. The resulting model outperforms usual Hammett and Perkins’ formulation in the thermal phase velocity range, for both the density response, the Landau damping rate and the bump-on-tail instability growth rate. The general method is very versatile, and should allow for efficient and cheap model order reduction for gyro-kinetic toroidal drift waves in the collisionless regime.



## Chapter 4

# Persistence of linear properties in flux-driven turbulence

A tokamak is an open system: it is forced out of equilibrium by a heat source, develops a self-consistent turbulent state, and transports the heat outwards. The excess is removed at the boundary by thermal sinks and dissipative processes. The conjoint evolution of the free energy sources and of the fluxes allows for rich dynamics at all scales. Modelling through *flux-driven* simulations allows to estimate the resulting state: the balance between sources, sinks, neoclassical and turbulent fluxes dictate density and temperature profiles. On the one hand, zonal flow (Diamond *et al.*, 2005) are a key player: their stabilising effect on turbulence (Biglari *et al.*, 1990; Terry, 2000) gives rise to complex patterns (Kosuga *et al.*, 2014; Dif-Pradalier *et al.*, 2015; Peeters *et al.*, 2016; Dif-Pradalier *et al.*, 2017b). The generation of zonal flows is a generic process in self-organised systems (Charney & Drazin, 1961; Balmforth *et al.*, 1998; Paparella & von Hardenberg, 2012). As a critically non-linear process, it has provided a puzzle for the community. On the other hand, turbulence saturation through avalanche formation (Garbet & Waltz, 1998; Beyer *et al.*, 2000; Idomura *et al.*, 2009; McMillan *et al.*, 2009; Sarazin *et al.*, 2010) and spreading (Garbet *et al.*, 1994; Hahn *et al.*, 2004) remains insufficiently understood. The interplay of all these dynamical events, together with their interaction with the equilibrium profiles, is expected to determine the generation of transport barriers (Miki *et al.*, 2012; Itoh & Itoh, 2016; Ashourvan & Diamond, 2016, 2017), eventually leading to bifurcations (Hinton, 1991; Itoh *et al.*, 1994). However, the impractical numerical cost of such simulations prompts the use of reduced models. In this context, two complementary assumptions are often used: the quasi-linear reduction, and the locality assumption. These will be addressed in the following, together with their relevance when confronted to the outputs of flux-driven gyro-kinetic simulations, by essence free of such simplifications.

### 4.1 Quasi-linear estimation of the fluxes

Efficient estimates of transport levels have been achieved through *local quasi-linear* modelling (Bourdelle *et al.*, 2007; Citrin *et al.*, 2017; van de Plassche *et al.*, 2020). These models have been extensively benchmarked against non-linear simulations (Jenko *et al.*, 2005; Casati *et al.*, 2009) and experiments (Kotschenreuther *et al.*, 1995; Waltz *et al.*, 1997). The turbulent intensity is not predicted, and has to be externally provided by a so-called saturation rule (Citrin *et al.*, 2017). Although it has proven robust beyond its assumptions (Besse *et al.*, 2011), quasi-linear theory relies on ad-hoc closures and debated assumptions (Elskens & Escande, 2002; Diamond *et al.*, 2010). It has not yet demonstrated an ability to simulate self-organisation processes such as zonal flows and staircases. Whether this is a dead-end of the approach or a limitation of current implementations is still unknown. Three assumptions are specifically under question: (1) the linearity of turbulent fluctuations; (2) the choice of a saturation rule; (3) the magnetic surface locality.

### 4.1.1 The quasi-linear problem

The *particular* quasi-linear theory attempts to describe the motion of particles subject to those perturbations. For stationary and toroidally symmetric electric field, the particles follow an integrable Hamiltonian motion. In the presence of perturbations, this is not longer guaranteed. Depending on the strength of this perturbation and the properties of the particle, the motion can remain nearly integrable or become chaotic. In the latter case, particles are no longer kept close to their reference flux-surfaces, and can be deconfined. On very short times, the particles see individual perturbations, and the motion remains predictable. Conversely, on larger time scales, the perturbations decorrelate and tend to resemble a stochastic process. In turn, the particles trajectories become stochastic and diffuse in phase space (Elskens & Escande, 2002).

Assuming each particle has a stochastic motion, the distribution function diffuses. From the particles' responses, matter and heat fluxes can be computed, formulating the *flux* quasi-linear model. Given an ambient toroidally symmetric distribution function  $F_{\text{eq}}$  and weak enough perturbations, the perturbed response of the distribution function  $f$  can be approximated as linear in the potential  $\tilde{\phi}$ , hence the quasi-*linear* name

$$f_{n\omega} = H_{n\omega} \cdot [\tilde{\phi} F_{\text{eq}}]_{n\omega} \quad (4.1)$$

where  $H_{n\omega}$  is some linear operator. This response notably depends on the temperature and density gradients, but also on the fluctuation's properties like the toroidal wave-number. This linear relation can be used to estimate the transport due to the fluctuations of the potential (Diamond *et al.*, 2010). For instance, the radial heat flux appears as

$$\begin{aligned} Q^r &= \int_{\text{fast}} d\omega \sum_{n \neq 0} \int \left( \frac{m}{2} v^2 + \mu B \right) f_{n\omega} v_{E,n\omega}^* B_{||}^* R d\theta d v d \mu \\ Q_{\text{QL}}^r[\phi_{n\omega}] &\approx \frac{1}{rB} \int_{\text{fast}} d\omega \sum_{n \neq 0} \int \left( \frac{m}{2} v^2 + \mu B \right) \partial_{\theta} \tilde{\phi}_{n\omega}^* H_{n\omega} \cdot \tilde{\phi}_{n\omega} F_{\text{eq}} R d\theta d v d \mu \end{aligned} \quad (4.2)$$

This heat flux still depends on the specific realisation of turbulent flows, but is a quadratic quantity in the potential field. Therefore, in the ergodic limit, its ensemble average on the potential fluctuations should be finite. This last quantity, the quasi-linear heat flux, only depends on the spectrum of the potential and ambient distribution function  $F_{\text{eq}}$ .

The vaguely labelled “fast” frequency integral in the equation deserves some explanation. The distribution function  $f_{n\omega}$  reacts to the product of the fluctuations of the potential  $\tilde{\phi}_{n\omega}$  and of the ambient distribution function  $F_{\text{eq}}$  (equation 4.1). This response is frequency dependent and causal, so embeds a time delay. For consistency of the ambient vs. fluctuation splitting, the profiles must evolve more slowly than this delay. In other words, in the frequency integral equation 4.2, “fast” means very large compared to the profile frequency, and of the order of fluctuation frequency. The exact same condition allows to approximate  $H_{n\omega} \cdot [\tilde{\phi} F_{\text{eq}}]_{n\omega} \approx [H_{n\omega} \cdot \tilde{\phi}_{n\omega}] F_{\text{eq}}$ . This temporal separation is justified for quasi-static profiles. But may becomes more brittle for flux-driven dynamics.

For instance, the time spectra of two GYSELA simulations are shown figure 4.1. The spectra of the profiles feature a dominant stationary component, and a weak higher-frequency spectrum. The turbulent  $n \neq 0$  modes have a consistently broad spectrum.

### 4.1.2 The saturation issue

The only remaining modelling knob is the potential fluctuation spectrum: the linear description makes no attempt to provide one. A closure is needed for effective use of this discussion in integrated transport estimation. Turbulent fluctuations tend to grow from linear unstable eigenmodes of the coupled Vlasov–Poisson system. As instabilities, they can be expected to dominate the dynamics, while stable modes are damped out. Indeed, several frameworks assume the spectrum only to contain unstable modes, with the amplitude given by the non-linear saturation level. A popular method is fitting on reference non-linear simulation (Waltz *et al.*, 1997; Staebler *et al.*, 2007; Citrin

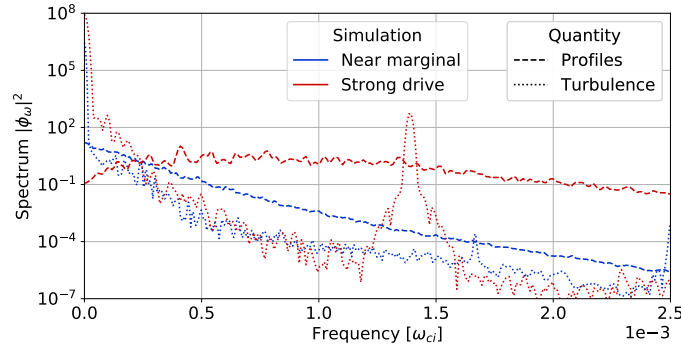


Figure 4.1: Frequency spectrum of axisymmetric (dashed lines) and non-axisymmetric modes (dotted lines) for the two simulations discussed in paragraph 4.2. The bump at frequency  $1.4 \times 10^{-3} \omega_{ci}$  in the “strong drive” simulation is due to a numerical artefact in the collision operator. It should not affect the results of this section.

*et al.*, 2017). We shall call this system *saturated* quasi-linear models, to distinguish from bare-bones flux estimation.

This modelling strategy faces several challenges. First, the resulting model is obviously not self-consistent, as it depends on exterior data. Second, restricting the spectrum to unstable modes is debatable: turbulence spreads into linearly stable regions, and can populate stable modes in unstable regions (Garbet *et al.*, 1994; Hahm *et al.*, 2004; Terry *et al.*, 2006; Hatch *et al.*, 2011). Third, the turbulent spectrum has no reason to saturate at a quasi-static value: it needs to respond to the dynamical evolution of the free energy source and large-scale flows in the problem. For instance, an ubiquitous feature in non-linear simulation of tokamak turbulent flows is the so-called avalanche effect (Garbet & Waltz, 1998; Beyer *et al.*, 2000; Idomura *et al.*, 2009; McMillan *et al.*, 2009; Sarazin *et al.*, 2010): heat and matter packets travel across the plasma domain with a seemingly ballistic motion. The precise dynamics of these avalanches is still to be known. Already, generation of and interplay with sheared zonal flows is believed to be critical (Terry, 2000; Diamond *et al.*, 2005). We expect that any self-consistent description of flux-driven dynamics requires a self-consistent back-reaction on zonal flows.

On the other hand, the rigorous evolution of the turbulent spectrum is accessible through the second-order cumulant equation (Farrell & Ioannou, 2007; Marston *et al.*, 2008; Srinivasan & Young, 2012). This equation is very complicated, depends on the third-order cumulant, unearthing a cumulant closure problem (Tobias & Marston, 2013). Nevertheless, this equation has proven useful in its ability to recover zonal flow growth. As an equation on the phase space of waves, postulating a scale separation between the turbulent waves and the profiles allows to formulate an optical approximation (Parker, 2016). The associated equation corresponds to a *wave-kinetic equation* (Weinberg, 1962).

Equation 4.1 and 4.2 contain the heart of the quasi-linear modelling: turbulent fluctuations obey linear dynamics, and only affect the profiles by non-linear self-coupling. As such, those turbulent fluctuations should be considered as infinitesimal non-interacting waves in a dispersive medium. This analogy turns out fruitful when pushed further. In a dispersive medium, waves tend to get moved and molded by their neighbourhoods. A full social theory of waves would require to understand the fully non-linear dynamics, but a macroscopic theory of non-interacting waves is accessible. Describing this motion can be done using the eikonal approximation (McDonald, 1988), which reduces to a wave-kinetic equation upon further scale separation.

### 4.1.3 Relation to the Hopf hierarchy

In chapter 1, we related the two problems of kinetic moment closure and non-linear flux closure using the Hopf hierarchy. Let us deepen this analogy. In the non-linear setting, probability distribution of realisations is not known. The relevant information is its average —the *profile*—, and its evolution. In the kinetic system, the associated object is the mean velocity  $u$ . Their

evolution 4.3–4.4 is bound to a quadratic quantity: the profile equilibrium dynamics and the Reynolds stress on its left-hand side; and a second-order quantity: the flux  $\vec{\Gamma}$  and the pressure tensor  $P$  on its right-hand side.

$$\partial_t F_{\text{eq}} - [H_{\text{eq}}, F_{\text{eq}}] = -\text{div } \vec{\Gamma} \quad (4.3)$$

$$\partial_t \vec{u} + \text{div}(\vec{u} \otimes \vec{u}) + \nabla \Phi_{\text{eq}} = -\text{div } P \quad (4.4)$$

The laminar dynamics correspond to no turbulent flux, and is analogous to a cold beam. The quasi-linear approximation seeks to relate the pressure tensor to the dynamics of particles around a reference position

$$\frac{d}{dt} \begin{pmatrix} \vec{x} - \vec{x}_0 \\ \vec{v} - \vec{u}(x_0) \end{pmatrix} = \begin{pmatrix} \vec{v} - \vec{u}(x_0) \\ -(\vec{x} - \vec{x}_0) \cdot \vec{\nabla} \vec{\nabla} \Phi_{\text{eq}}(x_0) \end{pmatrix} \quad (4.5)$$

where  $\vec{x}_0$  is in the fluid frame, moving at velocity  $\vec{u}$ . Instabilities of the beam correspond to regions where the electric field is divergent, widening the beam. A saturation rule corresponds to defining an effective pressure from a priori estimates of the velocity excursions in this dynamics.

The next step is embracing a non-zero pressure  $P$ . As usual, its dynamics depend on the laminar advection, and a third-order term. The wave-kinetic formulation here corresponds to using the linearised dynamics 4.5 to define the evolution of the tensor  $P$ . In our case, the tensor  $P$  is advected by the flow  $\vec{u}$ , and its components are rotated by the fluctuation dynamics. A non-linear saturation of the pressure can be defined in a quasi-normal fashion by adding a damping term proportional to  $P^2$ .

#### 4.1.4 The locality assumption

The quasi-linear assumption corresponds to a temporal and an intensity assumption, nothing is said about spatial scales. Still, linear turbulent structures are expected to be radially thin around a reference magnetic surface (Görler & Jenko, 2008), and to only depend on plasma parameters and their gradients close by. This is a result of the assumption which relates the distribution function fluctuations to the potential fluctuations through local equilibrium parameters. This induces a spatial scale separation between a *local* turbulent behaviour, and a slower and smoother evolution of the profiles (Peeters *et al.*, 2009). In the point of view of turbulence, the free energy source is static and externally defined. The system conserves enough degrees of freedom to non-linearly saturate turbulence and develop zonal flows, but back-action on the profiles is severely limited. In this so-called *gradient-driven* model, the turbulent heat flux becomes a non-linear function of stationary imposed gradients. As such, this model allows to infer a non-linear turbulent Fourier law. However, this contradicts flux-driven dynamics, where profile corrugations may render the scale separation insufficient, resulting in a brittle non-linear Fick's law (Dif-Pradalier *et al.*, 2010). Combined with the quasi-linear framework, the locality assumption reveals extremely powerful, and has been the ground for the development of quasi-linear transport models (Citrin *et al.*, 2017).

## 4.2 Persistence of linear properties in turbulent dynamics

In order to test these hypotheses, we perform two non-linear electrostatic gyro-kinetic turbulence simulations using GYSELA, compute key indicators from the three-dimensional potential and fluid moment outputs, and confront them to the quasi-linear code QuaLiKiz (Citrin *et al.*, 2017).

We feed QuaLiKiz with the temporal averages of the GYSELA profiles. QuaLiKiz (Citrin *et al.*, 2017) is a gyro-kinetic quasi-linear code for transport modelling. It solves the gyro-kinetic dispersion relation with adiabatic electrons. For efficiency, the analytic distribution response is simplified by computing the shape of the potential fluctuations in the fluid limit (Bourdelle *et al.*, 2007; Stephens, 2019), while keeping a kinetic treatment of the wave–particle resonance. The number of numerical integrations is limited by performing the resonant velocity integration analytically. The effect of zonal flow shear is done by perturbative modification of this response.

As we will see, both simulations exhibit Kubo numbers of a few units, suggesting assumption (3) is brittle. However, properties of turbulent fluctuations match expected linear properties both qualitatively and quantitatively, strengthening this assumption. As will be discussed, a static saturation rule would suggest the temporal variations of the heat flux to be determined by the fluctuations of the phase. However, this is not verified: the variations of the turbulent intensity explain most of the variations the flux. Furthermore, the turbulent transport exists in the linearly stable region. These results emphasise the need for a self-consistent prediction of the turbulent intensity, taking into account turbulent spreading.

### 4.2.1 The setup

We perform non-linear flux-driven simulations using the code GYSELA. It simulates electrostatic turbulence between the full gyro-kinetic ion distribution function and adiabatic electrons, from the centre to the last closed magnetic surface, with a buffer region extending beyond the “separatrix” at  $r/a > 1$ . With a centrally peaked heat source driving the system out of equilibrium, the simulations are run long into the turbulent regime, until convergence of the temperature and density profiles. Both cases are run in the so-called “local limit” (Lin *et al.*, 2002), at  $\rho_* = 1/350$ . In this limit, the scale separation between the profile behaviour ( $\sim a$ ) and the turbulent eddies ( $\sim 10\rho_i$ ) is often considered valid. In order to avoid cherry-picking an artificially unfavourable specific set of plasma parameters, all other main plasma parameters are different, as illustrated in table 4.1.

Case	$\rho_*$	Aspect ratio	$\nu_*$	$(q_{50}; q_{95})$	$T_i/T_e$
Near marginal	1/350	$A = 3.2$	0.24	(1.4; 4.0)	$\neq 1$
Strong drive	1/350	$A = 6$	0.02	(1.7; 2.8)	$= 1$

Table 4.1: Plasma parameters at mid-radius: normalised Larmor radius  $\rho_* = \rho_i/a$ ; aspect ratio  $A = R/a$ ; collisionality  $\nu_*$ ; safety profile  $q$ ; electron temperature ratio  $\tau = T_i/T_e$ .

The converged normalised temperature gradient profiles  $R/L_T = -R\partial_r T/T$  and mean zonal flow profiles are shown figure 4.2 ( $R$  is the tokamak major radius,  $r$  its minor radius, and  $T$  is the temperature profile). The linear instability threshold of the equivalent non sheared laminar plasma is estimated using (Jenko *et al.*, 2001). Because it neglects  $E \times B$  shear, this threshold should be thought as a lower bound (Terry, 2000; Garbet *et al.*, 2002; Dagnelie *et al.*, 2019). Also, the threshold is reported to be upshifted in collisionless regimes (Dimits *et al.*, 2000), although accounting for collisions somewhat weakens this assertion (Dif-Pradalier *et al.*, 2009).

One simulation is in a “strong drive” regime: the temperature gradient  $R/L_T$  is well above the no-flow threshold  $R/L_{T_c}$ . The zonal flow shear features a large stationary component (plain green line), with subdominant fluctuations (green shade). Part of the fluctuations resemble the avalanches observed in (McMillan *et al.*, 2009; Idomura *et al.*, 2009). In opposition, the second simulation is in a “near marginal” regime: the temperature gradient is around the threshold  $R/L_T \sim R/L_{T_c}$ , and zonal flow shear is dominated by its fluctuating component. A staircase pattern from the zonal mean flow exists but remains subdominant. Avalanche-like events are observed to propagate over a significant fraction of the entire radial domain.

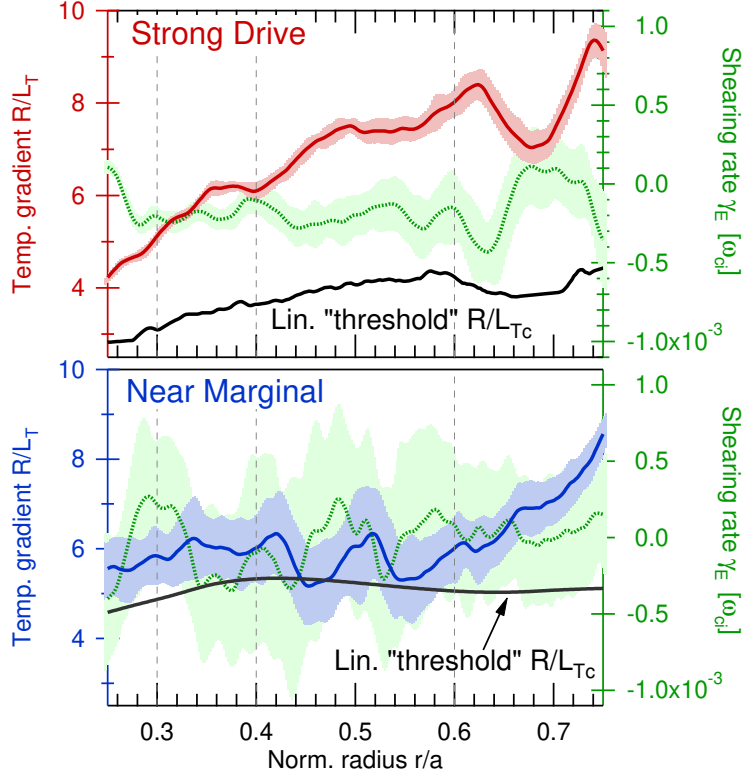


Figure 4.2: Radial profiles of the normalised temperature gradient (red and blue) and of the zonal flow (green) profile for the considered simulations. Upper: strong drive simulation. Lower: near marginal simulation. The plain black lines give an estimate for the instability threshold. The shaded are correspond to temporal standard deviation.

#### 4.2.2 Strength of the non-linear effects

The above hand-waving about slow vs. fast dynamics can be made more precise by estimating typical frequencies (Diamond *et al.*, 2010) and associated Kubo number. Quasi-linear modelling of the heat fluxes assumes turbulent fluctuations obey linear dynamics. The effect of non-linearities should remain weak enough not to upset the structure of the turbulent cells. From the point of view of mixing, particles must jump from one eddy to the next before being trapped by the eddy and engaging in its non-linear advection. Several estimates are proposed hereafter, and summarised table 4.2.

The non-linearity acts on two scales: individually on the particles and statistically on the potential and on fluid fields. Particles mostly transit along the field line, and transversely drift depending on their energy. Given a kinetic nature of the ITG instability, the resonant particle layer drifts at the diamagnetic frequency. Introducing the poloidal correlation length  $L_\theta$  of turbulence, we write the typical time scale required for non-resonant particles to cross the turbulent filament and jump to its neighbour

$$\omega_{*T} = \frac{1}{L_\theta} \frac{\nabla T}{eB} \quad (4.6)$$

with  $e$  the species charge,  $B$  the magnetic field strength. Turbulent structures over-impose their  $E \times B$  drift on this motion. Turbulent trapping happens if a particle has the time to turn around the eddy before being decorrelated by drifts. This exploration frequency around the centre of that structure is given by the vorticity  $\nabla_\perp^2 \tilde{\phi}/B$ . We estimate it using its root-mean-squared value

$$\omega_{\text{eddy}} = \left\langle \left| \frac{\nabla_\perp^2 \tilde{\phi}}{B} \right|^2 \right\rangle_{\text{FS}}^{1/2} \quad (4.7)$$

where the angle brackets denote the flux-surface average of the quantity, and the tilde denotes the non-axisymmetric part.

The potential field and fluid moments are expected to evolve more slowly, as they average over the dynamics of individual particles. A relevant time-scale is the correlation time of turbulent fluctuations, trying to evaluate the cycling between unstable growth and non-linear saturation. For kinetic instabilities, the eigen-frequency defines the phase velocity of the linear instability. The relevant Lagrangian correlation time (as opposed to the Eulerian one) has to be evaluated in a moving frame to remove the associated Doppler effect. We compute this Lagrangian correlation time  $\tau_{\text{corr}}$  by following the toroidal shift between turbulence snapshots, and only integrating after realignment. We emphasise the choice of a Lagrangian correlation time: the ratio of Lagrangian to Eulerian correlation time is of a few units, rising up to 25 in a limited region. Using the Eulerian correlation time would result in a significant underestimation. This correlation time can be thought as a jump from one turbulent eddy to a (temporal) successor.

Turbulence acts on the Vlasov equation as both radial  $\tilde{v}_E^r$  and poloidal  $\tilde{v}_E^\theta$  advections. Particles in this velocity field may follow a random walk motion. Using the transverse correlation lengths  $L_r$  and  $L_\theta$  computed from the GYSELA output, we estimate the turbulent diffusion time scale as  $\tau_{\text{diff}} = L_{r,\theta} / \langle |\tilde{v}_E^{r,\theta}|^2 \rangle^{1/2}$ . This diffusivity acts on turbulence itself, so should be small compared to  $\tau_{\text{corr}}$  itself.

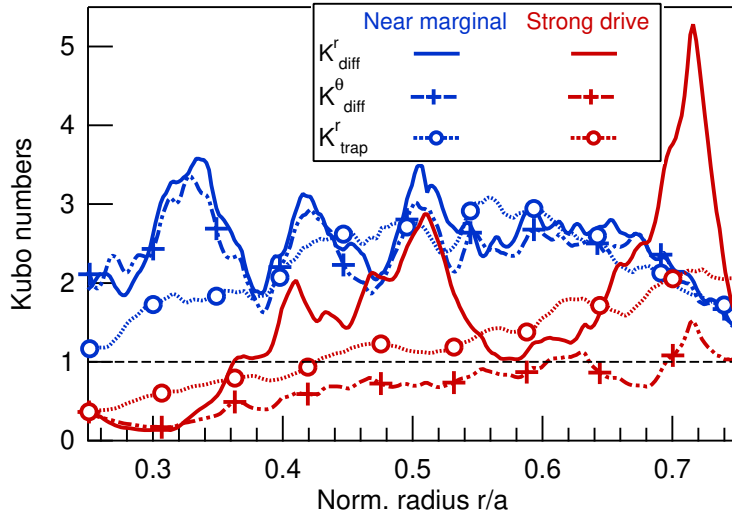


Figure 4.3: Kubo numbers for the principal non-linear dynamics in the problem. Plain and pluses: turbulent radial and poloidal  $E \times B$  velocity effect during a turbulent auto-correlation time. Circles: trapping of particles due to turbulent vorticity during transverse crossing of the turbulent filament.

The associated Kubo numbers —ratios of non-linear to linear frequency— are explicit table 4.2, and plotted figure 4.3. For the strong drive simulation, the value is around 1 consistently across the domain. This suggests that non-linear effects come into play in balance with the linear dynamics. The higher values for the near marginal simulation are consistent with self-organisation near criticality, where non-linear behaviours are enhanced (Pringle *et al.*, 2017). Overall, these values cast doubt on the validity of the quasi-linear assumption of wave turbulence, valid for low Kubo numbers. The different definitions of  $K$  with lead to similar magnitudes, strengthening the overall conclusion. Yet, quasi-linear theory is known to remain valid well beyond its domain of validity (G. Laval & Adam, 2018).

### 4.2.3 Comparison of heat fluxes

Yet, we know the relevance of quasi-linear modelling can extend beyond its immediate domain of validity (Besse *et al.*, 2011). In order to quantify this, we compare the fully integrated value of the heat flux between the two models. We feed QuaLiKiz with the temporal averages of the GYSELA profiles. The heat fluxes in the two simulations are shown figure 4.4.

$$\begin{aligned}
\text{Radial diffusion} & \quad K_{\text{diff}}^r = \sqrt{\langle |v_E^r|^2 \rangle} \frac{\tau_{\text{corr}}}{L_r} \\
\text{Poloidal diffusion} & \quad K_{\text{diff}}^\theta = \sqrt{\langle |v_E^\theta|^2 \rangle} \frac{\tau_{\text{corr}}}{L_\theta} \\
\text{Particle trapping} & \quad K_{\text{trap}} = \frac{\omega_{\text{eddy}}}{\omega_* T}
\end{aligned}$$

Table 4.2: Turbulent Kubo numbers shown figure 4.3.

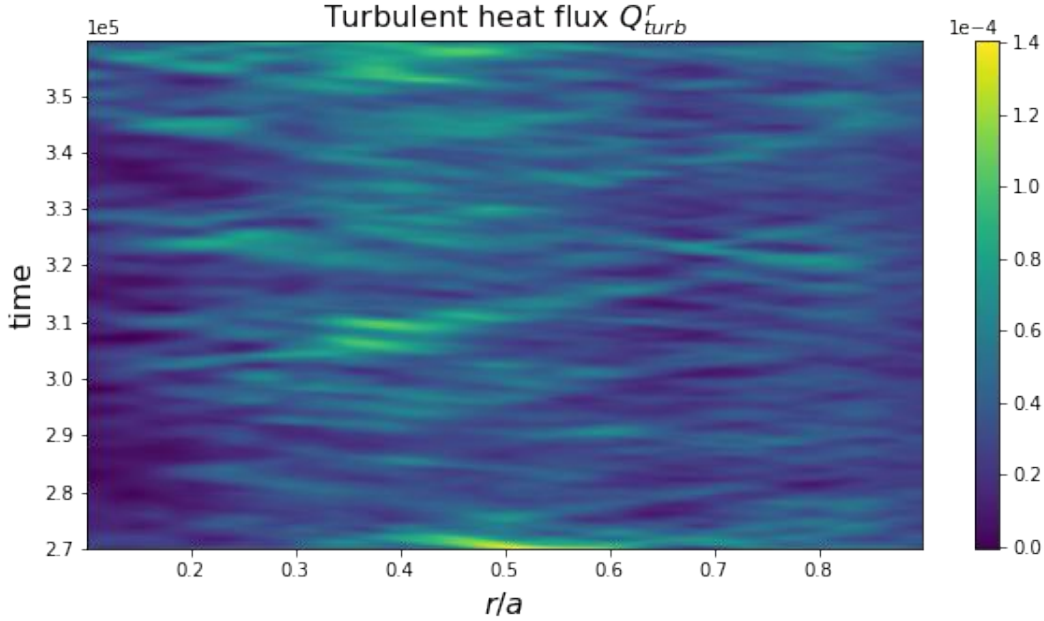


Figure 4.4: Heat flux from the GYSELA simulations as a function of radial direction (horizontal) and time (vertical).

The GYSELA heat flux is computed as the flux carried by the non-axisymmetric component of the radial  $E \times B$  velocity. Close to marginality, the heat flux is expected to strongly depend on the gradient. Since GYSELA's values of  $R/L_N$  and  $R/L_T$  vary in time, we need to account for the prediction uncertainty due to this stiffness effect. This is done by scanning the  $R/L_N$  and  $R/L_T$  values, using  $3 \times 3$  points within GYSELA's standard deviation. The local limit in which QuaLiKiz is derived requires the profiles to be smoother than the local instability width, of a few tens of  $\rho_i$ . To take this into account, we computed QuaLiKiz's heat flux with an additional radial smoothing of  $20 \rho_i$  and  $60 \rho_i$ . This smoothing has been computed by interpolating the profile from a reduced number of grid points, so as to avoid reducing the density and temperature gradients. The results are shown figure 4.5.

For the strong-flow test case, the discrepancy goes as high as a factor of 25 near  $r/a = 0.65$ . The zonal flow shear stabilisation effect accounts for a ten-fold reduction of the heat flux when comparing to the same QuaLiKiz simulation with shear removed (not shown). Because of the QuaLiKiz model for shear stabilisation, part of the difference could be attributed to modelling extrapolation: some very sharp peaks in the heat flux ratio correspond to positions of vanishing shear. For the near marginal simulation, the stationary zonal flow shear is smaller, so this shortcoming should be avoided. In that case, QuaLiKiz underestimates the heat flux by a factor of 3 for a large part of the simulation, and recovers the correct value on the far side of the chosen uncertainty range.

The local non-linear code GKW (Peeters *et al.*, 2007) has been run on both profiles at positions  $r/a = 0.3, 0.4, 0.6$ . The time-averaged flux are shown figure 4.5. The results for the near marginal simulation under-estimate the flux obtained by GYSELA. This is consistent with the results from QuaLiKiz.

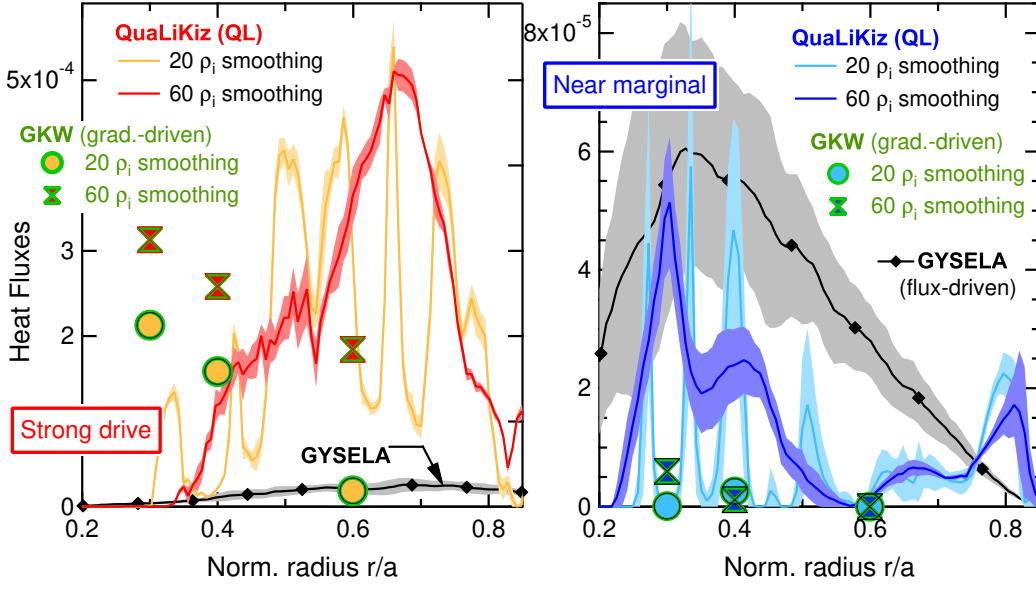


Figure 4.5: QuaLiKiz and GYSELA estimation of the heat flux for the profiles given figure 4.2. Left: strong drive simulation Right: near marginal simulation. Coloured lines correspond to QuaLiKiz output with different levels of smoothing: lighter is  $20\rho_i$ , darker is  $60\rho_i$ . The GYSELA value is shown in black. The shaded area gives the sensitivity to  $R/L_N$  and  $R/L_T$ .

#### 4.2.4 Possible origin of the discrepancy

We investigate further by testing the linearity hypothesis itself. Linear gyro-kinetic analysis predicts the linear response of the distribution function to an applied disturbance in the potential as (Garbet, 2001)

$$f_{n\omega} = - \left( 1 - \frac{\omega - k_\theta v_*}{\omega - k_{||} v_{||} - k_\theta v_D} \right) \mathcal{F} \frac{e\phi_{k\omega}}{T} \quad (4.8)$$

$$v_* = \frac{T}{eB} \partial_r \ln \mathcal{F} \quad (4.9)$$

with  $\mathcal{F}$  the equilibrium distribution function at temperature  $T$ .  $k_\theta$  denotes the poloidal Fourier mode number,  $k_{||}$  the parallel wave-number.  $v_D$  is the poloidal drift velocity, and  $v_*$  is the poloidal diamagnetic velocity. As part of its flux estimation, QuaLiKiz computes both the active and the reactive components of the particle and heat flux. This corresponds to the complex integrals

$$\Gamma_n = \int ik_\theta f_{n\omega} \phi_n^* d^3 v d\theta \quad (4.10)$$

$$Q_n = \int ik_\theta E f_{n\omega} \phi_n^* d^3 v d\theta \quad (4.11)$$

with  $E$  the energy, and where the frequency  $\omega$  is enslaved to  $k_\theta$  and  $k_{||}$  through the ambipolarity relation for adiabatic electrons

$$Z\Gamma_n(\omega) = \frac{N_e}{T_e} \int ik_\theta |\phi_n|^2 \quad (4.12)$$

In the linear setting, the value of  $|\phi_n|^2$  is unconstrained, it must be defined using the saturation rule. The total flux is then given by the sum over the toroidal mode number

$$\begin{aligned} \langle \Gamma \rangle &= \sum_{n>0} \Re[\Gamma_n] = 0 \\ \langle Q \rangle &= \sum_{n>0} \Re[Q_n] = \sum_{n>0} |Q_n| \sin \alpha_n \end{aligned}$$

We define the phase of the heat flux response as the complex argument of  $Q_n$ . This property can be compared to the value computed in the GYSELA simulation, defined as the complex argument  $\hat{\alpha}_n$  of

$$\hat{Q}_n = \int \left( \frac{1}{2} \hat{P}_{\parallel,n}^* + \hat{P}_{\perp,n}^* \right) \hat{v}_{E,n}^r d\theta = -i |\hat{Q}_n| e^{i\hat{\alpha}_n} \quad (4.13)$$

where  $\hat{P}_{\parallel,n}$ ,  $\hat{P}_{\perp,n}$  and  $\hat{v}_{E,n}^r$  are GYSELA output 3D data. In addition to the phase, linear theory also predicts the magnitude of the total heat flux relative to the convected heat flux. We compute it as

$$R_n = \left| \frac{Q_n}{T_{\text{eq}} \Gamma_n} \right| \quad (4.14)$$

for both QuaLiKiz and GYSELA. The computed estimates are shown figure 4.6. The relative contribution of each toroidal mode number to the total flux is shown in the lower panel. Both phase and magnitude ratios agree qualitatively, for both simulations, for  $n \gtrsim 15$ . Noticeably, for the near marginal simulation, QuaLiKiz predicts stable modes for  $n \gtrsim 40$ , while these modes contribute around 15% of the Gysela flux. For lower wave-numbers  $n \lesssim 15$ , the magnitudes ratios from two codes depart. This region only accounts for 10% of the Gysela fluxes, but between 35% and 55% of the QuaLiKiz output.

These results are consistent with previous findings (Casati *et al.*, 2009; Besse *et al.*, 2011). While it is unclear whether this difference should be attributed to approximations in QuaLiKiz or to hypothesis breakdown, the overall conclusion is that the fluctuation linearity assumption seems to hold in the flux-driven non-linear regime.

### 4.3 Influence of the turbulent intensity

The fluctuation linearity assumption seems to hold in the flux-driven non-linear regime, despite Kubo numbers around unity. This fortifies the case for quasi-linear integrated modelling. Meanwhile, the mismatch of the flux suggests a reduced involvement of the linear dynamics in the determination of the heat flux, replaced by a greater involvement of the turbulent intensity spectrum. Hence great care has to be taken in the definition of this modelling knob. For instance, QuaLiKiz's spectrum uses a double power law in  $k_\theta$  for unstable modes, and neglects stable modes. The coefficients have been fitted to non-linear gradient-driven simulations with the GENE code (Casati *et al.*, 2009; Görler *et al.*, 2011; Citrin *et al.*, 2017).

This property is compared to cross-correlation values in the GYSELA simulation. We decompose the heat flux into amplitude and phase effects

$$\begin{aligned} Q(t, r) &= \langle \hat{P} \hat{v}_E^r \rangle_{\text{FS}} = \mathcal{I} \mathcal{R} \sin \alpha(t, r) \\ \mathcal{I} &= \langle (\hat{v}_E^r)^2 \rangle_{\text{FS}} \\ \mathcal{R} &= \sqrt{\frac{\langle \hat{P}^2 \rangle_{\text{FS}}}{\langle (\hat{v}_E^r)^2 \rangle_{\text{FS}}}} \end{aligned} \quad (4.15)$$

where  $\mathcal{I}$  is the turbulent intensity.  $\mathcal{R}$  and  $\alpha$  represent the contribution of the pressure response magnitude and of fluctuation cross-phase to the heat flux. To test the sensitivity to the turbulent spectrum, we reconstruct the heat flux as

$$Q_{\mathcal{A}}(t, r) = \mathcal{I}(t, r) \mathcal{R}(t, r) \times \frac{\langle Q \rangle_t}{\langle \mathcal{I} \mathcal{R} \rangle_t} \quad (4.16)$$

$$Q_{\mathcal{I}}(t, r) = \mathcal{I}(t, r) \times \frac{\langle Q \rangle_t}{\langle \mathcal{I} \rangle_t} \quad (4.17)$$

$$Q_{\alpha}(t, r) = \sin \alpha(t, r) \times \frac{\langle Q \rangle_t}{\langle \sin \alpha(t, r) \rangle_t} \quad (4.18)$$

with the angle brackets denoting a time average. These different quantities correspond to synthetic models: part of the information is computed by a closure model, and the rest is self-consistent. For

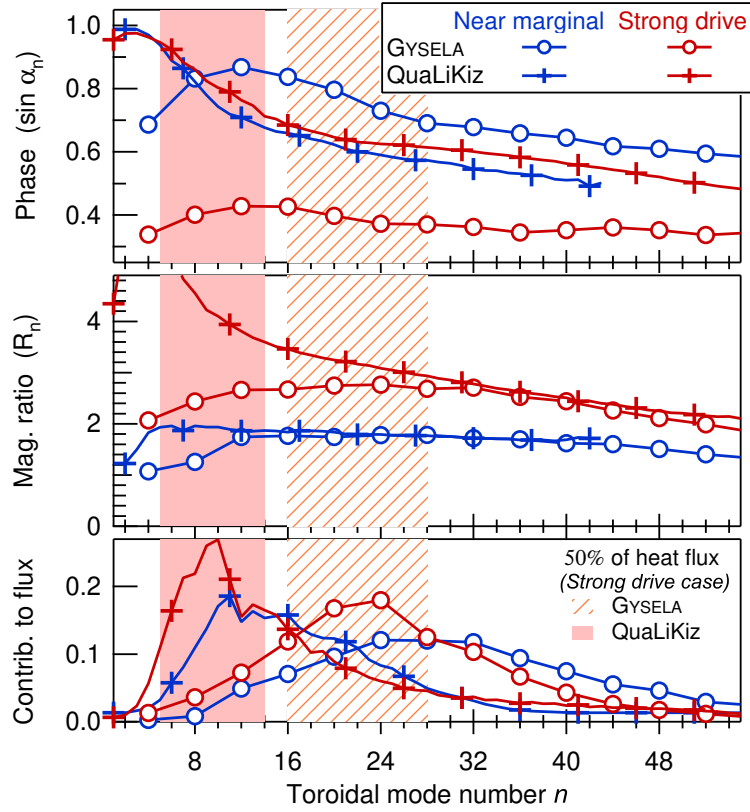


Figure 4.6: (a) Phase for each toroidal Fourier mode from GYSELA simulation (circles) and QuaLiKiz (stars). The statistics is done on a reduced radial span  $0.3 \leq r/a \leq 0.7$ . (b) Same plot for the magnitude  $R_n$  (equation 4.14) for each toroidal Fourier mode from GYSELA simulation (circles) and QuaLiKiz (plusses). The statistics is done on a reduced radial span  $0.3 \leq r/a \leq 0.7$ . (c) Normalised contribution of each mode number to the amplitude  $|\hat{Q}_n|$ .

$Q_{\mathcal{A}}$ , an average phase  $\langle Q \rangle_t / \langle \mathcal{I} \mathcal{R} \rangle_t$  is prescribed, for  $Q_g$  both the phase and the response magnitude are prescribed.  $Q_{\alpha}$  does the converse: we use the true phase, and the turbulent spectrum is modelled externally. For each radial position, we compute the relative error for these reconstructions as the root-mean-squared distance to the true flux  $Q$ , normalised to  $\langle Q \rangle$ . The results are shown figure 4.7. Only using the phase information,  $Q_{\alpha}$  does not lead to a significant gain in precision compared to just using the constant  $\langle Q \rangle$ . The reconstructions  $Q_{\mathcal{A}}$  and  $Q_g$  perform alike and much better, except for  $r/a > 0.6$  in the near marginal case where all reconstructions perform equally. This means that the fluctuations of the heat flux are dominated by the fluctuations in the turbulent intensity  $\mathcal{I}$  for large part of radial domain, while  $\mathcal{R}$  and  $\alpha$  could be prescribed externally.

## 4.4 Conclusion

Experimentally relevant flux-driven simulations of open systems like tokamak plasmas show that, although quasilinear assumptions may reveal valid, quasilinear modelling likely requires dedicated closures. Indeed, the magnitude of the turbulent heat flux computed in flux-driven simulations with the GYSELA is not recovered with the well benchmarked quasi-linear QuaLiKiz model. Kubo numbers found larger than unity would suggest that quasilinear validity assumptions are broken. However, the prevalence of linear properties of the fluctuations seem to hold even in the non-linear regime: magnitude and phase of the pressure response to the potential are well captured by linear predictions. The mismatch of heat fluxes partly results from the quasilinear closure on the turbulence intensity spectrum  $\mathcal{I}$ . Indeed, the latter governs most of heat flux fluctuations, while the phase contribution remains subdominant. Complementing quasilinear models with a dynamical equation for  $\mathcal{I}$  could represent an efficient alternative to present closures, for instance

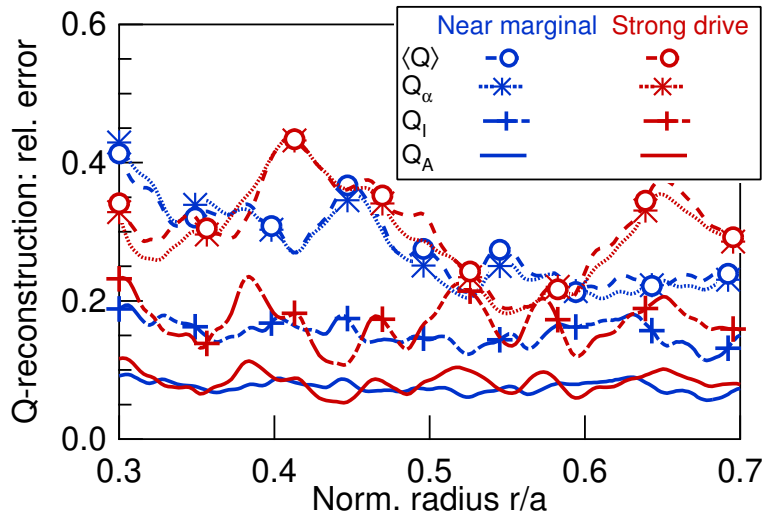


Figure 4.7: Relative error on the heat flux for the reconstructions 4.16–4.18.

in the form of  $k - \varepsilon$  equations. Also, the locality assumption of the quasilinear framework may need being revisited—or possibly also the role of damped modes—since the non-linear heat flux exhibits non-vanishing magnitudes in linearly stable regions.

As a final word, notice that the ground breaking observations reported in this chapter are not inconsistent with the relative success of present quasi-linear modelling in recovering the estimated experimental heat fluxes within the large error bars of equilibrium gradients. Indeed, this results from the large sensitivity of the fluxes to thermodynamical forces when operating close to marginal stability, the case of most discharges. However, the reported weakness are expected to become critical when using such models for prediction purposes, as is done routinely for ITER and DEMO.

The contents of this chapter have been submitted as (Gillot *et al.*, 2020b).

## Chapter 5

# Kinematics of turbulent fluctuations

From the previous chapter, we take away the following: turbulent fluctuations keep some linear properties in the non-linear regime, and the saturation rule is to blame for the mismatch between the turbulent heat flux measured by GYSELA and quasi-linear predictions coming from QuaLiKiz. This naturally leads us to reconsider the modelling choice for this saturation rule. Hence comes the question: how to self-consistently evolve the turbulent spectrum?

The QuaLiKiz saturation rule is a local model: everything depends on the quantities on the reference flux surface. Meanwhile, linear analysis of the ITG modes predict specific shapes and group velocities for the modes. Consistent estimations of turbulent spectra need to take this motion into account. Waves cannot be expected to remain inside their flux-surface, and this needs to be quantified. Thus, we need to assess the non-locality of this turbulent spectrum. A paramount concern is the interaction with the zonal flows, both mean flows and fluctuating flows.

In order to decipher this interaction, we analyse the kinematics of turbulent structures in the GYSELA simulations already used for the comparison to quasi-linearity, chapter 4. The results can then be compared to known linear properties, like the ones derived paragraph 2.2. Given access to three-dimensional fluctuations of the potential  $\phi(t, r, \theta, \varphi)$ , a variety of methods are available. In the following, we denote  $\tilde{\phi}_n$  the toroidal Fourier transform of the potential  $\phi$ , for  $n \geq 1$ . In the following, we will denote the zonal flow velocity by  $v_E = rv_E^\theta = ru_E$ . Its poloidal shear will be  $v_E'$ , and its toroidal shear  $\gamma_E = (qu_E)'/q'$  to match the notations from paragraph 2.2.

**Considered simulations** In addition to the two simulation cases we considered in chapter 4, we will make use of a third case dubbed “large flow”. The latter simulates a smaller plasma,  $\rho_* = 1/150$ , and features a large zonal flow with strongly marked extrema. Even though the main results from paragraph 4 are valid for this simulation, it has been excluded from the study because it does not qualify as in the *local limit* (Lin *et al.*, 2002). Nevertheless, the large flow and low avalanching makes it a relevant test case for analysing the effect of zonal flows on turbulent cells. The zonal flow velocity and shear for the three simulations are shown figure 5.1.

### 5.1 Interplay between turbulence and zonal flows

Modification of the free energy sources —density and temperature gradients— plays a role in the turbulent self-organisation of tokamak plasma. But, in addition, corrugated zonal flows emerge, and are expected to be a key player (Terry, 2000; Diamond *et al.*, 2005).

Both linear and non-linear effects of zonal flows are very difficult to assess, and subject to live debates. Several heuristic rules have been developed in the literature, relying on different and possibly complementary effects of zonal flow velocity  $v_E = -E_r/B$ , its shear rate  $v_E' = -\partial_r E_r/B$  (Biglari *et al.*, 1990; Diamond *et al.*, 2005) and its curvature  $-\partial_r^2 E_r/B$  (Ghendrih *et al.*, 2003; Itoh & Itoh, 2016; Nace, 2018). Sheared zonal flows naturally arise from turbulent state (Chen *et al.*, 2000; Manfredi *et al.*, 2001; Hallatschek & Diamond, 2003). A seed zonal flow shears and modulates

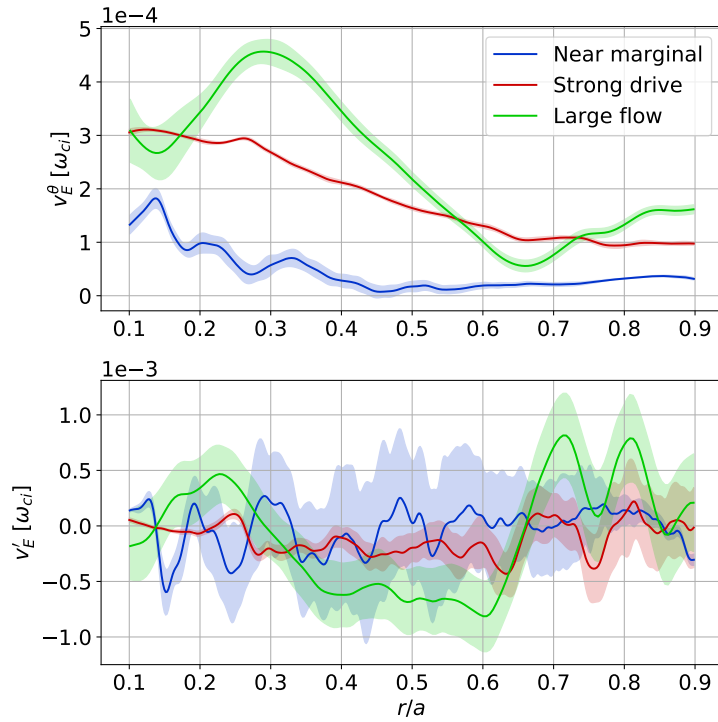


Figure 5.1: Zonal flow patterns in velocity (upper) and shear (lower) for the three considered simulations (“strong drive”, “near marginal” and “large flow”). The shaded area corresponds to one temporal standard deviation.

turbulent eddies. The so-sheared eddies induce a Reynolds stress. This stress reinforces the flow, feeding it with energy taken from the turbulence. This process naturally generates sheared zonal flows.

Sheared zonal flow phenomenology typically exists at two time scales: the so-called zonal mean flows and zonal fluctuating flows. For the “mean” component, simulations typically feature staircase-shaped patterns (Kosuga *et al.*, 2014; McIntyre, 2014; Paparella & von Hardenberg, 2014; Dif-Pradalier *et al.*, 2015). The typical distance between flow peaks, as well as the asymmetrical nature of these staircases with peaked maxima and flat minima —see (Dif-Pradalier *et al.*, 2015, fig. 1 and 4)—, are still unexplained. The fluctuating component is often taken as an indicator for avalanche dynamics (Beyer *et al.*, 2000; Idomura *et al.*, 2009; McMillan *et al.*, 2009). The related dynamics of geodesic acoustic modes (GAM) are candidates to trigger avalanches (Sasaki, 2018), and will be discussed chapter 6.

Interchange-like instabilities feature a ballooned character: their activity is higher on the low-field side than on the high-field side. This is due to the vertical diamagnetic drift, destabilising in former, stabilising in the latter. Zonal flows perturb this picture by moving turbulent structures poloidally. However, the poloidal position of the ballooning —the so-called ballooning angle— is not expected to follow the flow. It is bound by the diamagnetic drift, and cannot leave the low-field side. To compensate this restraint, the system makes use of the magnetic field tilting to convert the poloidal motion into a toroidal one. As such, two limiting behaviours are possible: either turbulence is weakly ballooned, and turbulent cells move poloidally, or it is strongly ballooned, and turbulent cells move toroidally.

In the latter case, the advection is done in the symmetrical toroidal direction. The stabilising effect is expected to come from the zonal flow shear. The central argument of the shear effect is the shrinking of the turbulent structures. One of them can be thought as a superposition of waves with given wave-vectors  $(k_r, k_\theta, n)$ . Each wave is subject to a stretching of the form (cf. paragraph

2.2.3)

$$\frac{dk_r}{dt} \approx k_\theta v'_E \quad (5.1)$$

With time, the structure thins further and further. Its transport becomes less efficient, until it is damped away by some kind of diffusive process (turbulent or collisional for instance). If the zonal flows fluctuate, the rapid variations of  $v'_E$  may produce a diffusive behaviour in  $k_r$  space (Diamond *et al.*, 2005).

A rule of thumb for the mean flow shear is the so-called Waltz's rule (Waltz *et al.*, 1994), which predicts a strong reduction in the turbulence as soon as  $v'_E$  dominates the turbulent growth rate  $\gamma_{\text{lin}}$ . In the transport point of view, Hinton's quenching model (Hinton, 1991) has been qualitatively successful (Malkov & Diamond, 2008) and quantitatively tested.

$$D_{\text{turb}} \rightarrow \frac{D_{\text{turb}}}{1 + (v'_E/\gamma_{\text{lin}})^2} \quad (5.2)$$

For fluctuating zonal flows, (Hahm *et al.*, 1999) suggests using an effective zonal shear.

Both rules are independent of the shear sign, and neglect the effect of the radial electric field curvature. The sign of the zonal mean flow shear is known to affect the motion of turbulent avalanches (McMillan *et al.*, 2009; Idomura *et al.*, 2009). Furthermore, the sign of the fluctuating zonal flow curvature has an effect on turbulence in the case of GAMs (Sasaki, 2018), and can affect the stability of the zonal flow in a turbulent bath (Zhu *et al.*, 2020).

## 5.2 Motion inside the flux-surface

The lifetime of turbulent structures can be estimated using a temporal correlation function. This must be done in the structures' reference frame. Since the structures move inside the plasma, the associated Doppler effect would lead to strong underestimation of the correlation time if computed in the laboratory frame. In order to remove it, we first perform a registration (Brown, 1992) of flux surfaces between time snapshots. This is achieved by minimising the squared error mismatch 5.3. If the potential  $\phi$  is purely advected,  $\mathbb{L}_{\text{nonlin}}$  is a positive function which vanishes at the advection velocity  $v_{\text{eff}}$ . Equation 5.4 formulates a linearised mismatch, for  $v_{\text{eff}}\Delta t$  small enough, and is used for linear registration. The minimisation is done independently for each flux surface and time step, by standard least-squares (linear registration) and Gauss–Newton iteration (non-linear registration).

$$\mathbb{L}_{\text{nonlin}}(v_{\text{eff}}^{\theta, \varphi} | t, r) = \frac{1}{2} \left\langle \left| \tilde{\phi}_n(t + \Delta t, r, \theta) - \tilde{\phi}_n(t, r, \theta - v_{\text{eff}}^\theta \Delta t) e^{in v_{\text{eff}}^\varphi \Delta t} \right|^2 \right\rangle_{\text{FS}} \quad (5.3)$$

$$\mathbb{L}_{\text{lin}}(v_{\text{lin}}^{r, \theta, \varphi} | t, r) = \frac{1}{2} \left\langle \left| \partial_t \tilde{\phi}_n(t, r, \theta) + (v_{\text{lin}}^r \partial_r + v_{\text{lin}}^\theta \partial_\theta + in v_{\text{lin}}^\varphi) \tilde{\phi}_n(t, r, \theta) \right|^2 \right\rangle_{\text{FS}} \quad (5.4)$$

We obtain two velocity estimates, namely  $v_{\text{eff}}$  and  $v_{\text{lin}}$ . The minimisation principle 5.4 for  $v_{\text{lin}}$  is a linearisation of equation 5.3, the two estimates should be similar. This allows to cross-check the computation. In addition, our algorithm for  $v_{\text{eff}}$  does not support computing the radial velocity, so we have to rely on the linear estimate  $v_{\text{lin}}^r$  in that direction.

The choice of quadratic error in 5.3–5.4 provides group velocities rather than phase velocities. For instance, focusing on the toroidal direction, the resulting velocity from the problem 5.4 is obtained by solving for the variation condition

$$\begin{aligned} 0 &= \frac{\partial \mathbb{L}_{\text{lin}}(v_{\text{lin}}^\varphi | t, r)}{\partial v_{\text{lin}}^\varphi} \\ &\approx \Re(\partial_t \tilde{\phi}_n(t, r, \theta)^* in \tilde{\phi}_n(t, r, \theta))_{\text{FS}} + v_{\text{lin}}^\varphi \langle n^2 |\tilde{\phi}_n|^2 \rangle_{\text{FS}} \\ &\approx -\langle n[\omega + n v_g(n)] |\tilde{\phi}_n|^2 \rangle_{\text{FS}} + v_{\text{lin}}^\varphi \langle n^2 |\tilde{\phi}_n|^2 \rangle_{\text{FS}} \end{aligned}$$

with  $v_g$  a  $n$ -dependent wave velocity,  $\omega$  a  $n$ -independent frequency. The averages  $\langle \cdot \rangle_{\text{FS}}$  are done on the whole turbulent spectrum, with both positive and negative non-zero  $n$ . The first term

containing  $\omega$  vanishes by symmetry  $n \mapsto -n$ . The second does not.  $v_{\text{lin}}^\varphi$  is an average of  $v_g$  over the toroidal mode number  $n$ , weighted by the turbulent spectrum  $n^2|\tilde{\phi}_n|^2$ .

$$v_{\text{lin}}^\varphi = \frac{\langle v_g(n)n^2|\tilde{\phi}_n|^2 \rangle_{\text{FS}}}{\langle n^2|\tilde{\phi}_n|^2 \rangle_{\text{FS}}} \approx v_g(n_{\text{eff}})$$

If  $v_g$  does not vary much with  $n$ , or if the spectrum is peaked, this can be thought as a group velocity taken at an effective wave-number  $n_{\text{eff}}$ . Conversely, using an absolute error would have computed a phase velocity (and could not have been done in Fourier space).

Figure 5.2 shows the components of the effective angular velocity inside the flux-surface  $v_{\text{eff}}^{\theta,\varphi}$ . Surprisingly, the inferred velocity profile is principally directed in the toroidal direction, rather than in the poloidal direction. The usual picture is one of poloidally moving turbulent cells, as observed in simulation movies. There is no contradiction. Turbulent cells are very elongated in the parallel direction. By observing a poloidal cut, the toroidal motion is projected onto the poloidal direction following this parallel direction.

We explain this phenomenon as a ballooning constraint. Turbulent fluctuations are unstable on the low-field side, and stable on the high-field side. When a turbulent structure gets moved poloidally by the zonal flow, it is favourable for it to go back to the low-field-side. This is achieved by means of the parallel dynamics. The parallel acoustic dynamics homogenises this direction at the thermal velocity, which is  $\rho_*^{-1}$  times faster than the typical drift velocities. Therefore, when the poloidal zonal flow acts, turbulent structures adiabatically return to their ballooning position at low-field side. This does not require a parallel velocity of particles  $V_{\parallel}$ , as those have larger inertia than the potential  $\phi$ .

The physics is reminiscent of the plasma reference frame, a toroidally moving reference frame designed to cancel the electric field on a given flux surface. This interpretation is comforted by the transverse projection of the velocity  $v_{\text{eff}}^\varphi - qv_{\text{eff}}^\theta$ , which follows faithfully and with little fluctuations the transverse projection of mean  $E \times B$  flow  $-qv_E^\theta$ . In those simulations, the toroidal projection of the parallel fluid velocity  $V_{\parallel}$  is small compared to the  $E \times B$  flow.

There remains a poloidal velocity component, even if weaker than the original zonal flow. This component is related to the motion of the structure along the parallel direction. The origin of this velocity is an open question.

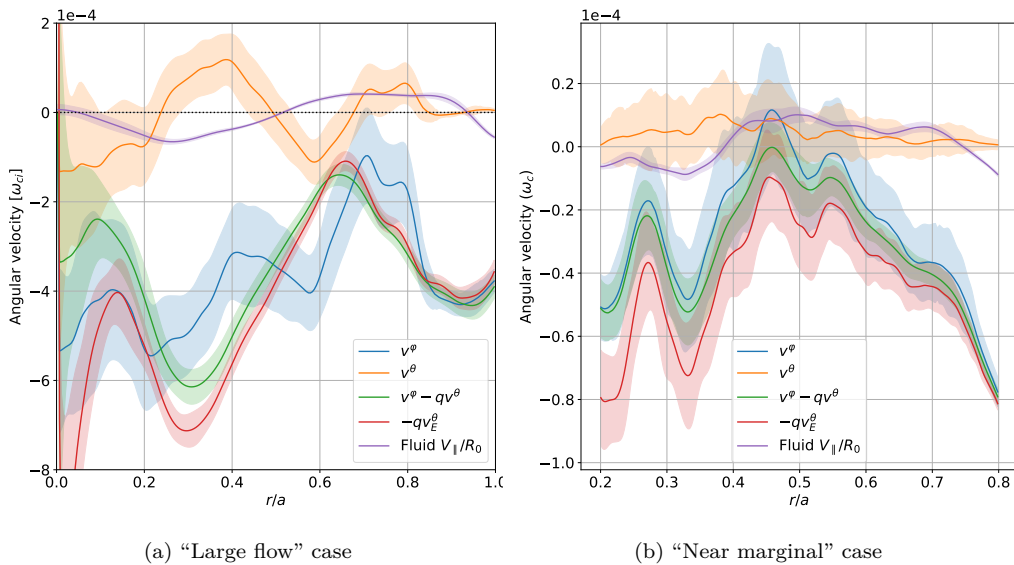


Figure 5.2: Time-averaged profile of effective structure velocity inside a flux-surface two simulations. Shaded area corresponds to one temporal standard deviation.

## 5.3 Dimensions of the turbulent filaments

### 5.3.1 Typical correlation lengths

The spatial dimensions of turbulent structures are also of interest to understand the effect of zonal shear. Physical considerations suggest preferred axes: the structures are expected to follow magnetic field lines. We expect the parallel ( $\vec{\partial}_\varphi + q^{-1}\vec{\partial}_\theta$ ), transverse ( $\vec{\nabla}\varphi - q\vec{\nabla}\theta$ ) and radial directions to play first-class roles. In order to cancel the magnetic helicity, we define the untwisted potential  $\bar{\bar{\phi}}$  as

$$\begin{aligned}\bar{\bar{\phi}}(t, r, \theta, \varphi) &= \tilde{\phi}(t, r, \theta, \varphi - q^*\theta^*) \\ q^* &= \frac{q}{\sqrt{1 - \varepsilon^2}} \\ \tan \frac{\theta^*}{2} &= \sqrt{\frac{1 - \varepsilon}{1 + \varepsilon}} \tan \frac{\theta}{2}\end{aligned}\tag{5.5}$$

where  $q^*$  and  $\theta^*$  are the effective  $q$  profile and intrinsic poloidal angle, taking into account GYSELA's poloidally varying local field-line pitch  $\frac{b_\varphi}{b_\theta} = q(r)\frac{R_0}{R}$  (Grandgirard *et al.*, 2016). The toroidal rotation is done in toroidal Fourier space. An example is given figure 5.3. It features a sharp discontinuity at  $\theta = \pm\pi$ . This is expected for irrational values of  $q^*$ . A mask is placed in the  $\theta = \pi \pm \frac{\pi}{5}$  range to avoid artefacts close to low-order rational  $q$  values.

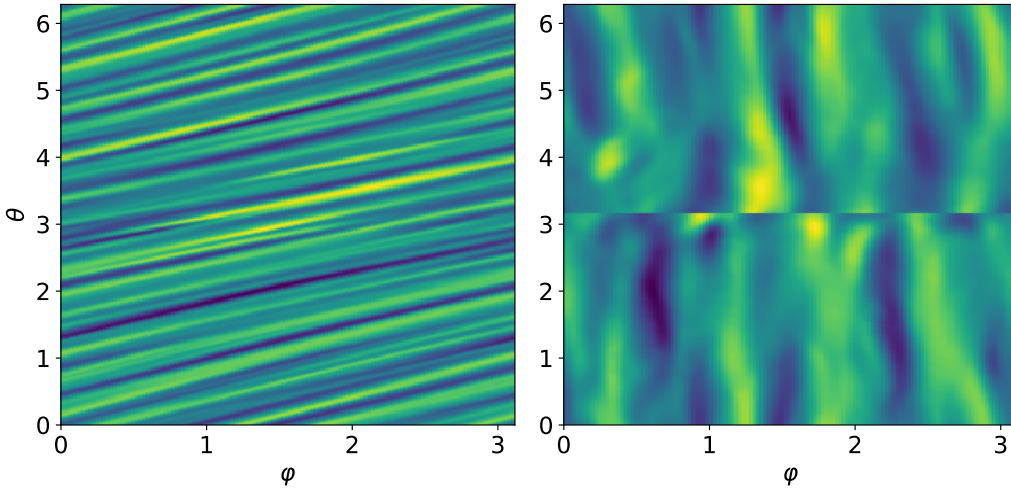


Figure 5.3: Left: sample cut of the fluctuations of the electrostatic potential on a flux-surface at  $\rho = 0.7$ . Right: untwisted version  $\bar{\bar{\phi}}$  of the same cut according to equation (5.5).

On these grounds, we compute the poloidal and parallel correlation functions

$$C_\theta(t, r, \Delta\theta) = \langle \tilde{\phi}(t, r, \theta) \tilde{\phi}(t, r, \theta + \Delta\theta) \rangle_{\text{FS}}\tag{5.6}$$

$$C_{\parallel}(t, r, \Delta\eta) = \langle \bar{\bar{\phi}}(t, r, \theta) \bar{\bar{\phi}}(t, r, \theta + \Delta\eta) \rangle_{\text{FS}}\tag{5.7}$$

where  $\eta$  plays the role of a coordinate along the parallel direction.  $C_\theta$  and  $C_{\parallel}$  are computed from the Fourier space power spectrum. The associated normalised correlation lengths  $L_\theta/r$  and  $L_{\parallel}/qR$  are computed as half-width at half-maximum.

The radial and poloidal correlation lengths are shown figure 5.4a for the “large flow” simulation. As expected, the poloidal and radial correlation lengths are of the same order of magnitude, around a few  $\rho_i$ . The parallel correlation length is very large in comparison, and scaled by the cubed aspect ratio for readability. This confirms the usual hypothesis of field-aligned modes. The radial correlation length features a bump around the zonal flow minimum at  $r/a = 0.65$ , while the poloidal correlation length remains smooth.

Slices of  $C_r$  and  $C_\theta$  are shown figure 5.4b and 5.4c for two radial positions: inside the shear layer at  $r/a = 0.4$  and inside the bump at  $r/a = 0.65$ . While  $C_\theta$  does not change beyond scaling,  $C_r$  exhibits a slower decay and strong asymmetry at  $r/a = 0.65$ . This asymmetry suggests a specific behaviour inside the shear layer at  $r/a = 0.4$ .

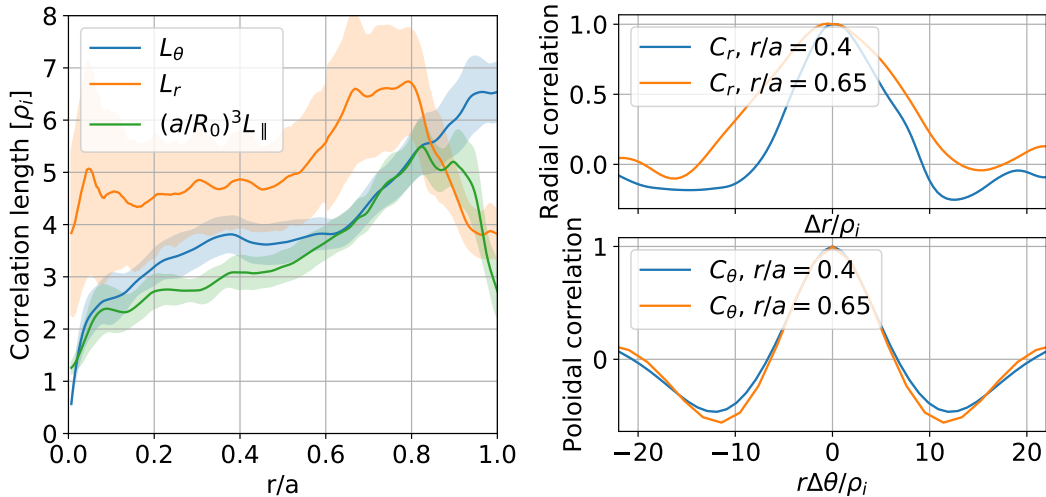


Figure 5.4: “Large flow” simulation: (Left) Poloidal and radial correlation length in units of the local ion Larmor radius  $\rho_i$ . To fit on the plot, the parallel correlation length is scaled down by the cubed aspect ratio  $(R_0/a)^3 = 216$ . The shaded area corresponds to temporal fluctuations. (Right) Slices of the radial and poloidal correlation coefficient, at one given time and two radial positions. The spatial shifts  $\Delta r$  and  $r\Delta\theta$  are normalised to the local ion Larmor radius.

**The case of field-aligned simulations:** The “marginal” simulation has been run using GYSELA’s aligned coordinates (Latu *et al.*, 2017). This coordinate system allows to reduce the run-time of the code by compressing the data representation. Since the dynamics are expected to be aligned along the field lines, the  $(m, n)$  spectrum of the potential is sparse, and the information is along the  $m + nq \approx 0$  line. By reducing the discretisation in the toroidal direction, the spectrum is aliased in  $n$  direction.

This grid invalidates the method outlined above, for instance making figure 5.3 terribly unresolved in the toroidal direction. In addition, most operations in the toroidal directions are wrong, even a simple toroidal average features spurious high- $m$  components. Two possibilities exist to avoid this issue. The first one is to re-grid the toroidal direction, taking care of unfolding the aliasing. This method is very expensive in memory space, and has been left out. The second one is to only work in  $(m, n)$  Fourier space, but adjusting the  $n$  value depending on  $q$  and  $m$  to remove this aliasing. This method has been preferred for practical computations.

### 5.3.2 Principal directions

In the analysis performed in the previous section, the relevant directions were prescribed *a priori* on the basis of the linear properties of the instability. Those are expected to adequately characterise turbulent structures. In complement, the directions of interest can also be determined purely numerically, using principal component analysis. If we consider turbulence to be a superposition of anisotropic Gaussian cells, we can estimate the co-variance matrix  $C$  using the derivatives of the potential  $\phi$  in the three dimensions

$$C_{ij} \approx \langle (\vec{e}_i \cdot \vec{\nabla}\phi)(\vec{e}_j \cdot \vec{\nabla}\phi) \rangle_{\text{FS}} \quad (5.8)$$

with  $\vec{e}_i = (\vec{e}_r, \vec{e}_\theta, \vec{e}_\varphi)$  the toroidal orthonormal basis. Diagonalising it with respect to the orthonormal metric yields the ellipsis principal axes as eigenvectors  $\vec{d}_i$  and associated principal lengths  $\ell_i$ . The results are presented figure 5.5 and 5.6. As shown figure 5.5b, the longest principal axis  $\ell_2$

approximates the parallel direction  $\partial_\varphi + q^{-1}\partial_\theta$ , consistently with the magnetic alignment. In the perpendicular plane,  $l_0$  and  $l_1$  are of the same magnitude, stating that the structures have low eccentricity. The preferred orientation can be estimated as the angle  $\chi$  of the longer axis with respect to  $\vec{e}_r$  (figure 5.6b). These properties are consistent with the correlation length computed in the previous paragraph.

The angle  $\chi$  features two sharp jumps of  $\pi/2$  for the “large flow” simulation. These are eigenvalue collisions, and correspond to passage through circular sections where the definition a larger axis is degenerate. The positions of these jumps happen to be related to the position of the flows. Outside these jumps, the tilt angle appears to follow a mixture of the magnetic shear  $s$  —a geometric effect due to the field-line alignment—, and of the zonal flow shear. This angle  $\chi$  is also related to the ballooning angle. This suggests a different poloidal position of the turbulent intensity depending on the zonal flow shear.

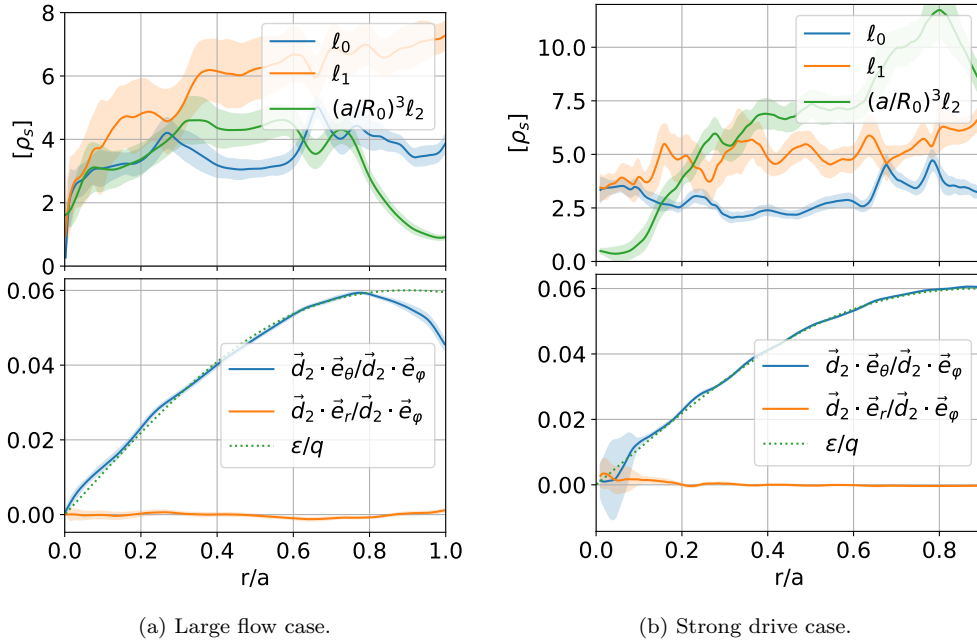


Figure 5.5: (Upper) Principal correlation length. (Lower) Projections of the longest principal direction  $\vec{d}_2$  on the perpendicular plane.

## 5.4 Radial motion of the structures

### 5.4.1 Lagrangian correlation time

We define for each flux-surface the Lagrangian correlation function between time  $t$  and  $t + \tau$  as in equation 5.9. For simplicity —to avoid dealing with poloidal asymmetry and ballooning—, we only remove the toroidal motion, which has been shown to dominate over the other components in paragraph 5.2. For instance, the radial motion of the structures is not cancelled. More elaborate schemes received limited testing, with no discernible advantage. The associated correlation time  $\tau_{\text{corr}}$  is computed as half-width at half-maximum, and shown figure 5.7c. As computed, it estimates how long a turbulent structure lives on a given flux surface. The limiting factors are the structure growth and damping, but also its motion towards another radial position. For reference, the eulerian correlation time  $\tau_{\text{corr}}^{\text{eul}}$  is shown in gray line figure 5.7c. The difference between the two can reach up to a factor of 25 due to this Doppler effect.

$$C_{\text{lag}}(t, r, \tau) = \Re \left\langle \tilde{\phi}_n^*(t + \tau) \tilde{\phi}_n(t) \exp \left( i n \int_t^{t+\tau} v_{\text{eff}}^\varphi dt \right) \right\rangle_{\text{FS}} \quad (5.9)$$

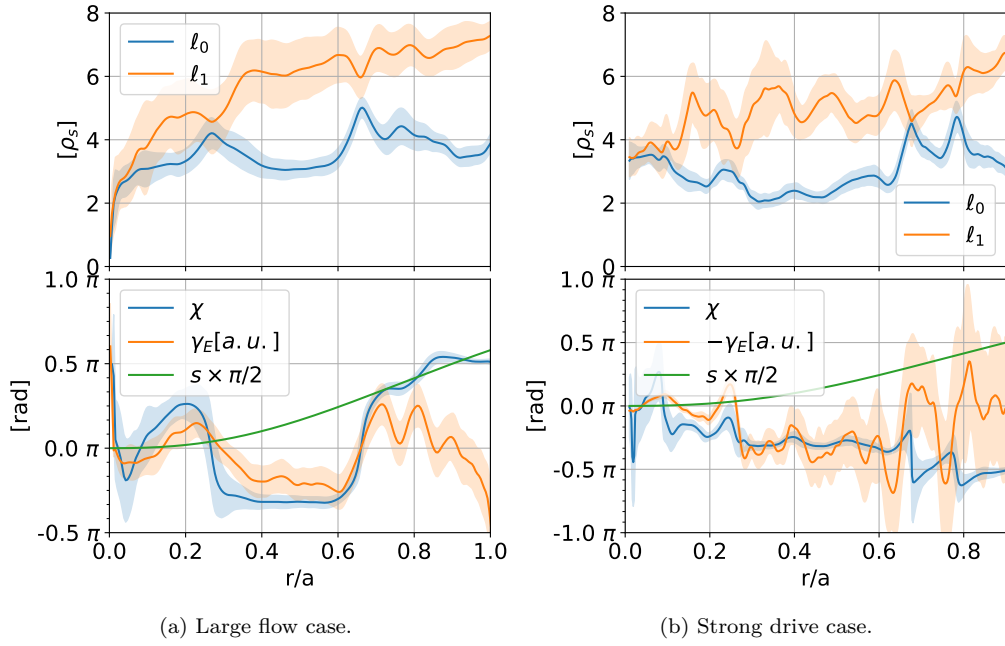


Figure 5.6: (Upper) Principal transverse correlation length. (Lower) Ellipsis tilt in the perpendicular plane. For reference are given the (scaled) zonal shear  $\gamma_E$  and magnetic shear  $s$ . Shaded area corresponds to one temporal standard deviation.

where the flux-surface average is replaced by an average on  $\theta$  and a sum over  $n$ . Figure 5.7b shows the effective radial velocity  $v_{\text{eff}}^r$  of the structures, as computed in paragraph 5.2. It is aligned with the background  $E \times B$  shear (figure 5.7a). The effective radial velocity appears to follow the  $E \times B$  shear rate. This is consistent with previous observations in the literature (Idomura *et al.*, 2009; McMillan *et al.*, 2009).

This relationship has a consequence on the structures lifetime (figure 5.7c) and width (figure 5.7d) at the  $E \times B$  flow extremes, especially where  $v_{\text{eff}}^r$  vanishes. In particular, this correlation is found to result in the yet unreported specific role of the sign of the shearing rate on the way turbulence is affected. Indeed, the flow maximum ( $r/a \approx 0.3$ ) exhibits an increase in correlation time and convergent  $v_{\text{eff}}^r$ , as if the turbulent structures were trapped. On the contrary, the flow minimum ( $r/a \approx 0.65$ ) exhibits an increase in structure width and no effect on correlation time, as if the divergent  $v_{\text{eff}}^r$  was chasing them. The sign of  $v_{\text{eff}}^r$  is such that the structures move towards the maximum of the flow whatever their radial position with respect to this maximum. On the other hand, the structures lifetime does not exhibit an inflexion close to  $r/a \approx 0.65$ , even with the strong variations of  $u_E^r$ . The same observation is made for the structure width close to  $r/a = 0.3$ .

For the “marginal” simulation (figure 5.8a), as the zonal flows are wobblier and less established, rendering correlation very difficult. Nevertheless, a similar tendency can be observed: the radial velocity  $v_{\text{lin}}^r$  changes sign in the same regions as the shear  $\gamma_E$ , for  $r/a$  in (0.28, 0.32), (0.46, 0.50), or (0.7, 0.9). The correlation time has a small peak around  $r/a = 0.32$ , 0.5 and 0.9, where the radial velocity changes sign from positive to negative. The radial correlation length works opposite, with small bumps at the beginning of those intervals, where the radial velocity changes from negative to positive.

Qualitatively, the same observation relation between the pattern of the radial velocity and the correlation time and length can be done on the “strong drive” simulation (figure 5.8b). However, the fluctuating component of the zonal flow is higher, making statistics more noisy. In the region  $0.6 \leq r/a \leq 0.8$ , the zonal flow shear oscillates twice. Surprisingly, the relationship between the radial velocity and the zonal flow shear is reversed. This may be caused by

The asymmetry between the flow minimum and maximum appears in the works of previous authors (Sasaki, 2018; Zhu *et al.*, 2020), and will be discussed in paragraph 6. Figures 5.7 and 5.8 provide numerical evidence for the trapping of turbulent cells inside the flow pattern. According

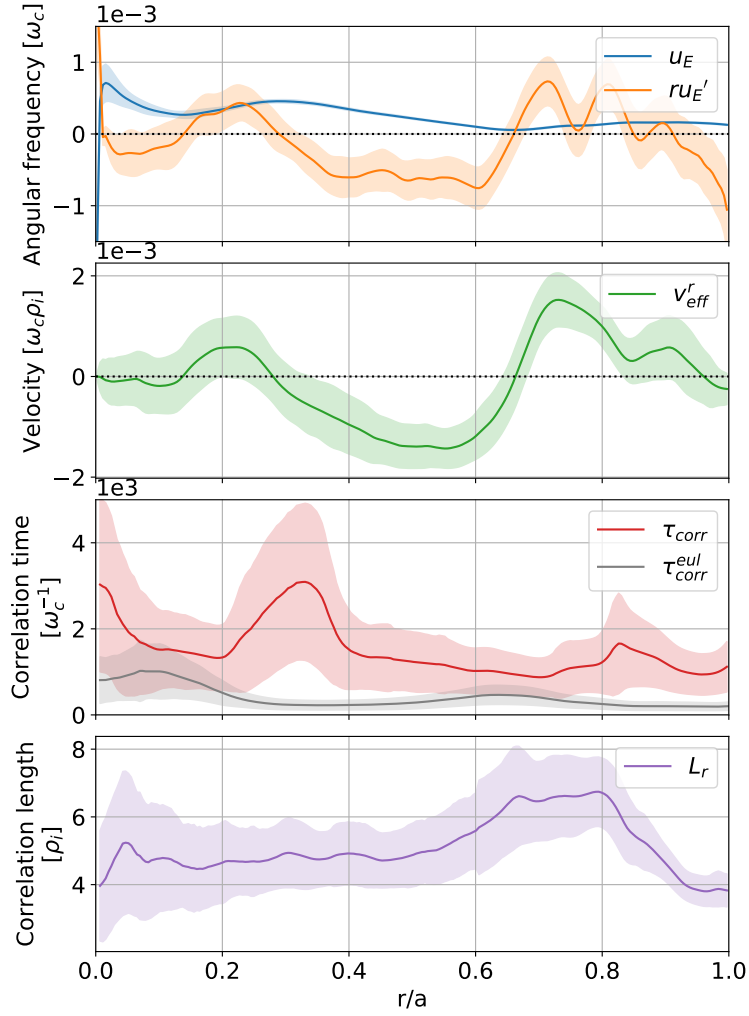


Figure 5.7: “Large flow” simulation: (a) Background mean poloidal  $E \times B$  flow and associated flow shear rate. (b) Radial effective velocity  $v_{\text{eff}}^r$ . (c) Lagrangian correlation time. (d) Radial correlation length. Shaded area corresponds to one temporal standard deviation.

to (Zhu *et al.*, 2020), this trapping has significant consequences on the stability of the underlying zonal flow. A self-consistent treatment of this trapping effect may provide useful insight into the formation of the zonal flow staircase pattern.

#### 5.4.2 Partition of energy

The ballooning character in our simulation is computed using the poloidal cross-section of the turbulent energy. The turbulent energy can be split into three contributions: adiabatic electron potential energy, the  $E \times B$  poloidal kinetic energy, and the  $E \times B$  radial kinetic energy. We chose to use the poloidal turbulent kinetic energy  $\varepsilon_\theta$  as a diagnostic, keeping only non-axisymmetric modes.

$$\varepsilon_\theta = \frac{m_i n}{2} \left\langle \left| \frac{\partial_r \tilde{\phi}}{B} \right|^2 \right\rangle_\varphi \quad (5.10)$$

Figure 5.9 features the time-average of  $\varepsilon_\theta$  for the three simulations. As expected, we observe a strong asymmetry between high- and low-field side. However, the ballooning itself is qualitatively different for each quantity. For the “large flow” simulation (figure 5.9a), the poloidal kinetic energy

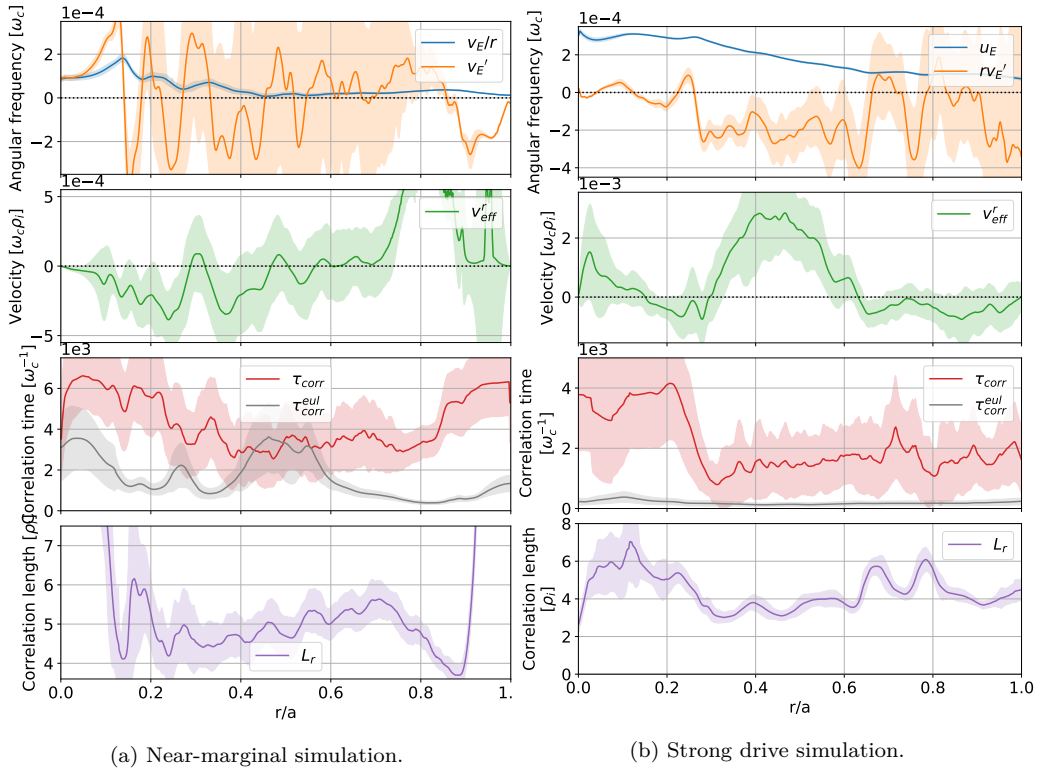


Figure 5.8: Same figure as 5.7: (a) Background mean poloidal  $E \times B$  flow and associated flow shear rate. (b) Radial effective velocity  $v_{\text{eff}}^r$ . (c) Lagrangian correlation time. (d) Radial correlation length. Shaded area corresponds to one temporal standard deviation.

exhibits a significant poloidal shift, around  $\pi/4$  with an inversion around  $r/a = 0.65$ . The other simulations exhibit the same kind of angular shift, although at different radial positions.

For the “large flow” and “near marginal” simulations, the variation of the ballooning angle provides an explanation to the radial motion. In the region of negative  $\gamma_E$  the turbulent structures are ballooned above the mid-plane. Since the distribution function linear response is proportional to the potential, more particles are involved in that region. The vertical magnetic drift pushes the particles downwards. Projecting on the radial direction, more particles move inwards than outwards. On average, the turbulent structure moves radially inwards. Conversely, where  $\gamma_E$  is positive, the ballooning is below the mid-plane, the diamagnetic drift still pushes downwards, and the structures move outwards.

### 5.4.3 Non-linear radial velocity

The same computations have been performed with various additional filters for the integration in the 5.4. This allows for instance to separate positive and negative vorticity structures.

$$\mathbb{L}(\vec{v}_{\geq} | t, r) = \frac{1}{2} \left\langle \left| \partial_t \tilde{\phi}_n(t, r, \theta) + (v_{\geq}^r \partial_r + v_{\geq}^\theta \partial_\theta + i n v_{\geq}^\varphi) \tilde{\phi}_n(t, r, \theta) \right|^2 \mathcal{K}[-\nabla^2 \tilde{\phi} \geq 0] \right\rangle_{\text{FS}} \quad (5.11)$$

In a linear setting, we do not expect the velocities  $\vec{v}_{\geq}$  to differ from  $\vec{v}_{\text{lin}}^{\rightarrow}$ . Numerical investigation shows this is actually the case for the poloidal and toroidal components. They are shown figure 5.10.

On both the “large flow” and “near marginal” case, the filtered radial velocities  $v_{\geq}^r$  depart from the unfiltered version  $v_{\text{lin}}^r$ . No departure is observed on the poloidal and toroidal projections. In the “near marginal” case, a positive vorticity appears to increase the radial velocity of the filament. In the “large flow” case, this behaviour appears in the region  $0.5 < r/a < 0.8$ , but is reversed in the  $0.3 < r/a < 0.5$  region. This behaviour has not been observed on the “strong drive” simulation.

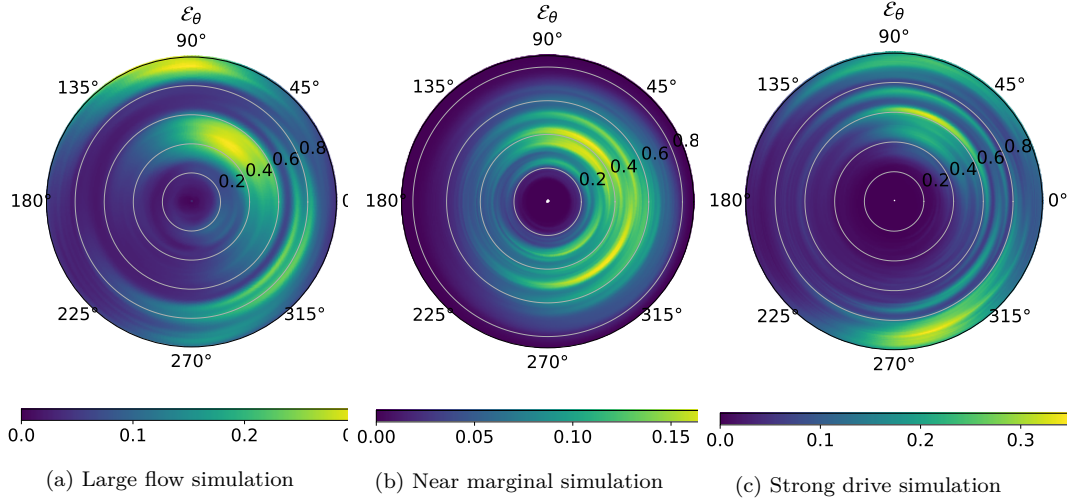


Figure 5.9: Poloidal partition of the poloidal  $E \times B$  kinetic energy of turbulent fluctuations. High-field side is on the left, low-field side on the right.

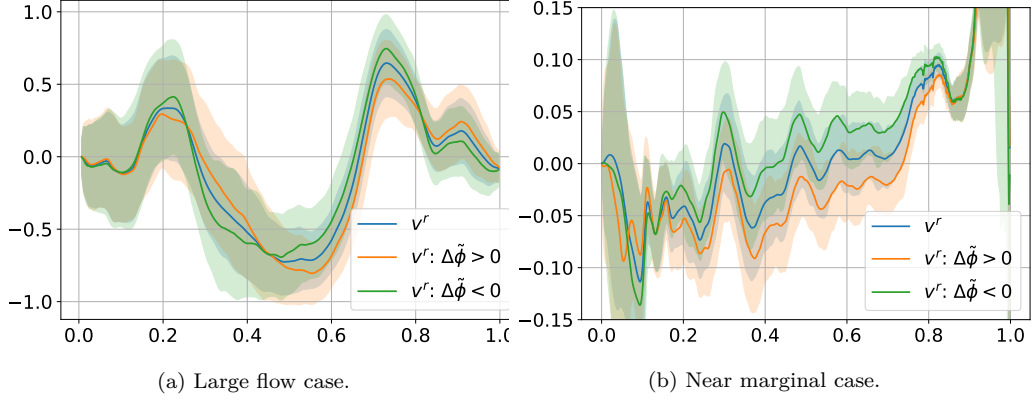


Figure 5.10: Pattern of the effective radial velocity depending on the sign of the turbulent filament vorticity computed by 5.11. Blue: unfiltered  $v_{\text{in}}^r$ . Orange: positive vorticity  $v_{>}^r$ . Green: negative vorticity  $v_{<}^r$ .

A tentative explanation is as follows: the particles constituting the turbulent filament feel a total vorticity given by the sum of the zonal flow shear  $v_E' = \partial_r^2 \phi$  and of the local vorticity. As a consequence, the radial velocity of the structure come from this total vorticity, and not only from the zonal component. This explanation is brittle and insufficient, because of the subtlety of non-linear interactions, and because of the behaviour reversal depending on the radial position.

## 5.5 Radial patterns in turbulence

The observed poloidal and toroidal motions are sheared. We observed the variations of the shear have an effect on the turbulence correlation time and length, rather than the shear itself. This begs the question of the effect of that shearing on the turbulent structures: is the eddy-stretching equation 5.1 observable?

At lowest order, the transverse tilt of the turbulent eddies is expected to be dominated by the magnetic shear: the local radial mode number is given by (see equation 2.53 and associated discussion)

$$k_r = -nq'(\theta - \zeta) \quad (5.12)$$

where  $\zeta$  is the ballooning angle. In a flux-surface-averaged setting, only the  $nq'\zeta$  quantity is of

interest. The registration method used earlier is used on the untwisted  $\bar{\phi}$  potential to measure the mismatch between neighbouring flux surfaces. This is done by minimising the squared error 5.13.

$$\mathbb{L}_{\text{shear}}(\vec{s}_{\text{eff}}|t, r) = \frac{1}{2} \left\langle \left| \bar{\phi}_n(t, r + \Delta r, \eta) - \bar{\phi}_n(t, r, \eta + s_{\text{eff}}^\eta \Delta r) e^{i n s_{\text{eff}}^\alpha \Delta r} \right|^2 \right\rangle_{\text{FS}} \quad (5.13)$$

This effectively provides an estimate of the shear strain

$$\begin{aligned} s_{\text{eff}}^\alpha &\approx - \left\langle \frac{k_r}{n} \right\rangle_{\text{FS}} \\ s_{\text{eff}}^\eta &\approx - \left\langle \frac{k_r}{m_{||}} \right\rangle_{\text{FS}} \end{aligned}$$

in the parallel  $\eta = \theta$  and the transverse  $\alpha = \varphi - q\theta$  directions.  $m_{||}$  is a parallel mode number. The  $s_{\text{eff}}^\alpha$  value should estimate the value  $q'\zeta$ . The temporal average of computed  $s_{\text{eff}}$  (equation 5.13) is shown figure 5.11. With the eddy stretching model,  $s_{\text{eff}}^\alpha$  should grow linearly in time as  $-q'\gamma_E t$ , at least on on short time scales. Therefore, we would expect a large temporal variance of  $s_{\text{eff}}^\alpha$ , and an irrelevant mean value.

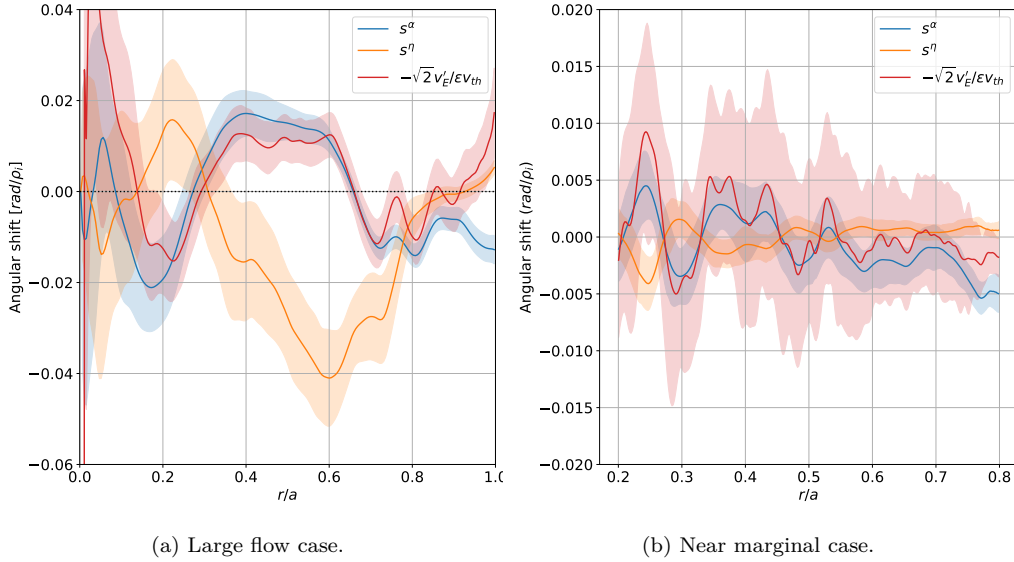


Figure 5.11: Time-averaged profile of effective shear inside a flux-surface. Mean negative  $E \times B$  shear rate is overlain. Shaded area corresponds to one temporal standard deviation.

Surprisingly, the numerically computed values for  $s_{\text{eff}}$  feature a strong stationary component on both simulations. On the transverse direction  $\vec{\nabla}\alpha = \vec{\nabla}(\varphi - q\theta)$ , along which the  $E \times B$  flow acts, the temporal variance is very low. The zonal flow shear  $\gamma_E$  seems to dictate  $s_{\text{eff}}^\alpha$  instead of its time derivative, as shown with the overlain  $v'_E$  figure 5.11. These observations suggest the effect of the  $E \times B$  flow shear rate is frozen in the structures, rather than externally applied. The parallel component  $s_{\text{eff}}^\eta$  is much wobblier, and no satisfactory explanation has been found to explain its magnitude nor its profile.

Recalling the linear analysis of the ITG instability paragraph 2.2, we found a stationary zonal flow embeds itself into the radial pattern of the local drift-wave mode.

$$\tilde{\phi} \approx \exp \left( in \left[ \varphi - q(\theta - \zeta) - (c + qu_E) \left( t - \frac{\sqrt{2} n q \rho_* s (\theta - \zeta)^2}{u_{\text{TR}}} \right) \right] \right) \quad (2.52)$$

The untwisted potential takes the following form

$$\bar{\phi}(r, \eta, \alpha) \approx \exp \left( in \left[ \alpha + q\zeta - (c + qu_E) \left( t - \frac{\sqrt{2} n q \rho_* s (\eta - \zeta)^2}{u_{\text{TR}}} \right) \right] \right) \quad (5.14)$$

As a result, we expect the  $s_{\text{eff}}^\alpha$  to have the following form

$$s_{\text{eff}}^\alpha \approx -\frac{k_r}{n} \approx -q'\zeta + q'\gamma_E t - q'\gamma_E \frac{nq\rho_*s}{\sqrt{2}u_{\text{TR}}} L_{\parallel}^2 \quad (5.15)$$

where we recall  $\gamma_E = \partial_r(qu_E)/\partial_r q$ .  $L_{\parallel}$  is an effective parallel correlation angle, which comes from the poloidal integration in equation 5.13 of the  $(\eta - \zeta)^2$  term in 5.14. Three terms appear in this last equation: a ballooning effect  $q'\zeta$ , a mode distortion effect  $q'\gamma_E t$ , and a parallel equilibration effect. Figure 5.11 suggests this last term to be dominant in the investigated simulations, where the  $nq^3\rho_*sL_{\parallel}^2/\sqrt{2}$  factor has been hand-picked to 1 for simplicity.

Equation 2.52 can be understood as a toroidal shift of the mode depending on the poloidal and radial position. The wave is actually centred around a toroidal position  $\varphi_{\text{ref}}$  given by

$$\varphi_{\text{ref}} \approx -\frac{\partial \ln \tilde{\phi}}{i\partial n} = q(\theta - \zeta) + (c + qu_E)t - 2(c + qu_E) \frac{\sqrt{2}nq\rho_*s}{u_{\text{TR}}} \frac{(\theta - \zeta)^2}{2} \quad (5.16)$$

This is confirmed by figure 5.12. As a consequence, the contours of  $\tilde{\phi}$  in a  $r$ - $\varphi$  snapshot follow the zonal flow velocity, as is shown figure 5.12. Here, the  $nq^3\rho_*s(\theta - \zeta)^2/\sqrt{2}$  factor is set to 2 on both figures.

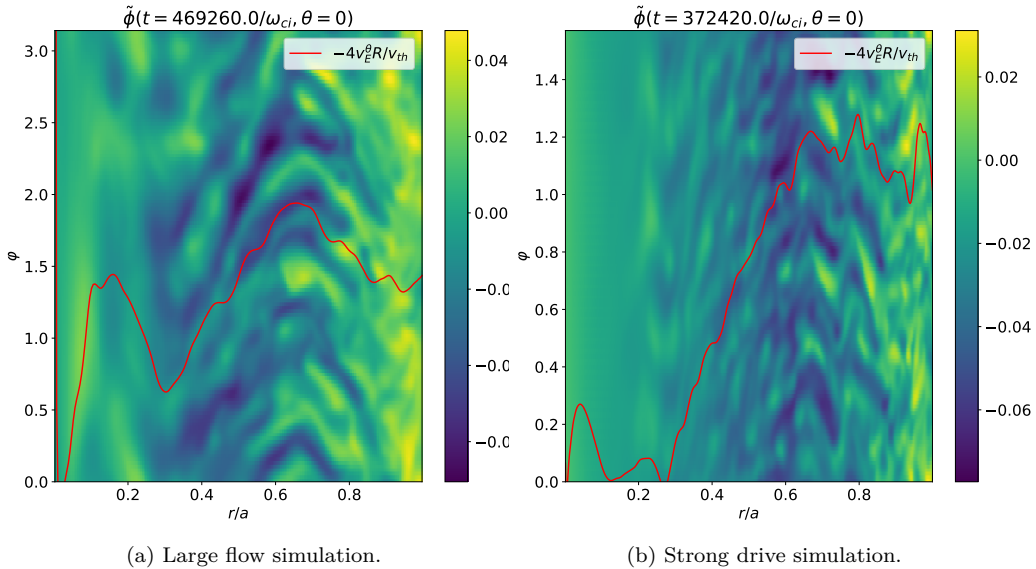


Figure 5.12: Cross-section of the fluctuating potential  $\tilde{\phi}$  at  $\theta = 0$ . The time step is chosen arbitrarily as the last simulation step. The profile of the zonal flow is overlain.

In time, the structures follow the local  $E \times B$  velocity. This velocity is sheared. However, after all shearing is accounted for, the radial pattern is given the zonal flow velocity multiplied by the parallel equilibration time. We suppose that the parallel transit forbids excessive tilting of the drift-wave mode at a given radial position. In order to resolve this paradox, we must call for some radial motion. When the filament experiences shearing, the additional tilting forces a radial motion in order to balance itself.

This picture contrasts with often observed shearing of the turbulent structures when looking at poloidal cross-sections. This can be explained using a projection effect: when looking at a poloidal cross-section of the plasma, the rotational transform projects the zonal pattern onto the cross-section. The additional zonal shear is evacuated through the parallel and radial directions, forming a global mode.

## 5.6 Conclusion

In this chapter, we have explored the properties of non-linear turbulent filaments in gyro-kinetic ITG turbulence. As could be expected from the linear analysis paragraph 2.2, the structures are

most elongated in the parallel direction, and are ballooned near (but not at) the low-field side.

The most awaited player in the regulation of turbulence is the sheared zonal flow. The numerically computed motion of the filament inside a flux-surface corresponds to the transverse projection of the poloidal zonal velocity onto the toroidal direction. This projection is done along the very correlated parallel direction. This effectively preserves the ballooned character of turbulence. The effect of the zonal flow shear is more subtle. Because of the structure of the ITG mode, the zonal flow velocity also appears as a radial pattern. From the numerical toroidal velocity, we were able to compute a Lagrangian correlation time of the turbulent structure. This Lagrangian correlation time is found to significantly differ from the Eulerian correlation time because of the Doppler shift by the toroidal motion due to the zonal flow.

The radial velocity of turbulent filaments has been investigated numerically. As expected, its direction and amplitude are related to the zonal flow shear. Near the zonal flow extremes, the radial velocity vanishes. In the case of zonal flow maxima, the radial velocity has a negative divergence  $\partial_r v_{\text{eff}}^r$ : turbulent filaments are trapped in the region, and feature increased correlation time. Conversely, zonal flow minima feature a radial velocity with positive divergence, hinting at repulsive behaviour. Both are consistent with the discussion by (Sasaki, 2018; Zhu *et al.*, 2020). This behaviour breaks the symmetry with respect to the shear flow sign, which is a common assumption of models of turbulence regulation by  $E \times B$  shear.

Such an asymmetry between the flow minimum and maximum casts doubt on shear-sign-agnostic models. Furthermore, the radial propagation of turbulent structures questions the validity of local turbulent spectrum estimations, as the information flows globally in the zonal flow pattern. The interaction between turbulence and zonal flow needs to be revisited.

Furthermore, the turbulent filaments' radial velocity appears to be influenced by the vorticity of the turbulent structure itself. This provides an additional saturation mechanism for turbulent growth: when the filament has accumulated enough vorticity, it moves radially, moves out of its energy source, and spreads out its contents.

In the presence of a sheared zonal mean flow, turbulent filaments tend to structure themselves according to the zonal flow velocity. When observed in a toroidal cross-section, radially elongated corridors appear in the fluctuations of the potential spectrum. The pattern of these corridors in the toroidal direction follows the zonal flow velocity according to  $\Delta\varphi \propto v_E^\theta / u_{\text{TR}}$  (equation 5.16). When correcting for this deformation, the corridors are reminiscent of the streamer structures observed in ETG turbulence (Dorland *et al.*, 2000). As electrons feature a much faster transit velocity  $u_{\text{TR},e}$ , the toroidal shift is more modest, and the streamer structure appears in a poloidal cross-section. As a consequence, the notion of turbulent “filaments” appears ill-posed, where turbulence can arrange itself in radially elongated ribbons.

## Chapter 6

# Investigation of tokamak turbulent avalanches using wave–kinetic formulation

The estimation of the quasi-linear fluxes requires proper knowledge of the turbulent spectrum. This is a complex endeavour. The turbulent fluxes require computing the two-point correlation function  $C_\phi(t_1, t_2, \vec{x}_1, \vec{x}_2)$  of the potential (Adam *et al.*, 1979). This correlation function is then weighted appropriately to express the flux carried at  $(t_1, \vec{x}_1)$  by a plasma parcel that was displaced from  $(t_2, \vec{x}_2)$ .

$$C_\phi(\vec{x}_1, \vec{x}_2) = \langle \phi(\vec{x}_1)\phi(\vec{x}_2) \rangle_{\text{turb}}$$

The average  $\langle \cdot \rangle_{\text{turb}}$  is taken on realisations of the system and on unobserved symmetry directions. Its determining equations are very complex and can be unpractical for both analytical and numerical works (Farrell & Ioannou, 2007; Srinivasan & Young, 2012). In the case of tokamak plasmas, turbulence is populated by drift-wave-like micro-instabilities at high toroidal mode number, driven by kinetic interchange coupling.

Explanations for turbulent saturation often revolve around mode coupling. Non-linear coupling pours an excess of energy from a turbulent eigenmode to stabler eigenmodes, through modulation by a mode with low wave-number or through scattering with another turbulent modes. In the near-marginal regime, avalanches provide an effective vector for heat transport (Diamond & Hahn, 1995; Newman *et al.*, 1996): bursts travel through the plasma in an almost ballistic fashion (Sarazin & Ghendrih, 1998; Sarazin *et al.*, 2010). Such avalanches have been linked to the transition from Bohm to gyro-Bohm scaling for turbulent transport (Carreras *et al.*, 1996; Garbet *et al.*, 1999; Lin *et al.*, 2002; Candy & Waltz, 2003a), and are routinely observed in non-linear flux-driven simulations (Beyer *et al.*, 2000; Idomura *et al.*, 2009; McMillan *et al.*, 2009; Dif-Pradalier *et al.*, 2017b). The coupling to the axisymmetric modes and especially zonal flows is of particular interest, because they shear turbulent eddies and act as an efficient mean to saturate turbulence. One of the drivers of the growth of zonal flows is the so-called zonostrophic instability. This instability is due to a modulational coupling of two drift waves giving energy to the sheared zonal flow (Champeaux & Diamond, 2001; Diamond *et al.*, 2005). When turbulent structures and zonal flows act on different radial and temporal scales, individual modulations can be thought of as infinitesimal: the problem can be modelled through the dynamics of a turbulent spectrum, alone forgetting individual wave–wave interactions. This approach has been applied to the modelling of drift waves, on temperature gradient and trapped electron modes, see (Anderson *et al.*, 2002, 2006; Srinivasan & Young, 2012; Parker, 2016; Gillot, 2016; Ruiz, 2017; Zhu *et al.*, 2018).

Wave-kinetic modelling (Weinberg, 1962) attempts to estimate the fluctuation spectrum in a simplified manner. The two-point correlations decay with the scale of the turbulent structures. If turbulent structures are much smaller than the background profile scale, the two-point separation can be represented in Fourier space as a local turbulent spectrum  $\mathcal{I}(\vec{x}, \vec{k})$ . As a result, both the driving gradients and the zonal flows are assumed axisymmetric and radially smooth. They should

evolve slowly enough for the turbulent structures to adapt adiabatically. In these conditions, an eikonal approach is accessible. By neglecting non-linear saturation mechanisms, the dynamics can be reduced to a kinetic equation on the spectrum  $\mathcal{G}$ . The so-called wave-kinetic equation is written as

$$\partial_t \mathcal{G} + \partial_{\vec{k}} \omega \cdot \partial_{\vec{x}} \mathcal{G} - \partial_{\vec{x}} \omega \cdot \partial_{\vec{k}} \mathcal{G} = 2\gamma \mathcal{G} + \text{Saturation} \quad (6.1)$$

The saturation term corresponds to non-linear couplings between turbulent cells, and the saturation level they prescribe. In full generality, this term requires the three-point correlation function. By analogy with the Boltzmann equation, it is often approximated by some kind “eddy-eddy” collision operator (Ruiz *et al.*, 2019). Here,  $\omega + i\gamma$  is the eigenmode angular frequency and growth rate, computed from the dispersion relation. The variable  $\mathcal{G}$  represents a conserved wave action. It can be defined using the Wigner density function of the potential, or equivalently the Fourier-transform of the two-point correlation function  $C_\phi$ .

$$\mathcal{G}(t, \vec{x}, \vec{k}) \delta(\omega - \omega(t, \vec{x}, \vec{k})) = \mathcal{D}_c \int C_\phi \left( t + \frac{\tau}{2}, t - \frac{\tau}{2}, \vec{x} + \frac{\vec{s}}{2}, \vec{x} - \frac{\vec{s}}{2} \right) e^{i\omega\tau - i\vec{k}\cdot\vec{s}} d\vec{s} d\tau \quad (6.2)$$

where the factor  $\mathcal{D}_c$  will be made explicit later. The choice of a wave-kinetic formulation in opposition to an eikonal formulation is not without consequences. The non-linear coupled evolution of the amplitude  $\mathcal{A}_p(t, \vec{x})$  and phase  $\sigma_p(t, \vec{x})$  of individual wave packets  $\phi_p = \mathcal{A}_p(t, \vec{x}) \exp i\sigma_p(t, \vec{x})$  is lost, and replaced by a statistical description. One may expect to lose valuable phase information, and the associated phase dynamics. Nevertheless, the wave-kinetic approach has been successfully implemented for the drift wave coupling to zonal flows in (Parker, 2015, 2016; Gillot, 2016; Ruiz *et al.*, 2016; Ruiz, 2017; Zhu *et al.*, 2018).

In this framework, and in a simplified slab geometry, a seed zonal flow shears the turbulent eddies, making the spectrum  $\mathcal{G}$  asymmetric in radial wave-number  $k_r$ . This induces a non-zero Reynolds stress  $\mathcal{R}$ , which reinforces the zonal flow.

$$\mathcal{R}(t, \vec{x}) = \int \frac{k_r k_\theta}{\mathcal{D}_c} \mathcal{G}(t, \vec{x}, \vec{k}) \frac{d\vec{k}}{(2\pi)^2} \quad (6.3)$$

As a consequence, the zonal flow grows as  $\gamma \propto k_{r,\text{ZF}} \sqrt{\mathcal{E}}$  with  $\mathcal{E}$  the turbulent energy, proportional to  $\mathcal{G}$ . This growth rate diverges at high zonal flow wave-number  $k_{r,\text{ZF}}$ . Actually, for thinner zonal flows, the free-energy source that is the density gradient is modified. The associated diamagnetic drift is sheared in the opposite direction ( $b \times \nabla n \sim -k_{r,\text{ZF}}^2 u_E$ ). The zonal flow growth is stabilised (Parker, 2016), with a weaker global growth as  $\gamma \propto k_{r,\text{ZF}} \sqrt{\mathcal{E}} \sqrt{1 - k_{r,\text{ZF}}^2 / k_{\perp,\text{turb}}^2}$ .

In the case of a tokamak plasma, toroidicity makes everything more complicated. On the one hand, turbulence has to make do with ballooning and magnetic shear. The radial mode number results from a competition between polarisation, magnetic shear and parallel acoustic dynamics. This severely impacts the shearing effect on turbulence (Garbet *et al.*, 2002) by providing an effective recall towards low-field-side ballooning. This constrains the accessible transverse mode numbers. On the other hand, the response of the zonal flows is also modified, as it is coupled to the Landau-damped geodesic acoustic modes (GAM) (Qiu *et al.*, 2018).

GAMs have been shown to have a mitigating effect on turbulence by various authors (Hal-latschek & Biskamp, 2001; Waltz & Holland, 2008). In addition, simulations with both ITG and energetic-particle-driven GAMs (EGAMs) feature increased turbulent avalanches, synchronised at the EGAM frequency (Zarzoso *et al.*, 2013). Furthermore, the non-linear interaction of a GAM on an ITG mode can produce another ITG mode through parametric decay (Girardo, 2015). ITG turbulence has a radial group velocity which scales with the magnetic drift. In certain conditions, the slab zonostrophic instability has been shown to have a travelling branch (Ruiz *et al.*, 2016). GAMs have a radial phase velocity that the slab Euler equation does not have, which also scales as the magnetic drift velocity. When the radial motion of turbulent structures matches the GAM’s, the turbulent wave gets trapped inside the GAM (Sasaki, 2018; Sasaki *et al.*, 2018b). The coupled system is unstable and features travelling solutions (Sasaki *et al.*, 2016, 2018a). These unstable solutions are investigated as candidates for turbulent avalanches.

We propose to extend the model from (Sasaki *et al.*, 2018a) to the kinetic description of GAMs. Along the way, we derive (section 6.1) a self-consistent wave–kinetic equation for any dispersion relation, along with its back-reaction on the profiles (section 6.2). As a consistency check, we apply the formalism to a simple slab drift-wave model (section 6.3). We model the laminar profiles using the axisymmetric component of the Vlasov equation, keeping the poloidal dependency to access GAM dynamics. The non-axisymmetric components are modelled using the wave–kinetic equation, using a general dispersion relation for the ITG mode (section 6.4 and 6.5).

We show that the GAM radial phase velocity and the wave–kinetic radial advection resonate, destabilising the GAM mode into a radially moving zonostrophic instability. When introducing a population of energetic particles, this resonance happens at the EGAM frequency, and so does the zonostrophic instability. When the turbulent growth rate is poloidally uniform, neither an up-down asymmetry in the turbulent intensity nor a background flow shear are enough to introduce a preferred radial direction for the unstable mode. However, this asymmetry can be triggered by the cooperation between both a background flow shear and a turbulent growth ballooned on the low-field side. The direction of this asymmetry is consistent with the observation from (Idomura *et al.*, 2009; McMillan *et al.*, 2009): avalanches propagate according to the sign of the background zonal flow shear rate. These features make this travelling unstable coupled mode between turbulence and GAMs a candidate explanation for turbulent avalanche processes.

## 6.1 Derivation of the wave–kinetic equation

The wave–kinetic equation models small-scale waves as pseudo-particles inside the plasma. The waves should maintain their coherence at their scale, and should only be affected by local properties of the background plasma. The pseudo-particles move according to geometrical optics. Their spatial motion is given by their group velocities. In an inhomogeneous or dispersive medium, the waves are distorted, and their wave-number change.

The wave–kinetic equation has found various applications in plasma physics since its introduction by (Weinberg, 1962). Its use in turbulence modelling has often relied on ad-hoc formulations like in (Diamond *et al.*, 2005; Sasaki *et al.*, 2018a). Conversely, several authors have attempted a simple self-consistent formulation of this model (Dodin & Fisch, 2012; Parker, 2016; Ruiz, 2017), and found earlier versions to be missing essential physics for the saturation of the zonal flows (Parker, 2015; Ruiz *et al.*, 2016).

Our derivation follows the one in (Whitham, 1965; Jimenez & Whitham, 1976). It is preferred to the formulation from (McDonald, 1988; Dodin & Fisch, 2012) for the flexibility in the choice of coordinate system. The idea is to define a variational principle for the waves, and to derive the wave–kinetic and Poisson equation from it. This allows to ensure the correct conservation properties. In paragraph 2.2, we computed a dispersion relation  $\mathcal{D}(c, r, \zeta)$  in mixed Fourier space for the local ITG modes.  $n$  is the toroidal mode number,  $c = \omega/n$  the mode phase velocity,  $r$  the reference radial position of the mode, and  $\zeta = k_r/nq'$  its ballooning angle. By symmetry, we assume  $n > 0$ . The eigenfrequency is obtained as a function of  $r$  and  $\zeta$  by solving  $\mathcal{D}(c) = 0$ . In case of multiple branches, an index can be introduced to lift the ambiguity. As a starting point, we recast it as an action principle

$$\mathcal{S} = \int \frac{ne^2}{2T} \mathcal{D}(c, r, \zeta, n) |\phi|^2 r dr n^2 q' d\zeta dc \quad (6.4)$$

Equivalently, the mode dispersion relation is obtained by setting  $\partial\mathcal{S}/\partial|\phi|^2 = 0$ . A scalar dispersion relation  $\mathcal{D}$  is defined up to a function of  $r, \zeta, n$ . The normalisation of the integrand is chosen so as to retrieve the action 2.12 in the high frequency limit.

$$\mathcal{S} \xrightarrow{c \rightarrow \infty} \int \frac{ne^2}{2T} k_\perp^2 \rho_i^2 |\phi|^2 r dr n^2 q' d\zeta dc \quad (6.5)$$

The wave–kinetic equation describes the behaviour of the amplitude of turbulent waves and abstracts out their precise shape. This argument can be made precise by introducing an amplitude–

phase decomposition of the potential as a sum of wave-packets  $p$

$$\phi(t, r, \theta, \varphi) = \sum_p \sqrt{\frac{2T \mathcal{A}_p(t, r)}{ne^2}} \exp(i\sigma_p(t, r, \theta) + in\varphi) \quad (6.6)$$

where  $\mathcal{A}_p$  plays the role of the energy in the fluctuation, and  $\sigma_p$  is a complex phase function.  $\mathcal{A}_p$  is a very smooth function, while  $\sigma_p$  contains the fine details. To avoid cluttering the notation, the subscript  $p$  will remain implicit except when otherwise noted.

The computations leading to 6.4 can be re-done using  $\omega = -\partial_t \sigma$ ,  $k_r = \partial_r \sigma$  instead of the ballooning phase function  $\sigma = -nct - nq(\theta - \zeta)$ , and neglecting the second derivatives of  $\sigma$ . These second derivatives are related to the coherence and finite extent of the waves, and are neglected by construction.  $\mathcal{A}$  is assumed to be constant at the scale of the waves, so its derivatives are neglected. This allows to define the eikonal action principle

$$\mathcal{S}_{\text{eik}} = \sum_p \Re \int \mathcal{D} \left( t, c = -\frac{\partial_t \sigma_p}{n}, r, \zeta = \frac{\partial_r \sigma_p}{nq'}, n \right) \mathcal{A}_p(t, r) \exp(-2\Im \sigma_p) r dr dt \quad (6.7)$$

with the exact same dispersion relation  $\mathcal{D}$ .  $\Re \sigma$  and  $\Im \sigma$  denote the real and imaginary parts of  $\sigma$ . The variations of  $\mathcal{S}_{\text{eik}}$  with respect to  $\mathcal{A}$  give the dispersion relation 6.8, but applied to derivatives of  $\sigma$ . The wave conservation equation 6.9 corresponds to the variations of  $\mathcal{S}_{\text{eik}}$  with respect to  $\sigma$ .

$$\mathcal{D} \left( t, c = -\frac{\partial_t \sigma}{n}, r, \zeta = \frac{\partial_r \sigma}{nq'}, n \right) = 0 \quad (6.8)$$

$$\partial_t (\mathcal{A} \partial_c \mathcal{D} e^{-2\Im \sigma}) - \frac{1}{r} \partial_r \left( r \mathcal{A} e^{-2\Im \sigma} \frac{\partial \zeta \mathcal{D}}{q'} \right) = 0 \quad (6.9)$$

Those two equations are valid for each wave packet individually. By analogy with traditional mechanics, 6.8 is called the Hamilton–Jacobi equation. In resolved form, it would write  $c(x, \partial_r \sigma) = -\partial_t \sigma$  with  $c(x, k)$  the wave phase velocity from the dispersion relation. The phase function  $\sigma$  serves as a pilot wave. It has a similar role as Hamilton’s function for the motion of the individual turbulent waves: it provides the evolution of the canonical momentum  $k = \partial_x \sigma$  as a function of space and time. Equation 6.9 is already in a conservative form. The convected quantity is  $\mathcal{A} \partial_c \mathcal{D}$ , the ratio of an energy to a toroidal phase velocity. It represents the toroidal momentum stored in the wave packet. We note that the derivative  $\partial_c \mathcal{D}$  must not vanish. This excludes from this description the case of reactive instabilities, caused by the unfortunate encounter of two stable branches. Conversely, this description is adequate for kinetic excited or damped waves, for which  $\partial_c \mathcal{D} \neq 0$ . The system 6.8–6.9 is of two non-linear equations, thus unpractical for a bath of wave packets. In order to derive the wave–kinetic equation, we introduce the Wigner density function (Moyal & Bartlett, 1949; McDonald & Kaufman, 1985; McDonald, 1988, 1991)

$$\begin{aligned} \mathcal{W}(t, r, \zeta) &= \frac{ne^2}{2T} \int \phi \left( t, r + \frac{x}{2} \right) \phi^* \left( t, r - \frac{x}{2} \right) \exp(-in\zeta q' x) \frac{nq' dx}{2\pi} \\ &\approx \sum_p \mathcal{A}_p \exp(-2\Im \sigma_p) \delta \left( \zeta - \frac{\partial_r \Re \sigma_p}{nq'} \right) \end{aligned} \quad (6.10)$$

where  $\delta$  is the Dirac distribution. The second equality is valid thanks to the radial scale separation between  $\mathcal{A}$  and  $\sigma$ . The function  $\mathcal{W}$  encodes both the amplitude and the phase. It serves as a Klimontovitch distribution for the wave packets. Using Whitham’s equation 6.9, the convection of the wave action density  $\mathcal{W}$  can be computed as

$$\begin{aligned} \partial_t (\mathcal{W} \partial_c \mathcal{D}) - \frac{1}{r} \partial_r \left( r \mathcal{W} \frac{\partial \zeta \mathcal{D}}{q'} \right) &= - \left[ \partial_c \mathcal{D} \frac{\partial_{tr}^2 \Re \sigma}{n} - \partial_c \mathcal{D} \partial_r \left( \frac{\partial_r \Re \sigma}{nq'} \right) \right] \partial_\zeta \mathcal{W} \\ &\quad - 2\mathcal{W} \left[ \partial_c \mathcal{D} \partial_t \Im \sigma + \frac{\partial \zeta \mathcal{D}}{q'} \partial_r \Im \sigma \right] \end{aligned} \quad (6.11)$$

The first square bracket quantifies how radially neighbouring wave trajectories get pulled apart. It will yield the wave stretching term in the wave–kinetic equation. The second square bracket

contains the growth rate  $\gamma = -\partial_t \Im \sigma$ , computed using the dispersion relation. Finally, we assume  $\partial_r \sigma$  to be real, corresponding to propagating waves (Suchy, 1981). To compute the first square bracket, we differentiate the Hamilton–Jacobi equation 6.8 with respect to  $r$

$$0 = \partial_r \left[ \mathcal{D} \left( c = -\frac{\partial_t \sigma}{n}, r, \zeta = \frac{\partial_r \sigma}{nq'}, n \right) \right] = -\partial_c \mathcal{D} \frac{\partial_{tr}^2 \sigma}{n} + \partial_\zeta \mathcal{D} \partial_r \left( \frac{\partial_r \sigma}{nq'} \right) + \partial_r \mathcal{D} \quad (6.12)$$

$$\partial_t (\mathcal{W} \partial_c \mathcal{D}) - \frac{1}{r} \partial_r \left( r \mathcal{W} \frac{\partial_\zeta \mathcal{D}}{q'} \right) = -\frac{\partial_r \mathcal{D}}{q'} \partial_\zeta \mathcal{W} + 2\gamma \partial_c \mathcal{D} \mathcal{W} \quad (6.13)$$

The parameters to  $\mathcal{D}$  in equation 6.13 are still the derivatives of  $\sigma$ . In order to replace mentions of  $\partial_r \sigma$  by  $\zeta$ , we use the absorbing property of the Dirac distribution<sup>1</sup> inside  $\mathcal{W}$ . We get the wave–kinetic equation as

$$\partial_t (\mathcal{W} \partial_c \mathcal{D}) - \frac{1}{r} \partial_r \left( r \mathcal{W} \frac{\partial_\zeta \mathcal{D}}{q'} \right) + \partial_\zeta \left( \mathcal{W} \frac{\partial_r \mathcal{D}}{q'} \right) = 2\gamma \partial_c \mathcal{D} \mathcal{W} \quad (6.14)$$

The value of  $\partial_t \sigma$  is completely defined by the Hamilton–Jacobi equation 6.8 as a function of  $r$  and  $\zeta$ .  $\sigma$  is completely eliminated from the description. The equation on  $\mathcal{W}$  can be recast as a conservation for the wave action  $\mathcal{G}$

$$\mathcal{G} = \mathcal{W} \partial_c \mathcal{D} = \frac{nc^2}{2T} |\phi|^2 \delta \left( \zeta - \frac{\partial_r \Re \sigma}{nq'} \right) \partial_c \mathcal{D} \quad (6.15)$$

$$\partial_t \mathcal{G} + \frac{1}{r} \partial_r (r v_g^r \mathcal{G}) + \partial_\zeta (v_g^\zeta \mathcal{G}) = 2\gamma \mathcal{G} \quad (6.16)$$

The growth rate arises from the solution of the complex analytic dispersion relation 6.8. The group velocity  $v_g^r$  and the wave distortion  $v_g^\zeta$  given by the usual formulas

$$q' v_g^r = -\frac{\partial_\zeta \mathcal{D}}{\partial_c \mathcal{D}} = \left( \frac{\partial c}{\partial \zeta} \right)_{\mathcal{D}=0} \quad (6.17)$$

$$q' v_g^\zeta = \frac{\partial_r \mathcal{D}}{\partial_c \mathcal{D}} = -\left( \frac{\partial c}{\partial r} \right)_{\mathcal{D}=0} \quad (6.18)$$

$$\gamma = -n \frac{\Im[\mathcal{D}]}{\partial_c \mathcal{D}} \quad (6.19)$$

Equation 6.16 is a kinetic equation. The waves are advected in phase space so as to conserve the wave phase velocity  $c(r, \zeta)$ . This phase velocity actually serves as a Hamiltonian for the waves. The additional  $n$  factor in the growth rate 6.19 comes from the choice of the phase velocity  $c$  as a variable of interest, instead of the frequency  $\omega$ . The turbulent energy can be derived using Noether’s theorem from the eikonal action 6.28, and coincides with the usual definition in dispersive media (Landau & Lifschitz, 1984, eq. 61.9)

$$E_{\text{turb}} = \int c \mathcal{G} d\zeta r dr = \int \partial_c [c \mathcal{D}] \frac{nc^2}{T} |\phi|^2 d\zeta r dr \quad (6.20)$$

where  $c$  is the real solution to the real part of the dispersion relation 6.8. By removing the function  $\sigma$  from the description, the non-linear phase dynamics associated to the Hamilton–Jacobi equation 6.8 is lost. Only a linearised version is kept, in the form of the advection velocities  $v_g^r$  and  $v_g^\zeta$ .

Dimensionally, the total wave action  $\int \mathcal{G} d\zeta$  from 6.15 is an energy divided by a toroidal angular velocity. It represents the momentum of turbulence when waves are sped up toroidally. Because of the parallel alignment of the turbulent structures,  $q\mathcal{G}$  serves as a poloidal momentum.

The growth rate is not self-consistent. This is expected: this description conserves energy, but does not contain the depletion of the free energy source. In order to obtain a self-consistent system of equations, we need to write the associated energy depletion in the evolution of the profiles. This problem is notoriously subtle. It involves the computation of quasi-linear particle fluxes, as well as introducing a ponderomotive force into the system. For reference, see (McDonald *et al.*, 1985; Kaufman *et al.*, 1987). In the following, we will consider marginally stable modes,  $\gamma = 0$ . As a consequence, the quasi-linear energy fluxes will be zero.

<sup>1</sup>This replacement is only possible on functions  $f$  that directly “touch” the  $\delta$  distribution:  $f(a)\delta(a-b) = f(b)\delta(a-b)$ . If a derivative is present, the expression needs to be shuffled to get it out of the way:  $f(a)\partial_b \delta(a-b) = \partial_b [f(a)\delta(a-b)] = \partial_b [f(b)\delta(a-b)]$ .

## 6.2 Coupling to the profile

Equation 6.16 is coupled to the Vlasov equation for the axisymmetric component of the distribution function  $\mathcal{F}$

$$\partial_t \mathcal{F} + \text{div} \vec{\Gamma}_{\text{traj}} + \text{div} \vec{\Gamma}_{\text{turb}} = \text{Sources} + \text{Collisions} \quad (6.21)$$

$\vec{\Gamma}_{\text{traj}}$  is the flux governed by the advection of  $\mathcal{F}$  by the trajectories of the gyro-centres, while  $\vec{\Gamma}_{\text{turb}}$  contains the heat flux coming from the non-linear coupling of non-axisymmetric fluctuations. The latter flux has components along directions  $r$ ,  $\theta$  and energy  $E$ . In our wave-centred description,  $\vec{\Gamma}_{\text{turb}}$  is approximated as the quasi-linear flux, an integral over the spectrum  $\mathcal{G}$ . The integrands encode the efficiency of turbulent transport depending on the class of particles. Those depend on the profiles, their gradients and on the wave phase space. Let the linear response  $f$  of the distribution function to the wave  $\phi$  be written symbolically as

$$\frac{f}{\mathcal{F}} = \Lambda \left[ c = -\frac{\partial_t \sigma}{n}, \zeta = \frac{\partial_r \sigma}{nq'}, n; r, \theta, E, \mu \right] \frac{e\phi}{T} \quad (6.22)$$

For a drift-kinetic system, the dispersion relation with adiabatic electrons can be written as

$$\mathcal{D}_{\text{adiab}} = \tau + k_{\perp}^2 \rho_i^2 - \int \Lambda \frac{\mathcal{F}}{n} d^3v \quad (6.23)$$

with  $\tau = T/T_e$  the ion to electron temperature ratio, and  $k_{\perp}^2 \rho_i^2$  corresponds to the ion polarisation. The extension to a gyro-kinetic model is straightforward by inserting the appropriate gyro-averaging. The quasi-linear fluxes of gyro-centres read as follows

$$\begin{aligned} \Gamma_{\text{turb}}^r &= \langle v_E^{r*} f \rangle_{\text{turb}} \\ &= -\Re \sum_{n>0} \frac{inq\phi^*}{rB} \Lambda \frac{e\phi}{T} \mathcal{F} \\ &= -\frac{2\mathcal{F}}{eN} \Re \sum_{n>0} \int \frac{inq}{rB} \Lambda \frac{\mathcal{G}}{\partial_c \mathcal{D}} d\zeta \end{aligned} \quad (6.24)$$

$$\Gamma_{\text{turb}}^{\theta} = \langle v_E^{\theta*} f \rangle_{\text{turb}} = \frac{2\mathcal{F}}{eN} \Re \sum_{n>0} \int \frac{inq'\zeta}{B} \Lambda \frac{\mathcal{G}}{\partial_c \mathcal{D}} d\zeta \quad (6.25)$$

where the brackets  $\langle \cdot \rangle_{\text{turb}}$  denote a sum over all the turbulent modes for all  $n$  and  $\zeta$ . The turbulent intensity is inserted using its definition equation 6.15. We suppose that the modes are marginally stable, so that the dispersion relation is real, and there is no direct energy exchange between the particles and the wave, so the energy flux  $\Gamma^E$  is zero.

It should be noted that the total quasi-linear charge flux ( $\sum_s e_s \int \Gamma_{\text{turb},s}^r d^3v$ ) vanishes. In the case of adiabatic electrons, the ion particle flux is ambipolar. This can be seen by integrating 6.24 and 6.25 on velocity.

$$\sum_s e_s \Gamma_{\text{turb},s}^r = \frac{2}{n_0} \sum_{n>0} \int \frac{nq}{rB} \Im \left[ \sum_s \int \mathcal{F}_s \Lambda_s d^3v \right] \frac{\mathcal{G}}{\partial_c \mathcal{D}} d\zeta \quad (6.26)$$

The factor inside the brackets is the total density response. The dispersion relation 6.23 tells us it is purely real. Hence, the total charge flux vanishes. This is unexpected: we should get a polarisation flux carried by the turbulence. This polarisation flux contains the Reynolds stress responsible for the growth of zonal flows (Taylor, 1915).

There is actually no issue with equations 6.24 and 6.25. The vanishing of the polarisation flux is consistent with our ordering on radial derivatives  $\partial_r \ll nq'\zeta$ . Because of this ordering, quantities involving an odd number of derivatives are purely imaginary. Instead, the polarisation flux is frozen in the turbulence, and appears as a additional charge density in the Poisson equation. For consistency, we need to adapt the Poisson equation to the eikonal action principle 6.7.

Let  $\Phi$  be the axisymmetric electrostatic potential. This potential is associated to a poloidal zonal flow angular velocity  $u_E = \partial_r \Phi / rB$ . Derivations of a dispersion relation are typically done

in the toroidally rotating plasma frame, where the zonal flow vanishes. In order to move back to the laboratory frame, we introduce the zonal flow as a toroidal Doppler shift

$$\mathcal{D}\left(c = -\frac{\partial_t \sigma}{n}, r, \zeta = \frac{\partial_r \sigma}{nq'}, n; u_E\right) = \mathcal{D}\left(c = -\frac{\partial_t \sigma}{n} + qu_E, r, \zeta = \frac{\partial_r \sigma}{nq'}, n\right) \quad (6.27)$$

The complete action principle becomes

$$\begin{aligned} \mathcal{S} &= \int \mathcal{D}\left(c = -\frac{\partial_t \sigma}{n} + \frac{q\partial_r \Phi}{rB}, r, \zeta = \frac{\partial_r \sigma}{nq'}, n\right) \mathcal{A}(t, r) e^{-2\Im\sigma} r dr \\ &+ \int \frac{m\mathcal{N}}{2B^2} (\vec{\nabla}_\perp \Phi)^2 r dr + \int \frac{ne^2}{2T_e} (\Phi - \Phi_{\text{FS}})^2 r dr - \int e\Phi \mathcal{F} d^3 v r dr \end{aligned} \quad (6.28)$$

The first line is our eikonal action. The second line contains the kinetic energy stored inside the zonal flow and the potential energy of the particles. As usual, the Poisson equation is obtained from the variations of  $\mathcal{S}$  with respect to  $\Phi$ .

$$\begin{aligned} -\text{div}_\perp \left( \frac{m\mathcal{N}}{B^2} \vec{\nabla}_\perp \Phi \right) + \frac{ne^2}{T_e} (\Phi - \Phi_{\text{FS}}) - e \int \mathcal{F} d^3 v &= \frac{1}{r} \partial_r \left[ r \frac{\partial \mathcal{D}}{\partial (\partial_r \Phi)} \mathcal{A}(t, r) e^{-2\Im\sigma} \right] \\ &= \text{div}_r \int \frac{q\mathcal{G}}{rB} d\zeta \end{aligned} \quad (6.29)$$

where the last equality uses 6.27 and the definition of the wave packet density  $\mathcal{G}$ . Turbulence is affected by the poloidal flow  $u_E$ . Modifying the flow costs energy according to a momentum  $q\mathcal{G}$ . This momentum is equivalent to a polarisation for the  $E \times B$  flow. By redefining the distribution function  $\mathcal{F}$ , this charge could be added to the Vlasov equation as our dearly missed polarisation flux. The final system of equations is composed of 6.16, 6.21 and 6.29. Once again, the total energy can be derived using Noether's theorem on the action 6.28

$$\begin{aligned} E_{\text{tot}} &= E_{\text{kin}} + E_{\text{pol}} + E_{\text{turb}} \\ E_{\text{kin}} &= \int \left[ \frac{m}{2} v_\parallel^2 + \mu B \right] F d^3 v r dr d\theta \\ E_{\text{pol}} &= \int \frac{m\mathcal{N}}{2B^2} |\vec{\nabla}_\perp \Phi|^2 r dr d\theta + \int \frac{ne^2}{2T_e} (\Phi - \Phi_{\text{FS}})^2 r dr d\theta \\ E_{\text{turb}} &= \int \left[ c + q \frac{\partial_r \Phi}{rB} \right] \mathcal{G} d\zeta r dr d\theta \end{aligned}$$

$E_{\text{kin}}$  is the energy stored in kinetic form by the particles.  $E_{\text{turb}}$  is the energy stored in the turbulence.  $E_{\text{pol}}$  is the energy stored in the zonal electric field. The Vlasov equation 6.21 is constructed so as to follow the Hamiltonian  $\frac{m}{2} v_\parallel^2 + \mu B + e\Phi$ . Similarly, the wave-kinetic equation 6.16 is constructed so as to always verify the dispersion equation: it conserves  $c + q \frac{\partial_r \Phi}{rB}$  along the trajectories in phase space. Both dynamics allow one to verify the energy conservation

$$\begin{aligned} \frac{dE_{\text{kin}}}{dt} &= \int \Gamma_{\text{turb}}^E d^3 v r dr d\theta - e \int \partial_t \Phi F d^3 v r dr d\theta \\ \frac{dE_{\text{pol}}}{dt} &= \int \frac{m\mathcal{N}}{B^2} \vec{\nabla}_\perp \Phi \cdot \partial_t \vec{\nabla}_\perp \Phi r dr d\theta + \int \frac{ne^2}{T_e} (\Phi - \Phi_{\text{FS}}) \partial_t \Phi r dr d\theta \\ \frac{dE_{\text{turb}}}{dt} &= \int q \frac{\partial_{rt}^2 \Phi}{rB} \mathcal{G} d\zeta r dr d\theta + \int 2\gamma \left[ c + q \frac{\partial_r \Phi}{rB} \right] \mathcal{G} d\zeta r dr d\theta \\ \frac{dE_{\text{tot}}}{dt} &= \int 2\gamma \left[ c + q \frac{\partial_r \Phi}{rB} \right] \mathcal{G} d\zeta r dr d\theta + \int \Gamma_{\text{turb}}^E d^3 v r dr d\theta = 0 \end{aligned}$$

where we have used the Poisson equation 6.29 multiplied by  $\partial_t \Phi$  to get the simplified last equation. The last equation corresponds to the energy exchange between the waves and the particles. For marginally stable modes, it is trivially zero. The conservation of the poloidal momentum can be

computed directly from the Poisson equation 6.29

$$\begin{aligned} \frac{r^2}{q} m n \partial_t u_E &= \frac{1}{r} \partial_r \int r v_g^r \mathcal{G} d\zeta - e \frac{r}{q} \int \Gamma_{\text{QL}}^r d^3v \\ &= -\frac{1}{r} \partial_r \int r \mathcal{W} \partial_\zeta \mathcal{D} d\zeta \end{aligned} \quad (6.30)$$

where we have used the definition of the radial group velocity  $v_g^r = -\partial_\zeta \mathcal{D} / \partial_c \mathcal{D}$ . The first equality corresponds to the definition of the Reynolds stress as a flux of toroidal momentum, while the second equality allows to relate it to the potential spectrum.

### 6.3 Drift wave model

As a pedagogical example, let us first apply our approach to the wave-kinetic equation to the well-known Charney-Hasegawa-Mima model for slab drift waves (Charney & Drazin, 1961; Hasegawa & Mima, 1978). The advection equation for the vorticity  $w(x, y)$  has a particularly simple form

$$\partial_t w + \vec{v}_E \cdot \vec{\nabla} w + \beta \partial_y \phi = 0 \quad (6.31)$$

We introduce the amplitude  $\mathcal{A}$  and phase function as in equation 6.6

$$\tilde{\phi} = \sqrt{2\mathcal{A}} \exp(i\sigma(t, x) + ik_y y)$$

Around a reference radial position  $x$ , with a background flow  $u_E = \partial_x \Phi$  in the  $y$  direction, the linearised response for 6.31 is easily computed as

$$\tilde{w} = \frac{\beta - \partial_x W}{c + u_E} \tilde{\phi}$$

with  $W$  the equilibrium vorticity profile, and  $c = -\partial_t \sigma / k_y$  the phase velocity in the  $y$  direction. The action principle for Poisson equation becomes

$$\begin{aligned} \mathcal{S} &= \frac{1}{2} \int [\rho_i^2 |\nabla \phi|^2 + \tau |\phi|^2 - \phi w[\phi]] \\ &= \int \mathcal{D} \left( -\frac{\partial_t \sigma}{k_y} + u_E, x, \frac{\partial_x \sigma}{k_y}, k_y \right) \mathcal{A} \\ \mathcal{D}(c, r, \zeta, n) &= k_y^2 \rho_i^2 (1 + \zeta^2) + \tau - \frac{\beta - \partial_x W}{c} = 0 \end{aligned} \quad (6.32)$$

where  $\zeta = \partial_x \sigma / k_y$ . The  $k_y^2 \rho_i^2 (1 + \zeta^2)$  is the Laplacian operator in the Poisson equation. The dispersion relation for the drift-waves is  $\mathcal{D}(c, r, \zeta, n) = 0$ . We introduce the Wigner function  $\mathcal{W}$  and the wave action density  $\mathcal{G}$

$$\begin{aligned} \mathcal{W} &= \int \phi(x + \delta x) \phi(x - \delta x) e^{-in\zeta x} n dx = 2\mathcal{A} \delta \left( \zeta - \frac{\partial_x \sigma}{n} \right) \\ \mathcal{G} &= \mathcal{W} \partial_c \mathcal{D} = \frac{\beta - \partial_x W}{c^2} \mathcal{W} = \frac{(\tau + k_y^2 \rho_i^2)}{\beta - \partial_x W} \mathcal{W} \end{aligned}$$

By following the steps in paragraphs 6.1 and 6.2, the wave-kinetic equation 6.16 and the Poisson equation 6.29 become

$$\partial_t \mathcal{G} - \partial_x \left[ \frac{\partial_\zeta \mathcal{D}}{\partial_c \mathcal{D}} \mathcal{G} \right] + \partial_\zeta \left[ \frac{\partial_x \mathcal{D}}{\partial_c \mathcal{D}} \mathcal{G} \right] = 0 \quad (6.33)$$

$$-\nabla^2 \Phi = \partial_x \int \mathcal{G} d\zeta dn \quad (6.34)$$

with the group velocities given by

$$v_g^x = -\frac{\partial_\zeta \mathcal{D}}{\partial_c \mathcal{D}} = -2\zeta n^2 \rho_*^2 \frac{\beta - \partial_x W}{[n^2 \rho_*^2 (1 + \zeta^2) + \tau]^2} \quad (6.35)$$

$$v_g^\zeta = \frac{\partial_x \mathcal{D}}{\partial_c \mathcal{D}} = -\frac{\partial c}{\partial x} = -\partial_x u_E + \frac{\partial_x^2 W}{n^2 \rho_*^2 (1 + \zeta^2) + \tau} \quad (6.36)$$

The expression of the Reynolds stress is retrieved by considering the time evolution of  $u_E$

$$-\partial_t \partial_x \Phi = \partial_x \int \frac{\partial \zeta \mathcal{D}}{\partial c \mathcal{D}} \mathcal{G} d\zeta dn = \partial_x \int \rho_*^2 n^2 \zeta \mathcal{W} d\zeta dn \quad (6.37)$$

We recover the conservation of the Wigner function of the vorticity, and not of the potential. This is consistent with the observations from the CE2–GO approach (Parker, 2016; Gillot, 2016). The formulation of the Reynolds stress exactly matches the expected  $k_x k_y |\phi|^2$  from Euler equation, with less usual notations. Although derived from a different formalism, the obtained wave–kinetic system with velocity 6.36 features the saturation mechanism highlighted in (Parker, 2015; Ruiz *et al.*, 2016). Its origin lies in the depletion of the free-energy source  $\partial_x W$ . The next section extends the physics application to the toroidal ITG mode.

## 6.4 Generalised ITG model

In order to avoid notation complexity, we consider a prototype generalised ITG model. The instability mechanism stems from the resonance between the toroidal phase velocity  $c$  of the mode and the toroidal drift  $\Omega_d$  of involved particles. In general,  $\Omega_d$  is an even function of  $\zeta$ . For this reason, we shall take  $\Omega_d = \Omega_{d0} + \Omega_{d1} \cos \zeta$ , with  $\Omega_{d0}$  and  $\Omega_{d1}$  of the order of  $u_{DT}$ . The dispersion relation writes

$$\mathcal{D}(c, r, \zeta, n) = D\left(\frac{c + qu_E}{\Omega_d(\zeta)}, n\right) = 0$$

Without loss of generality, we suppose there is only one branch of solutions,  $D(\delta_n + i\varepsilon_n, n) = 0$ . In the converse case, the wave–kinetic system can be replaced by a sum over the branches. In this framework, one has

$$c = \Omega_d(\zeta)(\delta_n + i\varepsilon_n) - qu_E$$

The wave–kinetic equation becomes

$$\begin{aligned} \partial_t \mathcal{G} + \frac{1}{r} \partial_r (r v_g^r \mathcal{G}) + \partial_\zeta (\gamma_E \mathcal{G}) &= 2\gamma \mathcal{G} \\ v_g^r &= \frac{\partial c}{q' \partial \zeta} = -v_g \sin \zeta \\ v_g^\zeta &= -\frac{\partial c}{q' \partial r} = \frac{(qu_E)'}{q'} = \gamma_E \\ \gamma &= \Omega_d(\zeta) \varepsilon_n \end{aligned} \quad (6.38)$$

where the group velocity  $v_g$  scales like the thermal magnetic drift. We recover the expected advection in  $\zeta$  space by the zonal flow shear  $\gamma_E$ . With the chosen expression of  $\Omega_d$ , the growth rate is maximal for  $\zeta$  close to 0, which is consistent with the preferred growth of the modes on the low-field side. Since we neglected the wave–particle energy exchange in paragraph 6.2, we will take  $\varepsilon_n = \gamma = 0$  to keep a consistent model.

## 6.5 Effect of toroidicity on the zonostrophic instability

Given these three equations 6.16, 6.21 and 6.29, we can discuss their behaviour around a plasma state  $(\mathcal{F}_{\text{eq}}, \mathcal{G}_{\text{eq}}, \Phi_{\text{eq}})$ . For a small departure in the profiles and turbulence intensity, the coupled second-order system can be analysed linearly.

The wave–kinetic equation contains a radial advection 6.38 that scales like the magnetic drift. In certain conditions, this advection gives a travelling branch to the slab zonostrophic instability. Conversely to the slab model, the profiles in the toroidal case respond according to the GAM dynamics. Therefore, one can expect the GAM radial phase velocity and the wave–kinetic radial advection to resonate, destabilising the GAM mode.

Moreover, the radial velocity scales like equation 6.38: the inwards/outwards direction depends on the effective ballooning angle. With a background zonal flow shear, the turbulent spectrum is asymmetric in  $\zeta$ . This effect should allow one to explain the relation between the direction of avalanches and the sign of the zonal shear, as reported in numerical simulations (Idomura *et al.*, 2009; McMillan *et al.*, 2009). We take the coupled system as

$$\partial_t \mathcal{G} + \frac{1}{r} \partial_r (r v_g^r \mathcal{G}) + \partial_\zeta (\gamma_E \mathcal{G}) = 0 \quad (6.39)$$

$$\partial_t \mathcal{F}(r, \theta, E, \mu) + \frac{v_{||}}{qR} \partial_\theta \mathcal{F} - u_D (\cos \theta \partial_\theta + \sin \theta r \partial_r) \mathcal{F} + \frac{b}{B} \times \vec{\nabla} \Phi \cdot \vec{\nabla} \mathcal{F} = -\text{div} \Gamma_{\text{QL}} \quad (6.40)$$

where we denote the magnetic drift angular velocity as

$$u_D = \frac{m v_{||}^2 + \mu B}{e B R r}$$

We chose to neglect the effect of the quasi-linear fluxes in 6.40. These fluxes balance the excitation in the wave-kinetic equation. In order to keep the energetic consistency, we put this excitation to zero.

We perturb the system with a fluctuation of the  $n = 0$  potential  $\tilde{\Phi}$ , with  $p/r$  the radial mode number. Let  $\omega$  be the mode frequency, and  $\omega_{||} = v_{||}/qR$ . For simplicity, we neglect the back-action onto the density and temperature gradients used as free energy sources for the ITG turbulence. As a consequence, the growth of the mode in the thin corrugation limit—around the eddy size—may be overestimated (Parker, 2016). In the Vlasov equation, we neglect the poloidal drifts (magnetic and  $E \times B$ ) compared to the poloidal projection of the parallel velocity. We suppose the equilibrium electric field is purely radial  $\Phi_{\text{eq}}(r)$ . The Poisson equation is obtained from equation 6.29.

$$-i\omega \tilde{\mathcal{G}} - ip \frac{v_g}{r} \sin \zeta \tilde{\mathcal{G}} + \gamma_E \partial_\zeta \tilde{\mathcal{G}} = \frac{p^2}{r^2} \frac{\tilde{\Phi}_0}{B} \partial_\zeta \mathcal{G}_{\text{eq}} \quad (6.41)$$

$$-i\omega \tilde{F} + \omega_{||} \partial_\theta \tilde{F} - u_D \sin \theta r \partial_r \tilde{F} = -[\omega_{||} \partial_\theta - u_D \sin \theta r \partial_r] \tilde{\Phi} \frac{\mathcal{F}_{\text{eq}} e}{T_{\text{eq}}} \quad (6.42)$$

$$(-p^2 \rho_*^2 + \rho_*^2 \partial_\theta^2 + \tau) \frac{n_{\text{eq}} e^2}{T_{\text{eq}}} \tilde{\Phi} = e \int \tilde{F} + ip \int \frac{q \tilde{\mathcal{G}}}{r^2 B} d\zeta \quad (6.43)$$

We denote as  $\Phi_{0,c,s}$  the symmetric, cosine and sine components of  $\tilde{\Phi}$ , likewise for  $\tilde{F}$ . We perform a similar decomposition for  $\tilde{\mathcal{G}}$  with the ballooning angle  $\zeta$ .

$$\begin{pmatrix} -2i\omega & -ip \frac{v_g}{r} & 0 \\ -ip \frac{v_g}{r} & -i\omega & -\gamma_E \\ 0 & +\gamma_E & -i\omega \end{pmatrix} \begin{pmatrix} \tilde{\mathcal{G}}_0 \\ \tilde{\mathcal{G}}_s \\ \tilde{\mathcal{G}}_c \end{pmatrix} = \frac{p^2}{r^2} \frac{\tilde{\Phi}_0}{B} \begin{pmatrix} 0 \\ -\mathcal{G}_{\text{eq},c} \\ \mathcal{G}_{\text{eq},s} \end{pmatrix} \quad (6.44)$$

$$\begin{pmatrix} -2i\omega & -ipu_D & 0 \\ -ipu_D & -i\omega & -\omega_{||} \\ 0 & +\omega_{||} & -i\omega \end{pmatrix} \begin{pmatrix} \tilde{F}_0 \\ \tilde{F}_s \\ \tilde{F}_c \end{pmatrix} = \frac{\mathcal{F}_{\text{eq}} e}{T_{\text{eq}}} \begin{pmatrix} 0 & ipu_D & 0 \\ ipu_D & 0 & -\omega_{||} \\ 0 & +\omega_{||} & 0 \end{pmatrix} \begin{pmatrix} \tilde{\Phi}_0 \\ \tilde{\Phi}_s \\ \tilde{\Phi}_c \end{pmatrix} \quad (6.45)$$

We can verify that the matrices on the left-hand side are skew-symmetric. This is consistent with the advection form of the Vlasov and wave-kinetic equations. For simplicity, we set the wave group velocity as  $v_g = u_{\text{DT}}/q'$ , with the thermal toroidal magnetic drift frequency  $u_{\text{DT}} = qT/eBRr$ . Let  $u_{\text{TR}}$  be the poloidal transit frequency,  $u_{\text{TR}} = v_{\text{th}}/qR$ . We introduce the normalised mode frequency  $\Omega = \frac{\omega}{u_{\text{TR}} \sqrt{2}}$ , mode number  $P = \frac{u_{\text{DT}}}{2u_{\text{TR}} q} p = qp_*/2$ , and background flow shear  $S = \frac{\gamma_E}{u_{\text{TR}} \sqrt{2}}$ . Inverting the two matrices gives the resolved form

$$\tilde{\mathcal{G}}_0 = \frac{iP^3/s}{\Omega^2 - S^2 - P^2/s^2} \left[ \mathcal{G}_{\text{eq},c} - i \frac{S}{\Omega} \mathcal{G}_{\text{eq},s} \right] \frac{2\tilde{\Phi}_0}{q^2 \rho_*^2 r^2 u_{\text{TR}} B} \quad (6.46)$$

$$\tilde{F}_0 = \frac{e \mathcal{F}_{\text{eq}}}{2T_{\text{eq}}} \frac{-\Omega P \sqrt{2} \frac{qu_D}{u_{\text{DT}}} \tilde{\Phi}_s + 2P^2 \left( \frac{qu_D}{u_{\text{DT}}} \right)^2 \tilde{\Phi}_0}{\Omega^2 - \Omega_{||}^2} \quad (6.47)$$

$$\tilde{F}_s = \frac{e \mathcal{F}_{\text{eq}}}{T_{\text{eq}}} \frac{-\sqrt{2} \Omega P \frac{qu_D}{u_{\text{DT}}} \tilde{\Phi}_0 + \Omega_{||}^2 \tilde{\Phi}_s + i\Omega \Omega_{||} \tilde{\Phi}_c}{\Omega^2 - \Omega_{||}^2} \quad (6.48)$$

with  $s = rq'/q$  the magnetic shear. For a symmetric distribution function, the only the even terms in  $\Omega_{\parallel}$  contribute, so  $\tilde{\Phi}_c$  disappears from the description. Integrating in velocity, we obtain

$$\tilde{N}_0 = \frac{e\mathcal{N}_{\text{eq}}}{2T_{\text{eq}}}[PI_1\tilde{\Phi}_s + P^2I_2\tilde{\Phi}_0] \quad (6.49)$$

$$\tilde{N}_s = \frac{e\mathcal{N}_{\text{eq}}}{T_{\text{eq}}}[PI_1\tilde{\Phi}_0 + I_3\tilde{\Phi}_s] \quad (6.50)$$

where we used the resonant integrals from (Girardo, 2015):

$$I_1 = \sqrt{2} \int \frac{\Omega \frac{qu_D}{u_{\text{DT}}}}{\Omega^2 - \Omega_{\parallel}^2} \frac{\mathcal{F}_{\text{eq}}}{n_{\text{eq}}} = -\sqrt{2} \left[ Z[\Omega] \left( \frac{1}{2} + \Omega^2 \right) + \Omega \right] \quad (6.51)$$

$$I_2 = 2 \int \frac{\left( \frac{qu_D}{u_{\text{DT}}} \right)^2}{\Omega^2 - \Omega_{\parallel}^2} \frac{\mathcal{F}_{\text{eq}}}{n_{\text{eq}}} = -2 \left[ Z[\Omega] \left( \frac{1}{2\Omega} + \Omega + \Omega^3 \right) + \frac{3}{2} + \Omega^2 \right] \quad (6.52)$$

$$I_3 = \int \frac{\Omega_{\parallel}^2}{\Omega^2 - \Omega_{\parallel}^2} \frac{\mathcal{F}_{\text{eq}}}{n_{\text{eq}}} = -1 - \Omega Z[\Omega] \quad (6.53)$$

Finally, Poisson equation gives

$$\frac{P^2}{q^2} \tilde{\Phi}_0 = \frac{1}{2}[PI_1\tilde{\Phi}_s + P^2I_2\tilde{\Phi}_0] + i \frac{2P}{r^2 \rho_* B} \frac{T_{\text{eq}}}{n_{\text{eq}} e^2} \tilde{\mathcal{J}}_0 \quad (6.54)$$

$$\begin{aligned} &= \frac{1}{2}[PI_1\tilde{\Phi}_s + P^2I_2\tilde{\Phi}_0] \\ &\quad - 4\tilde{\Phi}_0 \frac{P^4/s}{\Omega^2 - S^2 - P^2/s^2} \int \frac{\mathcal{J}_{\text{eq},c} - i \frac{S}{\Omega} \mathcal{J}_{\text{eq},s}}{n_{\text{eq}} m r^2 u_{\text{DT}}} d\zeta \\ \left( \tau + \rho_*^2 + \frac{P^2}{q^2} \right) \tilde{\Phi}_s &= PI_1\tilde{\Phi}_0 + I_3\tilde{\Phi}_s \end{aligned} \quad (6.55)$$

We introduce the turbulent intensity as  $\mathcal{J}_{c,s} = \frac{\int \mathcal{J}_{\text{eq},c,s} d\zeta}{n_{\text{eq}} m r^2 u_{\text{DT}}}$ . The dispersion relation is given by  $D_G(\Omega) = 0$  with

$$D_G(\Omega) = \frac{1}{q^2} - \frac{J_2(\Omega)}{2} - \frac{I_1^2(\Omega)}{2 \left( \tau + \frac{P^2}{q^2} - I_3(\Omega) \right)} \quad (6.56)$$

$$J_2 = I_2 - \frac{8P^2/s}{\Omega^2 - S^2 - P^2/s^2} \left[ \mathcal{J}_c - i \frac{S}{\Omega} \mathcal{J}_s \right] \quad (6.57)$$

The dispersion relation 6.56 is plotted figure 6.1. This plot is done with  $q = 1.6$ ,  $s = 1$  without any sheared flow  $S = 0$ . The turbulent intensity is chosen as  $\mathcal{J}_c = 10^{-2}$  and  $\mathcal{J}_s = 0$ . This corresponds to an in-out asymmetry of turbulent energy of the order of  $\mathcal{J}_c q^2 \rho_*^2 \varepsilon^2$  times the plasma pressure. For  $P = 0$ , we recover the usual GAM dispersion relation, with  $J_2$  becoming  $I_2$ . The GAM is located at  $\Omega_{\text{GAM}} = 3.1 - 0.02i$ .

$$D_{\text{GAM}}(\Omega, P, \mathcal{J}) = \frac{1}{q^2} - \frac{I_2}{2} - \frac{I_1^2}{2 \left( \tau + \frac{P^2}{q^2} - I_3 \right)} \quad (6.58)$$

For  $P/s$  far from  $\Omega_{\text{GAM}}$ , the zero due to the zonostrophic instability provides an unstable mode with growth rate  $\Gamma = 0.01$ , and is located near the resonance position  $\Omega = P/s$ . For  $P = 3$ , the two zeros interact. The zonostrophic instability is further destabilised at  $\Omega = 2.8 + 0.35i$ , while the GAM is strongly damped at  $\Omega = 2.8 - 0.38i$ . This example does not contain a linear growth rate for the turbulent structures, so the growth of the zonal flow comes from pumping energy from turbulence.

It is straightforward to extend the relation dispersion 6.56 to handle EGAMs (Girardo, 2015). The same plot can be done with a population of 7% of energetic particles going at 2.8 times the

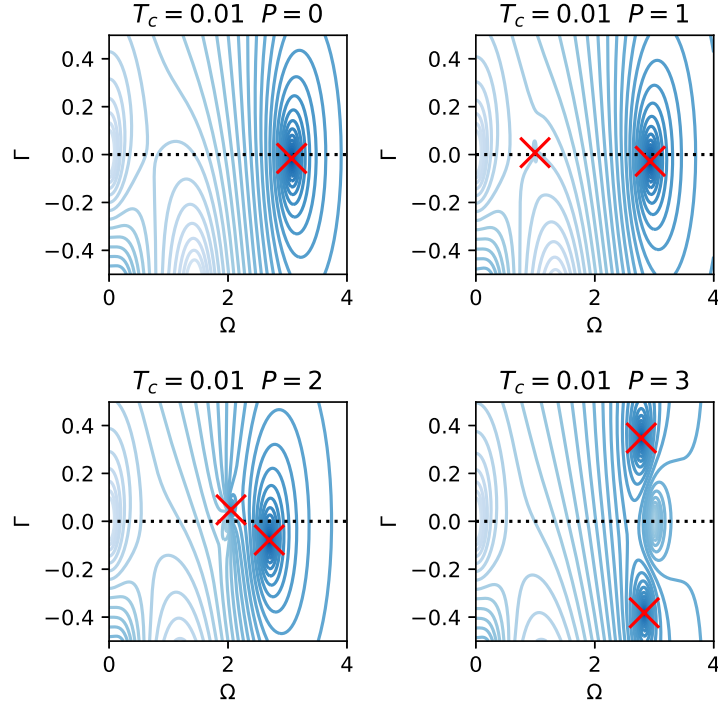


Figure 6.1: Contour lines of  $|D_G|$  for  $q = 1.6$  and  $s = 1$ .  $A = S = 0$ . The GAM frequency is  $\Omega = 3.07 - 0.02i$ . The zeros are in dark blue. The zeros due to the zonal instability is highlighted by a red cross.

thermal velocity, figure 6.2. The EGAM lies at  $\Omega = 2.5 + 0.07i$ . For  $P = 2.5$ , the zonal instability interacts with it. The EGAM is stabilised at  $\Omega = 2.4 - 0.17i$ , while the zonal mode is destabilised to  $\Omega = 2.3 + 0.24i$ . This behaviour is consistent with the observations from (Zarzoso *et al.*, 2013): the avalanche synchronises at the EGAM frequency when energetic particles are present.

If we add a non-zero background zonal shear, we expect the system to develop an asymmetry depending on the sign of  $\Omega$ . This is not the case without a turbulent growth rate. Turbulent structures are allowed to travel the full poloidal plane. The system is symmetric in phase velocity, and does not prefer a direction over the other. This is a consequence of the joint symmetry principle (Hwa & Kardar, 1992; Diamond & Hahm, 1995). In order to regain the asymmetry, we need to take into account the differential growth between the two sides. The damping on the high-field side cuts the poloidal travel of the turbulent structures. We add a growth rate  $\gamma = \alpha \cos \zeta$  to equation 6.39. The  $\alpha$  coefficient constrains a localised growth of the turbulence on the low-field-side. This effectively expresses the intensity growth where the instability growth is maximum. The  $J_2$  function becomes

$$J_2 = I_2 - \frac{P^2/s}{\Omega^2 + 2A^2 - S^2 - P^2/s^2} \left[ \left( 1 - \frac{ASs}{\Omega P} \right) \mathcal{J}_c - i \left( \frac{S}{\Omega} - \frac{As}{P} \right) \mathcal{J}_s \right] \quad (6.59)$$

where  $A = \alpha/u_{\text{TR}}$ . By introducing  $A \neq 0$ , the structures are damped when arriving at the high-field side. The symmetry between  $\zeta > 0$  and  $\zeta < 0$  is broken, and the instability can develop with a preferred direction. We consider this modified system with  $A = S = 2$ . The dispersion relation for  $P = 3$  is shown figure 6.3. The two instabilities are located at  $\Omega = -2.3 + 0.41i$  and  $\Omega = 2.3 + 0.11i$ . The direction is consistent with the observed inwards avalanches for positive zonal flow shear. Contrary to (Sasaki *et al.*, 2018a), we do not need to introduce an ad-hoc up-down asymmetry of the turbulent spectrum, it is generated self-consistently by the ballooned growth rate and the background flow shear. Although the wave-particle energy exchange is not self-consistent for  $\alpha \neq 0$ , the instability mechanism already exists in the self-consistent  $\alpha = 0$  case. As a result,

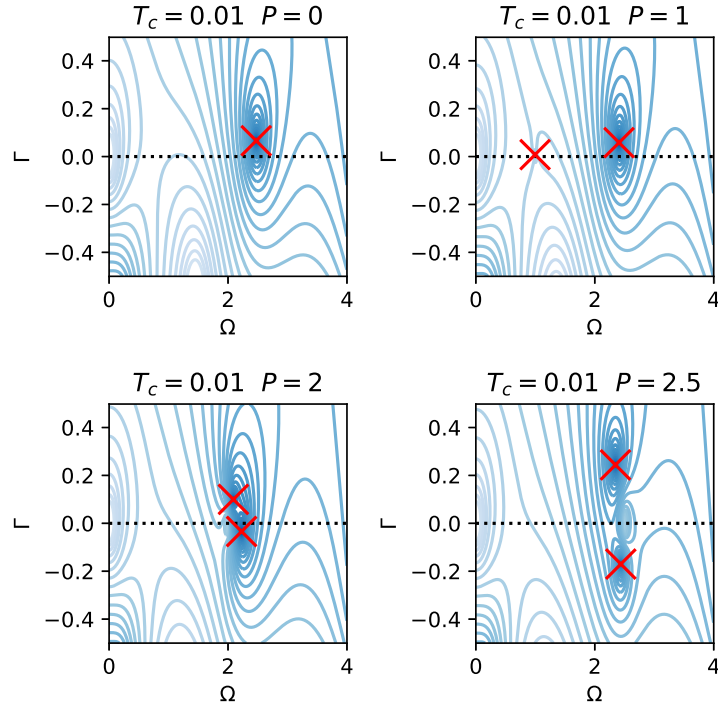


Figure 6.2: Contour lines of  $|D_G|$  for  $q = 1.6$  and  $s = 1$  with 7% energetic particles at 2.8 times the thermal velocity.  $A = S = 0$ . The EGAM frequency is  $\Omega = 2.47 + 0.07i$ . The zeros are in dark blue. The zeros due to the zonostrophic instability is highlighted by a red cross.

the computed instability is not spurious, but a modification of the former case.

## 6.6 Conclusion

In order to study the zonostrophic instability in toroidal plasmas, we developed a self-consistent and conservative formulation of the wave-kinetic equation coupled to a background plasma. This formulation is parameterised by the dispersion relation for the underlying turbulent linear wave, but is restricted to marginally stable modes. It is usable both in slab and toroidal geometry. This conservative formulation has been used to investigate the effect of toroidal geometry on the generation of zonal flows.

In toroidal geometry, as we have shown in paragraph 5, the zonal flows affect turbulent cells by moving them toroidally, and by shearing them. This shearing acts by moving the turbulent cells in the poloidal direction, making them ballooned above or below the mid-plane. As the toroidal drift velocity depends on the ballooning angle of turbulence, the ITG mode frequency follows the same dependency. Since the ballooning angle is related to the radial mode number of the turbulent cell, this induces a radial group velocity of the turbulent cells, mostly following the ion direction.

The generic zonostrophic instability carries over from slab to toroidal geometry. It is driven by the modulation of the drift-wave turbulence by a sheared zonal flow. This generic instability has its phase velocity close to the radial group velocity of the underlying turbulence. In toroidal geometry, the zonal flow responds according to the GAM dynamics, with a specific radial phase velocity. When the radial motion of turbulent cells resonates with the GAM radial phase velocity, the zonostrophic instability and the GAM interact. The zonostrophic instability is further destabilised, and the GAM has stronger damping. This mechanism could be responsible for the avalanche behaviour. It is able to explain the typical frequency of avalanches, close to the GAM frequency. Furthermore, it is able to reproduce the synchronisation to EGAM frequency (Zarzoso *et al.*, 2013). When a background zonal flow shear is present, a ballooned turbulence has an up-down

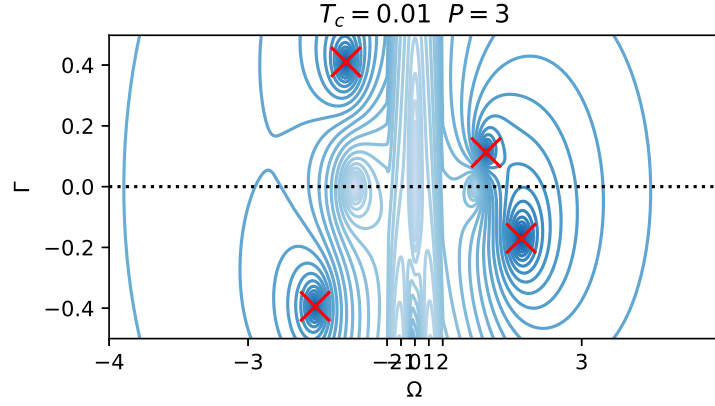


Figure 6.3: Contour lines of  $|D_G|$  for  $q = 1.6$  and  $s = 1$ .  $A = S = 2$ . The unstable inwards mode  $\Omega < 0$  is more unstable than the outwards one. The  $-2 < \Omega < 2$  region has been compressed to help visualisation in the  $2 < |\Omega| < 4$  regions.

asymmetry. The footprint of this asymmetry gets carried over to the avalanches by preferring the same propagation direction.

The resulting coupled instability develops at a resonance between the GAM frequency and the radial magnetic drift. As a consequence, the resonant radial wave-number  $k_r \rho_i$  is a few times  $s/q^2$ . In the weak magnetic shear regime,  $k_r \rho_i$  is a fraction of a unit, the radial scale separation between turbulence and GAMs is only marginally verified. Slower branches of GAMs, like trapped particles driven and precession driven (Sasaki *et al.*, 2016), may provide a more reasonable radial scale.

The non-linear regime with an established GAM has been described by (Sasaki, 2018; Sasaki *et al.*, 2018*b,a*). An extreme in the flow can act as a trap in phase space for turbulent cells. The toroidal drift wave phase velocity can be approximated as

$$c \approx -qu_E + \delta_n \Omega_d(\zeta) \approx c_0 - \frac{1}{2}(qu_E)''(r - r_0)^2 - \delta_n \Omega_d(\zeta) \frac{\zeta^2}{2}$$

For maxima of the flow,  $(qu_E)'' > 0$ , the phase velocity is a potential well, turbulent structures may become trapped. This corresponds to the increased correlation time featured on figure 5.7c. On the contrary, for minima of the flow,  $(qu_E)'' < 0$ , the phase velocity has a saddle point, turbulent structures are expelled. This corresponds to the increased radial correlation on figure 5.7d. By trapping turbulence inside its lobes, a GAM can carry it to a stable region, providing an effective turbulence spreading mechanism (Miki & Diamond, 2010; Sasaki *et al.*, 2017). The same generic mechanism exists for stationary zonal flow (Zhu *et al.*, 2020): the stability of the zonal flow pattern depends on the sign of the curvature. The formalism developed in this chapter should be extended to account for these additional phenomena. The idea of trapping relies on an eikonal description of the system. These trapped eikonal waves actually correspond to stationary radially-coherent waves inside the trap (McDonald, 1988). Lifting the eikonal hypothesis may provide useful insight into the nature of non-linear cooperative structures between GAMs and turbulence.

## Chapter 7

# Electromagnetic effects in GYSELA

Plasma core turbulence is strongly affected by the behaviour of the plasma edge (Dif-Pradalier *et al.*, 2017a; Caschera, 2019). In order to get a self-consistent simulation of the plasma, the different effects in this region need to be accounted for. Among them, electromagnetic effects come into play because of the strong density gradient in the edge. More importantly, the instabilities inside the H-mode pedestal are expected to have a strong magnetic component (Hamed, 2019).

The present version of GYSELA handles the self-consistent evolution of multiple particle species, including electrons, and of the electrostatic potential. The current push towards more integrated simulations of the interplay between core and edge turbulence requires alleviating the electrostatic hypothesis. Furthermore, the simulation of fully kinetic electron dynamics in the electrostatic regime are plagued by the so-called  $\omega_H$  mode. This  $\omega_H$  mode happens to be the electrostatic limit of Alfvén eigenmodes, for infinite Alfvén velocity. Successful simulation of fully electron dynamics therefore require electromagnetic effects.

### 7.1 Statement of the problem

In the electrostatic description, we consider a stationary magnetic field  $\vec{B} = B\vec{b}$ . Our objective here is to introduce fluctuations of this magnetic field. More precisely, we are interested by the magnetic fluctuations carried by the parallel component of the magnetic vector potential  $\psi = \vec{b} \cdot \delta\vec{A}$ . The associated Vlasov equation has been derived paragraph 2.1.6. It features additional terms in the equations of motion compared to the electrostatic version. Those additional terms are due to the deformation of the magnetic field lines  $\delta\vec{B} = \vec{\nabla} \times (\psi\vec{b})$ , and to the acceleration by the parallel electric potential  $E_{\parallel} = -\partial_t\psi - \nabla_{\parallel}\phi$ . For convenience, the equations of motion are reproduced

$$B_{\parallel}^* \dot{\vec{X}} = v\vec{B}^* + \vec{b} \times \vec{\nabla} \left[ \frac{\mu B}{e} + J[\phi - u\psi] \right] \quad (7.1)$$

$$mB_{\parallel}^* \dot{u} = -\vec{B}^* \cdot \vec{\nabla} [\mu B + eJ[\phi - u\psi]] \quad (7.2)$$

$$v = u - \frac{e}{m} J[\psi] \quad (7.3)$$

$$\vec{B}^* = \vec{B} + \frac{m\mu}{e} \nabla \times \vec{b} \quad (7.4)$$

where  $v = \vec{b} \cdot \dot{\vec{X}}$  is the “symplectic” gyro-centre parallel velocity, and  $m\mu$  its parallel Hamiltonian momentum. The magnetic field in those equations is the equilibrium magnetic field, and the perturbations appear explicitly through  $\psi$ . The perturbed magnetic potential  $\psi$  is given by the Ampère equation 7.6. In full generality, the Poisson and Ampère equations are coupled, but

decouple when the plasma is at rest  $0 = \sum_s m_s n_s V_{||,s}$ , as discussed paragraph 2.1.6.

$$-\operatorname{div}_\perp \left( \sum_{\text{species}} \frac{m n_0}{B^2} \nabla_\perp \phi \right) = \sum_{\text{species}} e \int J^\dagger [F B_{||}^*] d u d \mu \quad (7.5)$$

$$-\mu_0^{-1} \nabla_\perp^2 \psi + \sum_{\text{species}} \frac{n_0 e^2}{m} \psi = \sum_{\text{species}} e \int u J^\dagger [F B_{||}^*] d u d \mu - \mathcal{G}_{||,\text{eq}} \quad (7.6)$$

$$\beta = \frac{\mu_0 n_0 T_0}{B^2} \quad (7.7)$$

with  $\mathcal{F} = F B_{||}^*$  the gyro-centre distribution function, and  $J_{||,\text{eq}}$  is the current generating the equilibrium magnetic field. The Poisson equation keeps exactly the same form as for the electrostatic case. The second term in the Ampère equation is responsible for the magnetic skin effect. This makes the typical length scale of magnetic fluctuations of the order of the electron skin depth  $\delta_e = \rho_e / \sqrt{\beta}$ , where  $\rho_e$  is the electron Larmor radius. The  $\beta$  parameter is the ratio of kinetic to magnetic pressure. It quantifies the strength of magnetic perturbations:  $\psi$  scales like  $\beta$ . The limiting case of  $\beta = 0$  corresponds to the electrostatic case, where magnetic fluctuations are dwarfed by the background field.

### 7.1.1 Magnetic cancellation

The model can also be formulated using of the symplectic velocity  $v$  as a variable, instead of  $u$ . In that case, the skin term in the Ampère equation vanishes. Meanwhile, the equations of motion change, and depend on  $\partial_t \psi$ . The Lagrangian writes

$$\mathcal{L} = m v \vec{b} \cdot \dot{\vec{X}} + e \vec{A} \cdot \dot{\vec{X}} + e J[\psi] \vec{b} \cdot \dot{\vec{X}} - \frac{m}{2} v^2 - \mu B - e J[\phi] \quad (7.8)$$

$$B_{||}^* \dot{\vec{X}} = v \vec{B}^* + \vec{b} \times \vec{\nabla} \left[ \frac{\mu B}{e} + J[\phi] \right] \quad (7.9)$$

$$m B_{||}^* \dot{v} = -\vec{B}^* \cdot \vec{\nabla} [\mu B + e J[\phi]] - e B_{||}^* \partial_t \psi \quad (7.10)$$

$$\vec{B}^* = \vec{B} + \vec{\nabla} \times (\psi \vec{b}) + \frac{m u}{e} \nabla \times \vec{b} \quad (7.11)$$

$$-\mu_0^{-1} \nabla_\perp^2 \psi = \sum_{\text{species}} e \int v J^\dagger [F B_{||}^*] d v d \mu \quad (7.12)$$

There are three main changes. First, the magnetic field line bending terms have moved, from the gradient of the Hamiltonian in 7.1–7.2 to the effective magnetic field  $\vec{B}^*$ . Second, the skin term in the Ampère equation disappears. Third, the time derivative  $\partial_t \psi$  enters the equation. This is a major drawback: we would need a semi-implicit gyro-kinetic solver. GYSELA is inherently an explicit code. This alone means the symplectic coordinate system is a no-go.

The Ampère equation 7.6 as written is linear and solvable. However, it tends to be numerically challenging and prone to inaccurate solutions, due to the so-called gyro-kinetic magnetic cancellation (Cummings, 1996). In the Maxwell–Ampère equation 7.12, the relevant magnetic source is the current due to the charge motion, given by  $v$ . The “real” parallel current is

$$\mathcal{G}_{||} = \sum_{\text{species}} e \int v J^\dagger [\mathcal{F}] d v d \mu \quad (7.13)$$

$$\begin{aligned} &= \sum_{\text{species}} e \int \left( u - \frac{e}{m} \psi \right) J^\dagger [\mathcal{F}] d u d \mu \\ &\approx \sum_{\text{species}} e \int u J^\dagger [\mathcal{F}] d u d \mu - \frac{n_s e^2}{m} \psi \end{aligned} \quad (7.14)$$

where the last equality neglects the gyro-averaging. This current can be thought as the difference between the currents carried by two distribution functions, centred at two different positions, as

illustrated figure 7.1. The two components in equation 7.14 expected to be large, and to cancel out, resulting in a smaller real current 7.13. This is the magnetic cancellation.

The choice of the  $u$  variable tends to move the distribution function in the velocity grid. For the GYSELA storage of the distribution function, this comes as a serious risk of code breakdown: for larger values of  $\psi$ , the distribution function may get out of its velocity-space grid [A. Bottino, private communication]. For a typical GYSELA grid, this happens when  $e\psi$  reaches  $\sqrt{m_e T_{\text{ref}}}$ . This corresponds to a magnetic fluctuation of the order of  $\delta B/B \sim \rho_e k_{\perp}$ . Considering magnetic instabilities develop at  $k_{\perp} \sim 1/\delta_e$ , this amounts to  $\delta B/B \lesssim \rho_e/\delta_e = \sqrt{\beta}$ . This is actually a tight upper bound for purely numerical stability, notably in the non-linear regime where  $\delta B/B$  already approaches  $\beta \sim 1\%$ .

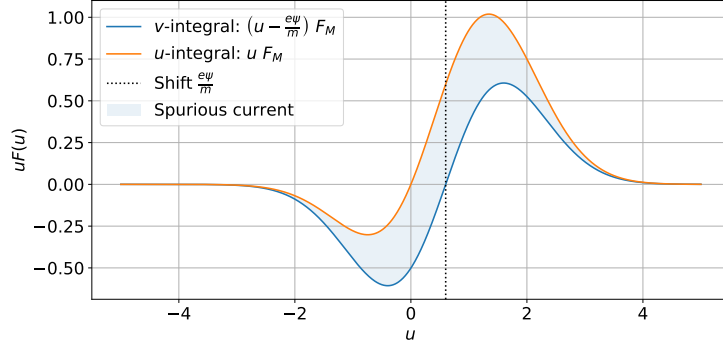


Figure 7.1: Illustration of the spurious shift in the parallel distribution function when formulated in the momentum variable  $u$ . Plain lines are the current integrals in 7.13 and 7.14 respectively. Chosen distribution function is  $F_M = \exp\left(-\frac{m}{2T}\left(u - \frac{e\psi}{m}\right)^2\right)$ . We chose  $\frac{e\psi}{m} = 0.6v_{\text{th}}$ .

### 7.1.2 Methods from the other codes

In the literature, the problem has been cured for  $\delta F$  and PIC codes. For  $\delta F$  codes, the magnetic flux  $\psi$  is assumed to remain small. Their coordinate of choice is the symplectic velocity  $v$ . The Vlasov equation is solved by introducing a modified distribution function  $g$

$$g = f - \frac{e}{m} J[\psi] \partial_v \mathcal{F}_{\text{eq}}$$

Rewriting the Vlasov equation with  $g$  effectively removes the  $\partial_t J[\psi]$ , and avoids an implicit scheme. This essentially corresponds to solving the Vlasov equation in Hamiltonian coordinates, and approximating  $v \approx u$  in the equations of motion.

The historical method in ORB5 is due to Hatzky (Hatzky *et al.*, 2007). PIC codes are especially sensitive to inaccuracy because of the sampling noise they contain. Their method is centred on a better computation of the skin term: it is replaced by a numerical integration on the locally present particles,

$$\frac{e^2}{m} n_0 \approx \frac{e^2}{m} \sum_u n_0 \frac{u^2}{v_{\text{th}}^2} \mathcal{F}_M(u)$$

with  $\mathcal{F}_M$  the reference Maxwellian distribution function. The accuracy of the density in the Ampère skin term is deemed critical in both GENE (Görler *et al.*, 2011), GWK (Peeters *et al.*, 2007) and GYRO (Candy & Waltz, 2003b). The skin term is computed numerically using the same velocity grid as the distribution function. This ensures a consistent numerical scheme, and cancellation of the spurious current including its own discretisation error. For the time being, GYSELA uses a Fourier-based scheme for solving the Poisson and Ampère equations. Therefore, we have to use a skin term which is uniform on flux-surfaces. For numerical simplicity, we ignore their advice, and use the analytical value for the skin term. However, the degraded accuracy may reveal a prohibitive price, and in that case will need proper treatment. This will have a consequence in the

expression of the conserved energy 7.32. This limitation is being removed with recent progress on non-circular geometry and a 2D Poisson solver.

Furthermore, the position of the gyro-average operator in the different terms depends on the code. For instance GENE and GKW gyro-average  $\psi$  in the skin term. This adds a  $\beta_{\perp}$  term in the permeability term, which is of the same order as the  $\beta_{\parallel}$  we neglected earlier. Taking this term into account would be a numerically costly for Ampère solvers based on direct matrix inversion, as the sparsity of the matrix is significantly degraded. Nevertheless, ongoing work on the GYSELA Poisson solver may render this possible.

### 7.1.3 Change of variable scheme

Recent works in EUTERPE and ORB5 have developed a new method based on a change of variable scheme (Mishchenko *et al.*, 2014*b,a*; Kleiber *et al.*, 2016; Mishchenko *et al.*, 2017, 2019). The idea is the following: magnetic cancellation is due to the distribution function shifting in  $u$  space. Meanwhile, the equations of motion in variable  $v$  require knowledge of  $\partial_t \psi$ .

#### Hand-waving explanation

The problem with equation 7.10 lies in the presence of the time derivative of  $\psi$ . Let us discretise the equations of motion explicitly at first order

$$\vec{X}_{t+\Delta t} - \vec{X}_t \approx \Delta t \dot{\vec{X}} \left( t + \frac{\Delta t}{2}, \vec{X}_t, v_{t+\frac{\Delta t}{2}} \right) \quad (7.15)$$

$$v_{t+\frac{3\Delta t}{2}} - v_{t+\frac{\Delta t}{2}} \approx \Delta t \dot{v} \left( t + \Delta t, \vec{X}_{t+\Delta t}, v_{t+\frac{\Delta t}{2}} \right) \quad (7.16)$$

$$\approx -\Delta t \frac{\vec{B}^*}{mB_{\parallel}^*} \cdot \vec{\nabla}[\mu B + eJ[\phi]] - \frac{e}{m} J[\psi_{t+\Delta t} - \psi_t] \quad (7.17)$$

One difficulty in this formulation lies in the computation of the current at  $t + \Delta t$  in order to get  $\psi_{t+\Delta t}$ . The time stepping for the velocity can be further split into the following

$$v_{t+\Delta t} - v_{t+\frac{\Delta t}{2}} = -\frac{\Delta t}{2} \frac{\vec{B}^*}{mB_{\parallel}^*} \cdot \vec{\nabla}[\mu B + eJ[\phi]] \quad (7.18)$$

$$v'_{t+\Delta t} - v_{t+\Delta t} = -\frac{e}{m} J[\psi_{t+\Delta t} - \psi_t] \quad (7.19)$$

$$v_{t+\frac{3\Delta t}{2}} - v'_{t+\Delta t} = -\frac{\Delta t}{2} \frac{\vec{B}^*}{mB_{\parallel}^*} \cdot \vec{\nabla}[\mu B + eJ[\phi]] \quad (7.20)$$

The first and third equations are electrostatic half pushes. The current can be computed using the position  $\vec{X}_{t+\Delta t}$  and the velocity  $v_{t+\Delta t}$ . The second equation can be thought as a change of variable, shifting the definition of  $v_{t+\Delta t}$  by  $\frac{e}{m} J[\psi_{t+\Delta t} - \psi_t]$ .

In the point of view of particle pushing, everything is contained in the above three equations. The subtlety arises when deciding which Ampère equation should be used to obtain a self-consistent semi-Lagrangian scheme. The following section resolves this ambiguity by introducing separate variables for the magnetic perturbation used in the advection, called  $\psi_s$ , and for the shift in equation 7.19,  $\psi_h = \psi_{t+\Delta t} - \psi_t$ .

#### Formal definition

Both magnetic cancellation and semi-implicitness can be cured by introducing an additional degree of freedom. We decompose the vector potential into a symplectic component  $\psi_s$  and a Hamiltonian component  $\psi_h$ . We introduce a mixed velocity coordinate  $w$  as

$$w = u - \frac{e}{m} J[\psi_s] = v + \frac{e}{m} J[\psi_h] \quad (7.21)$$

$$\psi = \psi_h + \psi_s \quad (7.22)$$

The equation of motion derive from the following Lagrangian

$$\begin{aligned}\mathcal{L} &= mw\vec{b} \cdot \dot{\vec{X}} + eJ[\psi_s]\vec{b} \cdot \dot{\vec{X}} + e\vec{A} \cdot \dot{\vec{X}} - \mathcal{H} \\ \mathcal{H} &= \frac{mw^2}{2} + \mu B + eJ[\phi] - ewJ[\psi_h]\end{aligned}$$

Their explicit form is

$$B_{\parallel}^* \dot{\vec{X}} = \left(w - \frac{e}{m}J[\psi_h]\right) \vec{B}^* + \frac{\vec{b}}{e} \times \vec{\nabla} \mathcal{H} \quad (7.23)$$

$$mB_{\parallel}^* \dot{w} = -\vec{B}^* \cdot \vec{\nabla} \mathcal{H} - eB_{\parallel}^* J[\partial_t \psi_s] \quad (7.24)$$

$$\vec{B}^* = \vec{B} + \frac{mw}{e} \nabla \times \vec{b} + \frac{m}{e} \nabla \times (J[\psi_s] \vec{b}) \quad (7.25)$$

As earlier, we need to know  $\partial_t \psi_s$ . Except this once, we have an available degree of freedom in the splitting  $\psi = \psi_s + \psi_h$ . We can chose whatever form we like for  $\partial_t \psi_s$ . The actual evolution of  $\psi$  is obtained by solving the Ampère equation for  $\psi_h$ . As such,  $\psi_s$  serves as a background magnetic perturbation for which we guess the evolution, while  $\psi_h$  gives the correct evolution of this perturbation by the Vlasov dynamics. Using the Boussinesq approximation for the skin term, the variational principle can be written as

$$\begin{aligned}\mathcal{S} &= \int \mathcal{L} \mathcal{F} d^3 \vec{X} dwd\mu + \int \frac{m\mathcal{N}_0}{2B^2} [\nabla_{\perp} \phi]^2 d^3 \vec{X} \\ &- \int \frac{\mu_0^{-1}}{2} [\nabla_{\perp} \psi_s + \nabla_{\perp} \psi_h]^2 d^3 \vec{X} - \int \frac{n_0 e^2}{2m} \psi_h^2 d^3 \vec{X}\end{aligned} \quad (7.26)$$

Cancelling the variations of  $\mathcal{S}$  with respect to  $\psi_h$  implies the following Ampère equation

$$-\mu_0^{-1} \nabla_{\perp}^2 (\psi_h + \psi_s) + \sum_{\text{species}} \frac{n_0 e^2}{m} \psi_h = \sum_{\text{species}} e \int w J^{\dagger} [F B_{\parallel}^*] dwd\mu - J_{\parallel, \text{eq}} \quad (7.27)$$

We emphasise the presence of both components  $\psi_h + \psi_s$  in the Laplacian term, while only the Hamiltonian component  $\psi_h$  appears in the skin term. The  $\nabla^2 \psi_s$  term acts as a current in the right-hand side of the equation. It contains the current already mobilised into generating  $\psi_s$ , so that  $\psi_h$  is generated only by the newly available current. We draw attention to the  $B_{\parallel}^*$  jacobian in the right-hand side of 7.27: it depends on  $\psi_s$ . To the contrary, the equilibrium current is a static value. It has to be evaluated with  $\psi_s = 0$ , with the equilibrium  $B_{\parallel, \text{eq}}^*$ , so as to always keep the same value.

$$J_{\parallel, \text{eq}} = \sum_{\text{species}} e \int v J^{\dagger} [F_{\text{eq}} B_{\parallel, \text{eq}}^*] dv d\mu$$

The strength of this approach comes from the following: by controlling the magnitude of  $\psi_h$ , the magnetic cancellation can be managed. The simplest way to achieve that is to use  $\psi_s$  as an accumulator for  $\psi_h$ : at each time step, increment  $\psi_s$  by  $\psi_h$ , and reset  $\psi_h$  to zero. From the point of view of the Vlasov equation, this resetting is a change of variable, moving from  $w^{\text{old}} = v + \frac{e}{m} J[\psi_h^{\text{old}}]$  to  $w^{\text{new}} = v + \frac{e}{m} J[\psi_h^{\text{new}}] = v$ . This change of variable is exactly the one in equation 7.19 with different notations. Since we suppose  $\psi_h$  to be of order  $\Delta t$ , we drop it from the equations of motion. As a result, the modification of the equations of motion only happens through the distortion of the effective magnetic field  $\vec{B}^*$ . The general algorithms is therefore:

1. Start a time step with  $\psi_s = \psi$  and  $\psi_h = 0$ .  
The distribution  $F$  is discretised in a  $w$  grid, with  $w = v + \frac{e}{m} J[\psi_h] = v$ .
2. Perform the Vlasov advection with equations 7.23–7.25.  
Now,  $F$  is still discretised with a  $w$  grid, but  $w = v + \frac{e}{m} J[\psi_h] \neq v$  where  $\psi_h \neq 0$  is unknown.
3. Solve the Ampère equation 7.27 to find  $\psi_h$ .

4. Change the variable, while keeping  $\psi = \psi_s + \psi_h$  and  $v = w - \frac{e}{m}J[\psi_h]$  constant

$$\psi_s^{\text{new}} = \psi_s^{\text{old}} + \psi_h^{\text{old}} \quad (7.28)$$

$$\psi_h^{\text{new}} = 0 \quad (7.29)$$

$$w^{\text{new}} = w^{\text{old}} - \frac{e}{m}J[\psi_h^{\text{old}}] \quad (7.30)$$

$$F^{\text{new}}(w^{\text{new}}) = F^{\text{old}}\left(w^{\text{old}} = w^{\text{new}} + \frac{e}{m}J[\psi_h^{\text{old}}]\right) \quad (7.31)$$

During a time step, the coordinate  $w$  essentially works as the Hamiltonian coordinate  $u$ . The whole distribution function gets shifted by  $J[\psi_h]$ . At the end of the time step, the Ampère equation solves for  $\psi_h$ . The spurious current  $ne^2\psi_h/m$  is of the order of  $\Delta t$  and much smaller than the full  $ne^2\psi/m$ , so *a priori* more manageable for numerical accuracy. Then, we change the variable  $w^{\text{old}}$  to  $w^{\text{new}}$ . This change of variable displaces the distribution function in velocity space, so as to centre it around the correct gyro-centre mean velocity  $V_{||}$ .

### 7.1.4 Boundary conditions

We need boundary conditions to solve the Poisson and Ampère equations. This requires choosing a model for the tokamak wall. This question is not precisely addressed in the literature. Local codes tend to use radially periodic boundary conditions (Peeters *et al.*, 2007; Görler *et al.*, 2011). Many global codes have decided to use a buffer region as “benign” boundary conditions (Candy & Waltz, 2003b; Bottino *et al.*, 2010; Görler *et al.*, 2011; Candy & Belli, 2015).

We chose a perfectly conducting wall: the electric field along the wall is zero. This can be written as the vanishing of both toroidal and poloidal components as

$$\begin{aligned} 0 = E_\varphi &= -b_\varphi \partial_t \psi - \partial_\varphi \phi \\ 0 = E_\theta &= -b_\theta \partial_t \psi - \partial_\theta \phi \end{aligned}$$

This implies the vanishing of both  $\psi_h = \Delta t \partial_t \psi$  and  $\phi$ .

### 7.1.5 Conserved quantities in mixed variables

Using the action principle 7.26, we can formulate conserved quantities as in paragraph 2.1.7. The conservation of the energy  $\mathcal{E}$  writes

$$\begin{aligned} 0 &= \partial_t \mathcal{E} + \text{div } \Gamma_\mathcal{E}^r \\ \mathcal{E} &= \sum_s \int \left[ \frac{mw^2}{2} + \mu B + eJ[\phi] - ewJ[\psi_h] \right] \mathcal{F} dw d\mu dS_{\text{FS}} \\ &\quad - \int \frac{mN_0}{2B^2} [\nabla_\perp \phi]^2 dS_{\text{FS}} + \int \frac{\mu_0^{-1}}{2} [\nabla_\perp \psi_s + \nabla_\perp \psi_h]^2 dS_{\text{FS}} + \int \frac{N_0 e^2}{2m} \psi_h^2 dS_{\text{FS}} \\ &= \sum_s \int \left[ \frac{m \left( u - \frac{e}{m} J[\psi_h] \right)^2}{2} + \mu B \right] FB_{||}^* dw d\mu dS_{\text{FS}} \\ &\quad + \int \frac{mN_0}{2B^2} [\nabla_\perp \phi]^2 dS_{\text{FS}} + \int \frac{[\nabla_\perp \psi_s + \nabla_\perp \psi_h]^2}{2\mu_0} dS_{\text{FS}} \\ &\quad + \sum_s \frac{e^2}{2m} \left[ \int \psi_h^2 n_{0,s} dS_{\text{FS}} - \int J[\psi_h]^2 FB_{||}^* dw d\mu dS_{\text{FS}} \right] \\ \Gamma_\mathcal{E}^r &= \sum_s \int \left[ \frac{mw^2}{2} + \mu B + eJ[\phi] - ewJ[\psi_h] \right] \dot{r} FB_{||}^* dw d\mu dS_{\text{FS}} \end{aligned} \quad (7.32)$$

with  $S_{\text{FS}}$  the flux-surface surface element. The equation has sensibly the same form as in paragraph 2.1.7: the sum of the kinetic energy of particles  $mv^2/2 + \mu B$ , the polarisation energy density, and the magnetic field self-energy. The extra term in  $\psi_h^2 - J[\psi_h]^2$  comes from our approximation in the treatment of the magnetic skin term in the Ampère equation. In the long-wavelength limit,

this term is positive and proportional to  $T_\perp[\nabla_\perp\psi_h]^2$ , so should create additional instabilities. The conservation of the toroidal momentum becomes

$$\begin{aligned} 0 &= \partial_t \mathcal{P} + \operatorname{div} \Gamma_\varphi^r \\ \mathcal{P} &= \sum_s \int [m v b_\varphi + e J[\psi_s] b_\varphi + e A_\varphi] F B_{||}^* d w d \mu d S_{\text{FS}} \\ \Gamma_\varphi^r &= \sum_s \int [m v b_\varphi + e J[\psi_s] b_\varphi + e A_\varphi] \dot{r} F B_{||}^* d w d \mu d S_{\text{FS}} \end{aligned}$$

## 7.2 Application to GYSELA

GYSELA is a backwards semi-Lagrangian code. In order to compute the distribution function  $\mathcal{F}$  at a time  $t$ , it tracks where each point on the phase space grid was at  $t - \Delta t$  by following the trajectory backwards in the 4D phase space  $r, \theta, \varphi, v_{||}$  ( $\mu$  is an invariant), and interpolates the former distribution function. The computation of the backwards trajectories is done explicitly using the potential computed from the distribution at  $t - \Delta t$ . This scheme is essentially performing a change of variables at each time step, in the shape of a map  $(r, \theta, \varphi, v_{||})_{t, \mu} \mapsto (r, \theta, \varphi, v_{||})_{t + \Delta t, \mu}$ .

The GYSELA main loop does four things<sup>1</sup>: evolve the distribution function, compute the potential, compute and store the diagnostics, and finally save the distribution function for restart. The first two steps are actually repeated in a prediction–correction sub-loop. The evolution of the distribution function is split into advections in different directions. The general algorithms can be summarised as follows

1. Start a time step with the distribution function  $\mathcal{F}$
2. Prediction–correction sub-loop:
  - (a) Copy  $\mathcal{F}$  into  $\mathcal{G}$
  - (b) Half-advection in  $v$  for  $\mathcal{G}$
  - (c) Half-advection in  $\varphi$  for  $\mathcal{G}$
  - (d) Advection in  $(r, \theta)$  for  $\mathcal{G}$
  - (e) Half-advection in  $\varphi$  for  $\mathcal{G}$
  - (f) Half-advection in  $v$  for  $\mathcal{G}$
  - (g) Solve Poisson equation for  $\phi$  from  $\mathcal{G}$
3. Compute diagnostics on  $\mathcal{G}$
4. Save the restart file on  $\mathcal{G}$
5. Swap  $\mathcal{F}$  and  $\mathcal{G}$ , and loop.

To make modifications granular, electromagnetic GYSELA is controlled by three parameters. `solve_Ampere` enables and disables the solving of the Ampère equation. `beta_toro` provides the value of the  $\beta = \mu_0 N_0 T_0 / B_0^2$  parameter, which specifies  $\mu_0$  in equation 7.6 ( $N_0$ ,  $T_0$  and  $B_0$  are the reference density, temperature and magnetic field). `advec_Ampere` enables and disables the effect of  $\psi$  in the equations of motion. Having `solve_Ampere` and `advec_Ampere` separate allows to test separately the Ampère solver and the advection. Most notably, enabling only `solve_Ampere` allows to verify the implementation of the Ampère equation without polluting the time stepper. Conversely, enabling only `advec_Ampere` allows to check for difficulties in data communications. As an extension, the same mode will allow to study the effect of a static magnetic island on the plasma.

In this paragraph, we will use the normalisation and naming from the code. `Phi` is the scalar potential  $\phi$  normalised to the thermal potential  $T_0/Z_0$ . `Apar` and `Apar_diff` are the symplectic

<sup>1</sup>For simplicity, we chose not to discuss additional operators like diffusion, Krook damping and collisions, nor alternate schemes like aligned coordinates (Latu *et al.*, 2017). The extension to these is straightforward.

$\psi_s$  and Hamiltonian  $\psi_h$  parts of the parallel vector potential, normalised to with  $\sqrt{A_0 T_0}/Z_0$ . The full parallel vector potential is thus  $\psi = \text{Apar} + \text{Apar\_diff}$ . The GYSELA parallel velocity grid `vparg` is normalised to the species thermal velocity  $\sqrt{T_0/A_s}$ . In consequence, it must be divided by  $\sqrt{\text{hatAs}} = \sqrt{A_s/A_0}$  to obtain the velocity in the  $\sqrt{T_0/A_0}$  dimension. We denote the normalised charge `hatZs` =  $Z_s/Z_0$ .

In the electrostatic version, there is only one velocity coordinate,  $v = u = w$ . In the electromagnetic case, the three are different. We re-purpose the GYSELA velocity grid `vparg` to be a uniform grid in  $w$ . As  $w$  is a moving target when we change the definition of  $\psi_s$  and  $\psi_h$ , we will specify when to interpret the grid as in  $w^{\text{old}}$  versus  $w^{\text{new}}$ .

### 7.2.1 Modifications to data structures

The algorithm in the previous section has been simplified for brevity. For instance, concerns about data decomposition and communication are hidden. Nevertheless, this engineering work contains a large part of the needs of a high-performance computing code. Instead of one three-dimensional field  $\phi$ , GYSELA now has three of them: `Phi`, `Apar` and `Apar_diff`. The complexity of the data storage stems from the need for adequate communication between processors with different data decompositions. Thankfully, the three fields have approximately the same requirements. Both  $\phi$  and  $\psi_h$  are solved in Poisson and Ampère solvers on a reduced set of processes with one value of the toroidal angle  $\varphi$  each. The resulting data needs to be (1) gyro-averaged, (2) differentiated with respect to  $r$ ,  $\theta$  and  $\varphi$ , (3) broadcast on the two data decompositions used for the Vlasov solver.

All the heavy lifting was already done for the potential `Phi`. This infrastructure has been adapted and re-used to compute the derivatives and broadcast both `Apar` and `Apar_diff`. The accumulation of `Apar_diff` into `Apar` is a straightforward operation. However, it implies `Apar` needs to be preserved between time steps. As a consequence, `Apar` must be stored into restart files to be reloaded later.

### 7.2.2 Modification to the time stepper

In order to adapt this algorithm to the electromagnetic case, we need to insert three key steps: (i) the change of variable from  $w^{\text{old}}$  to  $w^{\text{new}}$ , (ii) the resolution of Ampère equation of `Apar_diff`, and (iii) the accumulation of `Apar_diff` into `Apar`. Because of step (iii), the `Apar` has become an induction variable. Therefore, we have to take care of the predictor–corrector loop, and to avoid modifying `Apar` inside it.

For step (i), we chose to leverage the first half-advection in the velocity direction to operate the change of variable. This amounts to changing the foot of the characteristic according to 7.34, by `hatZsJ[Apar_diff]/sqrt(hatAs)`. Therefore, it leads to a low additional cost. As it is the first step of the Vlasov advection, it sets the grounds for the remainder of the Vlasov advection. This choice has two important consequences. First, we need to store the distribution function in variable  $w$  in the restart files. Second, we must preserve the value of `Apar_diff` from the previous time step during the prediction–correction sub-loop. Therefore, the resolution of the Ampère equation (ii) must happen after the sub-loop.

The new algorithm is the following:

1. Start a time step with the distribution function  $F(w^{\text{old}})$ 
  - (iii) if `solve_Ampere`: accumulate `Apar_diff` into `Apar`.

$$\text{Apar} := \text{Apar} + \text{Apar\_diff}.$$

From this point on, the invariant  $\psi = \text{Apar} + \text{Apar\_diff}$  is broken:  $\psi = \text{Apar}$  and `Apar_diff`  $\neq$  0.

This will be repaired by the change of variable step (i).

2. Prediction–correction sub-loop:
  - (a) Copy  $F(w^{\text{old}})$  into  $G(w^{\text{old}})$

- (b) Half-advection in  $v$  for  $G(w^{\text{old}})$ 
  - (i) if `advect_Ampere`: change variables into  $G(w^{\text{new}})$ . It is detailed paragraph 7.2.3.
- By assigning `Apar_diff:= 0`, we restore the invariant  $\psi = \text{Apar} + \text{Apar\_diff}^2$ .
- (c) Half-advection in  $\varphi$  for  $G(w^{\text{new}})$
- (d) Advection in  $(r, \theta)$  for  $G(w^{\text{new}})$
- (e) Half-advection in  $\varphi$  for  $G(w^{\text{new}})$
- (f) Half-advection in  $v$  for  $G(w^{\text{new}})$  with no change of variable
- (g) Solve Poisson equation for  $\phi$  from  $G(w^{\text{new}})$

The distribution function is now  $G(w^{\text{new}})$  with some unknown `Apar_diff`.

(ii) if `solve_Ampere`: solve Ampère equation 7.27 for the new `Apar_diff` from  $G(w^{\text{new}})$

3. Compute diagnostics on  $G(w^{\text{new}})$
4. Save the restart file on  $G(w^{\text{new}})$  and `Apar`
5. Swap  $F$  and  $G$ , and loop.

### 7.2.3 Change of variable

The advection routine computes the foot of the characteristic backwards from  $G(w^{\text{new}})$  at spatial position  $\vec{X}$ . This is done using the  $w^{\text{new}}$  coordinate, by solving equation 7.24 (7.35 in normalised form) backwards. The resulting position is  $w_{\text{foot}}^{\text{new}}$  at the same position  $\vec{X}_{\text{foot}} = \vec{X}$ .

Meanwhile, the distribution function is expressed in variable  $w^{\text{old}}$ . We need to find the foot of the characteristic in that variable. The passage rule is given by equation 7.30, involving  $J[\psi_h]$  at the spatial position of the foot  $\vec{X}_{\text{foot}}$ . Since the advection is split, the spatial position does not change, and we can access cheaply  $J[\psi_h]$  at the starting spatial grid point  $\vec{X}_{\text{foot}} = \vec{X}$ . In the GYSELA normalisation,  $w = \text{vparg}/\sqrt{\text{hatAs}}$ . Therefore, the normalised passage rule is

$$\begin{aligned} \text{vparg}_{\text{foot}}^{\text{old}} \left( \text{vparg}^{\text{new}}; \vec{X} \right) &= \text{vparg}_{\text{foot}}^{\text{new}} \left( \text{vparg}^{\text{new}}; \vec{X} \right) \\ &+ \frac{\text{hatZs}}{\sqrt{\text{hatAs}}} J[\text{Apar\_diff}] (\vec{X}) \end{aligned} \quad (7.33)$$

In consequence, the velocity advection is written

$$G(\text{vparg}^{\text{new}}) := G \left( \text{vparg}_{\text{foot}}^{\text{new}} \left( \text{vparg}^{\text{new}}; \vec{X} \right) + \frac{\text{hatZs}}{\sqrt{\text{hatAs}}} J[\text{Apar\_diff}] (\vec{X}) \right) \quad (7.34)$$

In the electrostatic case `Apar_diff= 0`, and the advection step is unchanged. This interpolation step requires boundary conditions. We keep the Neumann boundary conditions that were already in use.

---

<sup>2</sup>This zeroing is not actually done in code. The value of  $J[\psi_h]$  is just ignored.

### 7.2.4 Modifications to the advection equations

The advection equations are solved for  $\psi_h = \text{Apar\_diff} = 0$ . In normalised GYSELA notation, they write

$$\begin{aligned}
\dot{\vec{X}} &= \frac{\text{vparg}}{\sqrt{\text{hatAs}}} \vec{b}^* + \vec{v}_E + \vec{v}_D + \vec{v}_A \\
\sqrt{\text{hatAs}} \frac{\text{dvparg}}{\text{dt}} &= -\mu \vec{b}^* \cdot \vec{\nabla} B - e \vec{b}^* \cdot \vec{\nabla} J[\phi] + \frac{\sqrt{\text{hatAsvparg} + \text{hatZs} J[\text{Apar}]}}{B} \vec{v}_E \cdot \vec{\nabla} B \quad (7.35) \\
B_{\parallel}^* \vec{b}^* &= \vec{B} + \left( \frac{\sqrt{\text{hatAsvparg}}}{\text{hatZs}} + J[\text{Apar}] \right) \frac{\vec{\nabla} \times \vec{B}}{B} \\
B_{\parallel}^* \vec{v}_D &= \frac{\text{vparg} \left( \text{vparg} + \frac{\text{hatZs}}{\sqrt{\text{hatAs}}} J[\text{Apar}] \right) + \mu B}{ZB} \{B, \vec{X}\} \\
B_{\parallel}^* \vec{v}_E &= \{J[\text{Phi}], \vec{X}\} \\
B_{\parallel}^* \vec{v}_A &= -\frac{\text{vparg}}{\sqrt{\text{hatAs}}} \{J[\text{Apar}], \vec{X}\} \\
B_{\parallel}^* &= B + \left( \frac{\sqrt{\text{hatAsvparg}}}{\text{hatZs}} + J[\text{Apar}] \right) \frac{\vec{b} \cdot \vec{\nabla} \times \vec{B}}{B}
\end{aligned}$$

where we have set  $\partial_t \psi_s = 0$ . The modifications are shown in bold font. The Poisson bracket denotes  $\{F, G\} = \vec{b} \cdot \vec{\nabla} F \times \vec{\nabla} G$ . The  $B_{\parallel}^*$  is ubiquitous, as it serves as a jacobian in velocity space<sup>3</sup>. The Ampère equation writes in normalised form

$$\begin{aligned}
-\nabla_{\perp}^2 (\text{Apar\_diff} + \text{Apar}) + \text{beta\_toro} \sum_{\text{species}} \frac{\text{ns0}(r) \text{hatZs}^2}{\text{hatAs}} \text{Apar\_diff} &= \\
\sum_{\text{species}} \frac{\text{beta\_toro} \times \text{hatZs}}{\sqrt{\text{hatAs}}} \int \text{vparg} J^{\dagger} [F B_{\parallel}^* - F_{\text{eq}} B_{\parallel, \text{eq}}^*] \text{dvparg} \text{d}\mu &
\end{aligned}$$

where  $\int \text{dvparg}$  denotes the properly weighted integral in velocity space, and  $\text{ns0}$  is the equilibrium density profile.

### 7.2.5 Initial distribution function

In order to have consistent simulations, the magnetic field and the plasma current must agree. Since the current is carried almost exclusively by the electrons, this prescribes the parallel velocity around which the electron distribution function is centred. For the GYSELA magnetic equilibrium, the current is given by

$$\begin{aligned}
\mu_0 \vec{J} &= \frac{B_0}{qR} \left( 2 - s - \frac{r}{R} \cos \theta \right) R \vec{\nabla} \varphi \\
\mu_0 J_{\text{dot\_b}} = \mu_0 J_{\parallel} &= \frac{B_0}{\sqrt{r^2 + q^2 R^2}} \left( 2 - s - \frac{r}{R} \cos \theta \right)
\end{aligned}$$

with  $q$  the magnetic safety factor,  $s = \text{d} \ln q / \text{d} \ln r$  the magnetic shear. By rewriting the magnetic permeability  $\mu_0$  in terms of the plasma  $\beta = \mu_0 N_0 T_0 / B_0^2$ , this implies the electron velocity shift is

$$\text{Vpars0}(r, \theta) = -\frac{\sqrt{\text{hatAs}}}{\text{hatZs}} \times \frac{\mu_0 J_{\text{dot\_b}}(r, \theta)}{\text{beta\_toro} \times \text{ns0}(r)}$$

It should be noted that this parallel electron velocity scales like  $1/\beta$ . Because of this, a lower  $\beta$  means faster electrons to produce the same magnetic field. Therefore, a lower limit exists on the accessible  $\beta$  in the code, to avoid triggering a bump-on-tail instability. A brief scan in  $\beta$  shows the limit to be around  $\beta = 5 \times 10^{-4}$ .

<sup>3</sup>The modification to the  $B_{\parallel}^*$  and  $\vec{b}^*$  have actually been stalled due to the amount of modifications required. Furthermore, the difference between  $B$  and  $B_{\parallel}^*$  is underestimated at the moment, and this correction is blocked by a known bug in the collision operator.

## 7.3 Numerical tests

As a test bench, we consider the  $n = 1$  tearing and kink modes, respectively  $m = 2$  and  $m = 1$ . Since these instabilities should develop for the specific toroidal mode number  $n = 1$ , we chose to filter all modes  $n \neq 1$  from the simulations. Since our initial circular magnetic configuration is not a MHD equilibrium, it triggers a transient will pollutes the discussion. To simplify the discussion to the maximum, we simulate flat plasma profiles with unit density and temperature. In order to ensure the scale separation between the electron and ion dynamics, we use a near-realistic mass ratio  $m_i/m_e = 1600$ .

As discussed paragraph 5.3.1, the local magnetic field tilt depends on the poloidal position. As a consequence, the parallel resonance does not happen at  $q_{\text{GYS}} = m/n$ , but rather at  $q^*(r_{\text{res}}) = m/n$ . This induces a slight radial shift of the mode when analysing the simulation result.

$$q^*(r_{\text{res}}) = \frac{q_{\text{GYS}}}{\sqrt{1 - r^2/R_0^2}} \quad (7.36)$$

For all the tests, we will use a Wesson safety profile as presented paragraph 2.3. We reproduce the defining formula for reference. For  $r/a > 1$ , the profiles are extended with constant shear  $s = 2$ . Since  $\mu_0 \mathcal{G} = \frac{B_0}{R_0} \frac{2-s}{q}$ , this corresponds to an absence of current outside of the separatrix.

$$q = q_a \frac{(r/a)^2}{1 - (1 - (r/a)^2)^{\nu+1}} \quad (2.64)$$

The used parameters will be given in-text for the different test cases. The profiles are shown figure 7.2.

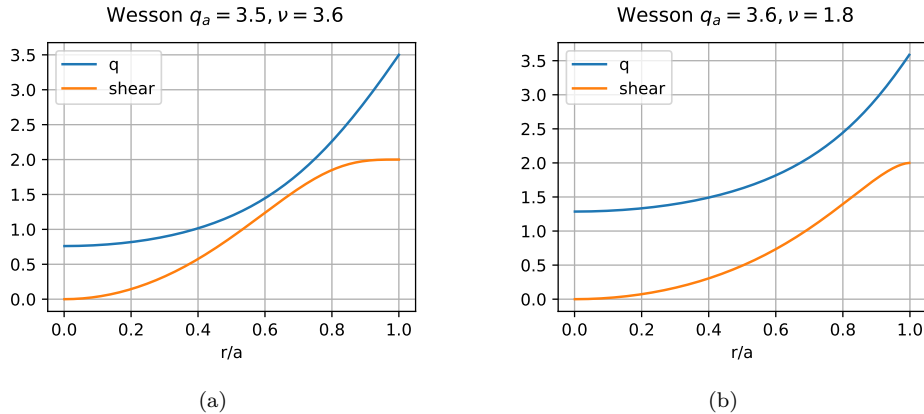


Figure 7.2: Safety factor profile used for the internal kink test case.

### 7.3.1 Internal kink mode test

One of the easiest MHD instabilities to trigger is the internal kink mode. The only requirements are a safety profile that dips below 1 close to the centre. We use the Wesson profile with  $q_a = 3.5$  and  $\nu = 3.6$  (equation 2.64), shown figure 7.2.

The simulation was first run in the purely magnetic case, by clamping the potential  $\phi = 0$ . The results are shown figure 7.3. The radial grid is chosen with 512 points. The normalised ion Larmor radius  $\rho_{*i} = 1/100$ . The normalised electron skin depth is  $\delta_e/a = 1/400$ , with  $\beta = 1\%$ . As such, the simulation marginally resolves the electron current sheet. The simulation time step is  $\omega_{ci}\Delta t = 0.1$ . Simulations with time steps up to  $\omega_{ci}\Delta t = 1$  were tested and converged.

The current sheet appears at the right position in figure 7.3 (red dotted line at  $r/a = 0.38$  and  $q^* = 1$ ). The magnetic perturbation is close to the expected shape  $\psi_{1,1}(r) \propto r(1 - 1/q)$ . The mode grows exponentially, with a subtle change of slope at the middle of the simulation. We associate it to pollution by the initial transient reorganisation. At the end of this simulation, a numerical

instability develops from the central position  $r = 0$  (not shown). Since this benchmark is synthetic, we did not compare the growth rate to a theoretical value.

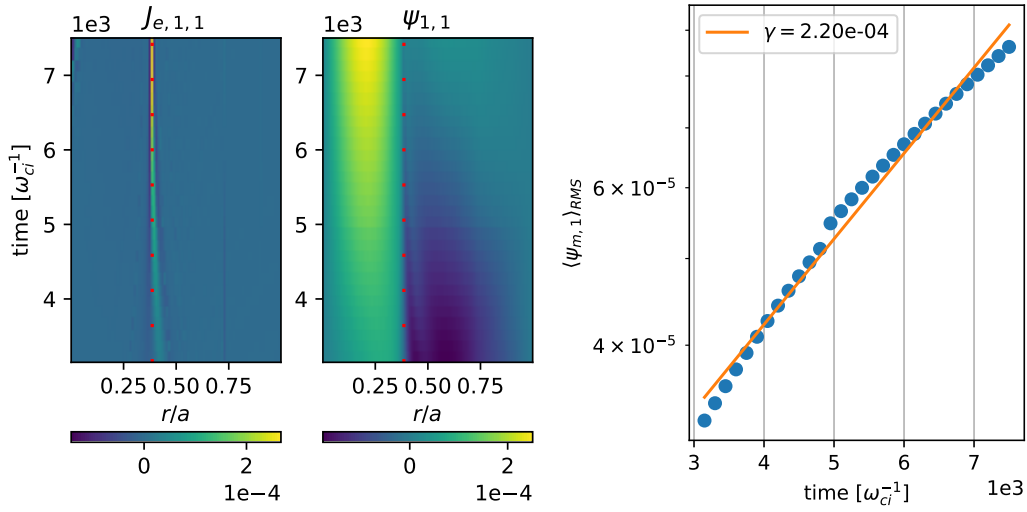


Figure 7.3: For a simulation of the internal kink mode with safety profile 7.2 in the purely magnetic case. (Left) Time evolution of the radial profile for the  $n = 1$ ,  $m = 1$  mode of (in order) the electron current and parallel vector potential  $\psi$ . (Right) Time evolution of the amplitude of  $\psi_{1,1}$  inside resonance position  $r_{\text{res}}$ .

The same simulation has been run in the fully electromagnetic case, with freely evolving  $\phi$ . The evolution of  $\phi$  implies the propagation of Alfvén waves in the parallel direction, as shown figure 7.4. As a consequence, the simulation time step is bounded above. We use the same value of  $\omega_{\text{ci}}\Delta t = 0.1$ . Contrary to the purely magnetic case, using  $\omega_{\text{ci}}\Delta t$  larger than 0.5 results in a numerical instability.

The shape of the parallel vector potential  $\psi_{1,1}$  remains essentially the same as in the former case. Meanwhile, the electric potential features the characteristic saw-tooth radial shape  $\phi_{1,1} \propto r\mathcal{K}[q^* < 1]$ , with traces of the propagating waves overlain. Both are shown figure 7.5. The mode appears to grow about twice more slowly. The reason for this slowdown remains to be investigated.

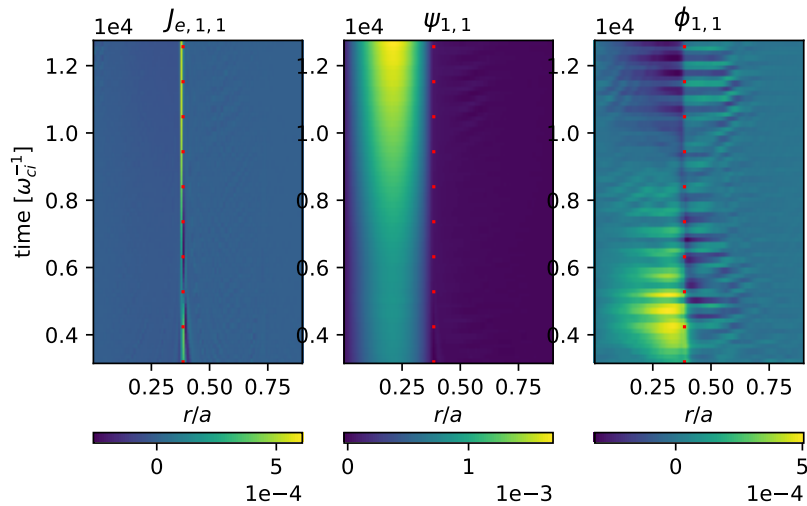


Figure 7.4: For a simulation of the internal kink mode with safety profile 7.2a in the purely magnetic case. (Left) Time evolution of the radial profile for the  $n = 1$ ,  $m = 1$  mode of (in order) the electron current and parallel vector potential  $\psi$  and electric potential  $\phi$ .

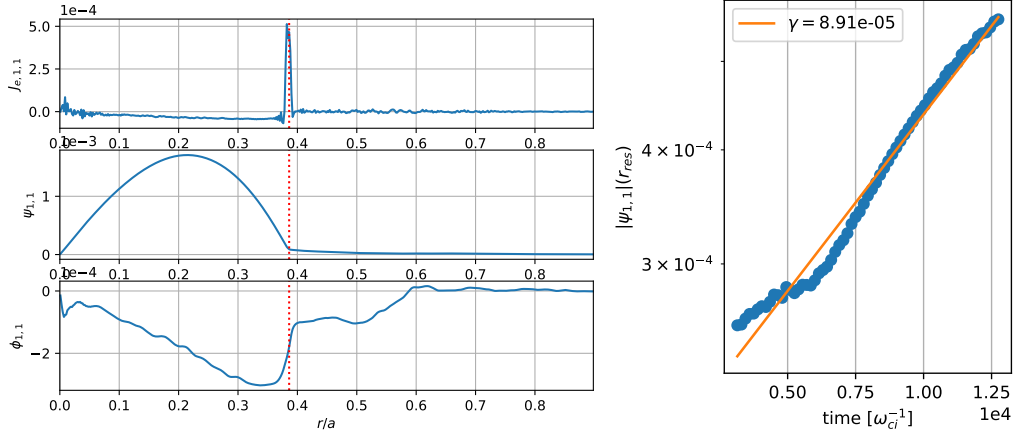


Figure 7.5: For a simulation of the internal kink mode with safety profile 7.2a in the purely magnetic case. (Left) Radial shape of  $(1, 1)$  mode of the current, vector potential and potential at final simulation time. (Right) Time evolution of the amplitude of  $\psi_{1,1}$  at the resonance position  $r_{\text{res}}$ .

### 7.3.2 Tearing mode test

A simulation test case has been run with a  $q_a = 3.6$ ,  $\nu = 1.8$  profile, shown figure 7.2 (right). This profile crosses both the  $q^* = 2$  at  $r_{\text{res}} = 0.65$ . We use the same grid, with  $\omega_{ci}\Delta t = 1$  and  $\beta = 10^{-3}$ . The associated electron skin depth is  $\delta_e/a = 1/135$ .

The results are shown figure 7.6. The growth rate is of the order of  $\gamma = 3.4 \times 10^{-6}\omega_{ci}$ . This is to be compared to the expected growth rate given by equation 2.72,  $\gamma_{\text{th}} = 3.1 \times 10^{-5}\omega_{ci}$ , with instability coefficient  $r\Delta' = 10.5$ .

$$\gamma_{\text{th}} = \frac{\delta_e^2 v_{\text{th},e}}{Rr^2} \frac{ms}{q^2} \frac{r\Delta'}{\sqrt{2\pi}} \quad (2.72)$$

The shape of the mode is shown figure 7.7. The current sheet is well resolved. The theoretical mode shape obtained from equation 2.66 is shown in dotted line. Both the current profile and the vector potential closely follow the expected shape. The resonance is placed at the right  $q^* = 2$  position. The departure can be attributed to the difference between  $q$  and  $q^*$ .

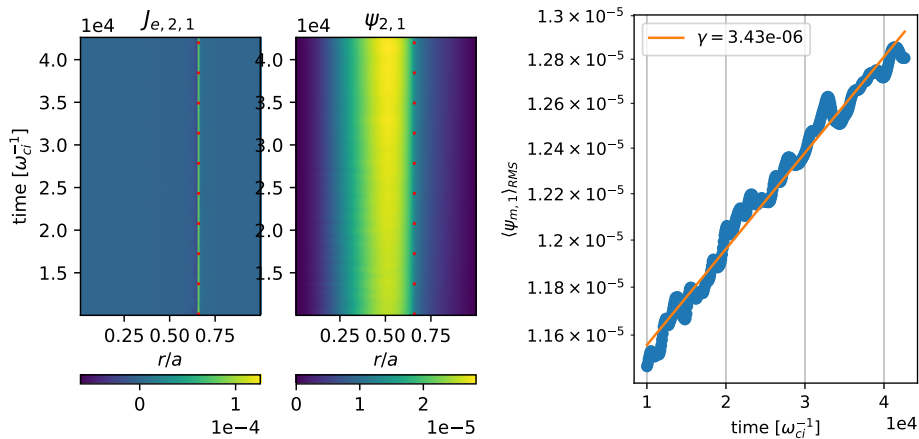


Figure 7.6: For the simulation of a tearing mode ( $m = 2, n = 1$ ) with safety profile 7.2b. (Left) Time evolution of the  $(2, 1)$  modes of the electron parallel current and of the magnetic potential. (Right) Time evolution of the amplitude of  $\psi_{2,1}$  at the resonance position  $r_{\text{res}}$ .

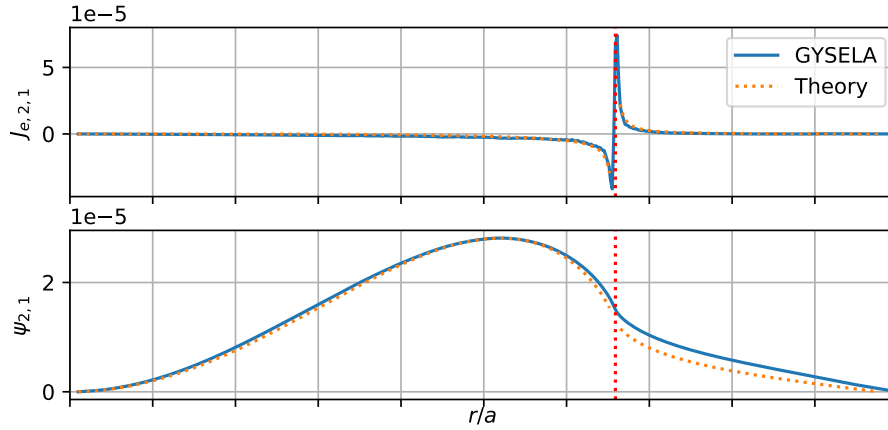


Figure 7.7: For the simulation of a tearing mode ( $m = 2, n = 1$ ) with safety profile 7.2b. Plain line: radial pattern of the current and vector potential at last time step. Dotted line: theoretical radial pattern solved using equation 2.66.

## 7.4 Future directions

The electromagnetic extension to GYSELA is at the moment a mere proof of concept. Before accessing full non-linear electromagnetic simulations, a few roadblocks need to be removed.

**Electromagnetic diagnostics:** the diagnostics have not been updated to include the effect of the magnetic fluctuations. Some care needs to be taken: the distribution function is to be interpreted in  $w$  variable with non-zero  $\psi_h$ .

**Prediction-correction of  $\psi_h$ :** Only the value of  $\psi_s$  is used to compute the electromagnetic perturbations in the equations of motion. This limits the order of the time stepping scheme by neglecting  $\psi_h$  of order  $\Delta t$ . This limitation comes from the re-use of the same storage space for  $\psi_h^{\text{old}}$  and  $\psi_h^{\text{new}}$  in step (ii). In a future extension, both  $\psi_h$  fields will need different storage space to use the prediction–correction scheme.

**Magnetic equilibrium:** At the moment, the background magnetic field used in GYSELA is not a magnetic equilibrium. Starting from an equilibrium governed by the Grad–Shafranov equation and lifting this constraint is on-going work, and will allow to self-consistently evolve the  $n = 0$  component of  $\psi$ .

**Alfvén waves:** The first transient in simulations is dominated by Alfvén waves. Those waves contain oscillations of the parallel electric field. They evolve very fast, with a frequency of the order of  $\omega = nv_a/R$  with  $v_a = v_{\text{th}}/\sqrt{\beta}$  the Alfvén velocity. Since  $\beta \ll 1$ , these oscillations are much faster than the GAM transient existing in electrostatic simulations. This results in a tight bound on the time step  $\Delta t \lesssim 0.1\omega_{ci}$  for numerical stability with realistic electrons. A possible correction would be to assume an ideal MHD prescription for  $\partial_t \psi_s = -\nabla_{\parallel} \phi$  instead of zero. This would make the advection by a parallel electric field implicit:

$$\begin{aligned} mB_{\parallel}^* \dot{w} &= \mu \vec{B}^* \cdot \vec{\nabla} [\mu B - wJ[\psi_h]] - e \vec{B}_{\perp}^* \cdot \vec{\nabla} J[\phi] \\ &- e B_{\parallel}^* [\nabla_{\parallel} J[\phi] - J[\nabla_{\parallel} \phi]] \end{aligned}$$

The second line is of the order  $\rho_i^4/R^4$ , so can be neglected at our approximation level. This formulation should allow to lighten the constraint from fast Alfvénic dynamics, and the associated numerical instability.

# Conclusion

Let us now take a step back, and examine where we stand. We set out looking to lighten the models for turbulent plasmas dynamics. Three approaches have been discussed in this manuscript. The first one is homogenisation, with the instance of the kinetic to gyro-kinetic reduction. The fast cyclotron dynamics are averaged out, and only remains an effective equation to describe the system.

The second one is subspace pruning. This area has received ample attention by the model order reduction community. In chapter 3, we borrowed two methods, balanced truncation and interpolatory model reduction to investigate the 1D–1V Vlasov–Poisson dynamics. The former is inspired by control theory, and aims at removing unreachable and unobservable subspace from the description. The sharp decrease of the Hankel singular values suggests the effective subspace to be low-dimensional. However, the models output by balanced truncation feature a spurious instability in the closed-loop Vlasov–Poisson setting. As an alternative, we considered formulating a reduced model by interpolating the expected kinetic response. The resulting model performs well, both on the bare Vlasov and the coupled Vlasov–Poisson problem. The versatility of the method allows to envision extensions to linear toroidal gyro-kinetic dynamics. Use of this method to construct a linearised Landau gyro-fluid could be worthwhile.

The third one —and the most difficult— is bypassing the turbulent non-linearity. We followed a phenomenological view, trying to characterise the non-linear turbulent filaments that swim inside the plasma. This led us to ask ourselves, how much of the linear properties are conserved in the non-linear regime? To answer that question, we analysed in depth the three-dimensional data output by GYSELA. We compared key linear quantities from GYSELA data to the expected results from the QuaLiKiz code (chapter 4). Even though the Kubo numbers are of a few units, the magnitude and phase of the pressure response to a potential perturbation qualitatively match the expected value. In addition, we developed an automated diagnostic tool to extract the motion and shape of turbulent structures (chapter 5). The reconstructed motion and shape tend to follow the group velocity dictated by the linear analysis. All in all, the plasma appears to obey quasi-linear theory.

But the total heat fluxes differ. Of course, the turbulent potential spectrum is not predicted by quasi-linear theory, and has to rely on a physically motivated closure. The problem may run deeper, as even the non-linear local code GKW disagrees. Turbulent filaments tend to move around the plasma: toroidally, poloidally and radially. Understanding this last motion is key to grasp the nature of turbulent avalanches in the plasma. First, contrary to oft-stated estimates, zonal flow shear does not necessarily distort and destroy turbulent cells. It may rather warp turbulent corridors. Those are akin to streamers observed for ETG turbulence, but following the zonal flow pattern. Second, the back-reaction of distorted turbulent cells on the zonal flow is enhanced by a resonance between the wave radial group velocity and the geodesic acoustic phase velocity. The coupled dynamics is unstable, and features many characteristic properties of avalanches seen in non-linear simulations (chapter 6).

As no reduction tale is ever complete without an extension, chapter 7 embarked into extending GYSELA with magnetic fluctuations. We formulated the scheme and implemented it in the code. In the occasion, many numerical and engineering challenges had to be overcome. Preliminary tests have been performed, validating the general algorithm, and identifying limitations of the model.

**Now what?** In our race to reduce the description of tokamak turbulence, we gathered knowledge and suspicions. However, we have yet to positively propose anything. Key questions remain unanswered. Are non-linear Landau fluid models adequate for turbulence modelling? Is turbulent

saturation quasi-linear —by coupling to the profiles—, or fully non-linear —through non-linear self-advection of turbulent structures? Or both, as usual in physics? On a related note, how non-local is turbulent saturation?

## Appendix A

# Derivation of the drift–kinetic Lagrangian

The easiest way is to formulate everything as differential forms, and apply the rules of exterior calculus (Brizard, 2017). This formalism allows to avoid the difficulties of vector calculus, and allows to remove exact derivatives as early as possible. The original Lagrangian 1-form is written as

$$\mathcal{L}_0 dt = m\vec{V} \cdot d\vec{X} + e\vec{A} \cdot d\vec{X} - \frac{mV^2}{2} dt \quad (\text{A.1})$$

with  $d$  the exterior derivative. It obeys the usual calculus rules, except for  $d^2 = 0$ .  $\vec{X}$  and  $\vec{V}$  are the position and velocity of the particle. The objective of this section is to compute the second order perturbation of  $\mathcal{L}_0$  by the Larmor motion  $\delta\vec{X} = \vec{\rho}$  and  $\delta\vec{V} = \vec{\pi}$ . Since the Lagrangian is defined up to a total derivative, we will opportunistically drop these. In the following, we denote as  $\wedge$  the antisymmetric exterior product. Let  $\vec{u} \circ \ell$  be the contraction of a vector  $\vec{u}$  with a form  $\ell$  by the left.

$$\begin{aligned} \vec{u} \circ dX^i &= u^i \\ \vec{u} \circ (\ell \wedge m) &= (\vec{u} \circ \ell) \wedge m - \ell \wedge (\vec{u} \circ m) \end{aligned}$$

The first order perturbation can be written as a Lie derivative

$$\begin{aligned} d[\mathcal{L}_0 dt] &= md\vec{V} \wedge d\vec{X} + \frac{e}{2}\vec{B} \times d\vec{X} - m\vec{V} \cdot d\vec{V} \wedge dt \\ \mathcal{L}_1 dt &= \left( \frac{\vec{\rho}}{\vec{\pi}} \right) \circ d[\mathcal{L}_0 dt] + d \left[ \left( \frac{\vec{\rho}}{\vec{\pi}} \right) \circ [\mathcal{L}_0 dt] \right] \\ &= -m\vec{\rho}d\vec{V} + (m\vec{\pi} + e\vec{B} \times \vec{\rho}) \cdot d\vec{X} - m\vec{V} \cdot \vec{\pi} dt + d[\dots] \end{aligned}$$

We have used the relation

$$d[\vec{A} \cdot d\vec{X}] = \frac{\partial A_i}{\partial X^j} dX^j \wedge dX^i = \frac{1}{2}(\vec{\nabla} \times \vec{A})_j dX^j \wedge dX^i$$

The factor in front of  $d\vec{X}$  cancels when the  $\vec{\pi}$  and  $\vec{\rho}$  describe a Larmor loop

$$\vec{\pi} + \frac{e}{m}\vec{B} \times \vec{\rho} = 0 \quad (\text{A.2})$$

The second order perturbation can be computed from the exterior derivative of  $\mathcal{L}_1$  as

$$\begin{aligned}
d[\mathcal{L}_1 dt] &= -m d\vec{\rho} \wedge d\vec{V} + m d\vec{\pi} \wedge d\vec{X} + \frac{e}{2} \vec{\nabla} \times [\vec{B} \times \vec{\rho}] \times d\vec{X} + eB \times d\vec{\rho} \cdot d\vec{X} \\
&\quad - (m\vec{V} \cdot d\vec{\pi} + m\vec{\pi} \cdot d\vec{V}) \wedge dt \\
\mathcal{L}_2 dt &= \frac{1}{2} \begin{pmatrix} \vec{\rho} \\ \vec{\pi} \end{pmatrix} \circ d[\mathcal{L}_1 dt] + d \left[ \begin{pmatrix} \vec{\rho} \\ \vec{\pi} \end{pmatrix} \circ [\mathcal{L}_1 dt] \right] \\
&= m\vec{\pi} \cdot d\vec{\rho} + \frac{e}{2} \nabla \times (\vec{B} \times \vec{\rho}) \times \vec{\rho} \cdot d\vec{X} - \frac{e}{2} B \times d\vec{\rho} \cdot \vec{\rho} - \frac{m}{2} \vec{\pi}^2 dt + d[\dots] \\
&= \left( m\vec{\pi} + \frac{e}{2} \vec{B} \times \vec{\rho} \right) \cdot d\vec{\rho} + \frac{e}{2} \nabla \times (\vec{B} \times \vec{\rho}) \times \vec{\rho} \cdot d\vec{X} - \frac{m}{2} \vec{\pi}^2 dt + d[\dots]
\end{aligned}$$

We can now parameter the Larmor motion A.2 by the Larmor radius  $\rho$  and the gyro-phase  $\xi$ . In addition, we force the unperturbed velocity  $\vec{V} = mv_{\parallel} \vec{b}$  to only have a parallel component. The Lagrangian becomes

$$\begin{aligned}
\mathcal{L} &\approx mv\vec{b} \cdot \dot{\vec{X}} + e\vec{A}(\vec{X}) \cdot \dot{\vec{X}} - \frac{m}{2} v^2 \\
&\quad + \frac{eB\rho^2}{2} \dot{\xi} - \frac{eB^2\rho^2}{2m} \\
&\quad + \frac{e}{2} \nabla \times [\vec{B} \times \vec{\rho}] \times \vec{\rho} \cdot \dot{\vec{X}} + \mathcal{O}(\rho^3)
\end{aligned}$$

The first line corresponds to the free streaming dynamics of the guiding centre  $\vec{X}$ . The second line corresponds to the Larmor motion. The third line denotes a correction to the dynamics due to the inhomogeneity of the magnetic field at the Larmor scale. It is of order  $\rho_i^2 \nabla^2 \ln B$ , and is neglected for a smooth background magnetic field.

## Appendix B

# Derivation of the electromagnetic action principle

The electromagnetic action principle can be defined in the same way as the electrostatic case

$$\begin{aligned}
\mathcal{S}[\dot{\mathbf{Z}}(\mathbf{Z}), \phi, \lambda, \mathcal{F}] &= \int \left[ m\mathbf{u}\vec{b} \cdot \dot{\mathbf{X}} + e\vec{A}_0 \cdot \dot{\mathbf{X}} - \frac{m}{2}u^2 - \mu B \right] \mathcal{F} d\mathbf{Z} dt \\
&- \int \left[ eJ \left[ \phi - u\psi + \frac{e}{2m}\psi^2 \right] - \frac{e^2}{2B} \partial_\mu [J[(\phi - u\psi)^2] - J[\phi - u\psi]^2] \right] \mathcal{F} d\mathbf{Z} dt \\
&+ \int \frac{\varepsilon_0}{2} [\vec{\nabla}\phi]^2 d^3\vec{x} dt - \int \frac{1}{2\mu_0} [\vec{\nabla} \times \vec{A}]^2 d^3\vec{x}
\end{aligned}$$

In the Boussinesq approximation, we replace the integration of the polarisation term in the second line by an integration against the reference Maxwellian  $\mathcal{F}_0$ . In the long wavelength limit,  $J \approx 1 - \rho_i^2 k_\perp^2 / 2$ , and this term simplifies to

$$\begin{aligned}
\int \frac{e^2}{2B} \partial_\mu [J[(\phi - u\psi)^2] - J[\phi - u\psi]^2] \mathcal{F} &\approx \int \frac{e^2}{2B} \partial_\mu \left[ \frac{\rho_i^2}{2} \vec{\nabla}_\perp [\phi - u\psi]^2 \right] \mathcal{F}_0 \\
&= \int \frac{m}{2B^2} [\vec{\nabla}_\perp \phi - u\vec{\nabla}_\perp \psi]^2 \mathcal{F}_0
\end{aligned}$$

using  $\rho_i^2 = 2m\mu/e^2B$ . This quantity can be integrated, introducing the density  $n_0$ , parallel velocity  $V_\parallel$  and temperature  $T_\parallel$

$$\int \frac{e^2}{2B} \partial_\mu [J[(\phi - u\psi)^2] - J[\phi - u\psi]^2] \mathcal{F} \approx \int \frac{m}{2B^2} [\vec{\nabla}_\perp \phi - V_\parallel \vec{\nabla}_\perp \psi]^2 n_0 + \int \frac{mT_\parallel}{2B^2} [\vec{\nabla}_\perp \psi]^2 n_0$$

We apply the same approximation to the ponderomotive term  $J[\psi]^2 \mathcal{F}$ . We obtain

$$\int \frac{e^2}{2m} J[\psi]^2 \mathcal{F} \approx \int \frac{e^2 \psi^2}{2m} \mathcal{F}_0 = \int \frac{e^2 \psi^2}{2m} n_0$$

Meanwhile, the magnetic field can be decomposed into

$$\vec{\nabla} \times \vec{A} = \vec{\nabla} \times \vec{A}_0 + \vec{\nabla} \times (\psi \vec{b})$$

The first term is the equilibrium stationary magnetic field. It is orthogonal to the other terms when integrating  $[\vec{\nabla} \times \vec{A}]^2$  in time. This is equivalent to removing the equilibrium current in the

source for the Ampère equation. The full action becomes

$$\begin{aligned}
\mathcal{S}[\dot{\mathbf{Z}}(\mathbf{Z}), \phi, \psi] &= \int \left[ m\mathbf{v}\vec{b} \cdot \dot{\vec{X}} + e\vec{A} \cdot \dot{\vec{X}} - \frac{m}{2}v^2 - \mu B - eJ[\phi - u\psi] \right] \mathcal{F} d\mathbf{Z} \\
&+ \int \frac{e^2}{2m}\psi^2 n_0 d\mathbf{Z} \\
&+ \int \frac{m}{2B^2} [\vec{\nabla}_\perp \phi - V_\parallel \vec{\nabla}_\perp \psi]^2 n_0 d^3 \vec{X} \\
&+ \int \frac{T_\parallel}{2B^2} [\vec{\nabla}_\perp \psi]^2 n_0 d^3 \vec{X} \\
&+ \int \frac{\varepsilon_0}{2} [\vec{\nabla} \phi]^2 d^3 \vec{x} dt - \int \frac{1}{2\mu_0} B_0^2 d^3 \vec{x} - \int \frac{1}{2\mu_0} [\vec{b} \times \vec{\nabla} \psi]^2 d^3 \vec{x}
\end{aligned}$$

The first line is the gyro-centre Lagrangian. The second line is the magnetic skin term. The third and fourth line is the charge polarisation. The fifth line is the electromagnetic Lagrangian.

# Appendix C

## Linearized Vlasov equation

The gyro-kinetic equation writes, in variables  $P_\varphi, \theta, \varphi, E, \mu$ , with  $E$  the kinetic energy and  $P_\varphi$  the toroidal momentum.

$$\begin{aligned}\partial_t \mathcal{F}(P_\varphi, \theta, \varphi, E, \mu) &+ \dot{\theta} \partial_\theta \mathcal{F} + \dot{\varphi} \partial_\varphi \mathcal{F} + \dot{P}_\varphi \partial_{P_\varphi} \mathcal{F} + \dot{E} \partial_E \mathcal{F} = 0 \\ E &= \frac{m}{2} v_{||}^2 + \mu B \\ P_\varphi &= m v_{||} b_\varphi + e A_\varphi\end{aligned}$$

where the particle velocity is given by

$$\begin{aligned}\dot{P}_\varphi \partial_{P_\varphi} + \dot{\theta} \partial_\theta + \dot{\varphi} \partial_\varphi &= v_{||} \vec{\nabla}_{||} + \vec{v}_D \cdot \vec{\nabla} + \vec{v}_E \cdot \vec{\nabla} \\ \dot{E} &= -e(\dot{r} \partial_r + \dot{\theta} \partial_\theta + \dot{\varphi} \partial_\varphi) \phi \\ \dot{P}_\varphi &= -e \partial_\varphi \phi\end{aligned}$$

We consider an ambient canonical Maxwellian plasma with distribution function  $\mathcal{F}(P_\varphi, E, \mu)$ , with density  $\mathcal{N}$ , and temperature  $T$ . We suppose a non-zero axisymmetric potential  $\Phi$  generating an equilibrium  $E \times B$  flow  $\vec{v}_{E,eq}$ .

$$\mathcal{F}(P_\varphi, E, \mu) = \frac{\mathcal{N}(r_{\text{ref}})}{\sqrt{2\pi m T}(r_{\text{ref}})^{3/2}} \exp\left(-\frac{E}{T(r_{\text{ref}})}\right)$$

where  $r_{\text{ref}}$  is the reference flux-surface for particles the particles with momentum  $P_\varphi$ , energy  $E$  and magnetic moment  $\mu$ . A small perturbation  $eJ[\phi]$  to the Hamiltonian leads to a small perturbation  $f$  of the distribution function. The fluctuations acts as a modification of the  $E \times B$  velocity and in  $\dot{E}$  and  $\dot{P}_\varphi$ . As the equilibrium distribution only depends on  $P_\varphi$ ,  $\mu$  and  $E$ . As a result, the linearised Vlasov equation can be simplified to

$$\partial_t f(P_\varphi, \theta, \varphi, E, \mu) + \dot{\theta} \partial_\theta f + \dot{\varphi} \partial_\varphi f = -e \partial_\varphi \phi \partial_{P_\varphi} \mathcal{F} - e(\dot{r} \partial_r + \dot{\theta} \partial_\theta + \dot{\varphi} \partial_\varphi) \phi \partial_E \mathcal{F}$$

since  $\dot{P}_\varphi = \dot{E} = 0$  for unperturbed dynamics. The Maxwellian equilibrium distribution function is

$$\begin{aligned}\partial_{P_\varphi} \mathcal{F} &= -\frac{eq}{rB} \partial_{r_{\text{ref}}} \mathcal{F} = \left[ A_N + \left( \frac{E}{T} - \frac{3}{2} \right) A_T \right] \times \frac{eq \mathcal{F}}{rRB} \\ \partial_E \mathcal{F} &= -\frac{\mathcal{F}}{T}\end{aligned}$$

where we have introduced the normalised logarithmic gradients

$$\begin{aligned}A_N &= -R \partial_r \ln \mathcal{N} \\ A_T &= -R \partial_r \ln T\end{aligned}$$

The resulting linearised Vlasov equation is

$$\begin{aligned}\partial_t f(P_\varphi, \theta, \varphi, E, \mu) + \dot{\theta} \partial_\theta f + \dot{\varphi} \partial_\varphi f &= \mathcal{F} \times \left[ A_N + \left( \frac{E}{T} - \frac{3}{2} \right) A_T \right] \frac{q \partial_\varphi \phi}{RrB} \\ &- \frac{e \mathcal{F}}{T} (v_{||} \vec{\nabla}_{||} + \vec{v}_D \cdot \vec{\nabla} + \vec{v}_{E,eq} \cdot \vec{\nabla}) \phi\end{aligned}$$

Let  $g = f + e\phi\mathcal{F}/T$ . The function  $g$  cancels the second term in the right-hand side, corresponding to the adiabatic response. The resulting equation is

$$\begin{aligned}\partial_t g(P_\varphi, \theta, \varphi, E, \mu) + \dot{\theta} \partial_\theta g + \dot{\varphi} \partial_\varphi g &= \left\{ \frac{q \partial_\varphi \phi}{RrB} \left[ A_N + \left( \frac{E}{T} - \frac{3}{2} \right) A_T \right] + \frac{e \partial_t \phi}{T} \right\} \times \mathcal{F} \\ &= \frac{e\mathcal{F}}{T} \left\{ \partial_t + \frac{qT}{eRrB_{\parallel}^*} \left[ A_N + \left( \frac{E}{T} - \frac{3}{2} \right) A_T \right] \partial_\varphi \right\} \phi\end{aligned}$$

Expressing  $g$  in the left-hand side in  $r, \theta, \varphi, E, \mu$  variables, we get

$$\partial_t g(r, \theta, \varphi, E, \mu) + v_{\parallel} \vec{\nabla}_{\parallel} g + \vec{v}_D \cdot \vec{\nabla} g + \vec{v}_{E, \text{eq}} \cdot \vec{\nabla} g = \frac{e\mathcal{F}}{T} [\partial_t + u_* \partial_\varphi] \phi$$

with the diamagnetic toroidal velocity

$$u_* = \frac{qT}{eRrB_{\parallel}^*} \left[ A_N + \left( \frac{E}{T} - \frac{3}{2} \right) A_T \right]$$

# Bibliography

- ABITEBOUL, J. 2012 Turbulent and neoclassical toroidal momentum transport in tokamak plasmas. Theses, Aix-Marseille Université.
- ABITEBOUL, J., GARBET, X., GRANDGIRARD, V., ALLFREY, S. J., GHENDRIH, P., LATU, G., SARAZIN, Y. & STRUGAREK, A. 2011 Conservation equations and calculation of mean flows in gyrokinetics. *Physics of Plasmas* **18** (8), 082503.
- ADAM, J. C., LAVAL, G. & PESME, D. 1979 Reconsideration of quasilinear theory. *Physical Review Letters* **43** (22), 1671–1675.
- ANDERSON, J., NORDMAN, H., SINGH, R. & WEILAND, J. 2002 Zonal flow generation in ion temperature gradient mode turbulence. *Physics of Plasmas* **9** (11), 4500–4506.
- ANDERSON, J., NORDMAN, H., SINGH, R. & WEILAND, J. 2006 Zonal flow generation in collisionless trapped electron mode turbulence. *Plasma Physics and Controlled Fusion* **48** (5), 651–661.
- ANTOULAS, A. C., BEATTIE, C. A. & GUGERCIN, S. 2010 Interpolatory model reduction of large-scale dynamical systems. In *Efficient Modeling and Control of Large-Scale Systems*, pp. 3–58. Springer US.
- ARNOLD, V. 1966 Sur la géométrie différentielle des groupes de lie de dimension infinie et ses applications à lhydrodynamique des fluides parfaits. In *Annales de l'institut Fourier*, , vol. 16, pp. 319–361. Cellule MathDoc/CEDRAM.
- ARNOLD, V. I. & KHESIN, B. A. 1999 *Topological Methods in Hydrodynamics*. Springer.
- ASHOURVAN, A. & DIAMOND, P. H. 2016 How mesoscopic staircases condense to macroscopic barriers in confined plasma turbulence. *Physical Review E* **94** (5).
- ASHOURVAN, A. & DIAMOND, P. H. 2017 On the emergence of macroscopic transport barriers from staircase structures. *Physics of Plasmas* **24** (1), 012305.
- BALMFORTH, N. J., SMITH, S. G. L. & YOUNG, W. R. 1998 Dynamics of interfaces and layers in a stratified turbulent fluid. *Journal of Fluid Mechanics* **355**, 329–358.
- BEATTIE, C. & GUGERCIN, S. 2012 Realization-independent  $\mathcal{H}_2$ -approximation. In *2012 IEEE 51st IEEE Conference on Decision and Control (CDC)*. IEEE.
- BEATTIE, C. & GUGERCIN, S. 2017 Model reduction by rational interpolation. In *Model Reduction and Approximation*, pp. 297–334. Society for Industrial and Applied Mathematics, arXiv: arxiv:1409.2140.
- BENNER, P. & BREITEN, T. 2012 Interpolation-based  $H_2$ -model reduction of bilinear control systems. *SIAM Journal on Matrix Analysis and Applications* **33** (3), 859–885.
- BENNER, P. & DAMM, T. 2011 Lyapunov equations, energy functionals, and model order reduction of bilinear and stochastic systems. *SIAM Journal on Control and Optimization* **49** (2), 686–711.
- BENNEY, D. J. & SAFFMAN, P. G. 1966 Nonlinear interactions of random waves in a dispersive medium. *Proceedings of the Royal Society A: Mathematical, Physical and Engineering Sciences* **289** (1418), 301–320.

- BESSE, N., ELSKENS, Y., ESCANDE, D. F. & BERTRAND, P. 2011 Validity of quasilinear theory: refutations and new numerical confirmation. *Plasma Physics and Controlled Fusion* **53** (2), 025012.
- BEYER, P., BENKADDA, S., GARBET, X. & DIAMOND, P. H. 2000 Nondiffusive transport in tokamaks: Three-dimensional structure of bursts and the role of zonal flows. *Physical Review Letters* **85** (23), 4892–4895.
- BIGLARI, H., DIAMOND, P. H. & TERRY, P. W. 1990 Influence of sheared poloidal rotation on edge turbulence. *Physics of Fluids B: Plasma Physics* **2** (1), 1–4.
- BOTTINO, A., SCOTT, B., BRUNNER, S., McMILLAN, B. F., TRAN, T. M., VERNAY, T., VILLARD, L., JOLLIET, S., HATZKY, R. & PEETERS, A. G. 2010 Global nonlinear electromagnetic simulations of tokamak turbulence. *IEEE Transactions on Plasma Science* **38** (9), 2129–2135.
- BOURDELLE, C., GARBET, X., HOANG, G. T., ONGENA, J. & BUDNY, R. 2002 Stability analysis of improved confinement discharges: internal transport barriers in tore supra and radiative improved mode in TEXTOR. *Nuclear Fusion* **42** (7), 892–902.
- BOURDELLE, C., GARBET, X., IMBEAUX, F., CASATI, A., DUBUIT, N., GUIRLET, R. & PARISOT, T. 2007 A new gyrokinetic quasilinear transport model applied to particle transport in tokamak plasmas. *Physics of Plasmas* **14** (11), 112501.
- BRIARD, A. 2017 Modelling of transport in homogeneous turbulence. Theses, UPMC - Université Paris 6 Pierre et Marie Curie ; Institut Jean le Rond d’Alembert.
- BRIZARD, A. 1992 Nonlinear gyrofluid description of turbulent magnetized plasmas. *Physics of Fluids B: Plasma Physics* **4** (5), 1213–1228.
- BRIZARD, A. J. 2017 Variational principle for the parallel-symplectic representation of electromagnetic gyrokinetic theory. *Physics of Plasmas* **24** (8), 081201, arXiv: 1702.04747v2.
- BRIZARD, A. J. & HAHM, T. S. 2007 Foundations of nonlinear gyrokinetic theory. *Reviews of Modern Physics* **79** (2), 421–468.
- BRIZARD, A. J. & TRONKO, N. 2011 Exact momentum conservation laws for the gyrokinetic vlasov-poisson equations. *Physics of Plasmas* **18** (8), 082307, arXiv: 1105.1145v2.
- BROCHARD, G. 2020 Dynamics of ion-driven fishbones in tokamaks: theory and nonlinear full scale simulations. PhD thesis.
- BROCHARD, G., DUMONT, R., LÜTJENS, H. & GARBET, X. 2020 Linear stability of the iter 15 ma scenario against the alpha fishbone , arXiv: <http://arxiv.org/abs/2002.02191v1>.
- BROWN, L. G. 1992 A survey of image registration techniques. *ACM Computing Surveys* **24** (4), 325–376.
- BUSSAC, M. N., PELLAT, R., EDERY, D. & SOULE, J. L. 1975 Internal kink modes in toroidal plasmas with circular cross sections. *Physical Review Letters* **35** (24), 1638–1641.
- CANDY, J. & BELLI, E. 2015 *GYRO Technical Guide*.
- CANDY, J. & WALTZ, R. E. 2003a Anomalous transport scaling in the DIII-D tokamak matched by supercomputer simulation. *Physical Review Letters* **91** (4).
- CANDY, J. & WALTZ, R. E. 2003b An Eulerian gyrokinetic-Maxwell solver. *Journal of Computational Physics* **186** (2), 545–581.
- CARRERAS, B. A., HIDALGO, C., SÁNCHEZ, E., PEDROSA, M. A., BALBÍN, R., GARCÍA-CORTÉS, I., VAN MILLIGEN, B., NEWMAN, D. E. & LYNCH, V. E. 1996 Fluctuation-induced flux at the plasma edge in toroidal devices. *Physics of Plasmas* **3** (7), 2664–2672.

- CARRERAS, B. A., NEWMAN, D., DIAMOND, P. H. & LIANG, Y.-M. 1994 Dynamics of low to high (“l” to “h”) confinement bifurcation: Poloidal flow and ion pressure gradient evolution **1** (12), 4014–4021.
- CASATI, A., BOURDELLE, C., GARBET, X., IMBEAUX, F., CANDY, J., CLAIRET, F., DIF-PRADALIER, G., FALCHETTO, G., GERBAUD, T., GRANDGIRARD, V., ÖZGÜR, D. GÜRCAN, HENNEQUIN, P., KINSEY, J., OTTAVIANI, M., SABOT, R., SARAZIN, Y., VERMARE, L. & WALTZ, R. E. 2009 Validating a quasi-linear transport model versus nonlinear simulations. *Nuclear Fusion* **49** (8), 085012.
- CASCHERA, E. 2019 Global confinement properties of tokamak plasmas in global, flux-driven, gyrokinetic simulations. Theses, Aix-Marseille Université, Marseille, France.
- CENDRA, H., HOLM, D. D., HOYLE, M. J. W. & MARSDEN, J. E. 1998 The maxwell–vlasov equations in euler–poincaré form. *Journal of Mathematical Physics* **39** (6), 3138–3157, arXiv: chaos-dyn/9801016v1.
- CHAMPEAUX, S. & DIAMOND, P. H. 2001 Streamer and zonal flow generation from envelope modulations in drift wave turbulence. *Physics Letters A* **288** (3-4), 214–219.
- CHANG, Z. & CALLEN, J. D. 1992 Unified fluid/kinetic description of plasma microinstabilities. Part I: Basic equations in a sheared slab geometry. *Physics of Fluids B: Plasma Physics* **4** (5), 1167–1181.
- CHARNEY, J. G. & DRAZIN, P. G. 1961 Propagation of planetary-scale disturbances from the lower into the upper atmosphere. *Journal of Geophysical Research* **66** (1), 83–109.
- CHEN, L., LIN, Z. & WHITE, R. 2000 Excitation of zonal flow by drift waves in toroidal plasmas. *Physics of Plasmas* **7** (8), 3129–3132.
- CITRIN, J., BOURDELLE, C., CASSON, F. J., ANGIANI, C., BONANOMI, N., CAMENEN, Y., GARBET, X., GARZOTTI, L., GÖRLER, T., GÜRCAN, O., KOEHL, F., IMBEAUX, F., LINDER, O., VAN DE PLASSCHE, K., STRAND, P. & AND, G. S. 2017 Tractable flux-driven temperature, density, and rotation profile evolution with the quasilinear gyrokinetic transport model QuaLiKiz. *Plasma Physics and Controlled Fusion* **59** (12), 124005.
- COTTER, C. J. & HOLM, D. D. 2012 On noether’s theorem for the euler–poincaré equation on the diffeomorphism group with advected quantities, arXiv: <http://arxiv.org/abs/1206.2976v1>.
- CROUSEILLES, N., RESPAUD, T. & SONNENDRÜCKER, E. 2009 A forward semi-lagrangian method for the numerical solution of the vlasov equation. *Computer Physics Communications* **180** (10), 1730–1745.
- CUMMINGS, J. 1996 Gyrokinetic simulation of finite-beta and self-generated sheared-flow effects on pressure-gradient-driven instabilities. PhD thesis.
- DAGNELIE, V. I., CITRIN, J., JENKO, F., PUESCHEL, M. J., GÖRLER, T., TOLD, D. & DOERK, H. 2019 Growth rates of ITG modes in the presence of flow shear. *Physics of Plasmas* **26** (1), 012502.
- DIAMOND, P. H. & HAHM, T. S. 1995 On the dynamics of turbulent transport near marginal stability. *Physics of Plasmas* **2** (10), 3640–3649.
- DIAMOND, P. H., ITOH, S.-I. & ITOH, K. 2010 *Modern Plasma Physics: Volume 1, Physical Kinetics of Turbulent Plasmas*. Cambridge University Press.
- DIAMOND, P. H., ITOH, S.-I., ITOH, K. & HAHM, T. S. 2005 Zonal flows in plasma—a review. *Plasma Physics and Controlled Fusion* **47** (5), 35–161.
- DIF-PRADALIER, G., CASCHERA, E., GHENDRIH, P., ASAHY, Y., DONNEL, P., GARBET, X., GRANDGIRARD, V., LATU, G., NORSCINI, C. & SARAZIN, Y. 2017a Evidence for global edge–core interplay in fusion plasmas. *Plasma and Fusion Research: Rapid Communications* **12** (1203012).

- DIF-PRADALIER, G., DIAMOND, P. H., GRANDGIRARD, V., SARAZIN, Y., ABITEBOUL, J., GARBET, X., GHENDRIH, P., STRUGAREK, A., KU, S. & CHANG, C. S. 2010 On the validity of the local diffusive paradigm in turbulent plasma transport. *Physical Review E* **82** (2), 025401.
- DIF-PRADALIER, G., GRANDGIRARD, V., SARAZIN, Y., GARBET, X. & GHENDRIH, P. 2009 Interplay between gyrokinetic turbulence, flows, and collisions: Perspectives on transport and poloidal rotation. *Physical Review Letters* **103** (6).
- DIF-PRADALIER, G., HORNING, G., GARBET, X., GHENDRIH, P., GRANDGIRARD, V., LATU, G. & SARAZIN, Y. 2017*b* The  $\mathbf{E} \times \mathbf{B}$  staircase of magnetised plasmas. *Nuclear Fusion* **57** (6), 066026.
- DIF-PRADALIER, G., HORNING, G., GHENDRIH, P., SARAZIN, Y., CLAIRET, F., VERMARE, L., DIAMOND, P. H., ABITEBOUL, J., CARTIER-MICHAUD, T., EHRLACHER, C., ESTÈVE, D., GARBET, X., GRANDGIRARD, V., GÜRCAN, Ö. D., HENNEQUIN, P., KOSUGA, Y., LATU, G., MAGET, P., MOREL, P., NORSCINI, C., SABOT, R. & STORELLI, A. 2015 Finding the elusive  $\mathbf{E} \times \mathbf{B}$  staircase in magnetized plasmas. *Physical Review Letters* **114** (8).
- DIMITS, A. M., BATEMAN, G., BEER, M. A., COHEN, B. I., DORLAND, W., HAMMETT, G. W., KIM, C., KINSEY, J. E., KOTSCHENREUTHER, M., KRITZ, A. H., LAO, L. L., MANDREKAS, J., NEVINS, W. M., PARKER, S. E., REDD, A. J., SHUMAKER, D. E., SYDORA, R. & WEILAND, J. 2000 Comparisons and physics basis of tokamak transport models and turbulence simulations. *Physics of Plasmas* **7** (3), 969–983.
- DODIN, I. Y. & FISCH, N. J. 2012 Adiabatic nonlinear waves with trapped particles. I. general formalism. *Physics of Plasmas* **19** (1), 012102.
- DORLAND, W., JENKO, F., KOTSCHENREUTHER, M. & ROGERS, B. N. 2000 Electron temperature gradient turbulence. *Physical Review Letters* **85** (26), 5579–5582.
- DRAKE, J. F. & LEE, Y. C. 1977 Kinetic theory of tearing instabilities. *Physics of Fluids* **20** (8), 1341.
- EBIN, D. G. & MARSDEN, J. 1970 Groups of diffeomorphisms and the motion of an incompressible fluid. *Annals of Mathematics* **92** (1).
- ELSKENS, Y. & ESCANDE, D. 2002 *Microscopic Dynamics of Plasmas and Chaos*. CRC Press.
- FARRELL, B. F. & IOANNOU, P. J. 2007 Structure and spacing of jets in barotropic turbulence. *Journal of the Atmospheric Sciences* **64** (10), 3652–3665.
- FRIED, B. D. & CONTE, S. D. 1961 The plasma dispersion function.
- G. LAVAL, D. P. & ADAM, J.-C. 2018 Wave-particle and wave-wave interactions in hot plasmas: a french historical point of view. *The European Physical Journal H* **43** (4-5), 421–458.
- GARBET, X. 2001 Instabilités, turbulence et transport dans un plasma magnétisé.
- GARBET, X., LAURENT, L., SAMAIN, A. & CHINARDET, J. 1994 Radial propagation of turbulence in tokamaks **34** (7), 963–974.
- GARBET, X., SARAZIN, Y., BEYER, P., GHENDRIH, P., WALTZ, R., OTTAVIANI, M. & BENKADDA, S. 1999 Flux driven turbulence in tokamaks. *Nuclear Fusion* **39**, 2063–2068.
- GARBET, X., SARAZIN, Y., GHENDRIH, P., BENKADDA, S., BEYER, P., FIGARELLA, C. & VOITSEKHOVITCH, I. 2002 Turbulence simulations of transport barriers with toroidal velocity. *Physics of Plasmas* **9** (9), 3893–3905.
- GARBET, X. & WALTZ, R. E. 1998 Heat flux driven ion turbulence. *Physics of Plasmas* **5** (8), 2836–2845.

- GHENDRIH, P., SARAZIN, Y., ATTUEL, G., BENKADDA, S., BEYER, P., FALCHETTO, G., FIGARELLA, C., GARBET, X., GRANDGIRARD, V. & OTTAVIANI, M. 2003 Theoretical analysis of the influence of external biasing on long range turbulent transport in the scrape-off layer. *Nuclear Fusion* **43** (10), 1013–1022.
- GILLOT, C. 2016 Study of the interaction between drift wave turbulence and zonal flows in a magnetic confinement device. Master’s thesis, Université Paris-Saclay.
- GILLOT, C., DIF-PRADALIER, G., GARBET, X., PANICO, O., SARAZIN, Y., VARENNES, R. & ZARZOSO, D. 2020a Investigation of tokamak turbulent avalanches using wave-kinetic formulation in toroidal geometry .
- GILLOT, C., DIF-PRADALIER, G., SARAZIN, Y., BOURDELLE, C., GARBET, X., GHENDRIH, P., GRANDGIRARD, V., PASSERON, C., CAMENEN, Y. & WIDMER, F. 2020b Failure of quasilinear modelling of flux-driven turbulent transport .
- GILLOT, C., DIF-PRADALIER, G., GARBET, X., GHENDRIH, P., GRANDGIRARD, V. & SARAZIN, Y. 2020c Model order reduction approach to one-dimensional collisionless closure problem .
- GIRARDO, J.-B. 2015 Control of instabilities and turbulence by fast particles in fusion plasmas. Theses, Ecode doctorale de l’Ecole Polytechnique (EDX).
- GOODRICH, L. C. 1972 General recurrence relation for use in evaluating moments of the integrand of the plasma dispersion function. *Physics of Fluids* **15** (4), 715.
- GOSEA, I. V. 2017 Model order reduction of linear and nonlinear systems in the loewner framework. PhD thesis.
- GOSEA, I. V. & ANTOULAS, A. C. 2017 Approximation of a damped Euler-Bernoulli beam model in the Loewner framework , arXiv: 1712.06031v1.
- GRANDGIRARD, V., ABITEBOUL, J., BIGOT, J., CARTIER-MICHAUD, T., CROUSEILLES, N., DIF-PRADALIER, G., EHRLACHER, C., ESTEVE, D., GARBET, X., GHENDRIH, P., LATU, G., MEHRENBERGER, M., NORSCINI, C., PASSERON, C., ROZAR, F., SARAZIN, Y., SONNENDRÜCKER, E., STRUGAREK, A. & ZARZOSO, D. 2016 A 5D gyrokinetic full- $f$  global semi-lagrangian code for flux-driven ion turbulence simulations. *Computer Physics Communications* **207**, 35–68.
- GRANDGIRARD, V., GARBET, X., EHRLACHER, C., BIANCALANI, A., BOTTINO, A., NOVIKAU, I., ASAHI, Y., CASCHERA, E., DIF-PRADALIER, G., DONNEL, P., GHENDRIH, P., GILLOT, C., LATU, G., PASSERON, C., SARAZIN, Y. & ZARZOSO, D. 2019 Linear collisionless dynamics of the GAM with kinetic electrons: Comparison simulations/theory. *Physics of Plasmas* **26** (12), 122304.
- GRIVET-TALOCIA, S. & GUSTAVSEN, B. 2016 *Passive macromodeling*. Hoboken, New Jersey: John Wiley & Sons, Inc.
- GUGERCIN, S. 2017 Model reduction via interpolation.
- GUGERCIN, S., ANTOULAS, A. & BEATTIE, C. 2006 A rational Krylov iteration for optimal H2 model reduction. In *Proceedings of MTNS*, , vol. 2006.
- GUGERCIN, S. & ANTOULAS, A. C. 2004 A survey of model reduction by balanced truncation and some new results. *International Journal of Control* **77** (8), 748–766.
- GUSTAVSEN, B. & SEMLYEN, A. 1999 Rational approximation of frequency domain responses by vector fitting. *IEEE Transactions on Power Delivery* **14** (3), 1052–1061.
- GÖRLER, T. & JENKO, F. 2008 Scale separation between electron and ion thermal transport. *Physical Review Letters* **100** (18).

- GÖRLER, T., LAPILLONNE, X., BRUNNER, S., DANNERT, T., JENKO, F., MERZ, F. & TOLD, D. 2011 The global version of the gyrokinetic turbulence code GENE. *Journal of Computational Physics* **230** (18), 7053–7071.
- HAHM, T. S., BEER, M. A., LIN, Z., HAMMETT, G. W., LEE, W. W. & TANG, W. M. 1999 Shearing rate of time-dependent  $e \times b$  flow. *Physics of Plasmas* **6** (3), 922–926.
- HAHM, T. S., DIAMOND, P. H., LIN, Z., ITOH, K. & ITOH, S.-I. 2004 Turbulence spreading into the linearly stable zone and transport scaling. *Plasma Physics and Controlled Fusion* **46** (5A), 323–333.
- HAHM, T. S. & TANG, W. M. 1989 Properties of ion temperature gradient drift instabilities in h-mode plasmas. *Physics of Fluids B: Plasma Physics* **1** (6), 1185–1192.
- HALLATSCHEK, K. & BISKAMP, D. 2001 Transport control by coherent zonal flows in the core/edge transitional regime. *Physical Review Letters* **86** (7), 1223–1226.
- HALLATSCHEK, K. & DIAMOND, P. H. 2003 Modulational instability of drift waves. *New Journal of Physics* **5**, 29–29.
- HAMED, M. 2019 Electron heat transport in tokamak H-mode pedestals. Theses, Aix Marseille Université.
- HAMMETT, G. W. & PERKINS, F. W. 1990 Fluid moment models for Landau damping with application to the ion-temperature-gradient instability. *Physical Review Letters* **64** (25), 3019–3022.
- HASEGAWA, A. & MIMA, K. 1978 Pseudo-three-dimensional turbulence in magnetized nonuniform plasma. *Physics of Fluids* **21** (1), 87.
- HATCH, D. R., TERRY, P. W., JENKO, F., MERZ, F. & NEVINS, W. M. 2011 Saturation of gyrokinetic turbulence through damped eigenmodes. *Physical Review Letters* **106** (11).
- HATZKY, R., KÖNIES, A. & MISHCHENKO, A. 2007 Electromagnetic gyrokinetic PIC simulation with an adjustable control variates method. *Journal of Computational Physics* **225** (1), 568–590.
- HELANDER, P. & SIGMAR, D. J. 2005 *Collisional Transport in Magnetized Plasmas*. Cambridge University Press.
- HINTON, F. L. 1991 Thermal confinement bifurcation and the l- to h-mode transition in tokamaks. *Physics of Fluids B: Plasma Physics* **3** (3), 696–704.
- HOLM, D. D., MARSDEN, J. E. & RATIU, T. S. 1998 The Euler–Poincaré equations and semidirect products with applications to continuum theories. *Advances in Mathematics* **137** (1), 1–81.
- HOPF, E. 1952 Statistical hydromechanics and functional calculus **1** (1), 87–123.
- HUNANA, P., ZANK, G. P., LAURENZA, M., TENERANI, A., WEBB, G. M., GOLDSTEIN, M. L., VELLI, M. & ADHIKARI, L. 2018 New closures for more precise modeling of Landau damping in the fluid framework. *Physical Review Letters* **121** (13), arXiv: <http://arxiv.org/abs/1809.05718v1>.
- HWA, T. & KARDAR, M. 1992 Avalanches, hydrodynamics, and discharge events in models of sandpiles. *Physical Review A* **45** (10), 7002–7023.
- IDOMURA, Y. 2016 A new hybrid kinetic electron model for full-f gyrokinetic simulations. *Journal of Computational Physics* **313**, 511–531.
- IDOMURA, Y., URANO, H., AIBA, N. & TOKUDA, S. 2009 Study of ion turbulent transport and profile formations using global gyrokinetic full-f Vlasov simulation. *Nuclear Fusion* **49** (6), 065029.

- ITOH, K. & ITOH, S.-I. 2016 A structural bifurcation of transport in toroidal plasmas. *Plasma Physics and Controlled Fusion* **58** (4), 045017.
- ITOH, S.-I., ITOH, K., FUKUYAMA, A. & YAGI, M. 1994 Theory of anomalous transport in H-mode plasmas. *Physical Review Letters* **72** (8), 1200–1203.
- JENKO, F., DANNERT, T. & ANGIONI, C. 2005 Heat and particle transport in a tokamak: advances in nonlinear gyrokinetics. *Plasma Physics and Controlled Fusion* **47** (12B), B195–B206.
- JENKO, F., DORLAND, W. & HAMMETT, G. W. 2001 Critical gradient formula for toroidal electron temperature gradient modes. *Physics of Plasmas* **8** (9), 4096–4104.
- JIMENEZ, J. & WHITHAM, G. B. 1976 An averaged Lagrangian method for dissipative wavetrains. *Proceedings of the Royal Society of London. A. Mathematical and Physical Sciences* **349** (1658), 277–287.
- JOLLIFFE, I. 2002 *Principal Component Analysis*. Springer-Verlag GmbH.
- KARACHALIOS, D. S., GOSEA, I. V. & ANTOULAS, A. C. 2018 Data-driven approximation methods applied to non-rational functions. *PAMM* **18** (1).
- KAUFMAN, A. N., YE, H. & HUI, Y. 1987 Variational formulation of covariant eikonal theory for vector waves. *Physics Letters A* **120** (7), 327–330.
- KLEIBER, R., HATZKY, R., KÖNIES, A., MISHCHENKO, A. & SONNENDRÜCKER, E. 2016 An explicit large time step particle-in-cell scheme for nonlinear gyrokinetic simulations in the electromagnetic regime. *Physics of Plasmas* **23** (3), 032501.
- KOSUGA, Y., DIAMOND, P. H., DIF-PRADALIER, G. & GÜRCAN, O. D. 2014  $E \times b$  shear pattern formation by radial propagation of heat flux waves. *Physics of Plasmas* **21** (5), 055701.
- KOTSCHENREUTHER, M., DORLAND, W., BEER, M. A. & HAMMETT, G. W. 1995 Quantitative predictions of tokamak energy confinement from first-principles simulations with kinetic effects. *Physics of Plasmas* **2** (6), 2381–2389.
- KROMMES, J. A. 2002 Fundamental statistical descriptions of plasma turbulence in magnetic fields. *Physics Reports* **360** (1-4), 1–352.
- LANDAU, L. D. & LIFSHITZ, E. M. 1984 *Electrodynamics of continuous media*. Oxford Oxfordshire New York: Pergamon.
- LANDREMAN, M. & CATTO, P. J. 2010 Trajectories, orbit squeezing and residual zonal flow in a tokamak pedestal. *Plasma Physics and Controlled Fusion* **52** (8), 085003.
- LATU, G., MEHRENBERGER, M., GÜÇLÜ, Y., OTTAVIANI, M. & SONNENDRÜCKER, E. 2017 Field-aligned interpolation for semi-lagrangian gyrokinetic simulations. *Journal of Scientific Computing* **74** (3), 1601–1650.
- LAWSON, J. D. 1957 Some criteria for a power producing thermonuclear reactor. *Proceedings of the Physical Society. Section B* **70** (1), 6–10.
- LEE, W. 1986 Gyrokinetic particle simulation model. *Tech. Rep.*.
- LEFTERIU, S., ANTOULAS, A. C. & IONITA, A. C. 2011 Parametric model reduction in the Loewner framework. *IFAC Proceedings Volumes* **44** (1), 12751–12756.
- LEHTINEN, N. G. 2010 Error functions.
- LIN, Z., ETHIER, S., HAHM, T. S. & TANG, W. M. 2002 Size scaling of turbulent transport in magnetically confined plasmas. *Physical Review Letters* **88** (19).
- LIONS, P. L., PAPANICOLAOU, G. & VARADHAN, S. R. S. 1987 Homogenization of hamilton-jacobi equations.

- LUKACS, E. 1970 Characteristic functions .
- MA, C., ZHU, B., XU, X.-Q. & WANG, W. 2020 Machine learning surrogate models for Landau fluid closure. *Physics of Plasmas* **27** (4), 042502.
- MADSEN, J. 2013 Full-f gyrofluid model. *Physics of Plasmas* **20** (7), 072301.
- MAGET, P. 2009 An introduction to magneto-hydro-dynamics in tokamaks.
- MALKOV, M. A. & DIAMOND, P. H. 2008 Analytic theory of l→h transition, barrier structure, and hysteresis for a simple model of coupled particle and heat fluxes. *Physics of Plasmas* **15** (12), 122301.
- MANFREDI, G., ROACH, C. M. & DENDY, R. O. 2001 Zonal flow and streamer generation in drift turbulence. *Plasma Physics and Controlled Fusion* **43** (6), 825–837.
- MARSDEN, J. E. & WEINSTEIN, A. 1981 The hamiltonian structure of the maxwell-vlasov equations. .
- MARSTON, J. B., CONOVER, E. & SCHNEIDER, T. 2008 Statistics of an unstable barotropic jet from a cumulant expansion. *Journal of the Atmospheric Sciences* **65** (6), 1955–1966.
- MATTOR, N. & PARKER, S. E. 1997 Nonlinear kinetic fluid equations. *Physical Review Letters* **79** (18), 3419–3422.
- MAYO, A. & ANTOULAS, A. 2007 A framework for the solution of the generalized realization problem. *Linear Algebra and its Applications* **425** (2-3), 634–662.
- MCDONALD, S. W. 1988 Phase-space representations of wave equations with applications to the eikonal approximation for short-wavelength waves. *Physics Reports* **158** (6), 337–416.
- MCDONALD, S. W. 1991 Wave kinetic equation in a fluctuating medium. *Physical Review A* **43** (8), 4484–4499.
- MCDONALD, S. W., GREBOGI, C. & KAUFMAN, A. N. 1985 Locally coupled evolution of wave and particle distribution in general magnetoplasma geometry. *Physics Letters A* **111** (1-2), 19–21.
- MCDONALD, S. W. & KAUFMAN, A. N. 1985 Weyl representation for electromagnetic waves: The wave kinetic equation. *Physical Review A* **32** (3), 1708–1713.
- MCINTYRE, M. E. 2014 The atmospheric wave–turbulence jigsaw **2**, 1.
- MCMILLAN, B. F., JOLLIET, S., TRAN, T. M., VILLARD, L., BOTTINO, A. & ANGELINO, P. 2009 Avalanchelike bursts in global gyrokinetic simulations. *Physics of Plasmas* **16** (2), 022310.
- MELROSE, D. B. 1989 *Instabilities in Space and Laboratory Plasmas*. Cambridge University Press.
- MIGLIANO, P., CAMENEN, Y., CASSON, F. J., HORNSBY, W. A. & PEETERS, A. G. 2013 Ion temperature gradient instability at sub-larmor radius scales with non-zero ballooning angle. *Physics of Plasmas* **20** (2), 022101.
- MIKI, K. & DIAMOND, P. H. 2010 Role of the geodesic acoustic mode shearing feedback loop in transport bifurcations and turbulence spreading. *Physics of Plasmas* **17** (3), 032309.
- MIKI, K., DIAMOND, P. H., GÜRCAN, Ö. D., TYNAN, G. R., ESTRADA, T., SCHMITZ, L. & XU, G. S. 2012 Spatio-temporal evolution of the L→I→H transition. *Physics of Plasmas* **19** (9), 092306.
- MISHCHENKO, A., BOTTINO, A., BIANCALANI, A., HATZKY, R., HAYWARD-SCHNEIDER, T., OHANA, N., LANTI, E., BRUNNER, S., VILLARD, L., BORCHARDT, M., KLEIBER, R. & KÖNIES, A. 2019 Pullback scheme implementation in ORB5. *Computer Physics Communications* **238**, 194–202.

- MISHCHENKO, A., BOTTINO, A., HATZKY, R., SONNENDRÜCKER, E., KLEIBER, R. & KÖNIES, A. 2017 Mitigation of the cancellation problem in the gyrokinetic particle-in-cell simulations of global electromagnetic modes. *Physics of Plasmas* **24** (8), 081206.
- MISHCHENKO, A., COLE, M., KLEIBER, R. & KÖNIES, A. 2014a New variables for gyrokinetic electromagnetic simulations. *Physics of Plasmas* **21** (5), 052113.
- MISHCHENKO, A., KÖNIES, A., KLEIBER, R. & COLE, M. 2014b Pullback transformation in gyrokinetic electromagnetic simulations. *Physics of Plasmas* **21** (9), 092110.
- MOORE, B. 1981 Principal component analysis in linear systems: Controllability, observability, and model reduction. *IEEE Transactions on Automatic Control* **26** (1), 17–32.
- MOUHOT, C. & VILLANI, C. 2009 Landau damping .
- MOYAL, J. E. & BARTLETT, M. S. 1949 Quantum mechanics as a statistical theory. *Mathematical Proceedings of the Cambridge Philosophical Society* **45** (01), 99.
- MULLIS, C. & ROBERTS, R. 1976 Synthesis of minimum roundoff noise fixed point digital filters. *IEEE Transactions on Circuits and Systems* **23** (9), 551–562.
- NACE, N. 2018 Dynamics of driven and spontaneous transport barriers in the edge plasma of tokamaks. PhD thesis.
- NASR, S. 2018 Fluid and kinetic descriptions of the mutual interaction between tearing modes and thermal and energetic particles in tokamak plasmas.
- NEWELL, A. C. 1968 The closure problem in a system of random gravity waves. *Reviews of Geophysics* **6** (1), 1.
- NEWMAN, D. E., CARRERAS, B. A., DIAMOND, P. H. & HAHM, T. S. 1996 The dynamics of marginality and self-organized criticality as a paradigm for turbulent transport. *Physics of Plasmas* **3** (5), 1858–1866.
- PAPARELLA, F. & VON HARDENBERG, J. 2012 Clustering of salt fingers in double-diffusive convection leads to staircaselike stratification. *Physical Review Letters* **109** (1).
- PAPARELLA, F. & VON HARDENBERG, J. 2014 A model for staircase formation in fingering convection. *Acta Applicandae Mathematicae* **132** (1), 457–467.
- PARKER, J. B. 2015 Zonal flows and turbulence in fluids and plasmas. PhD thesis, Princeton University.
- PARKER, J. B. 2016 Dynamics of zonal flows: failure of wave-kinetic theory, and new geometrical optics approximations. *Journal of Plasma Physics* **82** (6), arXiv: 1604.06904.
- PEARSON, K. 1901 LIII. On lines and planes of closest fit to systems of points in space. *Philosophical Magazine Series 6* **2** (11), 559–572.
- PEETERS, A., CAMENEN, Y., CASSON, F., HORNSBY, W., SNODIN, A., STRINTZI, D. & SZEPESE, G. 2009 The nonlinear gyro-kinetic flux tube code GKW. *Computer Physics Communications* **180** (12), 2650–2672.
- PEETERS, A. G., BUCHHOLZ, R., CAMENEN, Y., CASSON, F. J., GROSSHAUSER, S., HORNSBY, W. A., MANAS, P., MIGLIANO, P., SICCINIO, M., SNODIN, A. P., STRINTZI, D., SUNG, T., SZEPESE, G. & ZARZOSO, D. 2007 *GKW how and why*.
- PEETERS, A. G., RATH, F., BUCHHOLZ, R., CAMENEN, Y., CANDY, J., CASSON, F. J., GROSSHAUSER, S. R., HORNSBY, W. A., STRINTZI, D. & WEIKL, A. 2016 Gradient-driven flux-tube simulations of ion temperature gradient turbulence close to the non-linear threshold. *Physics of Plasmas* **23** (8), 082517.

- PENZL, T. 2006 Algorithms for model reduction of large dynamical systems. *Linear Algebra and its Applications* **415** (2-3), 322–343.
- VAN DE PLASSCHE, K. L., CITRIN, J., BOURDELLE, C., CAMENEN, Y., CASSON, F. J., DAGNELIE, V. I., FELICI, F., HO, A. & AND, S. V. M. 2020 Fast modeling of turbulent transport in fusion plasmas using neural networks. *Physics of Plasmas* **27** (2), 022310.
- PONTES DUFF PEREIRA, I. 2017 Large-scale and infinite dimensional dynamical model approximation. PhD thesis.
- POPE, S. B. 2000 *Turbulent Flows*. Cambridge University Pr.
- PORCELLI, F. 1991 Collisionless  $m=1$  tearing mode. *Physical Review Letters* **66** (4), 425–428.
- PRINGLE, C. C. T., MCMILLAN, B. F. & TEACA, B. 2017 A nonlinear approach to transition in subcritical plasmas with sheared flow. *Physics of Plasmas* **24** (12), 122307.
- QIU, Z., CHEN, L. & ZONCA, F. 2018 Kinetic theory of geodesic acoustic modes in toroidal plasmas: a brief review. *Plasma Science and Technology* **20** (9), 094004.
- RAX, J.-M. 2005 *Physique des plasmas : Cours et applications*. DUNOD.
- REIS, T. & STYKEL, T. 2009 Positive real and bounded real balancing for model reduction of descriptor systems. *International Journal of Control* **83** (1), 74–88.
- ROMANELLI, F. & BRIGUGLIO, S. 1990 Toroidal semicollisional microinstabilities and anomalous electron and ion transport. *Physics of Fluids B: Plasma Physics* **2** (4), 754–763.
- ROWLEY, C. W. 2005 Model reduction for fluids, using balanced proper orthogonal decomposition. *International Journal of Bifurcation and Chaos* **15** (03), 997–1013.
- RUIZ, D. E. 2017 A geometric theory of waves and its applications to plasma physics. PhD thesis, Princeton University.
- RUIZ, D. E., GLINSKY, M. E. & DODIN, I. Y. 2019 Wave kinetic equation for inhomogeneous drift-wave turbulence beyond the quasilinear approximation. *Journal of Plasma Physics* **85** (1).
- RUIZ, D. E., PARKER, J. B., SHI, E. L. & DODIN, I. Y. 2016 Zonal-flow dynamics from a phase-space perspective. *Physics of Plasmas* **23** (12), 122304.
- SARAZIN, Y., DIF-PRADALIER, G., ZARZOSO, D., GARBET, X., GHENDRIH, P. & GRANDGIRARD, V. 2009 Entropy production and collisionless fluid closure. *Plasma Physics and Controlled Fusion* **51** (11), 115003.
- SARAZIN, Y. & GHENDRIH, P. 1998 Intermittent particle transport in two-dimensional edge turbulence. *Physics of Plasmas* **5** (12), 4214–4228.
- SARAZIN, Y., GRANDGIRARD, V., ABITEBOUL, J., ALLFREY, S., GARBET, X., GHENDRIH, P., LATU, G., STRUGAREK, A. & DIF-PRADALIER, G. 2010 Large scale dynamics in flux driven gyrokinetic turbulence. *Nuclear Fusion* **50** (5), 054004.
- SARAZIN, Y., GRANDGIRARD, V., FLEURENCE, E., GARBET, X., GHENDRIH, P., BERTRAND, P. & DEPRET, G. 2005 Kinetic features of interchange turbulence. *Plasma Physics and Controlled Fusion* **47** (10), 1817–1839.
- SASAKI, M. 2018 Trapping of turbulence clumps by geodesic acoustic modes. In *AIP Conference Proceedings 1993*, 020007.
- SASAKI, M., ITOH, K., HALLATSCHKE, K., KASUYA, N., LESUR, M., KOSUGA, Y. & ITOH, S.-I. 2017 Enhancement and suppression of turbulence by energetic-particle-driven geodesic acoustic modes. *Scientific Reports* **7** (1).

- SASAKI, M., ITOH, K., KOBAYASHI, T., KASUYA, N., FUJISAWA, A. & ITOH, S.-I. 2018a Propagation direction of geodesic acoustic modes driven by drift wave turbulence. *Nuclear Fusion* **58** (11), 112005.
- SASAKI, M., KASUYA, N., ITOH, K., HALLATSCHKE, K., LESUR, M., KOSUGA, Y. & ITOH, S.-I. 2016 A branch of energetic-particle driven geodesic acoustic modes due to magnetic drift resonance. *Physics of Plasmas* **23** (10), 102501.
- SASAKI, M., KOBAYASHI, T., ITOH, K., KASUYA, N., KOSUGA, Y., FUJISAWA, A. & ITOH, S.-I. 2018b Spatio-temporal dynamics of turbulence trapped in geodesic acoustic modes. *Physics of Plasmas* **25** (1), 012316.
- SCOTT, B. 1997 Three-dimensional computation of drift alfvén turbulence. *Plasma Physics and Controlled Fusion* **39** (10), 1635–1668.
- SCOTT, B. & SMIRNOV, J. 2010 Energetic consistency and momentum conservation in the gyrokinetic description of tokamak plasmas. *Physics of Plasmas* **17** (11), 112302.
- SMITH, S. A. 1997 Dissipative closures for statistical moments, fluid moments, and subgrid scales in plasma turbulence. phdthesis.
- SQUIRE, J., QIN, H., TANG, W. M. & CHANDRE, C. 2013 The hamiltonian structure and euler-poincaré formulation of the vlasov-maxwell and gyrokinetic systems. *Physics of Plasmas* **20** (2), 022501.
- SRINIVASAN, K. & YOUNG, W. R. 2012 Zonostrophic instability. *Journal of the Atmospheric Sciences* **69** (5), 1633–1656.
- STAEBLER, G. M., KINSEY, J. E. & WALTZ, R. E. 2007 A theory-based transport model with comprehensive physics. *Physics of Plasmas* **14** (5), 055909.
- STEPHENS, C. 2019 Qualikiz: An analytic derivation. *Tech. Rep.*. DIFFER.
- SUCHY, K. 1981 Real hamilton equations of geometric optics for media with moderate absorption. *Radio Science* **16** (6), 1179–1182.
- SUGAMA, H. 2000 Gyrokinetic field theory. *Physics of Plasmas* **7** (2), 466–480.
- TAYLOR, G. I. 1915 I. Eddy motion in the atmosphere. *Philosophical Transactions of the Royal Society of London. Series A, Containing Papers of a Mathematical or Physical Character* **215** (523–537), 1–26.
- TERRY, P. W. 2000 Suppression of turbulence and transport by sheared flow. *Reviews of Modern Physics* **72** (1), 109–165.
- TERRY, P. W., BAVER, D. A. & GUPTA, S. 2006 Role of stable eigenmodes in saturated local plasma turbulence. *Physics of Plasmas* **13** (2), 022307.
- TOBIAS, S. M. & MARSTON, J. B. 2013 Direct statistical simulation of out-of-equilibrium jets. *Physical Review Letters* **110** (10).
- VUILLEMIN, P. & POUSSOT-VASSAL, C. 2019 Discretisation of continuous-time linear dynamical model with the Loewner interpolation framework , arXiv: 1907.10956v1.
- WALTZ, R. E. & HOLLAND, C. 2008 Numerical experiments on the drift wave–zonal flow paradigm for nonlinear saturation. *Physics of Plasmas* **15** (12), 122503.
- WALTZ, R. E., KERBEL, G. D. & MILOVICH, J. 1994 Toroidal gyro-landau fluid model turbulence simulations in a nonlinear ballooning mode representation with radial modes. *Physics of Plasmas* **1** (7), 2229–2244.

- WALTZ, R. E., STAEBLER, G. M., DORLAND, W., HAMMETT, G. W., KOTSCHENREUTHER, M. & KONINGS, J. A. 1997 A gyro-landau-fluid transport model. *Physics of Plasmas* **4** (7), 2482–2496.
- WANG, L., ZHU, B., XU, X.-Q. & LI, B. 2019 A Landau-fluid closure for arbitrary frequency response. *AIP Advances* **9** (1), 015217.
- WEINBERG, S. 1962 Eikonal method in magnetohydrodynamics. *Physical Review* **126** (6), 1899–1909.
- WESSON, J. 2011 *Tokamaks*. Oxford New York: Oxford University Press.
- WHITHAM, G. B. 1965 A general approach to linear and non-linear dispersive waves using a Lagrangian. *Journal of Fluid Mechanics* **22** (2), 273–283.
- YAKHOT, V. & ORSZAG, S. A. 1986 Renormalization group analysis of turbulence. i. basic theory. *Journal of Scientific Computing* **1** (1), 3–51.
- ZARZOSO, D., NASR, S., GARBET, X., SMOLYAKOV, A. I. & BENKADDA, S. 2019 Gyro-kinetic theory and global simulations of the collisionless tearing instability: The impact of trapped particles through the magnetic field curvature. *Physics of Plasmas* **26** (11), 112112.
- ZARZOSO, D., SARAZIN, Y., GARBET, X., DUMONT, R., STRUGAREK, A., ABITEBOUL, J., CARTIER-MICHAUD, T., DIF-PRADALIER, G., GHENDRIH, P., GRANDGIRARD, V., LATU, G., PASSERON, C. & THOMINE, O. 2013 Impact of energetic-particle-driven geodesic acoustic modes on turbulence. *Physical Review Letters* **110** (12).
- ZHU, H., ZHOU, Y. & DODIN, I. Y. 2020 Theory of the Tertiary Instability and the Dimits Shift from Reduced Drift-Wave Models. *Physical Review Letters* **124** (5).
- ZHU, H., ZHOU, Y., RUIZ, D. E. & DODIN, I. Y. 2018 Wave kinetics of drift-wave turbulence and zonal flows beyond the ray approximation. *Physical Review E* **97** (5), arXiv: 1712.08262v4.